Wave Overtopping and Stability Performance of Rubble Mound Breakwaters Exposed to Shallow Water Waves

Eldrup, Mads Røge

DOI (link to publication from Publisher):
10.54337/aau310867381

Publication date:
2019

Document Version
Publisher's PDF, also known as Version of record

WAVE OVERTOPPING AND STABILITY PERFORMANCE OF RUBBLE MOUND BREAKWATERS EXPOSED TO SHALLOW WATER WAVES

BY
MADS RØGE ELDRUP

DISSERTATION SUBMITTED 2019

AALBORG UNIVERSITY
DENMARK

Wave Overtopping and Stability Performance of Rubble Mound Breakwaters Exposed to Shallow Water Waves

Ph.D. Dissertation

Mads Røge Eldrup

Dissertation submitted April 2019

Dissertation submitted: April, 2019

PhD supervisor: Associate Professor Thomas Lykke Andersen
Aalborg University

PhD committee: Associate Professor Jens Peter Kofoed (chairman)
Aalborg University

Professor Josep R. Medina
Universitat Politècnica de València

Professor Peter Troch
Ghent University

PhD Series: Faculty of Engineering and Science, Aalborg University

Department: Department of Civil Engineering

ISSN (online): 2446-1636
ISBN (online): 978-87-7210-425-6

Published by:
Aalborg University Press
Langagervej 2
DK – 9220 Aalborg Ø
Phone: +45 99407140
aauf@forlag.aau.dk
forlag.aau.dk

Printed in Denmark by Rosendahls, 2019

Contents

Preface

This thesis is the outcome of my work since August 2015, when I was employed as a PhD student at Aalborg University. During this time, I have had the pleasure of meeting several of the people whose research I had only read about as a M.Sc. student. I have enjoyed my time as a PhD student during which I have been able to study in depth a specific topic and investigate any gaps within that topic. However, life as a PhD student is also a busy one where time for family and friends is limited. Yet without their and my colleagues' support, completing this PhD thesis would not have been possible.

I would first like to thank my supervisor Thomas Lykke Andersen who gave me the opportunity to become a PhD student. He generously spent time guiding me and discussing my research. I have been lucky to have a supervisor who cared so much for my work and assisted me promptly whenever I had questions.

I would also like to thank my colleagues at the Department of Civil Engineering. I am thankful to be surrounded by people who are not only my co-workers, but also my friends. I appreciate every constructive, work-related discussion and every social experience we have had together. A great thank you to the technicians who assisted me in all my experimental work. Thanks to everybody I have met during the past years at seminars, conferences, and PhD courses. Most of you have had some kind of impact on my work.

Thanks to my family and friends outside the university. The last three years have been tough and largely focused on research, but I have felt the support from everybody. A special thanks to my sister Pernille Røge for proofreading my thesis, and my son Nikolai for making me laugh until I forget about it.

Finally, I have to thank my wife, Ellen. My last year as a PhD student has been hectic. Ellen took care of everything at home so I could focus on my work; her efforts and dedication were at least as necessary for finishing this work as mine were.

Mads Røge Eldrup
Aalborg University, April, 2019

Curriculum Vitae

Mads Røge Eldrup

DATE OF BIRTH:
15 November 1990

WORK ADDRESS:
Department of Civil Engineering
Thomas Manns Vej 23
9220 Aalborg Ø, DK

ACADEMIC CAREER:

2015 to present	PhD Student, Division of Reliability, Dynamics and Marine Engineering, Aalborg University
2014 - 2015	Scientific Assistant, Aalborg University
2014	M.Sc. Structural and Civil Engineering, Aalborg University
2012	B.Sc. Civil Engineering, Aalborg University

EXPERIENCE:
Mads Røge Eldrup has a M.Sc. degree in Coastal Engineering from Aalborg University. After his M.Sc. degree, he worked at AAU performing model tests on a new breakwater located at Punta Catalina in the Dominican Republic. Since August 2015 he has been employed as a PhD student. His current research involves wave generation and wave separation analysis, hydraulic rock armour stability and wave overtopping of rubble mound breakwaters. His research is aimed at improving existing design tools related to the response of rubble mound breakwaters in shallow water conditions. His research covers both experimental work, corresponding analysis of data, and use of numerical models. In addition to his research, he has also taken part in teaching and supervising bachelor and master degree students.

Thesis Details

Thesis Title:	Wave Overtopping and Stability Performance of Rubble Mound Breakwaters Exposed to Shallow Water Waves
Ph.D. Student:	Mads Røge Eldrup
Supervisor:	Assoc. Prof. Thomas Lykke Andersen, Aalborg University

The main body of this thesis is composed of a collection of the following eight papers.

[A] Eldrup, M. R. and Lykke Andersen, T. (2019a). Applicability of nonlinear wavemaker theory. *Journal of Marine Science and Engineering*, 7(1):14

[B] Lykke Andersen, T., Eldrup, M. R., and Frigaard, P. (2017). Estimation of incident and reflected components in highly nonlinear regular waves. *Coastal Engineering*, 119:51–64

[C] Eldrup, M. R. and Lykke Andersen, T. (2019b). Estimation of incident and reflected wave trains in highly nonlinear two-dimensional irregular waves. *Journal of Waterway, Port, Coastal, and Ocean Engineering*, 145(1)

[D] Eldrup, M. R., Lykke Andersen, T., and Burcharth, H. F. (2019). Stability of rubble mound breakwaters – a study of the notional permeability factor. *Submitted to Water*

[E] Eldrup, M. R. and Lykke Andersen, T. (2019c). New formulae for rock armour stability in shallow water. *Submitted to Coastal Engineering*

[F] Christensen, N. F., Røge, M. S., Thomsen, J. B., Lykke Andersen, T., Burcharth, H. F., and Nørgaard, J. Q. H. (2014). Overtopping on rubble mound breakwaters for low steepness waves in deep and depth limited conditions. *Coastal Engineering Proceedings*, 1(34):6

[G] Eldrup, M. R. and Lykke Andersen, T. (2018a). Recalibration of overtopping roughness factors of different armour types. In *Coasts, Marine Structures and Breakwaters 2017*, pages 1011–1020

[H] Eldrup, M. R., Lykke Andersen, T., Thomsen, J. B., and Burcharth, H. F. (2018). Overtopping on breakwaters with a permeable crest. *Coastal Engineering Proceedings*, 1(36):17

In addition to the main papers, a number of papers and reports have been produced and are listed below, but not appended to this thesis. The publications are an extension of the work presented in the main body and focuses on experimental testing of rubble mound breakwater response, wave separation analysis and performance of active absorption systems.

[1] Burcharth, H. F. and Røge, M. S. (2015). *Undersøgelse af udviklingen i maksimale vandstande i den østligste del af Limfjorden Aalborg – Hals*. Department of Civil Engineering, Aalborg University

[2] Eldrup, M. R. and Lykke Andersen, T. (2016). *Two-Dimensional Model Test Study of New Western Breakwater Proposal for Port of Hanstholm*. Department of Civil Engineering, Aalborg University

[3] Eldrup, M. R. and Lykke Andersen, T. (2018b). *Three-Dimensional Model Test Optimisation of the New Cubipod Armoured Western Breakwater for Port of Hanstholm*. Department of Civil Engineering, Aalborg University

[4] Eldrup, M. R. and Lykke Andersen, T. (2018c). *Three-Dimensional Model Test Optimisation of the Spur Breakwater for Port of Hanstholm*. Department of Civil Engineering, Aalborg University

[5] Eldrup, M. R. and Lykke Andersen, T. (2018d). *Three-Dimensional Model Test Verification of the New Cubipod Armoured Western Breakwater for Port of Hanstholm*. Department of Civil Engineering, Aalborg University

[6] Eldrup, M. R. and Lykke Andersen, T. (2018e). *Two-Dimensional Model Test Verification of the New Cubipod Armoured Western Breakwater for the Port of Hanstholm*. Department of Civil Engineering, Aalborg University

[7] Lykke Andersen, T., Clavero, M., Eldrup, M. R., Frigaard, P., and Losada, M. (2018). Active absorption of nonlinear irregular waves. *Coastal Engineering Proceedings*, 1(36):12

[8] Lykke Andersen, T., Eldrup, M. R., and Clavero, M. (2019). Separation of long-crested nonlinear bichromatic waves into incident and reflected components. *Journal of Marine Science and Engineering*, 7(2):12

[9] Thomsen, J. B., Røge, M. S., Christensen, N. F., Lykke Andersen, T., and Van der Meer, J. W. (2014). Stability of hardly reshaping berm breakwaters exposed to long waves. *Coastal Engineering Proceedings*, 1(34):65

[10] Røge, M. S., Christensen, N. F., Thomsen, J. B., Nørgaard, J. Q. H., and Lykke Andersen, T. (2014a). Wave loads on rubble mound breakwater crown walls in long waves. *Coastal Engineering Proceedings*, 1(34):64

[11] Røge, M. S. and Lykke Andersen, T. (2015). *Three-Dimensional Model Test Study of Xbloc Armoured Breakwaters at Punta Catalina, Dominican Republic*. Department of Civil Engineering, Aalborg University

[12] Røge, M. S., Lykke Andersen, T., and Burcharth, H. F. (2014b). *Wave Analysis Study for the Punta Catalina Jetty, Dominican Republic*. Department of Civil Engineering, Aalborg University

Abstract

Conventional rubble mound breakwaters have been used mainly in shallow water wave conditions for constructing harbour basins or as coastal protection. However, most research has been performed with deep water wave conditions, and therefore some design codes still have gaps with shallow water wave conditions. Until the last decade, existing wave analysis and wave generation methods were only valid for deep water wave conditions. Yet more recently, wave generation methods for highly nonlinear irregular waves in intermediate and shallow water have been developed, but no studies with response of rubble mound breakwaters have used these methods. The present thesis investigates wave overtopping and rock armour stability of conventional rubble mound breakwaters exposed to shallow water wave conditions.

The validity range of the typical existing wave generation methods is tested in order to ensure high-quality waves in the tests with rubble mound breakwaters. Furthermore, new nonlinear wave separation methods are presented making it possible to obtain the incident waves that the rubble mound breakwater is exposed to.

The present hydraulic rock armour stability tests lead to a simple empirical formula for estimating the notional permeability factor of a conventional rubble mound breakwater. This has been a significant gap in more than 30 years as designers only estimated this value based on experience or physical model tests. Moreover, the present stability tests show that existing design tools underestimate the rock armour stability when exposed to highly nonlinear non-broken waves. Improved formulae valid for shallow water wave conditions are given in the present work.

The present wave overtopping tests with surging waves showed significantly more wave overtopping than estimated with existing formulae. A modification to the formulae given in the EurOtop Manual is proposed which significantly increases the reliability for surging waves without decreasing the reliability for plunging waves. Furthermore, the roughness coefficient

for existing armour units is refitted to the proposed modified formulae. For some rubble mound breakwaters, the armour crest freeboard is larger than the crest freeboard i.e vertical distance from still water level to the top of the crownwall or the level of the horizontal part of an impermeable layer in the breakwater. Thus water can flow trough the permeable armour crest and add additional wave overtopping to the total wave overtopping. For a situation like that, the EurOtop Manual provides guidelines for the freeboard height used in the wave overtopping estimations, but these guidelines have never been validated. However, the present work shows that the estimated wave overtopping based on the guidelines by the EurOtop Manual fits with the measured wave overtopping.

Resumé

Bølgebrydere har hovedsageligt været placeret steder hvor lavtvandsbølger forekommer som f.eks. ved konstruktion af havnebassiner eller som kystbeskyttelse. De fleste eksisterende laboratorieundersøgelser er hidtil blevet udført med dybtvandsbølger, og derfor har nogle designstandarder stadig mangler for lavtvandsbølger. Tilsvarende var eksisterende bølgeanalyse- og bølgegenereringsmetoder indtil det forrige årti kun gyldige for dybtvandsbølger. For nyligt er der udviklet ulineære bølgegenereringsmetoder gyldige for lavt vand, men disse metoder har endnu ikke været anvendt med tests af bølgebrydere. Denne afhandling undersøger bølgeoverskyl og dæklagsstabilitet af bølgebrydere, der udsættes for lavtvandsbølger ved hjælp af nye tests.

Gyldighedsområdet for de typiske eksisterende bølgegenereringsmetoder undersøges for at sikre, at bølgerne er af højeste kvalitet i testene med bølgebrydere. Derudover udvikles nye, ulineære bølgeseparationsmetoder som gør det muligt at estimere de indkommende bølger, som bølgebrydere er udsat for.

Testene med dæklagsstabilitet har ført til en simpel empirisk formel til at estimere den nominelle permeabilitetsfaktor for en bølgebryder. Dette har været en betydelig mangel igennem de sidste 30 år. Vandbygningsingeniører har førhen kun kunnet skønne denne værdi baseret på erfaring eller fysiske model forsøg. Desuden viser de udførte stabilitetsforsøg, at eksisterende designværktøjer undervurderer stabiliteten af dæklaget når bølgebryderen udsættes for stærkt ulineære, ikke-brydende bølger. Forbedrede formler, der er gyldige for lavtvandsbølger, præsenteres i det nuværende arbejde.

En række udførte tests med måling af overskyl for bølger der bryder ved total brænding viser signifikant mere overskyl end estimeret med eksisterende formler. En ændring af formlerne, der er givet i EurOtop Manual, foreslås, hvilket øger pålideligheden for total brænding bølger uden at reducere pålideligheden for styrtbrydende bølger. Endvidere justeres ruhedskoefficienten for eksisterende dæklagstyper til de modificerede formler. For nogle

bølgebrydere ligger dæklagsstenene højere end overbygningen eller over det horizontale niveau for det impermeable lag i bølgebryderen. Dette betyder at vandet kan strømme igennem dæklagsstenene og tilføre yderlig overskyl og bidrage til det totale overskyl. I sådan en situation giver EurOtop Manualen retningslinjer for fribordshøjden der skal anvendes i estimeringen af overskyl selvom disse retningslinjer aldrig er blevet valideret. Arbejdet i denne afhandling viser dog at det estimerede overskyl ud fra retningslinjerne givet i EurOtop Manualen passer med det målte overskyl.

Nomenclature

Abbreviations

CLASH	Crest Level Assessment of coastal Structures by full scale monitoring, neural network prediction and Hazard analysis on permissible wave overtopping
DHI	Danish Hydraulic Institute
EurOtop	European Overtopping Manual
SWL	Still Water Level
TAW	Technical Report on Wave run up and wave overtopping at dikes

Latin Nomenclature

a	Wave amplitude
A_c	Armour crest freeboard
C_r	Crest width reduction factor
CR	Wave reflection coefficient
g	Gravity acceleration
G_c	Crest width
$H_{1/3}$	Time domain significant wave height (average wave height of the 1/3 highest waves)
$H_{2\%}$	Wave height excceded by 2%
H_{m0}	Spectral significant wave height ($H_{m0} = 4\sqrt{m_0}$)
k	Wave number ($2\pi/L$)
K	Fictitious permeability

m_0	Zero order moment of the spectrum
m_{-1}	First order negative moment of the spectrum
N_w	Number of waves
N	Wave order
P	Notional permeability factor
q	Mean wave overtopping discharge
$q/\sqrt{gH_{\mathrm{m0}}^3}$	Dimensionless mean wave overtopping discharge
R_c	Crest freeboard
S	Wave nonlinearity parameter
T_P	Peak wave period
$T_{\text{-1,0}}$	Energy wave period ($T_{\text{-1,0}} = m_{-1}/m_0$)
T_m	Mean wave period
Π_0	Wave nonlinearity parameter (based on H_{m0} and T_P)
W_{50}	Median rock weight

Greek Nomenclature

α	Front slope angle
Δ	Reduced relative density ($\Delta = \rho_\mathrm{rock}/\rho_\mathrm{water} - 1$)
γ_f	Constant roughness factor
$\gamma_{\mathrm{f,mod}}$	Varying roughness factor
$\gamma_{\mathrm{f,surging}}$	Varying roughness factor
ω	Cyclic frequency
ϕ	Phase
η	Surface elevation
ρ_rock	Density of rock material
ρ_water	Density of water

1 Introduction

This thesis addresses responses of rubble mound breakwaters in shallow water. Rubble mound breakwaters are used worldwide to create harbours that shelter ships from the surrounding sea. The harbour enables ships to load or unload cargo without interruptions from possible ship displacements caused by waves. Furthermore, rubble mound breakwaters are used to ensure safe maneuvering by sheltering ships from waves at the harbour entrance. Another use of rubble mound breakwater is the protection of the coast from erosion or flooding of hinterlands.

Rubble mound breakwaters are often placed in shallow water where depth-induced wave breaking is typical for the design conditions. However, existing design tools for wave overtopping and rock armour stability are established mainly on physical model tests in deep water with no wave breaking on the foreshore. This might have been due to limitations in the wave generation and wave analysis methods that were available at the time. In recent decades, researchers have started to perform experimental model tests in shallow water, but in many cases the design tools have not been updated or accepted in the coastal engineering community. Thus, the validity of the design tools for the hydraulic response of rubble mound breakwaters remains unclear. Moreover, there is little knowledge of how to correctly perform model tests in shallow water. This chapter introduces problems pertaining to existing design tools.

1.1 Rubble Mound Breakwaters

Rubble mound breakwaters typically consist of a core, underlayer and an armour layer, cf. Fig. 1.1. The core is normally constructed with quarry run and rock material for the underlayer. The armour layer is constructed with either rocks or concrete armour units. Rock is the preferred option if rock material of significant size is available from nearby quarries. In areas where large fractions of rocks cannot be quarried or are too expensive in

transportation, concrete armour units are used.

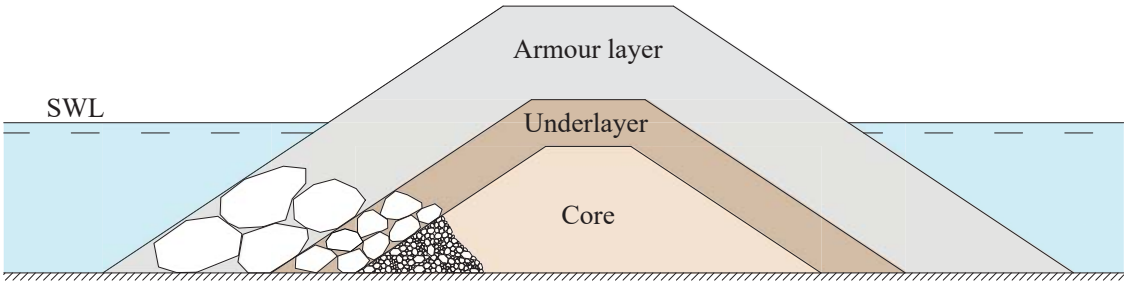

Fig. 1.1: Conventional rubble mound breakwater.

Berm breakwaters can be used in cases where the hydraulic response of a conventional rubble mound breakwater is insufficient or when equipment of large enough size is not available, cf. Fig. 1.2. The rock material used in the armour layer for berm breakwaters may have a larger variation in the size compared to the rocks used for conventional rubble mound breakwaters. The design of berm breakwaters allows for some reshaping of the armour layer until equilibrium is obtained, while no or minor movements are allowed in a conventional rubble mound breakwater.

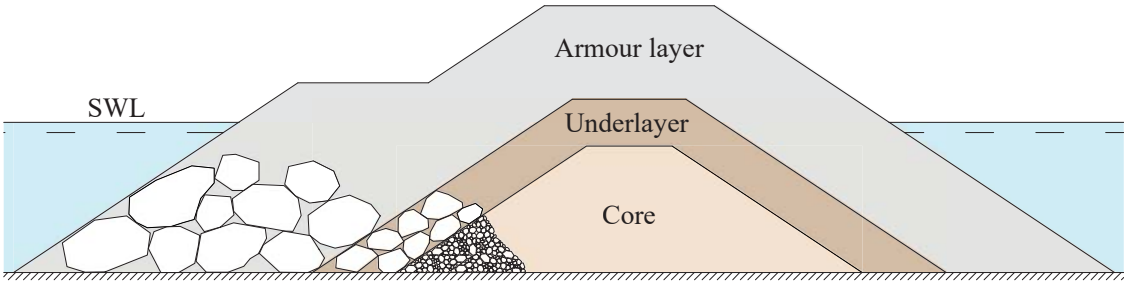

Fig. 1.2: Berm breakwater.

Rubble mound breakwaters are the preferred solution in shallow waters. Constructing a rubble mound in deeper water will significantly increase the amount of quarried rock needed for construction and thus vertical breakwaters or caissons should be considered as an alternative. Caissons are in many cases the preferred solution if the waves are small relative to the water depth. In such cases the wave loads will be quasi-static ($H_{1/3}/h < 0.2$). Caissons are large concrete structures which are typically built onshore and then floated to its final location. At that location, the structure is filled with sand and lowered onto a rubble mound foundation, cf. Fig. 1.3. A disadvantage of the caisson is the low dissipation of the wave energy compared to a rubble

mound breakwater. Therefore, rubble mound breakwaters are used more typically, as it leads to better navigational condition and less disturbance in the harbour basins. (CIRIA; CUR; CETMEF, 2007)

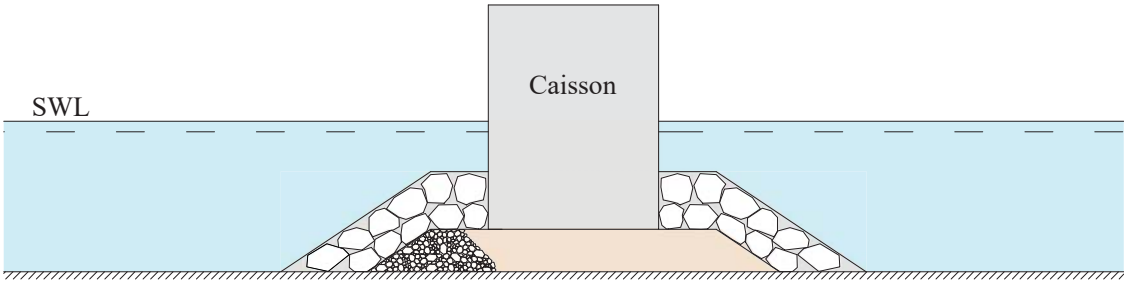

Fig. 1.3: Caisson/vertical breakwater.

Rubble mound breakwaters are different in size and layout from location to location due to difference in wave climate, available construction materials and construction equipment for the various sites. Because of these differences the presented rubble mound breakwaters and caissons are sometimes combined in different ways to obtain the needed performance at the given site, see U.S Army Corps of Engineers (2012).

Reliable design tools are important as new designs are made from location to location. However, most of these tools are not tested thoroughly for shallow water wave conditions with breaking and non-breaking waves on the foreshore. This is the situation even though these wave conditions are the most typical design conditions in exposed areas.

1.2 Shallow Water Wave Conditions

Design tools for wave overtopping and hydraulic stability of rubble mound breakwaters have a lack of knowledge for shallow water wave conditions. Shallow water waves are characterised by waves having a large wave height or wavelength compared to the water depth. Long waves ($h/L < 0.05$) can only be described with linear wave theory if the wave height is very small. Fig. 1.4 shows the Le Méhauté diagram which is a quantitative method to describe the linearity of a given sea state. Long waves close to the depth-induced breaking point are highly nonlinear as both H/L and H/h are large.

For an irregular sea state, the wave characteristics can be described by time and frequency domain parameters. The time domain significant wave height $H_{1/3}$ is the average of the one-third highest waves in the time domain. The spectral significant wave height H_{m0} is obtained from a frequency domain analysis (from the area of the spectrum). It is not always clear which

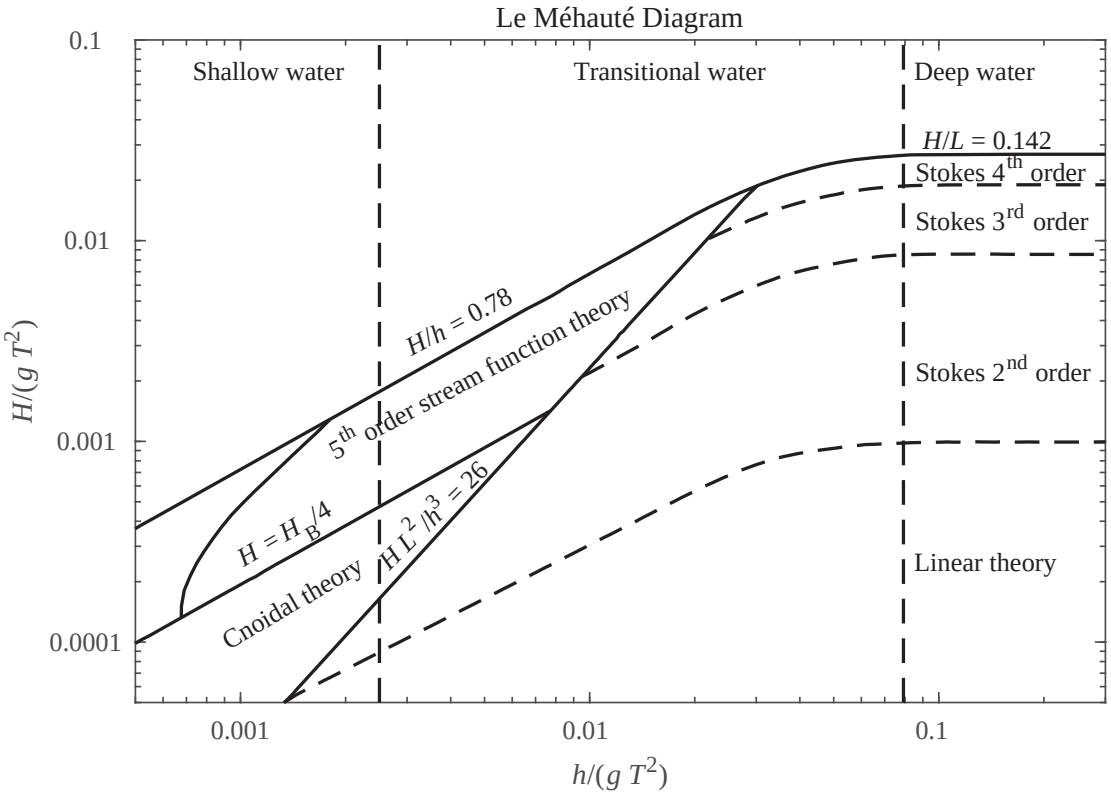

Fig. 1.4: Diagram indicating the validity of wave theories. Adapted from Le Méhauté (1969).

of the two wave heights is referred to in a given formula. The reason for this lack of clarity might be that the wave heights are almost identical for linear waves. However, for nonlinear waves, a large difference between the two wave heights is observed. Goda (2010) used the wave nonlinearity parameter Π_0 and the wave steepness to describe the ratio between the wave heights $H_{1/3}/H_{\mathrm{m0}}$. Large values of Π_0 are observed for sea states with a low wave steepness and wave heights close to the depth-induced wave breaking criteria. To describe locations where these shallow water conditions occur, wave data from the WAVEWATCH III model by Tolman et al. (2009) and bathymetry data by Amante and Eakins (2009) have been used. The WAVEWATCH III model contains global wave hindcast data from 1979 - 2009 with 30 min intervals. Fig. 1.5 shows the lowest wave steepness based on the peak wave period T_{P} which has the criteria $H_{\mathrm{m0}}/h \geq 0.4$ fulfilled at a water depth of 15 m. The figure shows that the west coast of North America and the south west coast of South America are exposed to nonlinear waves. The western part of Europe and the south and west coast of Australia are also exposed to highly nonlinear waves (depth limited long waves). These parts of the world are areas where existing design tools for rubble mound breakwaters might be unreliable.

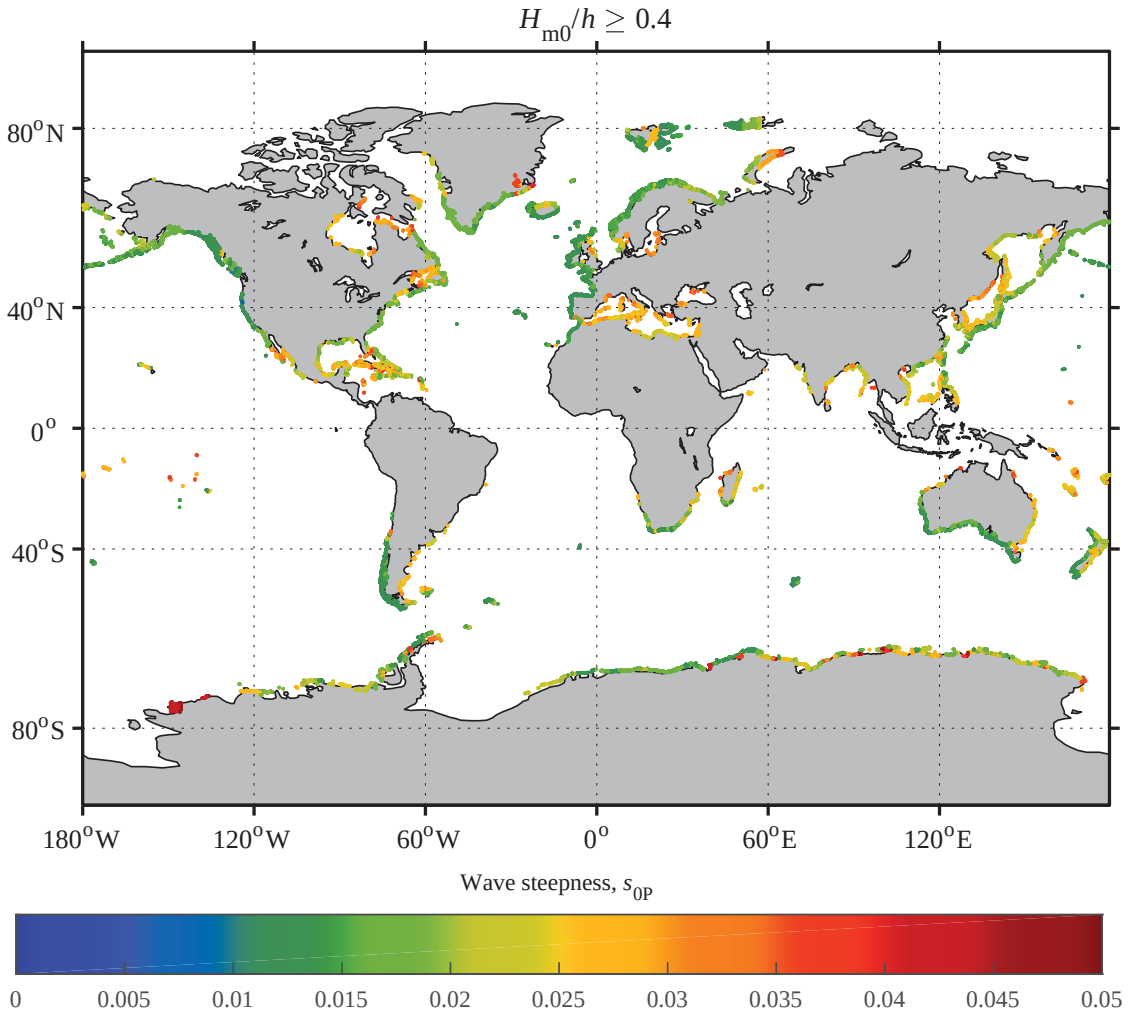

Fig. 1.5: Locations with depth-induced wave breaking at 15 m water depth based on wave hindcast data with WAVEWATCH III by Tolman et al. (2009) and bathymetry data by Amante and Eakins (2009). The colour shows the lowest deep water wave steepness based on WAVEWATCH III with $H_{m0}/h \geq 0.4$.

1.3 Thesis Outline

This thesis is structured as a collection of eight papers and an extended summary of five chapters that describes the outcome of the present work. Fig. 1.6 describes the structure of the research topics in the present thesis and the related papers. Chapter 2 describes existing methods for wave generation and the validity of each presented theory. Furthermore, new wave separation methods are presented and compared to existing methods.
Chapter 3 presents new formulae for rock armour stability in shallow water and a comparison with existing formulae are made. Moreover, a formula to estimate the notional permeability factor used in the rock armour stability

formulae are presented.
Chapter 4 presents a modification to the EurOtop Manual which increases the reliability of wave overtopping estimates for low steepness waves. Furthermore, the chapter evaluates a specific guideline given in the manual related to mean wave overtopping discharge estimation of rubble mound breakwaters without a crown wall.
Chapter 5 summarises the work with conclusions and perspectives for further work.

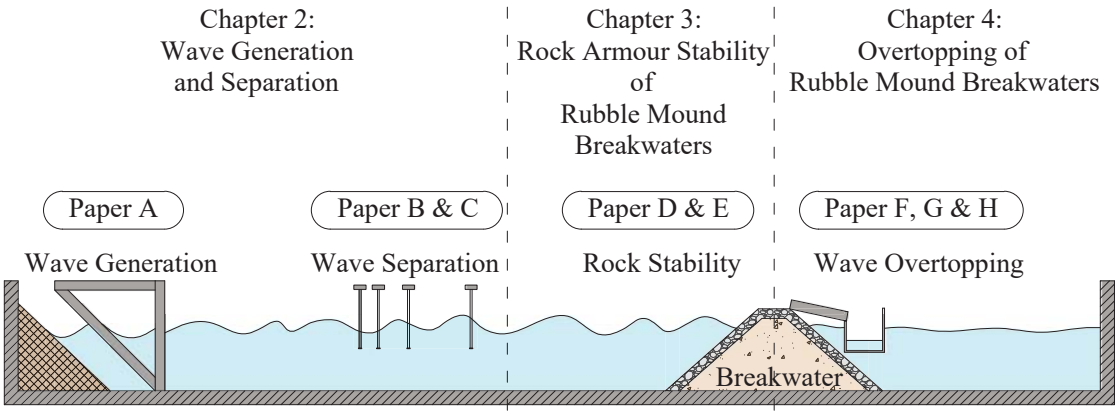

Fig. 1.6: Structure of research topics and papers in the this thesis.

2 Wave Generation and Separation

As explained in Chapter 1 the existing design tools for rubble mound breakwaters have not been tested in depth for nonlinear and shallow water waves so far. In the past, the existing wave generation theories and wave separation methods were based on linear wave theory. Thus, tests with nonlinear wave conditions would have been difficult unless a long foreshore was present in the facility. However, since then nonlinear wave generation methods have been developed and thus tests in shallow water can be performed with a short foreshore. This chapter compares nonlinear wave generation theories to linear and mildly nonlinear wave generation theories. Furthermore, it presents new nonlinear wave separation methods. As the later performed model tests are with long-crested waves, the studied methods will also include this limitation.

2.1 Wave Generation

Accurate generation of waves with similar characteristics as in nature is important when performing model tests. Incorrect wave generation might provide unreliable results on the response of the tested structure. Linear wave generation theory was first developed by Havelock (1929). Later, Schäffer (1993, 1996) developed a fully second-order theory for irregular waves. Zhang and Schäffer (2007) developed an ad-hoc unified highly nonlinear wave generation theory for regular waves in intermediate and shallow water while Zhang et al. (2007) extended that method to irregular waves. These nonlinear wave generation theories use the depth-averaged velocity from the incident wave field as input for the motion of the wavemaker. For regular waves, stream function wave theory by Fenton and Rienecker (1980) was used to calculate the depth-averaged velocity. For irregular waves they used

the Boussinesq wave model by Madsen and Sørensen (1992) implemented in MIKE 21 BW by Danish Hydraulic Institute (DHI).

The surface elevation of an incident nonlinear regular wave can be expressed by Eq. (2.1).

$$\eta = a^{(1)} \cos(kx - \omega t + \phi^{(1)}) + \sum_{n=2}^{N} a_{\mathrm{B}}^{(n)} \cos\left(n(kx - \omega t) + \phi_{\mathrm{B}}^{(n)}\right) + \sum_{n=2}^{N} a_{\mathrm{F}}^{(n)} \cos\left(k^{(n)} x - n\omega t + \phi_{\mathrm{F}}^{(n)}\right) \tag{2.1}$$

Here η is the surface elevation. a is the amplitude, k is the wave number of the primary component and k^n is the wave number of the nth-order free component. ω is the cyclic frequency and ϕ is the phase. Subscript B and F denote the bound and free harmonic components. x is location, and t is time. N is the wave order.

The bound wave components travel with the same celerity as the primary wave, while the free components travel with their own celerity. For regular waves, this means that the wave shape is not constant for any x when free wave components are present.

Free wave components can be present in a wave field for example due to wave breaking or if the bathymetry changes from a sloping foreshore to a horizontal one. Furthermore, nonlinear wave components can be released as free wave components if the water depth increases (Beji and Battjes, 1993). Free waves are also generated at the wavemaker if the wavemaker theory is not valid for the given sea state. Therefore, a valid wave generation theory should be used to avoid generating unwanted free wave components. So far there has not been a clear recommendation for the applicability of linear, second-order, and ad-hoc unified wave generation theories. Schäffer (1996) found for second-order wave generation theory that this theory was unreliable when a secondary wave crest was observed in the wave trough of the primary wave, see Fig. 2.1.

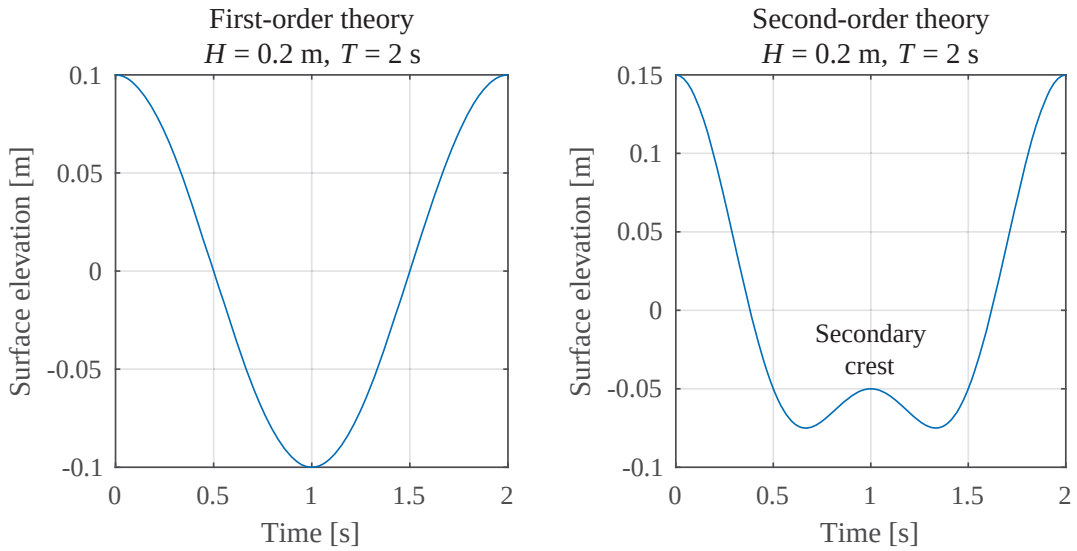

Fig. 2.1: Left figure shows a regular wave without any secondary wave crest. Right figure shows a secondary crest in the wave trough of the primary wave.

The secondary crest is observed when the second-order wave amplitude $a^{(2)}$ is larger than $1/4$ of the first-order wave amplitude $a^{(1)}$. To describe the validity of the second-order wave generation theory, Schäffer (1996) introduced a wave nonlinearity parameter S. In case this parameter is larger than one, the second-order theory is not valid. Le Méhauté (1969) introduced a diagram which also has been used by many to describe the applicability of the different wave generation theories. However, he described that further investigations were needed and that the diagram could only be used as a qualitative description of the validity.

Eldrup and Lykke Andersen (2019a) (Paper [A]) investigated the applicability of different wave generation theories with linear to highly nonlinear regular and irregular waves. They performed physical model tests with use of the wave generation theories by Havelock (1929), Schäffer (1996), Zhang and Schäffer (2007) and Zhang et al. (2007). Furthermore, Eldrup and Lykke Andersen (2019a) proposed a modification to the second-order theory by Schäffer (1996). For highly nonlinear waves, the theory by Schäffer (1996) estimates second-order amplitudes significantly larger than the first-order wave amplitude which is physically impossible. Instead, the modified second-order theory by Eldrup and Lykke Andersen (2019a) limits the second-order wave amplitude to be a maximum of $1/4a^{(1)}$.

Eldrup and Lykke Andersen (2019a) generated linear to highly nonlinear regular and irregular waves with the different wave generation theories and compared the results to theoretical surface profiles. For regular waves, the theoretical wave surface elevation was calculated with Fenton and Rienecker

(1980). For irregular waves no analytical model for highly nonlinear waves exists, instead Eldrup and Lykke Andersen (2019a) used the Boussinesq wave model COULWAVE by Lynett and Liu (2004). The time series generated with the COULWAVE model was also used as input for the nonlinear wave generation theory by Zhang et al. (2007).

Fig. 2.2 shows the surface elevation for a highly nonlinear regular wave generated with the different wavemaker theories with different distance x from the wavemaker. Regular waves with free wave components present shape change in the wave direction. The figure shows that only the waves generated with the theory by Zhang and Schäffer (2007) is a close match to the theoretical profile and remains of constant form. The constant wave form shows that this method has efficiently suppressed unwanted free waves. Furthermore, it should be noticed that the waves generated with the modified second-order theory by Eldrup and Lykke Andersen (2019a) are significantly better than the theory by Schäffer (1996) which has generated large secondary crests. However, the modified second-order theory by Eldrup and Lykke Andersen (2019a) is still deviating significantly from the theoretical profile with Fenton and Rienecker (1980) as the test is significantly outside the applicability range of second-order theory. In fact, the modified second-order theory did not extend the applicability range, although it did significantly improve the wave quality outside the applicability range.

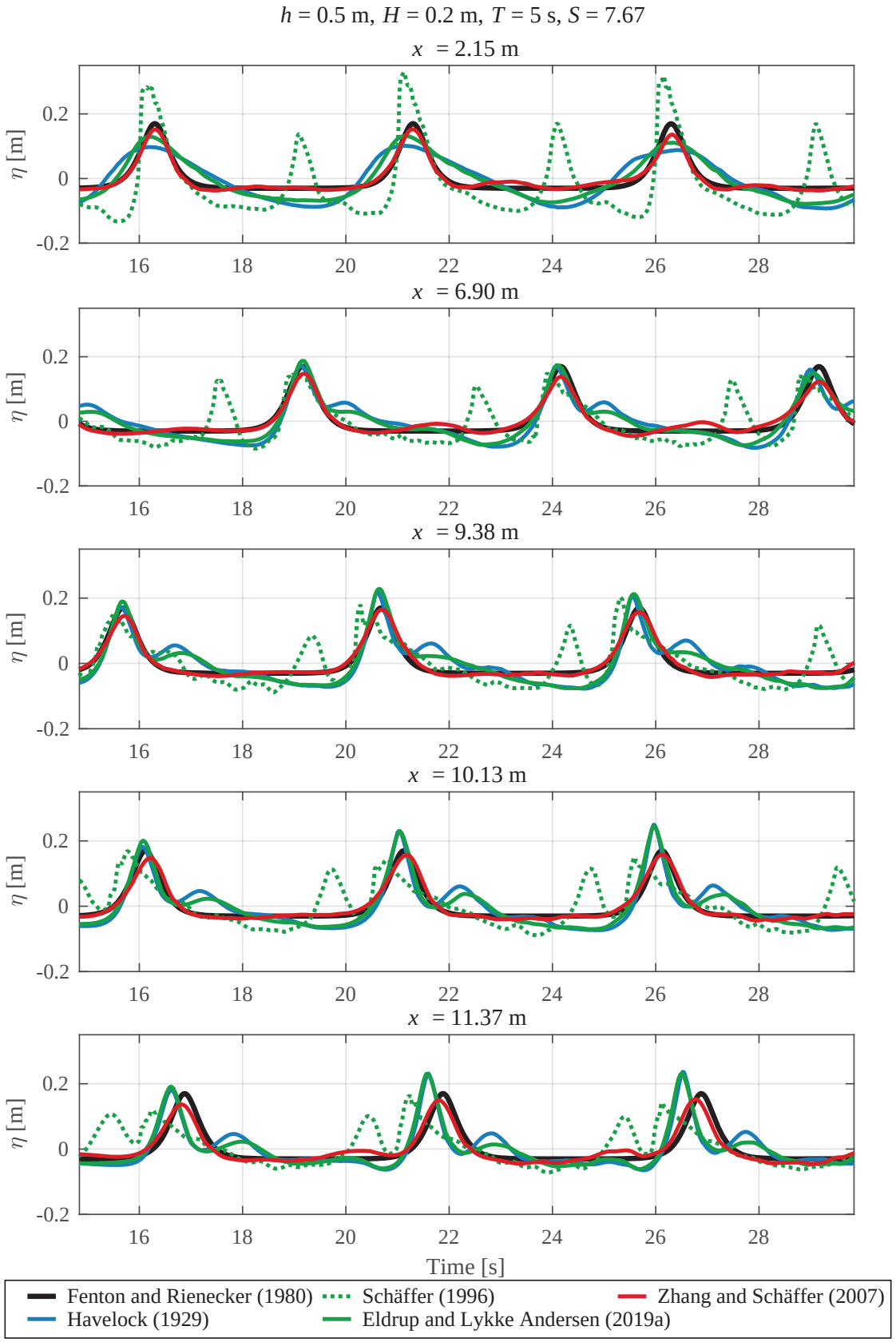

Fig. 2.2: Comparison between theoretical and generated regular waves with different wave generation theories. The distance to the wavemaker is given by x.

Based on the results by Eldrup and Lykke Andersen (2019a) applicability ranges of the tested wave generation methods are given for regular and irregular waves. The applicability is given as a function of the S parameter and the calculation of S for regular and irregular waves can be found in Eldrup and Lykke Andersen (2019a). Fig. 2.3 illustrates the validity of the tested wave generation theories in a diagram similar to the one by Le Méhauté (1969).

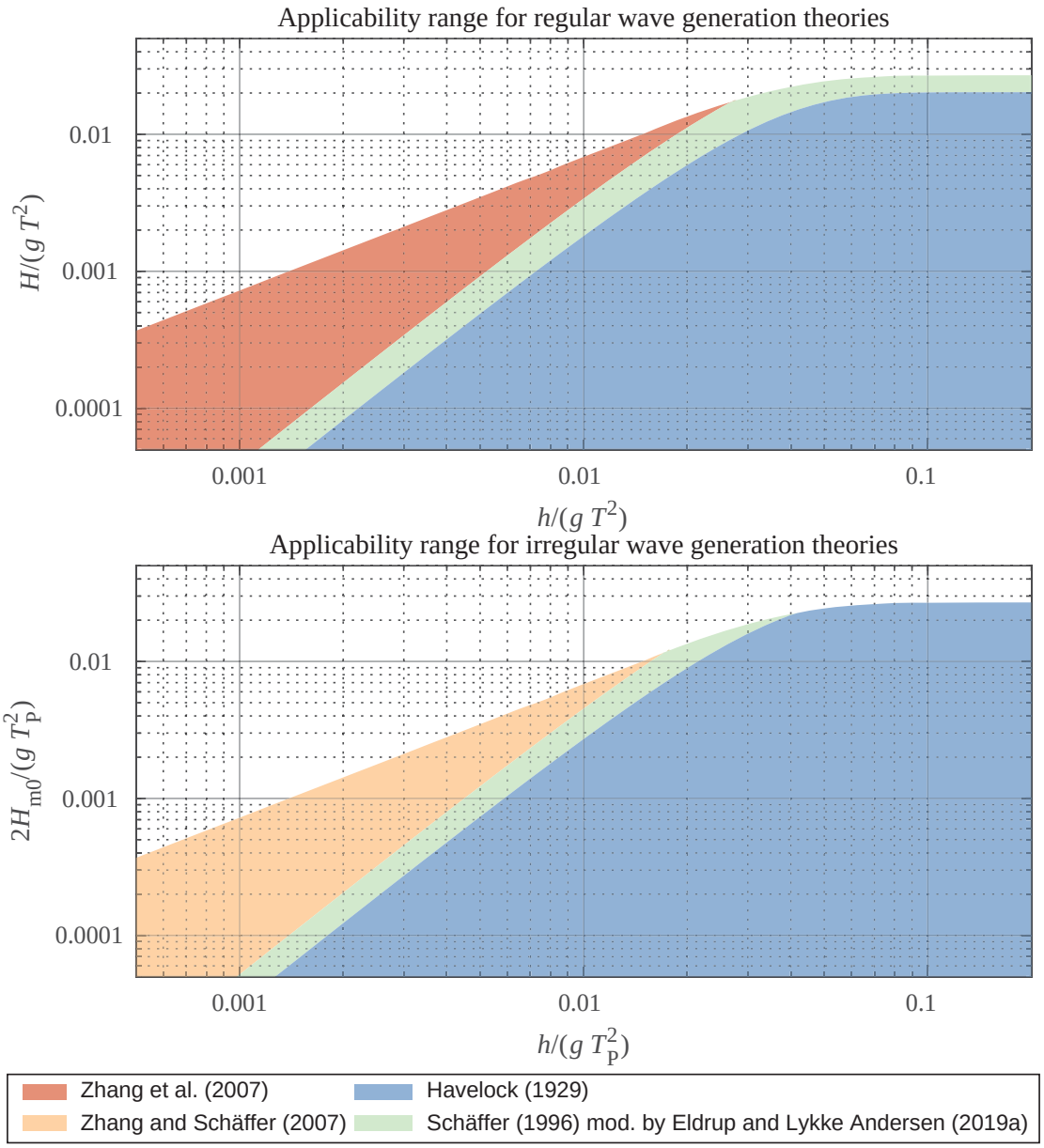

Fig. 2.3: Applicability ranges for the wave generation theories by Havelock (1929), modified Schäffer (1996) by Eldrup and Lykke Andersen (2019a), Zhang and Schäffer (2007) and Zhang et al. (2007). The coloured areas show the upper limit for the applicability range.

2.2 Separating Wave Field into Incident and Reflected Components

When performing hydraulic model tests, the total surface elevation is measured and it consists of incident waves from the wavemaker and reflected waves from the model. The incident waves are those of interest as these are related to the response of the structure, i.e. wave overtopping and armour stability. Therefore, wave separation methods are applied in order to separate the total surface elevation into incident and reflected waves. The incident waves can also be measured without the structure in place by repeating the same control signal of the wavemaker used with the model in place. However, to have identical incident waves with and without the model it would require a highly effective active absorption system of the wavemaker. For the calibration tests, it would require a highly effective passive absorber at the end of the flume. Even if effective absorption is used, the incident waves with and without the structure might not be identical, see Figure 9 in Eldrup and Lykke Andersen (2019b) (Paper [C]).

Most of the well-known wave separation methods are based on linear wave theory, cf. Goda and Suzuki (1976), Mansard and Funke (1980), Zelt and Skjelbreia (1992) and Frigaard and Brorsen (1995). Linear methods assume that the celerity of the wave can be described with the linear dispersion relation. These methods are widely used even though they are not valid for nonlinear waves. Figueres et al. (2003) developed a time domain solution, LASA V which is a nonlinear wave separation method. This method fits a 5^{th} order Stokes wave to the incident and reflected waves in local windows. Compared to the linear methods which are solved in the frequency domain, the computational demand is significantly larger for time domain solutions. Lin and Huang (2004) developed a nonlinear frequency domain wave separation method including bound and free components for regular waves. This method can separate the bound and free wave components due to their differences in celerity, but the method does not include amplitude dispersion which is important for highly nonlinear waves.

Lykke Andersen et al. (2017) (Paper [B]) extended the method by Lin and Huang (2004) to include amplitude dispersion which is calculated with the stream function wave theory by Fenton and Rienecker (1980). Lykke Andersen et al. (2017) tested linear to highly nonlinear waves consisting of six synthetic regular stream function waves with wave reflection coefficients $CR = H_R/H_I$ of 0, 0.5 and 1. To include tests with an asymmetric profile they further analysed two sea states on a 1:100 slope with zero wave reflection calculated with the COULWAVE model. The method by Lykke Andersen et al.

(2017) proved to be a significant improvement for the analysed sea states compared to the existing methods.

Fig. 2.4 shows a highly nonlinear sea state with $CR = 0$ calculated with stream function wave theory. With such highly nonlinear waves, a significant amount of the energy is bound to the primary component. Thus, linear methods provide unreliable results. The figure shows the estimated wave profile with use of Zelt and Skjelbreia (1992), Figueres et al. (2003) and Lykke Andersen et al. (2017). The result by Lykke Andersen et al. (2017) is a close match to the theoretical surface elevation. The two other methods show estimated surface profiles with a lot of ripples and the surface elevation of the wave crest is underestimated. Because most rubble mound breakwater tests are performed with irregular waves an extension of the method by Lykke Andersen et al. (2017) is needed.

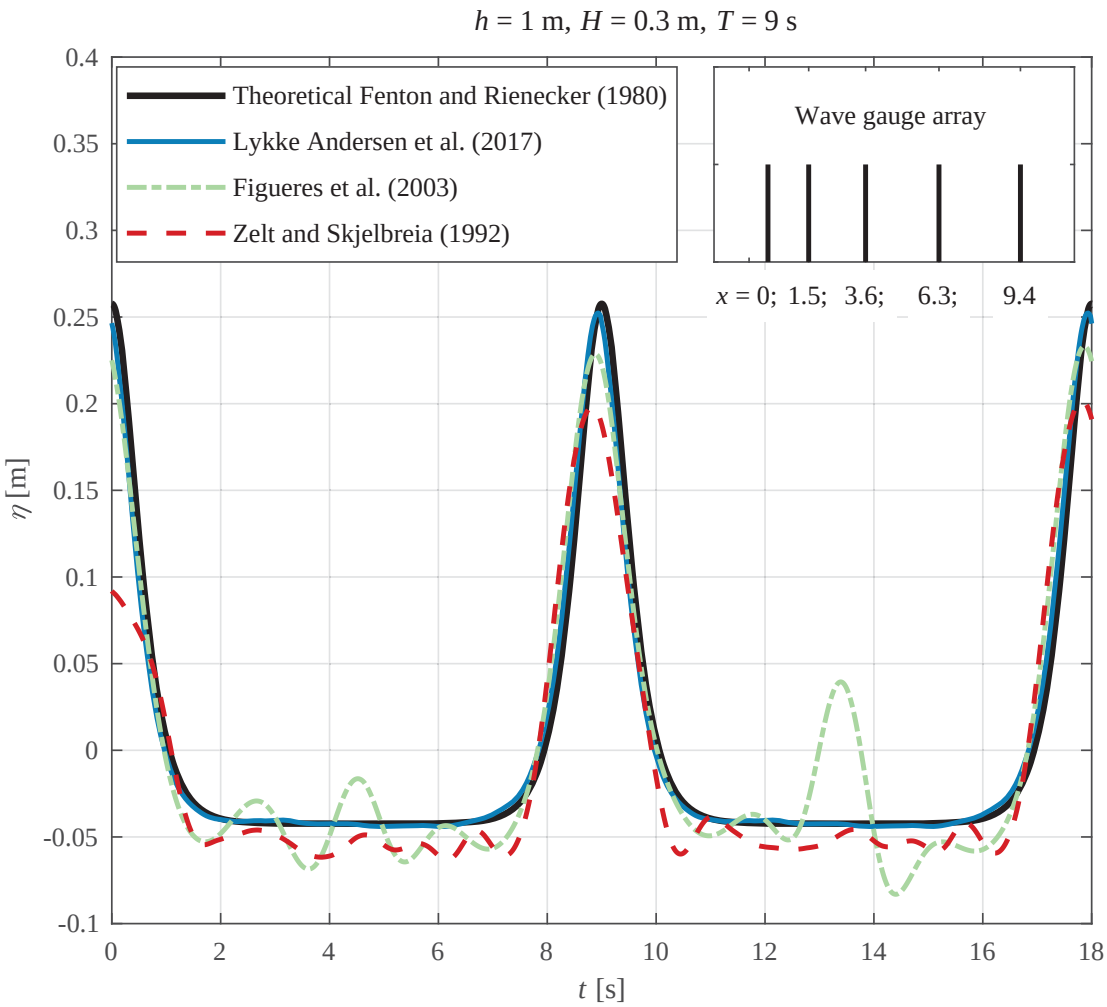

Fig. 2.4: Separation of regular waves with zero reflection. The surface elevation is estimated at $x = 0$ m.

Eldrup and Lykke Andersen (2019b) (Paper [C]) extended the method by Lykke Andersen et al. (2017) to irregular waves. In regular waves, all the bound energy is bound to a single primary component. However, irregular waves consist of many primary components and all combinations of these lead to bound harmonics. For a given frequency, multiple bound components can thus exist and these may have different celerities. Therefore, the celerity of the bound components at a given frequency is not easy to estimate. Eldrup and Lykke Andersen (2019b) assumed that the wave spectra were narrow banded, meaning that the bound components at a given frequency have identical celerity and may be calculated from a self-self interaction similar to regular waves. Based on second-order wave theory this assumption was found acceptable for wider spectra. For irregular waves, subharmonic wave components are present which stem from the interaction of many primary components. The celerity of the subharmonics was assumed to be equal to the group velocity at the peak frequency. Finally, the amplitude dispersion was also considered for irregular waves. The amplitude dispersion is not constant with time but is largest in the time series where the largest waves are observed. However, a constant value is assumed as the method by Eldrup and Lykke Andersen (2019b) is a frequency domain solution. Eldrup and Lykke Andersen (2019b) estimated the amplitude dispersion by comparing the linear wavelength to the stream function wavelength calculated with the peak wave period T_P and the spectral wave height H_{m0}. This assumption was compared to numerical data with nonlinear waves and the assumption was found to be acceptable.

Eldrup and Lykke Andersen (2019b) compared their model with the linear method by Zelt and Skjelbreia (1992) and the nonlinear LASA V model by Figueres et al. (2003) for nine numerical irregular wave conditions. Furthermore, one irregular wave series measured in the wave flume at Aalborg University was tested. Fig. 2.5 shows a highly nonlinear sea state with $CR = 0$ calculated with COULWAVE. The figure shows that the method by Eldrup and Lykke Andersen (2019b) provides an estimated wave profile close to the correct profile and wave heights from COULWAVE. The LASA V model shows large undulations and underestimations of the wave crest for the largest waves. The method by Zelt and Skjelbreia (1992) shows only minor undulations, but an underestimation of 13% is observed for the maximum wave height. Because of the wrong celerity the Zelt and Skjelbreia (1992) method would provide undulations if the profile was not estimated in the middle of the wave gauge array.

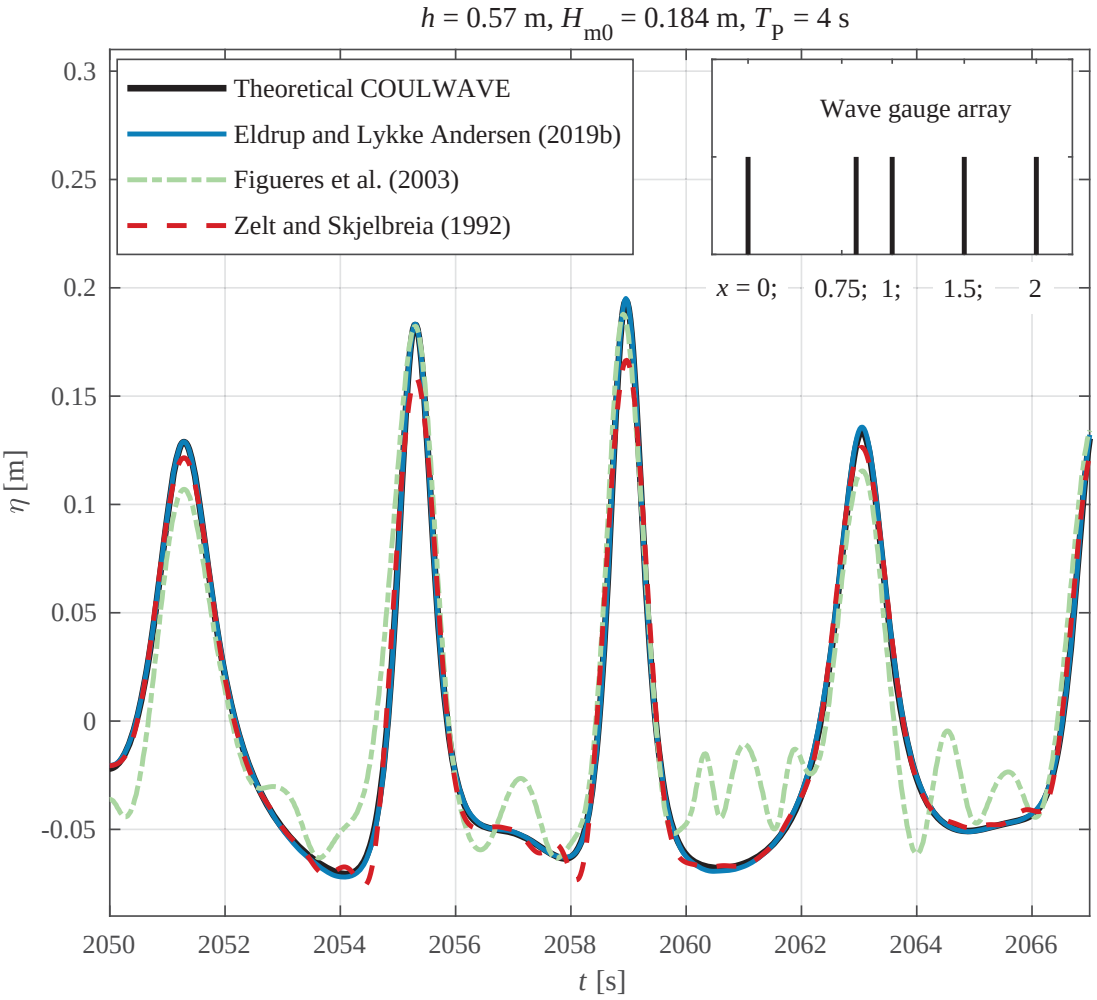

Fig. 2.5: Separation of irregular waves with zero reflection. The surface elevation is estimated at $x = 1$ m.

Thus, the needed tools to generate and analyse accurately nonlinear long-crested waves have been found.

3 Rock Armour Stability of Rubble Mound Breakwaters

Chapter 1 explained that the existing design tools for rock armour stability have not been tested thoroughly for shallow water wave conditions. With the gained information on the applicability of wave generation theories and the developed nonlinear wave separation methods from Chapter 2, this chapter presents new hydraulic model tests and tools for designing rock armour stability for rubble mound breakwaters.

3.1 Existing Stability Formulae

Some of the early research on hydraulic stability of rock armoured rubble mound breakwaters were performed in the 1930s. Iribarren (1938) and Hudson (1959) were some of the first to investigate the hydraulic stability of rock armoured rubble mound breakwaters. They tested regular waves with deep water wave conditions. Iribarren (1938) and Hudson (1959) established a formula to estimate the required weight of the rock material based on front slope angle, rock density, wave height and breaker type.

The description of the wave breaking type was first introduced by Iribarren and Nogales (1949) by the surf similarity parameter, also known as the Iribarren number. Battjes (1974) used the surf similarity parameter to separate the wave breaking types into three categories: spilling, plunging, and surging or collapsing breakers, see Fig. 3.1. Even though the figure describes the wave breaking type on the foreshore, the same descriptions are used to describe the wave breaking type on the front slope of the breakwater.

Thompson and Shuttler (1975) performed tests with irregular waves in deep water wave conditions from which they established a stability formula.

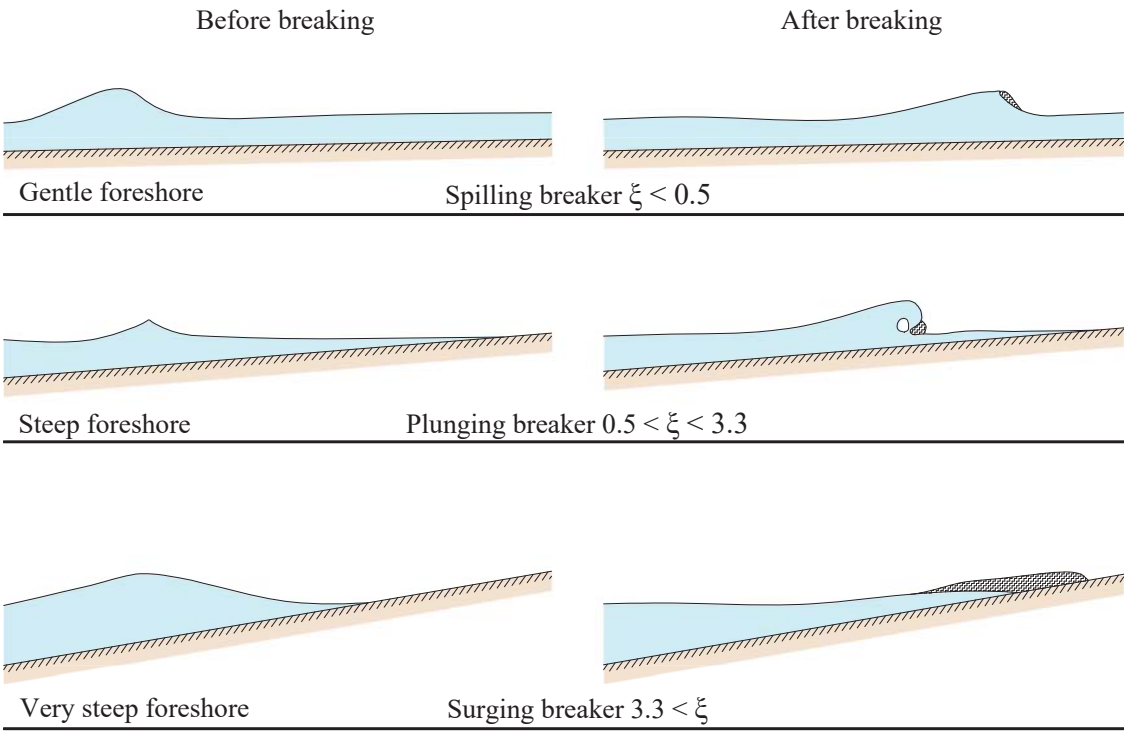

Fig. 3.1: Breaking wave types.

Van der Meer (1988) extended the work by Thompson and Shuttler (1975) to include tests with three different layer compositions and three rock armour densities. Van der Meer (1988) tested mainly deep water wave conditions without any depth-induced wave breaking. Van der Meer (1988) established two formulae for each of the tested layer compositions, and combined these by including a notional permeability factor P. For each tested structure, P values of 0.1, 0.5 and 0.6 were fitted and included in Eq. (3.1). He estimated a P of 0.4 for a fourth layer composition with a core, underlayer, and armour layer. Fig. 3.2 shows the notional permeability factors given by Van der Meer (1988).

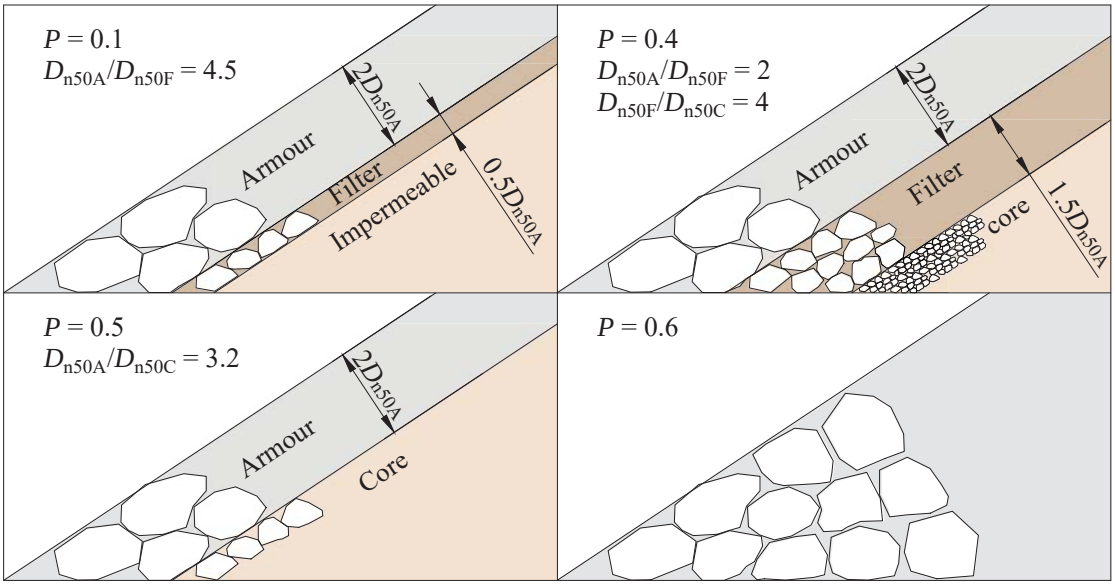

Fig. 3.2: Notional permeability factor given by Van der Meer (1988).

The two stability formulae by Van der Meer (1988) were separated by the type of wave breaking, one for plunging waves and one for surging waves, see Eq. (3.1).

Plunging waves ($\xi_{0m} < \xi_{0m,cr}$ or $\cot(\alpha) \geq 4$):

$$\frac{H_{1/3}}{\Delta D_{n50A}} = 6.2P^{0.18}\left(\frac{S_d}{\sqrt{N_w}}\right)^{0.2}\xi_{0m}^{-0.5}$$

Surging waves ($\xi_{0m} \geq \xi_{0m,cr}$ and $\cot(\alpha) < 4$):

$$\frac{H_{1/3}}{\Delta D_{n50A}} = P^{-0.13}\left(\frac{S_d}{\sqrt{N_w}}\right)^{0.2}\sqrt{\cot(\alpha)}\xi_{0m}^{P} \tag{3.1}$$

Transition between plunging and surging formulae:

$$\xi_{0m,cr} = \left(6.2P^{0.31}\sqrt{\tan(\alpha)}\right)^{\frac{1}{P+0.5}}$$

Here $H_{1/3}$ is the significant wave height from time domain, $\Delta = \rho_{rock}/\rho_{water}$ - 1 is the reduced relative density of the armour rocks and D_{n50A} is the nominal rock armour size based on the median stone mass W_{50}. P is the notional permeability factor, α is the front slope angle. N_w is the number of waves. The surf similarity parameter ξ_{0m} is defined in Eq. (3.2). Van der Meer (1988)

recommended to replace $H_{1/3}$ with $H_{2\%}/1.4$ for cases with breaking waves on the foreshore, but this recommendation was only based on a few tests.

$$\xi_{0\mathrm{m}} = \frac{\tan(\alpha)}{\sqrt{\frac{2\pi H_{1/3}}{g T_m^2}}} \tag{3.2}$$

The formulae by Van der Meer (1988) is widely used to estimate the required size of the rock armour units for conventional rubble mound breakwaters. However, since the tests by Van der Meer (1988) were mainly with deep water wave conditions, the validity for shallow water wave conditions is questionable.

Van Gent et al. (2004) noted that the stability formulae by Van der Meer (1988) was mainly tested with deep water waves. Therefore, Van Gent et al. (2004) performed a large study with shallow water wave conditions with breaking and broken waves. They tested a gentle (1:100) and a steep (1:30) foreshore in front of the rubble mound breakwater. Based on these tests, they modified the formulae by Van der Meer (1988) to include the wave energy period $T_{-1,0}$ instead of the mean wave period T_{m}. Van Gent and Smith (1999) and Van Gent (2001) found that $T_{-1,0}$ was also better to describe the wave run-up and wave overtopping in shallow water wave conditions. The modified stability formulae by Van Gent et al. (2004) read:

Plunging waves ($\xi_{\mathrm{s,-1}} < \xi_{\mathrm{c}}$ or $\cot(\alpha) \geq 4$):

$$\frac{H_{2\%}}{\Delta D_{\mathrm{n50A}}} = 8.4 P^{0.18} \left(\frac{S_{\mathrm{d}}}{\sqrt{N_{\mathrm{w}}}} \right)^{0.2} \xi_{\mathrm{s,-1}}^{-0.5}$$

Surging waves ($\xi_{\mathrm{s,-1}} \geq \xi_{\mathrm{c}}$ and $\cot(\alpha) < 4$):

$$\frac{H_{2\%}}{\Delta D_{\mathrm{n50A}}} = 1.3 P^{-0.13} \left(\frac{S_{\mathrm{d}}}{\sqrt{N_{\mathrm{w}}}} \right)^{0.2} \sqrt{\cot(\alpha)} \xi_{\mathrm{s,-1}}^{P} \tag{3.3}$$

Transition between plunging and surging formulae:

$$\xi_{\mathrm{c}} = \left(\frac{8.4}{1.3} P^{0.31} \sqrt{\tan(\alpha)} \right)^{\frac{1}{P+0.5}}$$

Here $H_{2\%}$ is the wave height exceeded by 2% of the waves, $\Delta = \rho_{\mathrm{rock}}/\rho_{\mathrm{water}}$ - 1 is the reduced relative density of the armour rocks and D_{n50A} is the nominal rock armour size based on the median stone mass W_{50}. P is the notional

permeability factor, α is the front slope angle. N_w is the number of waves. The surf similarity parameter $\xi_{s,-1}$ is defined in Eq. (3.4).

$$\xi_{s,-1} = \frac{\tan(\alpha)}{\sqrt{\frac{2\pi H_{1/3}}{g T_{-1,0}^2}}} \tag{3.4}$$

Muttray and Reedijk (2009) investigated the rock armour stability and the influence of a steep foreshore. As expected, they found that the stability was related to the wave characteristic at the toe of the structure instead of the wave characteristic offshore. However, they concluded this based on the spectral wave height H_{m0} and not from time domain parameters like $H_{1/3}$ or $H_{2\%}$. Herrera et al. (2017) observed that the spectral wave height H_{m0} was better to describe the rock amour stability than $H_{1/3}$ or $H_{2\%}$. They tested the rock armour stability with a foreshore slope 1:50 with breaking and non-breaking waves. Herrera et al. (2017) established a formula with use of H_{m0}, but their test programme included only one front slope angle and two wave steepnesses and therefore their formula has a limited range of applicability.

3.2 New Tool for Predicting the Notional Permeability Factor

The formulae by Van der Meer (1988) includes the influence from the permeability of the rubble mound breakwater by the notional permeability factor P. The notional permeability factor is largest for a homogeneous composition and smallest for an impermeable composition consisting of a two-layered armour layer and a very thin underlayer. Thus, the notional permeability factor is a function of the permeability of the core and the material size and thickness of the armour and filter/underlayer. The notional permeability factor is also included in the modified Van der Meer formulae by Van Gent et al. (2004). Van der Meer (1988) gave four values for four different layer compositions where one of these layer compositions was never tested. Kik (2011) and Kluwen (2012) performed tests on two new layer compositions and fitted P factors with use of the stability formulae by Van der Meer (1988). Van der Meer et al. (2018a) tested the influence from layer thickness and grading to the notional permeability factor. They found for a wide grading that the notional permeability factor decreased compared to typical used narrow gradings. Furthermore, by increasing the layer thickness an increase of the notional permeability factor was observed. Based on a layer composition with an impermeable core, a thick filter layer with a wide grading and a two-layered rock armour, a P factor of 0.15-0.20 was recommended.

The notional permeability factor is an important parameter when estimating the required size of the rock material in the armour layer. Designers are typically using different layer compositions from location to location due to the available rock material and construction equipment. Thus, the notional permeability factor often varies for each location. Designers are estimating P from experience or based on new hydraulic stability tests. A reliable formula to estimate the notional permeability factor for untested layer compositions is necessary for an easier design process and for more reliable designs.

Eldrup et al. (2019) (Paper [D]) performed several tests with rock armour stability for seven different layer compositions. Based on their tests and the tested layer compositions by Van der Meer (1988), Kik (2011), Kluwen (2012) and Van der Meer et al. (2018a) a total of 13 layer compositions and notional permeability factors were found. Based on these layer compositions Eldrup et al. (2019) established an empirical formula to estimate the notional permeability factor. They found that the notional permeability factor was a function of the material size and the distance from the layer to the armour surface. The material size and layer thickness were combined into a fictitious permeability K in Eq. (3.5).

$$K = \int_0^{Z^*_{\max}} f(z^*) g(z^*)\, dz^* \tag{3.5}$$

Here f and g are functions describing the influence from distance and material size respectively. z^* is a relative depth parameter, see Eldrup et al. (2019) for the definition. The maximum depth for the integration was found to be $Z^*_{\max} = 13$. Eq. (3.5) can be rewritten into a closed form solution:

$$K = 0.79 \sum_{i=1}^{N} \left[1 - \exp\left(-4.1 \frac{D_{\mathrm{n50},i}}{D_{\mathrm{n50A}}} \right) \left(\frac{\exp(-0.62 z_1^*) - \exp(-0.62 z_2^*)}{0.62} \right) \right] \tag{3.6}$$

Here $D_{\mathrm{n50},i}$ is the nominal size of the units in layer i and D_{n50A} is the rock armour size. The definition of z_1^* and z_2^* is illustrated for $i = 2$ in Fig. 3.3.

Eq. (3.7) was established based on K to estimate the notional permeability factor P.

$$P = \max \begin{cases} 0.1 \\ 1.72K - 1.58 \end{cases} \tag{3.7}$$

The estimation of P was found to be within $\pm$ 0.03 of the fitted P for the 13 tested conditions.

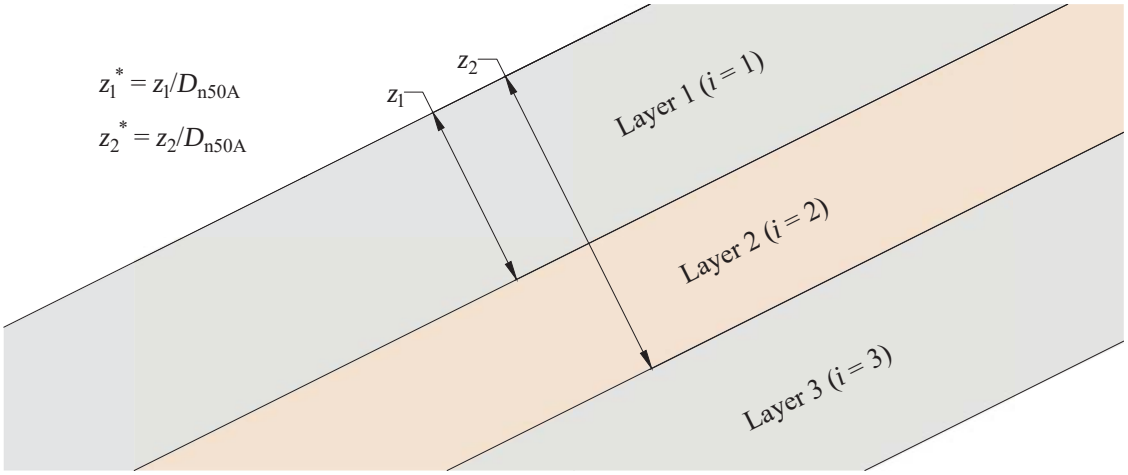

Fig. 3.3: Definition of the relative depth z_1^* and z_2^* for layer two (i = 2).

3.3 New Shallow Water Stability Formulae

In the study by Eldrup et al. (2019) deviations from the stability formulae were observed. Therefore, Eldrup and Lykke Andersen (2019c) (Paper [E]) performed new hydraulic stability tests with rock armoured rubble mound breakwaters to investigate rock armour stability in wave conditions not tested by Van der Meer (1988) and Van Gent et al. (2004). Eldrup and Lykke Andersen (2019c) tested one layer composition on gentle and steep foreshores (1:100 and 1:30). The tests on the gentle foreshore included mildly nonlinear waves in deep and shallow water, while the steep foreshore included highly nonlinear waves in shallow water. Eldrup and Lykke Andersen (2019c) observed that the rock armour stability for the mildly nonlinear waves were acceptable estimated with Eq. (3.3). However, for the highly nonlinear waves the stability was significantly larger than estimated with Eq. (3.3). Eldrup and Lykke Andersen (2019c) found that for these nonlinear waves the wave height ratio $H_{1/3}/H_{m0} \gg 1$ was found while for the mildly nonlinear waves $H_{1/3}/H_{m0} \approx 1$ was found. Goda (2010) describes that the difference between H_{m0} and $H_{1/3}$ increases as the nonlinearity of the waves increases. Eldrup and Lykke Andersen (2019c) found that by using H_{m0} instead of $H_{2\%}$ the rock armour stability for mildly nonlinear and highly nonlinear waves was better described. Based on this finding Eldrup and Lykke Andersen (2019c) established new rock armour stability formulae:

Plunging waves ($\xi_{-1,0} < \xi_{\text{-1,0,cr}}$):

$$\frac{H_{\text{m0}}}{\Delta D_{\text{n50A}}} = 4.5 \left(\frac{S_{\text{d}}}{\sqrt{N_{\text{w}}}} \right)^{0.2} 1.6^{P} \xi_{-1,0}^{(0.4P-0.67)}$$

Surging waves ($\xi_{-1,0} \geq \xi_{\text{-1,0,cr}}$):

$$\frac{H_{\text{m0}}}{\Delta D_{\text{n50A}}} = 3.1 \left(\frac{S_{\text{d}}}{\sqrt{N_{\text{w}}}} \right)^{0.2} P^{0.17} \min(\cot(\alpha), 2)^{0.23} \tag{3.8}$$

Transition between plunging and surging formulae:

$$\xi_{\text{-1,0,cr}} = \left(\frac{0.69 P^{0.17} \min(\cot(\alpha), 2)^{0.23}}{1.6^{P}} \right)^{\frac{1}{0.4P-0.67}}$$

Here $\xi_{-1,0}$ is defined in Eq. (3.9).

$$\xi_{-1,0} = \frac{\tan(\alpha)}{\sqrt{\frac{2\pi H_{\text{m0}}}{g T_{-1,0}^{2}}}} \tag{3.9}$$

The stability formulae by Eldrup and Lykke Andersen (2019c) were not validated for deep water conditions as the data by Thompson and Shuttler (1975) and Van der Meer (1988) does not include the wave parameters H_{m0} and $T_{\text{-1,0}}$. The formulae were fitted to the data by Van Gent et al. (2004), Eldrup et al. (2019), and Eldrup and Lykke Andersen (2019c) which mainly includes waves with shallow foreshore to very shallow foreshore according to the relative water depth definition by Hofland et al. (2017), see Fig. 3.4. In the figure it is assumed that $H_{\text{m0}} \approx H_{1/3}$ for the tests by Van der Meer (1988). The tests by Van der Meer (1988) are mainly performed in deep water according to the relative water depth definition. Until new deep water tests have been carried out it is recommended to use the formulae by Van der Meer (1988) for deep water conditions $H_{\text{m0, deep}}/h < 0.25$ and only the present formulae for shallow foreshore conditions $H_{\text{m0, deep}}/h \geq 0.25$.

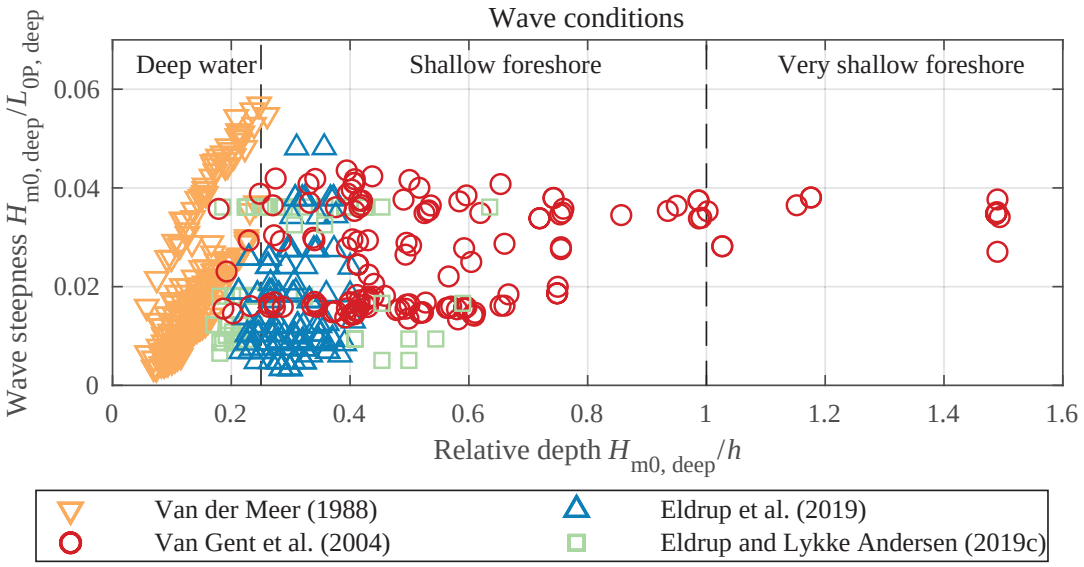

Fig. 3.4: Wave steepness in deep water and the relative water depth at the toe compared to the wave height in deep water.

The new formulae showed to be a significant improvement on the reliability when considering the rock armour stability for nonlinear waves. Furthermore, the new formulae showed similar accuracy as Eq. (3.3) on the data by Van Gent et al. (2004). Fig. 3.5 shows the estimated and measured damage for the data by Van Gent et al. (2004), Eldrup et al. (2019) and Eldrup and Lykke Andersen (2019c) for Eq. (3.3) and (3.8). The figure shows that Eq. (3.8) reduces the scatter significantly compared to Eq. (3.3).

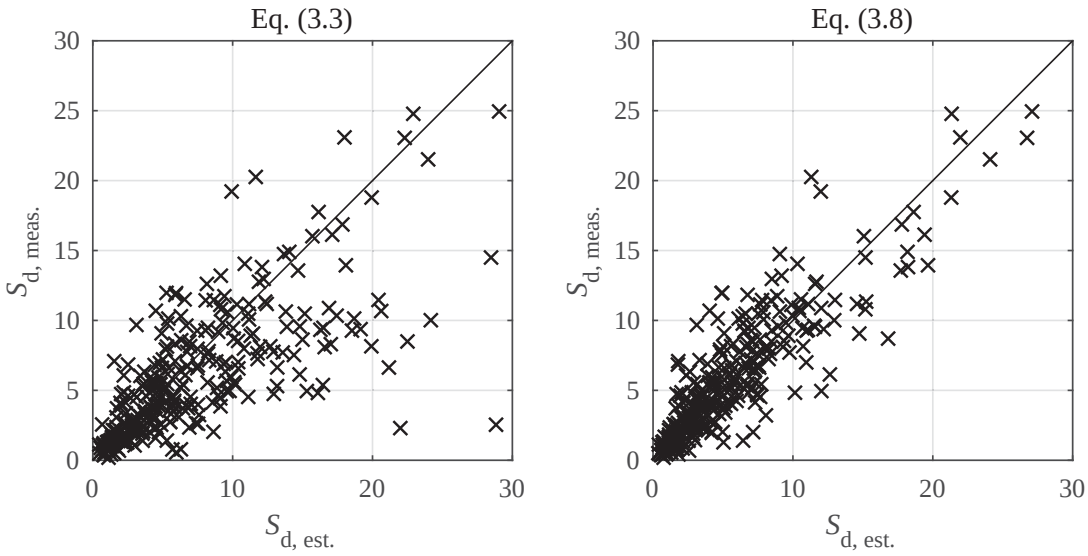

Fig. 3.5: Measured and estimated damage S_d for the data by Van Gent et al. (2004), Eldrup et al. (2019) and Eldrup and Lykke Andersen (2019c). Left shows the estimations with the modified Van der Meer formulae by Van Gent et al. (2004). Right shows the estimations with the formulae by Eldrup and Lykke Andersen (2019c).

4 Overtopping of Rubble Mound Breakwaters

Chapter 1 explained that the existing design tools for mean wave overtopping discharge have not been tested in detail for shallow water wave conditions. For this reason new tests were carried out and reported in Paper [F] and [G]. The present chapter presents the new design tools developed based on these tests. Furthermore, the recommendation given in the EurOtop Manual (Van der Meer et al., 2018b) for estimating wave overtopping discharge for cases where water can flow through the armour crest is investigated in Paper [H] and found to be accurate.

4.1 Existing Overtopping Tools

Wave overtopping is an important parameter in the design of the crest freeboard and thus the total height of the rubble mound breakwater. The height of the breakwater is often a balance between total cost and the tolerable wave overtopping. If too much wave overtopping is present, both the breakwater and objects behind might be damaged.

Many designers use the EurOtop Manual for estimating the mean overtopping discharge. The first edition of the manual was released in 2007. Before that, different manuals were used by different countries. In the UK, the EA Manual (Besley, 1998) were used; in the Netherlands the Technical Report on Wave run up and wave overtopping at dikes (TAW) (Van der Meer, 2002), and in Germany the Die Küste (für Küstenschutzwerke, 2002). The first version of the EurOtop Manual was based on a large EU project (CLASH) where a large amount of wave overtopping data from laboratories in different countries were collected. New experimental tests were also performed. The collected data resulted in the first EurOtop Manual and the CLASH Neural Network (Van Gent et al., 2007). The CLASH Neural Network is a com-

puter trained model based on the CLASH database containing approximately 10,000 physical model tests. The model works as a black box, which means that the user cannot directly see the influence from each input parameter. Because the database mainly includes data with $\xi_{-1,0}$ = 2.8 - 4.5, estimations with $\xi_{-1,0}$ > 4.5 (surging waves) might be unreliable with use of the EurOtop Manual and the Neural Network.

The estimation of mean wave overtopping discharge by the first version of the EurOtop Manual (Pullen et al., 2007) for a conventional rubble mound breakwater exposed to perpendicular wave attack reads:

$$\frac{q}{\sqrt{gH_{m0}^3}} = \frac{0.067}{\sqrt{\tan(\alpha)}}\xi_{-1,0}\exp\left(-4.75\frac{R_c}{H_{m0}}\frac{1}{\xi_{-1,0}\gamma_f}\right) \tag{4.1}$$

with a maximum of:

$$\frac{q}{\sqrt{gH_{m0}^3}} = 0.2\exp\left(-2.6\frac{R_c}{H_{m0}}\frac{1}{\gamma_f}\right) \tag{4.2}$$

Here q is the time-averaged wave overtopping per unit length of the breakwater. g is the gravity acceleration, H_{m0} the spectral wave height at the toe of the structure, α the front slope angle. γ_f is a constant roughness factor dependent on the armour type. R_c is the crest freeboard which is defined as the vertical distance from still water level to the point where the water cannot run back to the sea, i.e. a crown wall or an impermeable layer, see Fig. 4.5. $\xi_{-1,0}$ is the surf similarity parameter based on the spectral wave period $T_{-1,0}$ and is calculated by (3.9).

Since the first version of the EurOtop Manual, new studies have been made covering lacking data for wave overtopping with very steep slopes and vertical structures, and estimations with crest levels located at Still Water Level (SWL). This led to an updated manual (Van der Meer et al., 2018b). The new version of the EurOtop Manual updated the formulae to increase the reliability for low-crested structures. Furthermore, a varying roughness factor was presented but did only change the estimations for $\xi_{-1,0} > 5$. However, no studies on wave overtopping with surging waves have been included in the new EurOtop Manual and thus the new $\gamma_{f,mod}$ was not validated. The updated formulae for perpendicular wave attack on conventional rubble mound breakwaters read:

$$\frac{q}{\sqrt{gH_{m0}^3}} = \frac{0.023}{\sqrt{\tan(\alpha)}}\xi_{-1,0}\exp\left(-\left(4.75\frac{R_c}{H_{m0}}\frac{1}{\xi_{-1,0}\gamma_{f,mod}}\right)^{1.3}\right) \tag{4.3}$$

with a maximum of:

$$\frac{q}{\sqrt{gH_{m0}^3}} = 0.09 \exp\left(-\left(1.5 \frac{R_c}{H_{m0}} \frac{1}{\gamma_{f,mod}}\right)^{1.3}\right) \tag{4.4}$$

Here is $\gamma_{f,mod}$ the varying roughness factor and is calculated by:

$$\gamma_{f,mod} = \begin{cases} \gamma_f, & \text{if } \xi_{-1,0} \leq 5. \\ \gamma_f + (\xi_{-1,0} - 5)(1 - \gamma_f)/5, & \text{if } \xi_{-1,0} > 5. \end{cases} \tag{4.5}$$

with a maximum of

$$\gamma_{f,mod} = \begin{cases} 1.0, & \text{for impermeable core.} \\ 0.6, & \text{for permeable core.} \end{cases} \tag{4.6}$$

The Neural Network by Van Gent et al. (2007) is a reliable tool, but the model is a black box, and therefore it is not directly known how the input parameters influence the output. The tool is a reliable method if the input variables are within the range that the model was trained with but can also provide unrealistic results if the input variables are deviating significantly from the tests that the tool was trained with. The model can be illustrated by Fig. 4.1 where there are 15 input variables, a hidden layer with 20 artificial neurons from which the input is converted into the output.

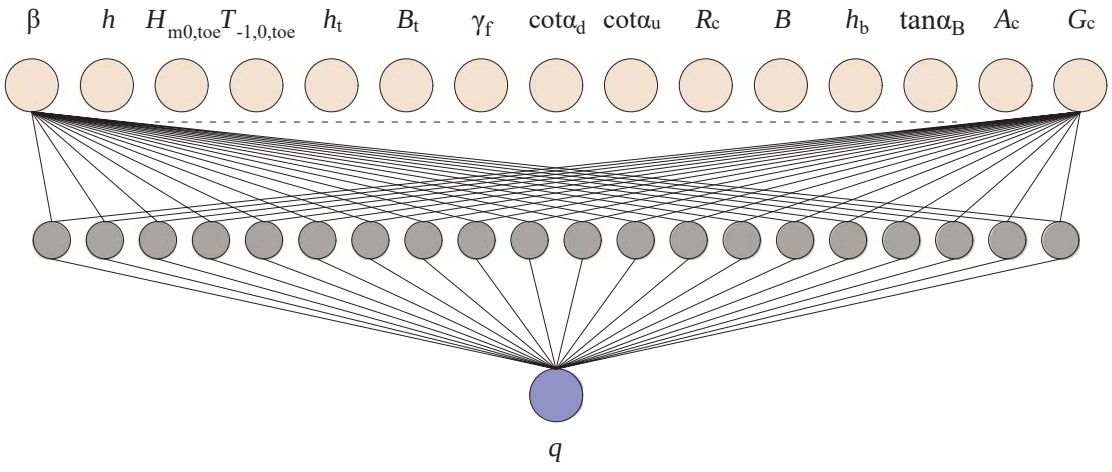

Fig. 4.1: Input layer, hidden layer, and output layer of the Neural Network by Van Gent et al. (2007)

4.2 New Developments in Overtopping Estimation for Shallow Water

Christensen et al. (2014) (Paper [F]) investigated wave overtopping for low steepness waves before the updated version of the EurOtop Manual (Van der Meer et al., 2018b). Christensen et al. (2014) found that the discharge for surging waves was underestimated significantly with the first version of the EurOtop Manual formulae. They suggested to replace the constant roughness factor with a varying roughness factor so that more overtopping was estimated for surging waves. This modification improved the estimations with the EurOtop Manual significantly. The varying roughness factor was already include in the EurOtop Manual, but only used for wave run-up and is calculated by Eq. (4.7). However, the use of $\gamma_{f,surging}$ was not included in the updated version of the EurOtop Manual, but instead $\gamma_{f,mod}$ was introduced. The tests performed by Christensen et al. (2014) were without the knowledge of wave generation applicability and nonlinear wave separation.

$$\gamma_{f,surging} = \begin{cases} \gamma_f, & \text{if } \xi_{-1,0} \leq 1.8. \\ \gamma_f + (\xi_{-1,0} - 1.8)(1 - \gamma_f)/8.2, & \text{if } 1.8 < \xi_{-1,0} \leq 10. \\ 1, & \text{if } \xi_{-1,0} > 10. \end{cases} \tag{4.7}$$

The effect of Eq. (4.7) starts at $\xi_{-1,0}$ = 1.8 and has a maximum value at $\xi_{-1,0}$ = 10 where the roughness corresponds to a smooth impermeable slope.

Eldrup and Lykke Andersen (2018a) (Paper [G]) performed several tests with high and low steepness waves on permeable and impermeable rubble mound breakwaters, see Eldrup and Lykke Andersen (2018a). Eldrup and Lykke Andersen (2018a) used the wave generation applicability guidance by Eldrup and Lykke Andersen (2019a) and the new nonlinear wave separation method by Eldrup and Lykke Andersen (2019b) in their tests and observed that an increase of the wave overtopping was seen for surging waves compared to plunging waves. Therefore, with new accurately performed wave tests, they could conclude that the observations made by Christensen et al. (2014) were correct.

Eldrup and Lykke Andersen (2018a) observed that the wave overtopping discharge was significantly underestimated for long waves with use of the formulae (Eqs. 4.3 - 4.6) even though the EurOtop Manual had included $\gamma_{f,mod}$. Eldrup and Lykke Andersen (2018a) modified the formulae in the EurOtop Manual to include the varying roughness factor $\gamma_{f,surging}$ proposed by Christensen et al. (2014), see Eq. (4.7). The EurOtop Manual suggests

using a crest width reduction factor C_r by Besley (1998) for $G_c > 3\ D_{n50A}$, but Eldrup and Lykke Andersen (2018a) found that using C_r also for $G_c \leq 3D_{n50A}$ improved the estimations. The modified formulae read:

$$\frac{q}{\sqrt{gH_{m0}^3}} = \frac{0.023}{\sqrt{\tan(\alpha)}}\xi_{-1,0}\exp\left(-\left(4.75\frac{R_c}{H_{m0}}\frac{1}{\xi_{-1,0}\gamma_{f,surging}}\right)^{1.3}\right)C_r \quad (4.8)$$

with a maximum of:

$$\frac{q}{\sqrt{gH_{m0}^3}} = 0.09\exp\left(-\left(1.5\frac{R_c}{H_{m0}}\frac{1}{\gamma_{f,surging}}\right)^{1.3}\right)C_r \quad (4.9)$$

The crest width reduction factor by Besley (1998) is estimated by:

$$C_r = 3.06\exp\left(-1.5\frac{G_c}{H_{m0}}\right) \text{ with a maximum of } 1 \quad (4.10)$$

With the modified formulae, Eldrup and Lykke Andersen (2018a) observed that the constant roughness factor γ_f also had to be updated to fit with the modified formulae Eq. (4.8) and (4.9). Table 4.1 shows the γ_f given by the EurOtop Manual (Van der Meer et al., 2018b) and the updated values by Eldrup and Lykke Andersen (2018a).

Type of armour	No. layers	(Van der Meer et al., 2018b)	Eldrup and Lykke Andersen (2018a)
Acropode ™ I	1	0.46	0.42
Antifer	2	0.50	0.45
CORE-LOC ™	1	0.44	0.38
Cubes smooth	1	0.49	0.47
Cubes smooth	2	0.47	0.45
Cubes random	2	0.47	0.41
HARO	2	0.47	0.43
Rock impermeable	2	0.55	0.48
Rock permeable	2	0.40	0.39
Tetrapod	2	0.38	0.30
Xbloc ®	1	0.44	0.38

Table 4.1: Roughness factor γ_f for different armour units and calculation methods.

Fig. 4.2 shows a comparison of the measured and estimated dimensionless overtopping discharge $q/\sqrt{gH_{m0}^3}$. The data used in the figure is described in Eldrup and Lykke Andersen (2018a). The Neural Network by Van Gent et al. (2007) has the lowest error, but the model gives no prediction if $q/\sqrt{gH_{m0}^3} < 10^{-6}$. Neither does it give a prediction if any of the input conditions are outside the valid range. Even though the Neural Network is the most reliable method, the methods by Van der Meer et al. (2018b) and Eldrup and Lykke Andersen (2018a) are still highly relevant. This could, for example, be in cases where the Neural Network model is not estimating any value or in case a new complex structure is used which the model was not trained with. In such cases, it is easy to introduce a new reduction factor to be used in the empirical formulae.

The method by Van der Meer et al. (2018b) (Eq. (4.3) and (4.4)) shows a significant amount of the data outside the 90% confidence band and a tendency to overestimate for $1.8 < \xi_{-1,0} \leq 3$ and underestimate for $3 < \xi_{-1,0} \leq 5$. For the modification by Eldrup and Lykke Andersen (2018a) (Eq. 4.8 and

4.9), only a few data are outside the confidence band and the predictions are on average only slightly worse than by the Neural Network.

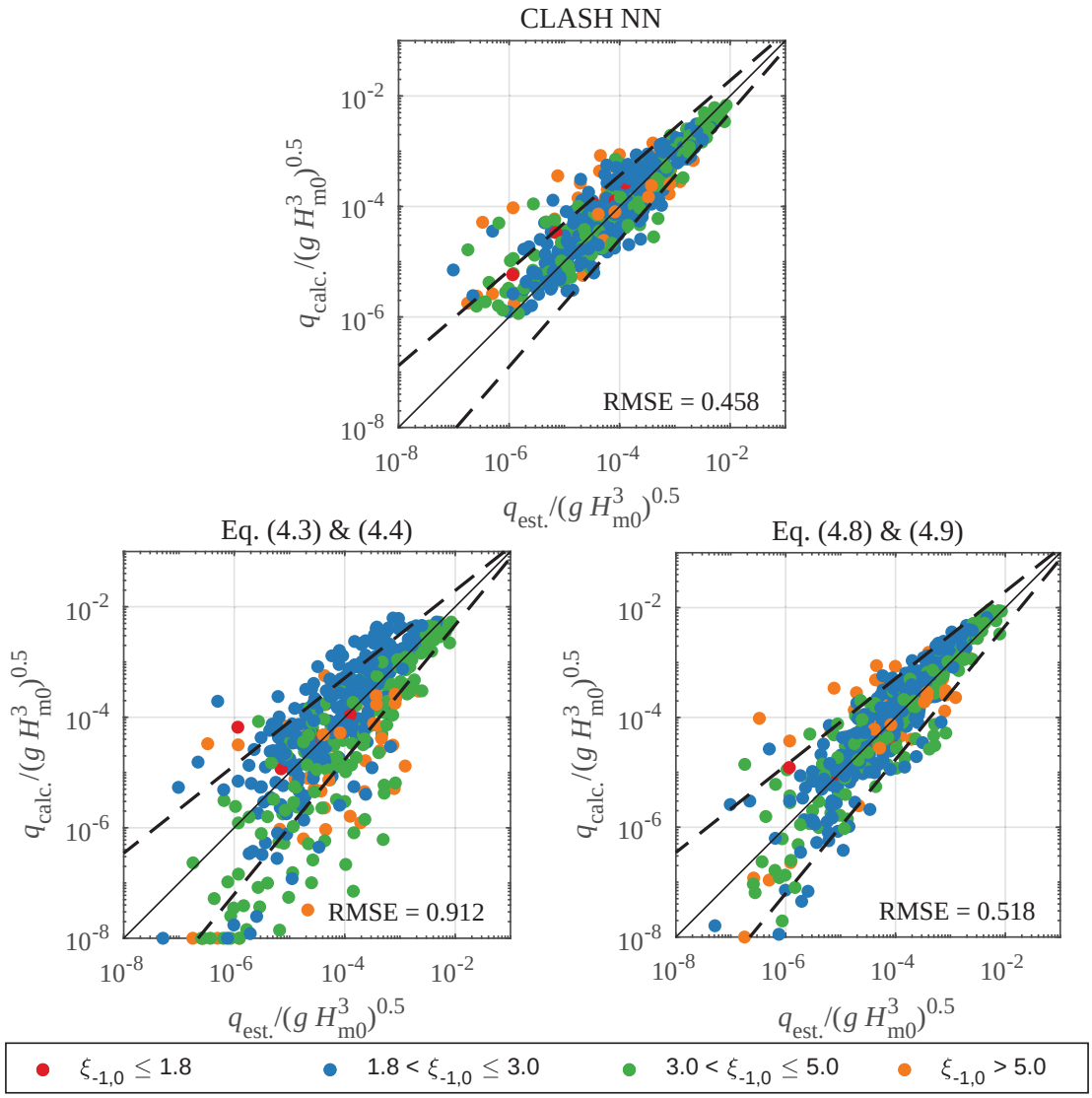

Fig. 4.2: Measured and estimated mean wave overtopping discharge with 90% confidence band shown as dashed lines. The confidence bands of Eq. (4.3), (4.4), (4.8) and (4.9) are those given in Van der Meer et al. (2018b). The RMSE is calculated for $q_{est.}/\sqrt{gH_{m0}^3}$ - $q_{calc.}/\sqrt{gH_{m0}^3}$.

4.3 New Studies on Wave Overtopping with a Permeable Crest

In the present work, the influence of a permeable crest on the mean wave overtopping discharge is also investigated. For some designs, the armour freeboard A_c is higher than the crest freeboard R_c, see Fig. 4.3. An example of this is the promenade of Naples in Italy, see Fig. 4.4.

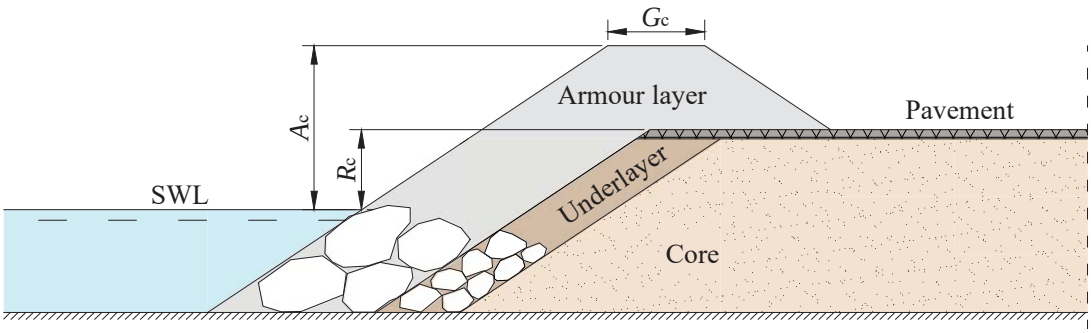

Fig. 4.3: Sketch of promenade. The definitions of A_c and R_c are according to Van der Meer et al. (2018b).

In case the wave overtopping behind the crest G_c is desired, the EurOtop Manual recommends using the average value of the armour freeboard and the crest freeboard as the estimation height. However, this procedure has never been validated as the wave overtopping in small scale tests has typically only been measured at the crest rear shoulder (at A_c in Fig. 4.3).

Fig. 4.4: Promenade of Naples in Italy.

For the two cases seen in Fig. 4.5 overtopping water might also occur by porous flow in the armour layer. Depending on the studied failure mode for overtopping, this flow should be included or not. The water can also flow through a permeable core, but that is normally not considered to be wave overtopping. The first version of the EurOtop Manual (Pullen et al., 2007) used the lowest value of A_c and R_c, see Fig. 4.5. The updated EurOtop

Manual (Van der Meer et al., 2018b) recommends for a case with a crown wall using the largest value of A_c and R_c, Fig. 4.5 (a). For a case without a crown wall, the manual recommends using an average of A_c and R_c, see Fig. 4.5 (b). However, the procedure without the crown wall has never been verified by model tests. Eldrup et al. (2018) (Paper [H]) investigated the procedure given by both versions of the EurOtop Manual for the case in Fig. 4.5 (b) by measuring wave overtopping discharges q_{crest} and $q_{crest} + q_{armour}$ for permeable and impermeable cores.

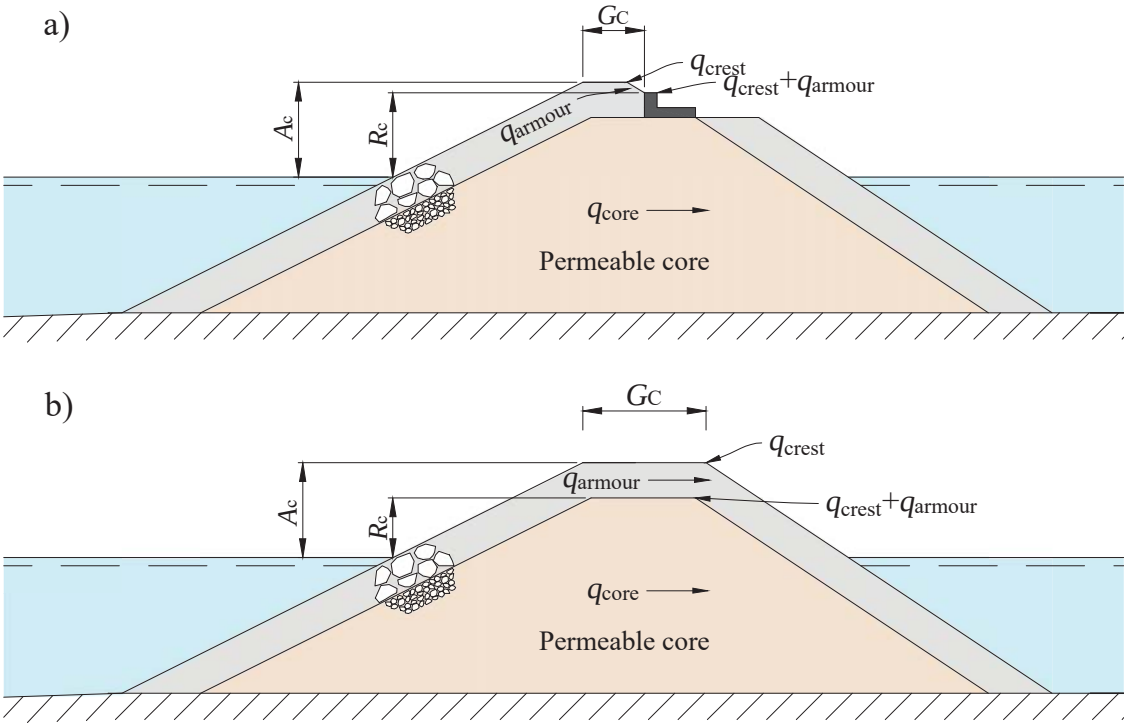

Fig. 4.5: Definition of relative freeboard height parameters A_c, and R_c according to (Van der Meer et al., 2018b). The mean wave overtopping discharge can be defined as q_{crest} and $q_{crest} + q_{armour}$.

Fig. 4.6 shows the measured overtopping discharge as markers and the estimations with Eldrup and Lykke Andersen (2018a) as the continuous line. The triangles show the results for the case with an impermeable core and the circles show the results for the permeable core. The colours of the markers illustrate the different definitions of the relative freeboard height. The estimations are overestimated compared to the measured data if the markers are below the continuous line.
Fig. 4.6 (a) shows that the measured overtopping q_{crest} is best estimated with a relative freeboard height $R^* = A_c/(H_{m0}\gamma_{fsurging})$. This could also be expected as wave overtopping in model tests without a crown wall is typically measured at the height of A_c. Conservative estimations of the mean wave

overtopping discharge q_{crest} are provided when using the recommended freeboard height by Van der Meer et al. (2018b).
Fig. 4.6 (b) shows that the measured overtopping $q_{crest} + q_{armour}$ is well estimated with the guideline given by Van der Meer et al. (2018b) and thus their recommendations are verified by the study of Eldrup et al. (2018). However, the data shows that a separation of the results into the impermeable core and the permeable core reveals that a permeability correction is needed. Moreover, the difference between both cores is expected to be more significant for wider crests, but this has not been investigated in the present work.

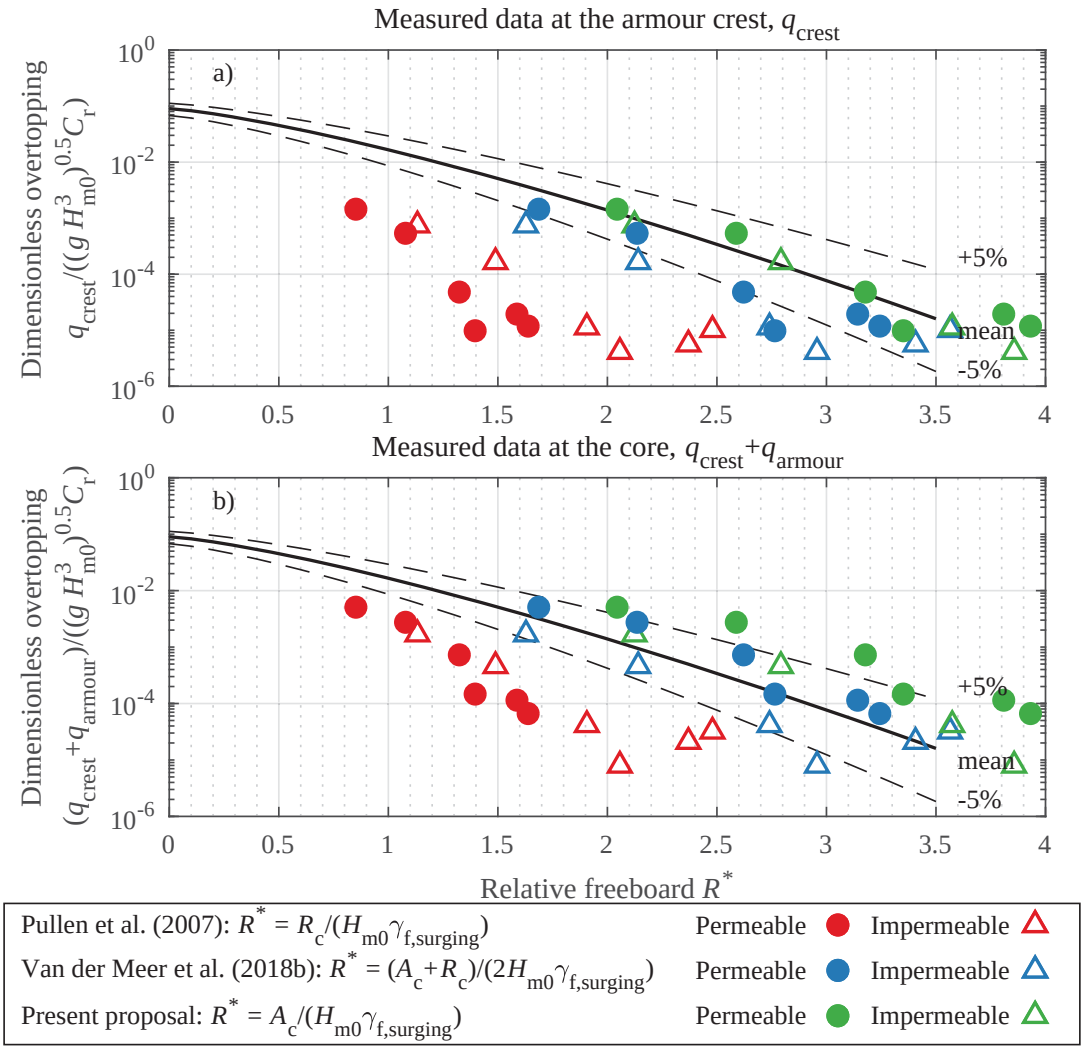

Fig. 4.6: Comparison between measured and estimated overtopping with different relative freeboard heights R^*. (a) shows the measured values for q_{crest} and (b) shows the measured results for $q_{crest} + q_{armour}$. The continuous line shows the estimations with the modified EurOtop formulae by Eldrup and Lykke Andersen (2018a). The colours show the estimated mean overtopping discharge with the different definitions of the relative freeboard height.

5 Conclusion

This thesis dealt with response of rubble mound breakwaters exposed to shallow water waves and addressed four topics: Evaluation and modification of wave generation theories for linear and nonlinear waves, development of nonlinear methods to separate nonlinear waves into incident and reflected wave trains, new formulae for the stability of rock armoured rubble mound breakwaters, and modification of existing mean wave overtopping discharge formulae.

Physical model tests of structures performed in shallow water wave conditions need accurate wave generation. Typically, model tests have been carried out with first-order or second-order wave generation theory, but for the present thesis highly nonlinear theories were needed. Alternatively, a long foreshore would have to be present in the facility. Therefore, linear and nonlinear wave generation methods were tested with physical model tests, and concrete guidelines were given for when the wave generation theories for highly nonlinear waves were needed and when the first-order or second-order theory could be used.

For model tests performed in this thesis, accurate wave separation of the incident and reflected nonlinear waves were needed even for highly nonlinear waves. Linear wave separation methods have typically been used in laboratories around the world, but the present study showed that these methods underestimate the wave height for highly nonlinear waves. Therefore, nonlinear wave separation methods have been developed in this thesis for regular and irregular waves. These methods were validated with a relatively gentle slope. In (Paper [E]), some of the tests with rubble mound breakwaters were performed with a steep foreshore. These tests showed that for steep foreshores it was necessary to measure the waves without the model in place because the waves changed significantly through the wave gauge array which was especially the case for highly nonlinear or breaking waves.

Rock armour stability tests were performed for several layer compositions and wave nonlinearities. A formula was established to estimate the notional

permeability factor in the Van der Meer, the modified Van der Meer and present rock armour stability formulae. The notional permeability formula was reliable with estimated observations of $\pm$ 0.03. The modified Van der Meer stability formulae provided acceptable estimations for the tests with the mildly nonlinear waves. However, for the highly nonlinear waves, the stability was significantly underestimated. The tests with highly nonlinear waves showed a large difference between the spectral wave height H_{m0} and the significant wave height $H_{1/3}$. New formulae were therefore established, and the spectral wave height was found to describe the stability better for both mildly and highly nonlinear waves.

Mean wave overtopping discharge was analysed for rubble mound breakwaters exposed to low steepness waves in shallow water. The analysis revealed that the empirical design formulae by the EurOtop Manual underestimate the wave overtopping discharge significantly for surging waves. Therefore, a modification to the formula was proposed which corrected the observed underestimation. The CLASH Neural Network had the lowest error on the estimated wave overtopping in the present study, but the modified EurOtop formulae were almost as good as the Neural Network. However, one advantage of the modified EurOtop formulae is that it provides estimations for all wave conditions and can include new reduction factors for structural modifications which are not included in the Neural Network tool. The guideline that was given by the EurOtop Manual for estimating wave overtopping discharge for cases where the armour freeboard was higher than the crest freeboard was investigated. The present study showed that the guidelines given in such cases are reliable.

Future Perspectives

The present work provides new tools for wave separation and guidance of wave generation which makes the testing of nonlinear waves more reliably in the future. Furthermore, new design tools for rock armour stability and mean wave overtopping discharge were developed which improve the reliability of designs with shallow water wave conditions. However, this work can still be improved in future work.

The new rock armour stability formulae were only verified for shallow water conditions and thus the reliability for deep water conditions remains unknown. The stability of rubble mound breakwaters with extremely steep foreshores and extremely shallow foreshores also still remains unknown.

Wave separation on steep foreshores is still a challenge that needs to be dealt with. This includes knowledge on nonlinear shoaling and the influence of wave breaking.

References

Amante, C. and Eakins, B. (2009). Etopo1 1 arc-minute global relief model: procedures, data sources and analysis. *http://www.ngdc.noaa.gov/mgg/global/global.html*.

Battjes, J. A. (1974). Surf similarity. *Coastal Engineering Proceedings*, 1(14):466–480.

Beji, S. and Battjes, J. (1993). Experimental investigation of wave propagation over a bar. *Coastal Engineering*, 19(1-2):151–162.

Besley, P. (1998). Wave overtopping of seawalls, design and assessment manual. *R&D technical report W178*.

Burcharth, H. F. and Røge, M. S. (2015). *Undersøgelse af udviklingen i maksimale vandstande i den østligste del af Limfjorden Aalborg – Hals*. Department of Civil Engineering, Aalborg University.

Christensen, N. F., Røge, M. S., Thomsen, J. B., Lykke Andersen, T., Burcharth, H. F., and Nørgaard, J. Q. H. (2014). Overtopping on rubble mound breakwaters for low steepness waves in deep and depth limited conditions. *Coastal Engineering Proceedings*, 1(34):6.

CIRIA; CUR; CETMEF (2007). *The Rock Manual. The use of rock in hydraulic engineering (2nd edition)*. C683, CIRIA, London.

Eldrup, M. R. and Lykke Andersen, T. (2016). *Two-Dimensional Model Test Study of New Western Breakwater Proposal for Port of Hanstholm*. Department of Civil Engineering, Aalborg University.

Eldrup, M. R. and Lykke Andersen, T. (2018a). Recalibration of overtopping roughness factors of different armour types. In *Coasts, Marine Structures and Breakwaters 2017*, pages 1011–1020.

Eldrup, M. R. and Lykke Andersen, T. (2018b). *Three-Dimensional Model Test Optimisation of the New Cubipod Armoured Western Breakwater for Port of Hanstholm*. Department of Civil Engineering, Aalborg University.

Eldrup, M. R. and Lykke Andersen, T. (2018c). *Three-Dimensional Model Test Optimisation of the Spur Breakwater for Port of Hanstholm*. Department of Civil Engineering, Aalborg University.

Eldrup, M. R. and Lykke Andersen, T. (2018d). *Three-Dimensional Model Test Verification of the New Cubipod Armoured Western Breakwater for Port of Hanstholm*. Department of Civil Engineering, Aalborg University.

Eldrup, M. R. and Lykke Andersen, T. (2018e). *Two-Dimensional Model Test Verification of the New Cubipod Armoured Western Breakwater for the Port of Hanstholm*. Department of Civil Engineering, Aalborg University.

Eldrup, M. R. and Lykke Andersen, T. (2019a). Applicability of nonlinear wavemaker theory. *Journal of Marine Science and Engineering*, 7(1):14.

Eldrup, M. R. and Lykke Andersen, T. (2019b). Estimation of incident and reflected wave trains in highly nonlinear two-dimensional irregular waves. *Journal of Waterway, Port, Coastal, and Ocean Engineering*, 145(1).

Eldrup, M. R. and Lykke Andersen, T. (2019c). New formulae for rock armour stability in shallow water. *Submitted to Coastal Engineering*.

Eldrup, M. R., Lykke Andersen, T., and Burcharth, H. F. (2019). Stability of rubble mound breakwaters – a study of the notional permeability factor. *Submitted to Water*.

Eldrup, M. R., Lykke Andersen, T., Thomsen, J. B., and Burcharth, H. F. (2018). Overtopping on breakwaters with a permeable crest. *Coastal Engineering Proceedings*, 1(36):17.

Fenton, J. and Rienecker, M. (1980). Accurate numerical solutions for nonlinear waves. *Coastal Engineering Proceedings*, 1(17):50–69.

Figueres, M., Garrido, J., and Medina, J. (2003). Cristalización simulada para el análisis de oleaje incidente y reflejado con un modelo de onda stokes-v. *VII Jornadas de Puertos Y Costas, Almeria*.

für Küstenschutzwerke, A. (2002). Eak 2002 : Ansätze für die bemessung von küstenschutzwerken. *Sonderdruck" Die Küste" ISSN 0452-7739 ISBN 978-3-8042-1056-1*.

Frigaard, P. and Brorsen, M. (1995). A time-domain method for separating incident and reflected irregular waves. *Coastal Engineering*, 24(3-4):205–215.

Goda, Y. (2010). Reanalysis of regular and random breaking wave statistics. *Coastal Engineering Journal*, 52(01):71–106.

Goda, Y. and Suzuki, Y. (1976). Estimation of incident and reflected waves in random wave experiments. *Coastal Engineering Proceedings*, 1(15):828–845.

Havelock, T. (1929). Lix. forced surface-waves on water. *The London, Edinburgh, and Dublin Philosophical Magazine and Journal of Science*, 8(51):569–576.

Herrera, M. P., Gomez-Martín, M. E., and Medina, J. R. (2017). Hydraulic stability of rock armors in breaking wave conditions. *Coastal Engineering*, 127:55–67.

Hofland, B., Chen, X., Altomare, C., and Oosterlo, P. (2017). Prediction formula for the spectral wave period tm-1, 0 on mildly sloping shallow foreshores. *Coastal Engineering*, 123:21–28.

Hudson, R. Y. (1959). Laboratory investigation of rubble-mound breakwaters. *Reprint of the original paper as published in the Journal of the Waterways and Harbors Division of ASCE, proceedings paper 2171*.

Iribarren, C. R. (1938). *Una fórmula para el cálculo de los diques de escollera*. M. Bermejillo Usabiaga.

Iribarren, C. R. and Nogales, C. (1949). Protection des ports. In *XVIIth International Naval Congress (Lisbon, Portugal), 1949*, pages 31–80.

Kik, R. (2011). The notional permeability of breakwaters: Experimental research on the permeability factor p. *M.Sc. thesis*.

Kluwen, J. (2012). Physical model tests of the notional permeability on breakwaters. *M.Sc. thesis*.

Le Méhauté, B. (1969). An introduction to hydrodynamics and water waves volume ii: Water wave theories.

Lin, C.-Y. and Huang, C.-J. (2004). Decomposition of incident and reflected higher harmonic waves using four wave gauges. *Coastal engineering*, 51(5-6):395–406.

Lykke Andersen, T., Clavero, M., Eldrup, M. R., Frigaard, P., and Losada, M. (2018). Active absorption of nonlinear irregular waves. *Coastal Engineering Proceedings*, 1(36):12.

Lykke Andersen, T., Eldrup, M. R., and Clavero, M. (2019). Separation of long-crested nonlinear bichromatic waves into incident and reflected components. *Journal of Marine Science and Engineering*, 7(2):12.

Lykke Andersen, T., Eldrup, M. R., and Frigaard, P. (2017). Estimation of incident and reflected components in highly nonlinear regular waves. *Coastal Engineering*, 119:51–64.

Lynett, P. and Liu, P. L.-F. (2004). A two-layer approach to wave modelling. In *Proceedings of The Royal Society of London A: Mathematical, Physical and Engineering Sciences*, volume 460, pages 2637–2669. The Royal Society.

Madsen, P. A. and Sørensen, O. R. (1992). A new form of the boussinesq equations with improved linear dispersion characteristics. part 2. a slowly-varying bathymetry. *Coastal engineering*, 18(3-4):183–204.

Mansard, E. P. and Funke, E. (1980). The measurement of incident and reflected spectra using a least squares method. *Coastal Engineering Proceedings*, 1(17):154–172.

Muttray, M. and Reedijk, B. (2009). Reanalysis of breakwater stability with steep foreshore. In *Coastal Engineering 2008: (In 5 Volumes)*, pages 3346–3357. World Scientific.

Pullen, T., Allsop, N., Bruce, T., Kortenhaus, A., Sch, H., Van der Meer, J., et al. (2007). Wave overtopping of sea defences and related structures: assessment manual.

Røge, M. S., Christensen, N. F., Thomsen, J. B., Nørgaard, J. Q. H., and Lykke Andersen, T. (2014a). Wave loads on rubble mound breakwater crown walls in long waves. *Coastal Engineering Proceedings*, 1(34):64.

Røge, M. S. and Lykke Andersen, T. (2015). *Three-Dimensional Model Test Study of Xbloc Armoured Breakwaters at Punta Catalina, Dominican Republic*. Department of Civil Engineering, Aalborg University.

Røge, M. S., Lykke Andersen, T., and Burcharth, H. F. (2014b). *Wave Analysis Study for the Punta Catalina Jetty, Dominican Republic*. Department of Civil Engineering, Aalborg University.

Schäffer, H. A. (1993). Laboratory wave generation correct to second order. In *Wave Kinematics and Environmental Forces*, pages 115–139. Springer.

Schäffer, H. A. (1996). Second-order wavemaker theory for irregular waves. *Ocean Engineering*, 23(1):47–88.

Thompson, D. and Shuttler, R. (1975). Riprap design for wind-wave attack, a laboratory study in random waves. *Wallingford report EX707 for CIRIA*.

Thomsen, J. B., Røge, M. S., Christensen, N. F., Lykke Andersen, T., and Van der Meer, J. W. (2014). Stability of hardly reshaping berm breakwaters exposed to long waves. *Coastal Engineering Proceedings*, 1(34):65.

Tolman, H. L. et al. (2009). User manual and system documentation of wavewatch iii tm version 3.14. *Technical note, MMAB Contribution*, 276:220.

U.S Army Corps of Engineers (2012). *Coastal Engineering Manual – Part VI: Design of Coastal Project Elements (EM 1110-2-1100)*. Books Express Publishing.

Van der Meer, J., Van Gent, M., Wolters, G., and Heineke, D. (2018a). No access new design guidance for underlayers and filter layers for rock armour under wave attack. In *Coasts, Marine Structures and Breakwaters 2017*, pages 1069–1079.

Van der Meer, J. W. (1988). Rock slopes and gravel beaches under wave attack.

Van der Meer, J. W. (2002). Technical report wave run-up and wave overtopping at dikes. *TAW report*.

Van der Meer, J. W., Allsop, N., Bruce, T., De Rouck, J., Kortenhaus, A., Pullen, T., Schüttrumpf, H., Troch, P., and Zanuttigh, B. (2018b). Eurotop, 2018. manual on wave overtopping of sea defences and related structures. an overtopping manual largely based on european research, but for worldwide application. www.overtopping-manual.com. Accessed: 2018-01-23.

Van Gent, M. and Smith, G. (1999). Physical model investigations on coastal structures with shallow foreshores: 2d model tests with single and double-peaked wave energy spectra.

Van Gent, M. R. (2001). Wave runup on dikes with shallow foreshores. *Journal of Waterway, Port, Coastal, and Ocean Engineering*, 127(5):254–262.

Van Gent, M. R., Smale, A. J., and Kuiper, C. (2004). Stability of rock slopes with shallow foreshores. In *Coastal Structures 2003*, pages 100–112.

Van Gent, M. R., van den Boogaard, H. F., Pozueta, B., and Medina, J. R. (2007). Neural network modelling of wave overtopping at coastal structures. *Coastal Engineering*, 54(8):586–593.

Zelt, J. and Skjelbreia, J. E. (1992). Estimating incident and reflected wave fields using an arbitrary number of wave gauges. *Coastal Engineering Proceedings*, 1(23):777–789.

Zhang, H. and Schäffer, H. A. (2007). Approximate stream function wavemaker theory for highly non-linear waves in wave flumes. *Ocean engineering*, 34(8-9):1290–1302.

Zhang, H., Schäffer, H. A., and Jakobsen, K. P. (2007). Deterministic combination of numerical and physical coastal wave models. *Coastal engineering*, 54(2):171–186.

I
Paper Collection

Paper A

Applicability of Nonlinear Wavemaker Theory

Mads Røge Eldrup
Thomas Lykke Andersen

The paper has been published in
Journal of Marine Science and Engineering, ISSN: 2077-1312, 7(1):14, 2019
DOI: 10.3390/jmse7010014

Journal of
Marine Science and Engineering

MDPI

Article

Applicability of Nonlinear Wavemaker Theory

Mads Røge Eldrup * and Thomas Lykke Andersen

Department of Civil Engineering, Aalborg University, 9220 Aalborg, Denmark; tla@civil.aau.dk
* Correspondence: mre@civil.aau.dk

Received: 22 November 2018; Accepted: 8 January 2019; Published: 14 January 2019

Abstract: Generation of high-quality waves is essential when making numerical or physically model tests. When using a wavemaker theory outside the validity area, spurious waves are generated. In order to investigate the validity of different wave generation methods, new model test results are presented where linear and nonlinear wave generation theories are tested on regular and irregular waves. A simple modification to the second-order wavemaker theory is presented, which significantly reduces the generation of spurious waves when used outside its range of applicability. For highly nonlinear regular waves, only the ad-hoc unified wave generation based on stream function wave theory was found acceptable. For irregular waves, similar conclusions are drawn, but the modified second-order wavemaker method is more relevant. This is because the ad-hoc unified generation method for irregular waves requires the wave kinematics to be calculated by a numerical model, which might be quite time-consuming. Finally, a table is presented with the range of applicability for each wavemaker method for regular and irregular waves.

Keywords: linear waves; nonlinear waves; wavemaker theory; wavemaker applicability

1. Introduction

When performing tests in laboratories or numerical models, high-quality waves representing conditions in prototype as close as possible is of highest priority. In the early 20th century, linear wavemaker theory was developed by Havelock [1], which was later extended to a fully second-order irregular wavemaker theory by Schäffer [2,3]. This extension made it possible to generate mildly nonlinear waves without spurious free waves. The spurious free waves contaminate the wave field and can easily be seen for regular waves for cases with low wave reflection, as the wave shape is not constant in space. For example, Orszaghova et al. [4] showed that using first-order wavemaker theory could lead to erroneously wave run-up and wave overtopping results compared to generating the waves with second-order wavemaker theory. Furthermore, Sriram et al. [5] showed that the breaking point of focused waves is different when using first-order and second-order wavemaker theory. This was expected to be caused by the influence from the free spurious long-wave components generated with first-order theory.

Recently, ad-hoc unified wavemaker theories were proposed by Zhang and Schäffer [6] for regular waves and by Zhang et al. [7] for irregular waves. These ad-hoc unified wave generation methods make it possible to generate highly nonlinear waves of high quality in intermediate and shallow water. These methods require a depth-averaged velocity as input to control the motion of the piston wavemaker. For regular waves, a fully nonlinear wave theory is available in the form of the stream function wave theory by Fenton and Rienecker [8], and from this, the depth-averaged velocity can be calculated. At the moment, there exists no analytical model to calculate the kinematics for highly nonlinear irregular waves, but the kinematics can be obtained by numerical models, for example, Boussinesq type wave models. The propagation of waves from deep to shallow water with numerical models can be time-consuming. Therefore, it is more efficient to use the first or second-order wavemaker theory for irregular waves when they are valid.

Unwanted free waves are generated when using a wavemaker theory outside its validity area. Schäffer [3] specified that the second-order wavemaker theory is not valid for regular waves when a secondary crest is produced in the wave trough. This happens when the second-order amplitude is larger than $\frac{1}{4}$ of the first-order amplitude. To describe this, he introduced the nonlinearity parameter, S which must not exceed unity for the second-order wavemaker theory to be valid. For regular waves, Schäffer [3] defined S as four times the ratio between the amplitudes of the second-order and the first-order components in regular waves and is given by:

$$S = 2\left|HG_{nm}^{\pm}\right| \quad (1)$$

where $G_{nm}^{\pm}$ is the second-order surface elevation transfer function given for example in Schäffer [3], H is the wave height. For the application of Equation (1) on irregular waves Schäffer [3] proposed to use a characteristic wave height ($H = H_{1/3}$) and $f_n = f_m = f_p$ to calculate $G_{nm}^{\pm}$.

A more well-known approach to check the applicability of wave maker theories is the diagram by Le Méhauté [9], which described what wave theory was valid depending on the relative water depth and the wave steepness. Figure 1 shows an example of the Le Méhauté diagram and colored areas that illustrates different S ranges calculated with Equation (1). From the figure, it is seen that using the applicability criteria for second-order waves given by Schäffer [3] corresponds to fourth order Stokes waves according to the diagram by Le Méhauté [9]. This clearly shows the need of testing the applicability range of the existing methods and to provide some recommendations that can easily be followed.

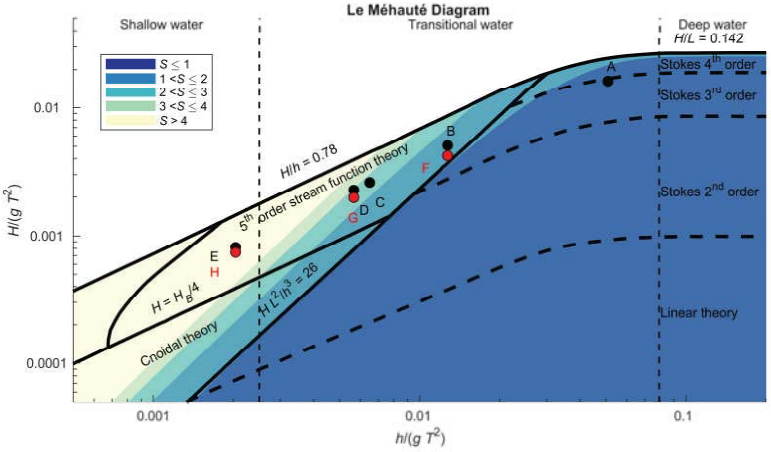

Figure 1. Tested sea states, where black dots are for the regular waves and red dots are for irregular waves. The colored areas show different ranges for the nonlinearity parameter S calculated with Equation (1). (Adapted from Le Méhauté [9]).

The present paper presents new physical model test results to study the applicability of the different wavemaker methods for regular and irregular waves. A simple modification to the second-order wavemaker theory by Schäffer [3] is proposed to extend its range of applicability and to significantly reduce errors for highly nonlinear cases. Furthermore, recommendations are given for the validity of each of the tested wavemaker theories.

2. Present Study

New model tests covering linear to highly nonlinear waves have been performed in the new wave flume at Aalborg University for regular (5 tests) and irregular (3 tests) waves, see Figure 1.

The purpose of the tests is to study the applicability of each wavemaker theory and to provide a clear definition for the applicability range of each wavemaker theory. Furthermore, is it investigated if the applicability range of the second-order wavemaker theory can be extended with a simple modification. The second-order wavemaker theory is modified in the present paper by introducing a maximum allowed relation between the second-order amplitude and the first-order amplitude. This limitation is controlled by a S_{max} value, so for example, $S_{max} = 1$ means that the second-order amplitude will be reduced to $\frac{1}{4}$ of the first-order amplitude if it was predicted higher. Without this upper limit, the second-order amplitude might be even larger than the first-order amplitude which is physically incorrect. Instead the second-order component should saturate at a level smaller than the primary component and third and higher order components should increase instead.

The second-order components generated by two interacting components were scaled by introducing a more generalized form of S. This is done by rewriting Equation (1) to consider the two interacting components:

$$S(f_n, f_m) = HG^{\pm}_{nm}/\delta_{nm} \quad (2)$$

where f_n and f_m are the frequencies of the two interacting components. δ_{nm} is 0.5 for $f_n = f_m$ and 1 for $f_n \neq f_m$. In the present paper the characteristic wave height is on the safe side taken as the maximum wave height ($H = 2H_{m0} \approx H_{max}$).

The modification to the second-order wavemaker theory is performed by the scaling factor, λ, given by Equation (3).

$$\lambda_{nm} = \min\left(1, \frac{S_{max}}{S(f_n, f_m)}\right) \quad (3)$$

The scaling factor should be calculated for all interacting frequencies in the first-order wave spectra and be multiplied to both second-order transfer functions $G^{\pm}_{nm}$ and $F^{\pm}_{nm}$. $G^{\pm}_{nm}$ is the transfer function for the second-order surface elevation and $F^{\pm}_{nm}$ is the transfer function of the second-order paddle movement. This reduces the amount of second-order energy so no secondary crest is calculated for the interaction of the individual frequencies. The optimal value of S_{max} is expected in this interval ($1 \leq S_{max} \leq 4$) which corresponds to a second-order amplitude of 25–100% of the first-order amplitude. Although the criteria of $S \leq 1$ given by Schäffer [3] is for superharmonics in regular waves the scaling is applied also to irregular waves. The present paper focus only on superharmonics (G^{+}_{nm} and F^{+}_{nm}), but the scaling is expected necessary also to subharmonics (G^{-}_{nm} and F^{-}_{nm}). Correct generation of the subharmonics is very important for response of many structures, but the present paper focus only on the superharmonics for which free energy is much easier to observe in the measured time series.

3. Theoretical Optimal S_{max}

The nonlinear wave theory by Fenton and Rienecker [8] can estimate the correct amount of second-order energy that exists for a given regular wave over a horizontal sea bed. With the use of nonlinear wave theory, it is thus possible to estimate what artificial limit (S_{max} in Equation (3)) should be used in the second-order wave theory to obtain the best results. In Figure 2, the calculated amplitude of the second-order component by second-order wavemaker theory is compared with the calculated by stream function wave theory by Fenton and Rienecker [8]. This is done for different values of S_{max}, where $S_{max} = \infty$ corresponds to no limit on the second-order energy (unmodified Schäffer [3] method).

The given applicability range by Schäffer [3] ($S \leq 1$) shows errors smaller than 10% when using the second-order wavemaker theory by Schäffer [3], see Figure 2. The figure shows that the recommendations given by Le Méhauté [9] based on this analysis might be on the safe side. However, this comparison though only considers the amplitude of the second-order component, but higher order components might be relevant.

By limiting the second-order energy to $S_{max} = 1$ the modified second-order wave generation gives errors smaller than 10% for wave conditions up to $S \approx 1.5$ as illustrated by the dotted line in the figure. Using values of $S_{max} = 1.5$–1.75 gives a larger area where the error is below 10%. Even

though S_{max} = 1.5–1.75 gives a larger area where the second-order amplitude is calculated with a small error, the second-order wavemaker theory is not necessarily valid as the third, and higher order energy might have a significant contribution. Therefore, the relation between the second-order and third order components must additionally be small. In Figure 3, the third order amplitude is compared to the first-order amplitude calculated by stream function wave theory. The figure shows that for sea states with $S \leq 1.5$ the amplitude of the third order component is below 10% of the first-order component. From these results, an optimum of S_{max} = 1 is found, and the expected range of applicability is extended from S = 1 to S = 1.5 with the modified second-order wavemaker theory.

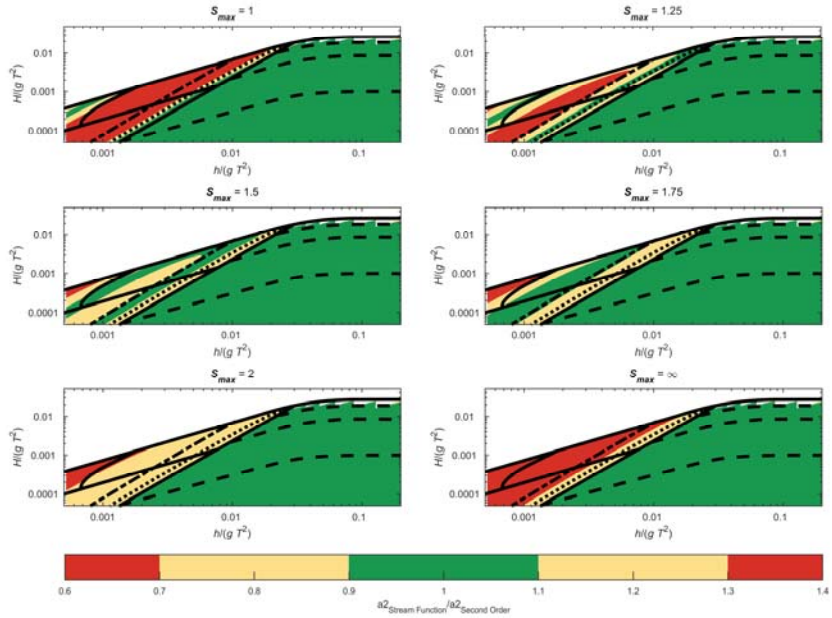

Figure 2. Comparison between the second-order amplitude calculated with second-order and stream function wave theory. S = 1.5 for the dotted line and S = 3 for the dashed-dotted line, which can also be seen in Figure 1 by the colored areas.

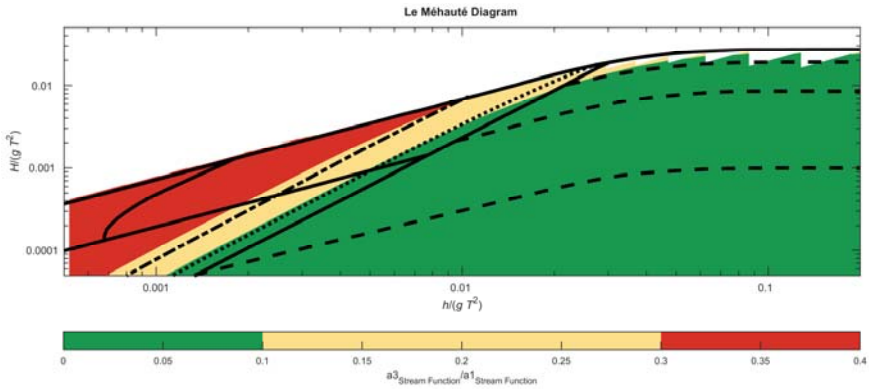

Figure 3. Comparison between the third order and first-order amplitude calculated with stream function wave theory. S = 1.5 for the dotted line and S = 3 for the dashed-dotted line.

4. Model Test Setup and Methodology

To verify the results from Section 3, physically experiments have been performed where the surface elevation was measured in different locations in the wave flume, see Figure 4.

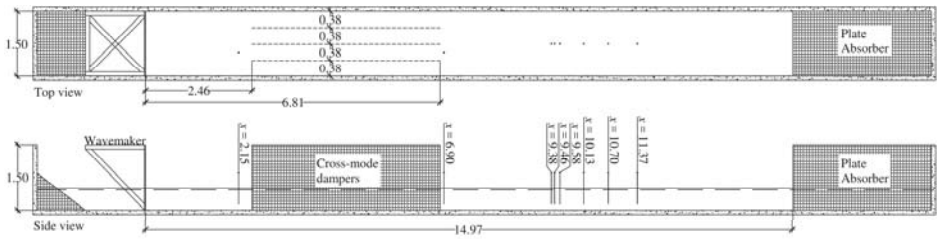

Figure 4. Experimental setup of the wave flume. Measures in meters.

The flume is equipped with a piston-type wavemaker, cross-mode dampers and a passive absorption system with perforated sheets in the end of the flume. The cross-mode dampers are a permanent installation in the flume and not installed due to specific cross-mode problems with the generated waves in the present study. The wavemaker has two sets of flush mounted resistance wave gauge on the wave board, which is used to avoid re-reflected waves from the wave board with use of the active wave absorption method by Lykke Andersen et al. [10]. The active absorption system has proven also to be effective for nonlinear irregular waves, cf. Lykke Andersen et al. [11]. The control signals are thus the wavemaker position and the surface elevation in the nearfield.

To evaluate the validity of each wavemaker theory, the measured surface elevation is compared to the theoretical surface elevation. The regular waves are compared to the predicted surface elevation by Fenton and Rienecker [8] and the irregular waves are compared to the COULWAVE Boussinesq wave model by Lynett and Liu [12]. The COULWAVE model is an accurate model when it comes to shoal waves from deep to shallow water including nonlinear interactions, see [13,14]. The results from the COULWAVE model was also used to generate the input for the ad-hoc unified irregular wave generation method by Zhang et al. [7].

The COULWAVE model was used to propagate irregular waves from deep water to the water depth used in the laboratory (0.5 m). The water depth at the wavemaker in COULWAVE is a compromise between the wave regime where the model is valid, $kh < 6$, and that regime where first-order wavemaker theory can be used. The waves were generated in the COULWAVE model on a horizontal part using a narrow banded JONSWAP spectrum ($\gamma = 10$) and truncated at 0.5 to 1.5 times the peak frequency. Thus, the primary spectrum does not significantly overlap with the bound harmonics. Then followed a 1:100 slope to the depth of 0.5 m and finally a horizontal part with a water depth of 0.5 m. The point where the 1:100 slope end, the surface elevation time series was extracted and used as a target for the different wave generation methods. The last horizontal part is where the target values are extracted to be compared with the measured surface elevation in the laboratory. Table 1 shows the numerical model parameters and the sea state conditions at the generation point and at $h = 0.5$ m.

Table 1. Wave conditions of the irregular waves at the generation point in COULWAVE.

	Model Parameters		Generation Point			h = 0.5 m
Case	**Cells per Wavelength**	**Courant Number**	h [m]	H_{m0} [m]	T_P [s]	H_{m0} [m]
F	200	0.5	2.5	0.102	2	0.083
G	200	0.5	4.0	0.087	3	0.087
H	300	0.5	8.0	0.068	5	0.091

The number of cells pr. wavelength is based on the wavelength of the peak wave period at the generation point. Thus, the discretisation of the model is, Δx = (cells per wavelength)/wavelength. The courant number is calculated by $C = c_0 \Delta t / \Delta x$, where c_0 is the shallow water celerity at the generation point and Δt is the timestep.

The method by Zhang et al. [7] uses the averaged velocity in the wave direction, but since only the surface elevation is provided from the COULWAVE model, a conversion to depth-averaged velocity is performed by assuming shallow water wave theory being valid. That is not entirely correct in intermediate water, but a fair approximation.

Because the generated primary spectrum in COULWAVE is narrow banded and truncated (0.5 to 1.5 times the peak frequency), the primary components can be separated from the bound harmonics by bandpass filtering at $0.5 f_P < f < 1.5 f_P$. This truncated spectrum was used as primary spectrum for the second-order wave generation method. The signal without bandpass was used as input for the method by Zhang et al. [7]. The measured waves in the laboratory were then compared with the unfiltered signals from the numerical model in the wave gauge locations.

The theoretical surface elevations calculated with COULWAVE and Fenton and Rienecker [8] might differ from the measured surface elevation due to the cross-mode dampers. The cross-mode dampers might slightly dissipate some of the energy in the physical flume. This is likely to be seen as a reduction in wave height when comparing the measured surface elevation at x = 2.15 m and x = 6.90 m. Furthermore, the theoretical surface elevation is without reflected waves which is difficult to entirely avoid in the physical model. Therefore, reflection in the experimental tests should be reduced to a minimum. The amplitude reflection coefficient in the physical tests was in the range of 11% to 16%, which was calculated with the nonlinear irregular wave separation method by Eldrup and Lykke Andersen [15]. The amount of reflection in the physical experiments is found acceptable for comparing the total measured surface elevation with the theoretical surface elevation.

5. Regular Wave Results

For regular waves, the different wavemaker theories are evaluated against the theoretical stream function wave theory. This evaluation is performed at different distances from the wavemaker. Linear to highly nonlinear waves were generated and compared to the theoretical wave profiles. The measured surface elevations are shown after the ramp-up of the wavemaker is completed and if possible before reflection is present in the signals.

Figure 5 shows the results for Sea State A. The measured profiles are almost identical for the different wave generation methods. However, a reduction in the amplitude is observed for $x \geq 6.90$ m. The reduction in amplitude might be due to the cross-mode dampers. The shape of the measured surface elevations for all the wavemaker theories are similar to the theoretical. Therefore, it can be concluded that all the tested wavemaker methods are valid for Sea State A, and thus the first and second-order wave generation methods lead to acceptable waves, in a more extensive area than given by the Le Méhauté diagram. However, Sea State A is within the validity range given by Schäffer [3] ($S < 1$).

The results for Sea State B are shown in Figure 6 from which it appears that the first-order wavemaker method lead to some minor deviations in the wave shape, indicating some free higher harmonics energy exist. The surface profile for the second-order methods and the ad-hoc unified generation method are similar, and these are close to the theoretical profile. The wave height of the generated waves is slightly lower than the theoretical, but the wave shape is a close match to the target. From the section with the theoretical analysis of an optimum of S_{max}, a difference was expected to be seen between the original second-order and the modified second-order method when $S > 1.0$, but this is not observed from Figure 6 for a case with S = 1.46.

Results for Sea State C shows that the wave profile generated with first and second-order wavemaker theory is not constant in the various gauge positions, cf. Figure 7. This is due to free unwanted waves being generated by these theories when the nonlinearity is too high. The second-order

wavemaker theory is slightly better than first-order theory, but the ad-hoc unified wave generation is a close match to the theoretical profile. For x = 2.15 m, the wave crest of the generated waves by the second-order wavemaker theory by Schäffer [3] is much larger than the theoretical wave crest, and the proposed correction to the second-order method leads to a wave profile closer to the theoretical profile. These results shows that Schäffer [3] overestimates the second-order amplitude when $S > 1$.

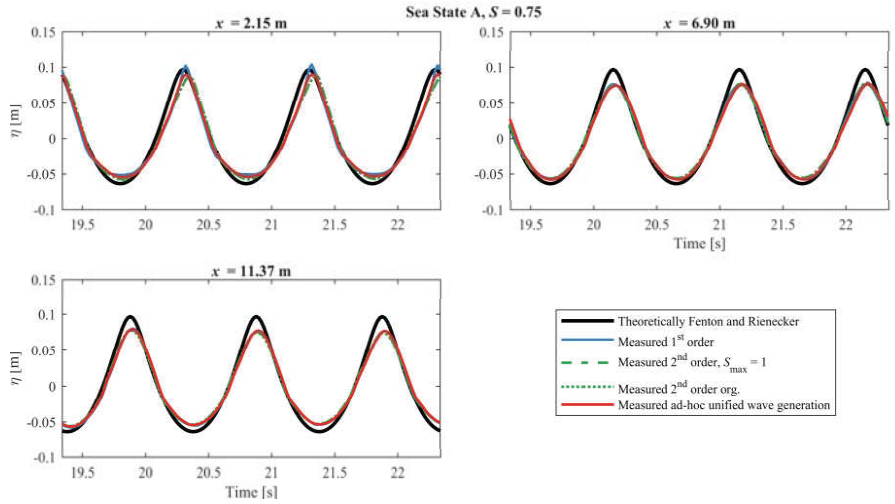

Figure 5. Theoretically surface elevation compared with the first-order, second-order, modified second-order and the ad-hoc unified wavemaker methods for Sea State A.

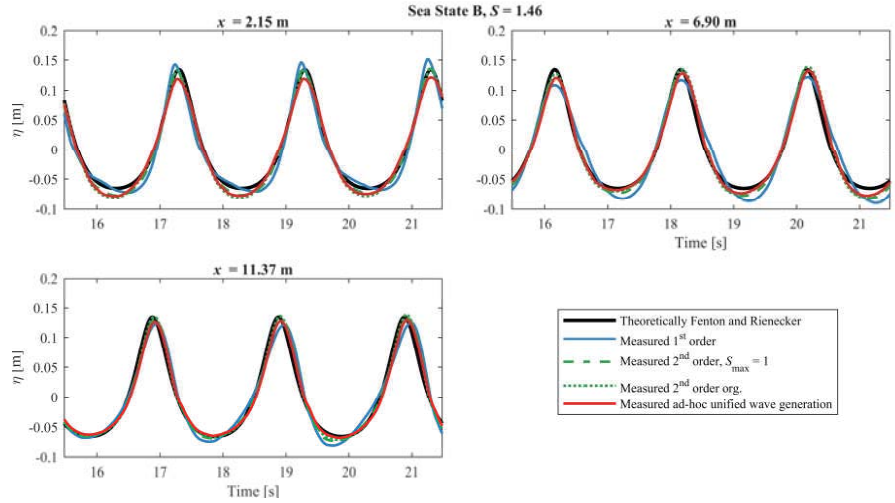

Figure 6. Theoretically surface elevation compared with the first-order, second-order, modified second-order and the ad-hoc unified wavemaker methods for Sea State B.

Sea State D is shown in Figure 8. Again, large waves are observed in x = 2.15 m for the second-order wavemaker theory, and a small wave crest is seen in the wave trough. The first-order wavemaker theory is actually better than the second-order wavemaker theory for x = 2.15 m. This indicates

the second-order method actually increases the amplitude of the free waves compared to first-order wavemaker theory. The large waves generated by second-order wavemaker theory were causing breaking waves, which did not occur for the other generation methods. The modified second-order wavemaker theory is performing better than first-order and second-order wavemaker theory, but free waves are also observed for that method. The ad-hoc unified wave generation is a close match to the theoretical wave profile except for the observed reduction in amplitude for $x \geq 6.90$ m, which is likely due to the cross-mode dampers.

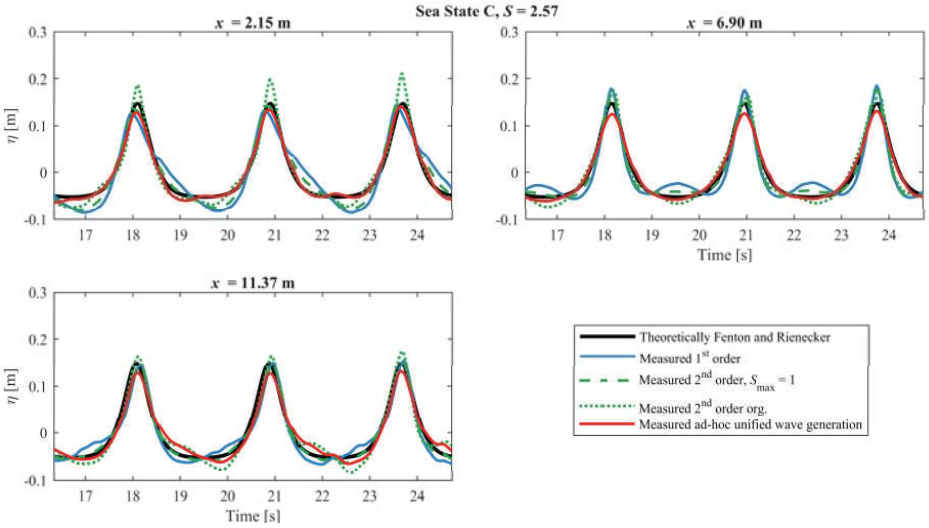

Figure 7. Theoretically surface elevation compared with the first-order, second-order, modified second-order and the ad-hoc unified wavemaker methods for Sea State C.

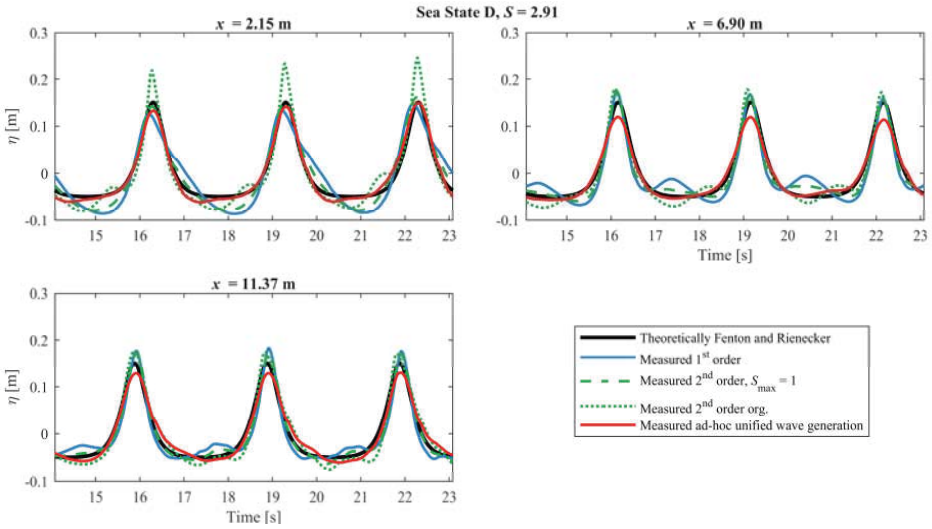

Figure 8. Theoretically surface elevation compared with the first-order, second-order, modified second-order and the ad-hoc unified wavemaker methods for Sea State D.

Results for Sea State E is shown in Figure 9. For that case second-order wavemaker theory generates too large waves in x = 2.15 m and a secondary wave is also seen in the wave trough of the primary wave. The first-order wavemaker theory is significantly better than the second-order wavemaker theory as no secondary waves are seen in x = 2.15 m. As in Figure 8, the waves generated by second-order wavemaker theory are breaking during the tests, which is the reason for the large wave crest are not observed for the two other locations in the figure. The modified second-order wavemaker theory is slightly better than the first-order wavemaker theory, but they are both far from the theoretical profile. The ad-hoc unified wave generation is a close match to the theoretical profile except for small deviations in the trough, but this is most likely due to reflections from the passive absorber in the wave flume.

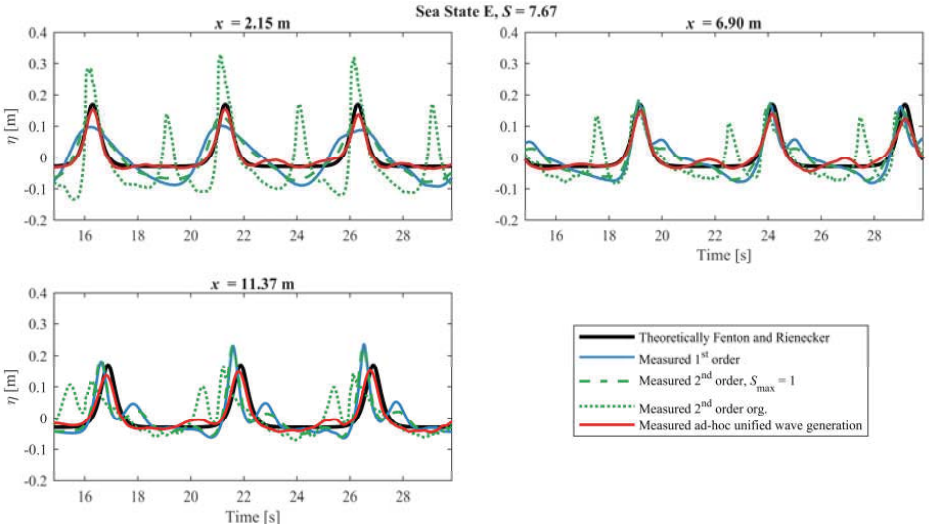

Figure 9. Theoretically surface elevation compared with the first-order, second-order, modified second-order and the ad-hoc unified wavemaker method for Sea State E.

A more detailed analysis of the measured waves for Sea State E is shown in Figure 10 for x = 2.15 m. The time series of the primary and the first three superharmonics is calculated by Fourier transformation on the discrete frequencies $n\omega$. Thus, the measured components can be compared with the theoretical stream function wave components. The figure shows that the original second-order wavemaker theory generates higher harmonics that are significantly higher than the theoretical stream function wave. It also shows that only the ad-hoc method generates the correct amplitudes of the different contributions. Furthermore, a phase shift between the superharmonics and the first-order component is observed especially for the first-order generation method and the original second-order method. This phase shift demonstrates significant free energy to be present. Only the ad-hoc method has correct amplitudes and phases for all components.

It has been shown that first-order wavemaker theory can be used for $S \leq 0.8$ and that the modified second-order wavemaker theory gives identical results as the second-order theory by Schäffer [3] when the second-order theory is valid. However, the modified second-order method performs significantly better when used outside the validity area. This is due to a more realistic value of the amplitude for the second-order harmonic, which for the method by Schäffer [3] has no upper limit and for the present tests is calculated to approximately two times the first-order amplitude in the worst case (Sea State E). In that case, the higher order harmonics have a significant influence, and therefore second-order theory is not valid for this case. This is shown in Figure 10 by comparing the contributions of the first

four harmonics with the theoretical amplitudes. The second-order wavemaker theory can be used for $S \leq 1.5$ with reasonable results. The ad-hoc unified generation can be used for all the tested conditions (tested up to $S = 7.7$).

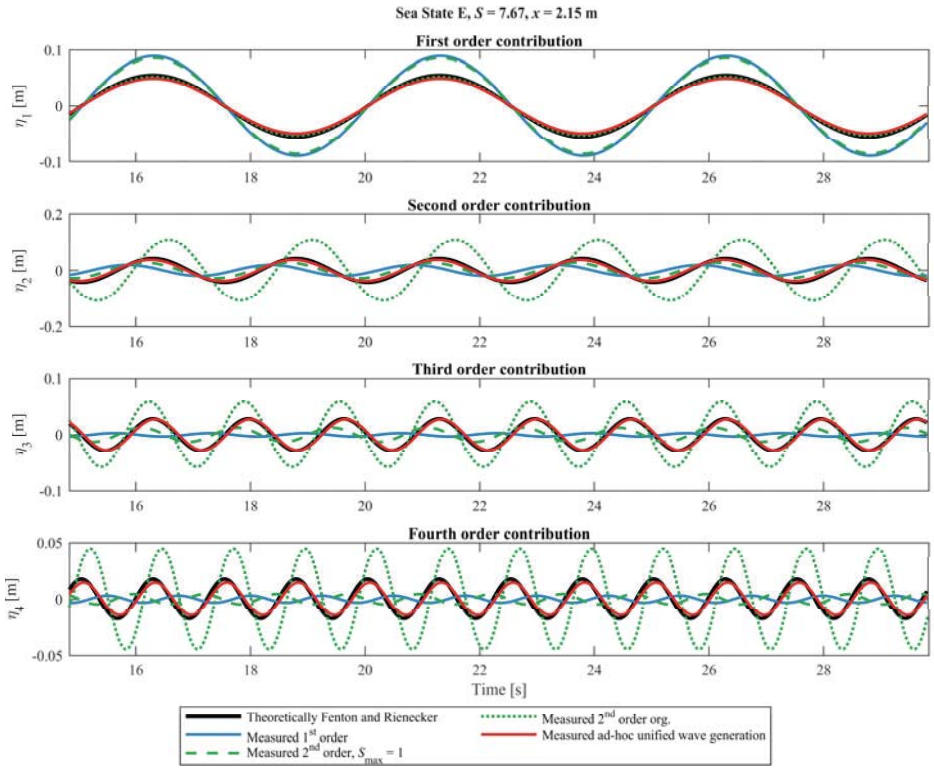

Figure 10. Contribution of the first four harmonics to the surface elevation for Sea State E at x = 2.15 m. First-order, second-order, modified second-order and the ad-hoc unified wavemaker method are compared with the theoretical harmonics in stream function waves.

6. Irregular Wave Results

The performance of the different wavemaker methods for the irregular waves are compared with the results from the COULWAVE model at different distances from the wavemaker. The measured surface elevations are shown for a time window including the highest wave.

Results for Sea State F are given in Figure 11. The first and second-order wavemaker theories are according to the Le Méhauté diagram not expected to be valid for this sea state. Furthermore, the test is also outside the applicability range given by Schäffer [3]. However, the figure shows that all the tested methods give similar results and that they are a close match to the COULWAVE model with only minor deviations.

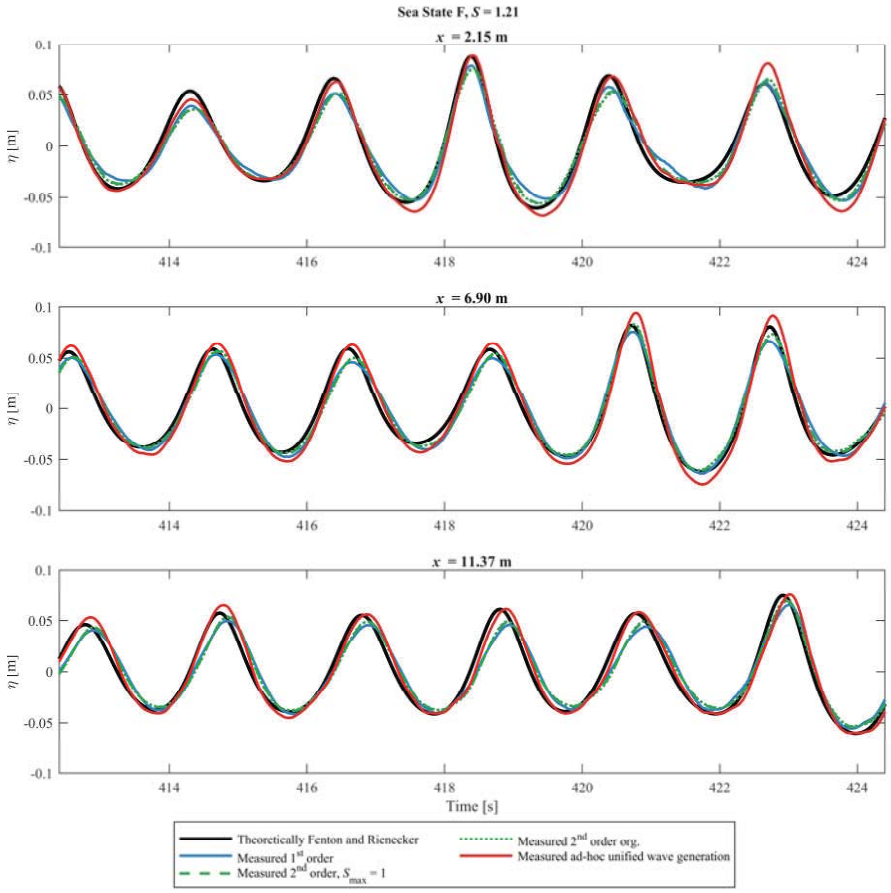

Figure 11. Numerically surface elevation compared with the first-order, second-order, modified second-order and the ad-hoc unified wavemaker methods for Sea State F.

Figure 12 presents the results for Sea State G. For this case is the wave crest of the largest wave with the first-order wavemaker theory significantly smaller than the theoretical wave profile at x = 2.15 m. The original second-order wavemaker theory is closer to the numerical profile except for some deviations in the wave trough for x = 2.15 m. For the three wave gauges, it can be seen that the wave crest is too small for the largest waves when the waves are generated with the modified second-order wavemaker method, but except for that, it is a close match. The shape of the waves generated by the ad-hoc unified generation method is a close match but with a deeper wave trough at x = 2.15 m, but this is likely due to long reflected waves as it is not seen for the two other gauges.

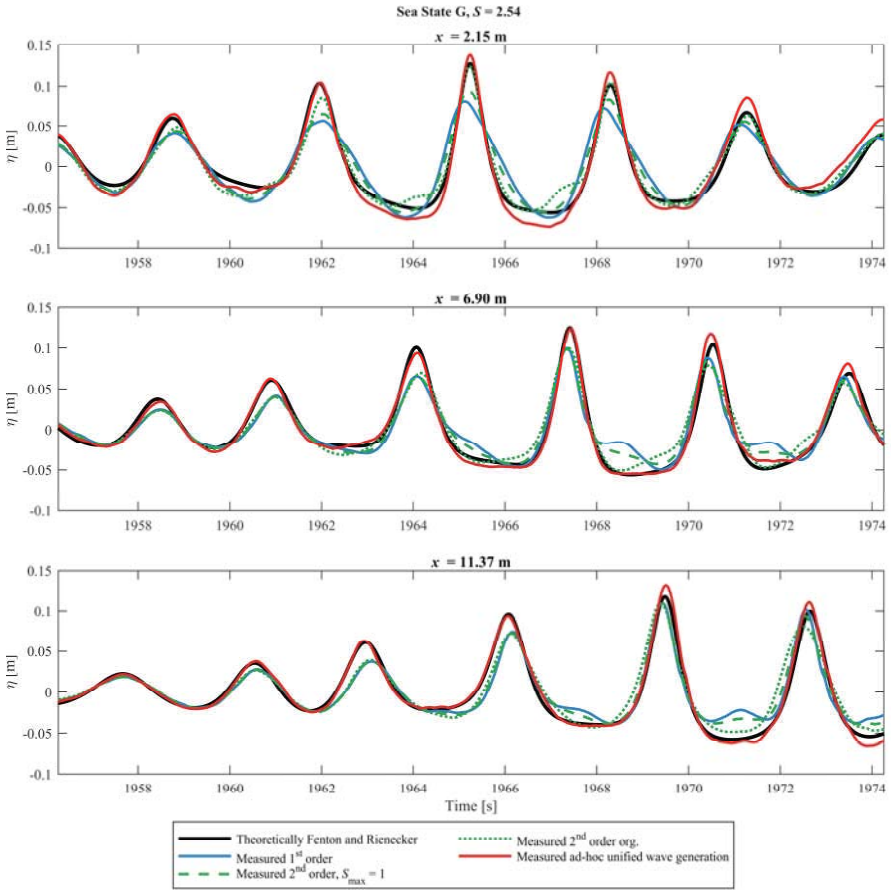

Figure 12. Numerically surface elevation compared with the first-order, second-order, modified second-order and the ad-hoc unified wavemaker methods for Sea State G.

For Sea State H, the first-order wavemaker theory is deviating significantly from the numerical profile as the wave trough is not flat and long and the wave crest is not high and narrow, cf. Figure 13. The wave profile generated by the first-order wavemaker theory has a step front followed by a gentler rear as the waves propagate away from the wavemaker—this is due to the free and bound waves having different celerity. For $x = 11.37$, the free and bound waves are phase shifted to such a degree that the crest of both the free and the bound waves are visible. The second-order wavemaker method has a secondary crest in the wave trough, which is reduced significantly with the modified second-order method. The wave crest with the modified second-order wavemaker method is though significantly smaller than the theoretical but is still closer to the theoretical compared to the first-order wavemaker method. The modified method is better than the original second-order method as less free energy is generated, but for this case the amount of secondary energy is also much smaller than the target. The ad-hoc unified wavemaker method provides a close match to the numerical profile with only minor deviations, and for this sea state, only this method leads to acceptable results.

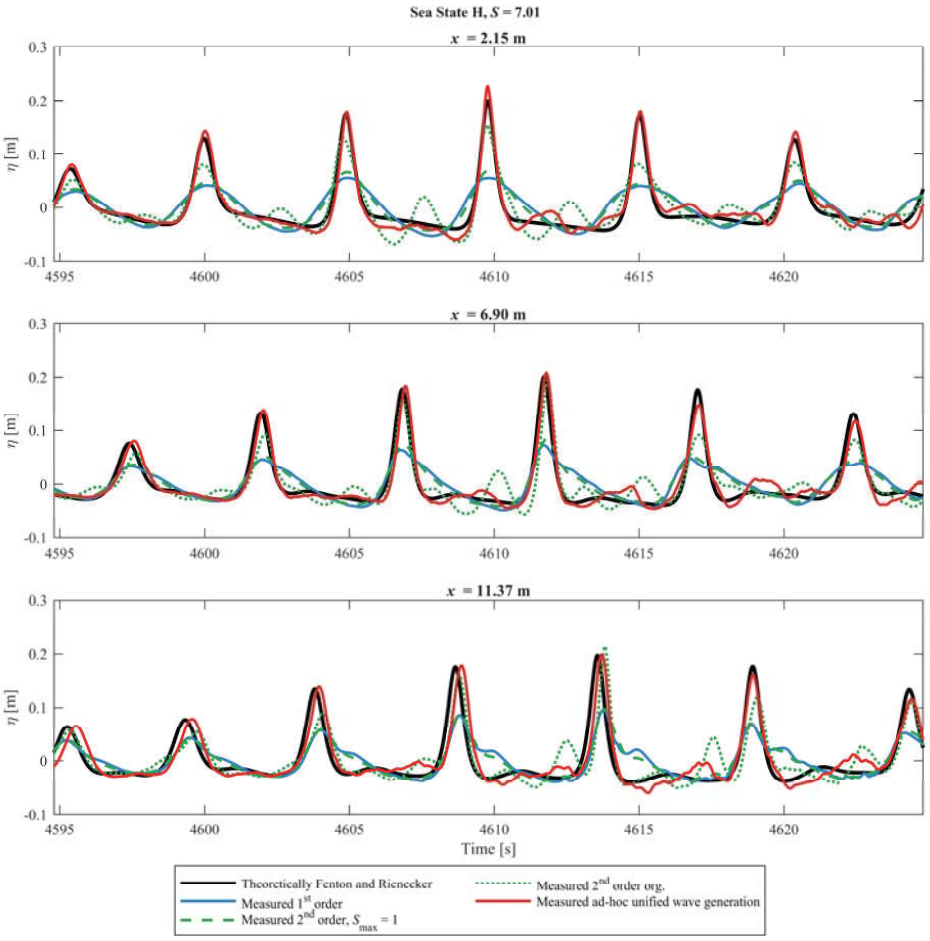

Figure 13. Numerically surface elevation compared with the first-order, second-order, modified second-order and the ad-hoc unified wavemaker methods for Sea State H.

For irregular waves, the present tests showed that first-order wavemaker theory can be used for $S \leq 1.2$, while the second-order wavemaker theory can be used for $S \leq 2$ with reasonable results. The ad-hoc unified generation showed good performance and can be used for all the tested conditions (tested up to $S = 7.0$).

7. Conclusions

Model tests have been performed with the purpose to generate waves of various nonlinearity and evaluate different wavemaker methods. First-order, second-order and ad-hoc unified generation methods have been tested, and the validity range of each method has been found by physical experiments. Furthermore, a modification to the second-order wavemaker method was proposed to increase the validity to more nonlinear waves. The ad-hoc unified generation method for the regular waves was the most accurate wavemaker method, and if possible, it should be used, otherwise the modified second-order is preferable. For the irregular waves, the ad-hoc unified generation method is also the most accurate one, but it is also much more time-consuming in synthesize the signals. This is

because a time series has to be prepared by a numerical model before waves can be generated in the physical model. Therefore, it is recommended to use the modified second-order wavemaker theory when it is valid.

Table 2 summarizes the applicability ranges of each wavemaker method. For the regular waves, acceptable results are found with first-order wavemaker when $S < 0.8$, while second-order methods extends the validity to $S < 1.5$. The ad-hoc method is applicable for all the tested conditions ($S < 7.7$), but is expected to be reliable for all S values. For the irregular waves, acceptable results are found with first-order theory when $S < 1.2$. For both second-order methods acceptable results for irregular waves were found when $S < 2.0$. The ad-hoc method showed also for irregular waves good results for all the tested conditions. As it has not been possible to test all possible sea states these results should be taken as preliminary, but can be used until more tests have been performed.

Table 2. Applicability of each tested wavemaker method.

	Regular Waves				**Irregular Waves**			
	First-order	Second-order	Modified second-order	Ad-hoc unified	First-order	Second-order	Modified second-order	Ad-hoc unified
S	0.8	1.5	1.5	∞	1.2	2.0	2.0	∞

Author Contributions: M.R.E. wrote the original draft and performed all the simulations, experiments and analysis. Furthermore, he established the modified second-order wavemaker theory; T.L.A. reviewed the paper and contributed to the performed analysis and in establishing the modified second-order wavemaker theory.

Funding: This research received no external funding.

Conflicts of Interest: The authors declare no conflict of interest.

References

1. Havelock, T.H. LIX. Forced surface waves on water. *Philos. Mag.* **1929**, *8*, 569–576. [CrossRef]
2. Schäffer, H.A. Laboratory Wave Generation Correct to Second Order. In *Wave Kinematics and Environmental Forces: Papers Presented at a Conference Organized by the Society for Underwater Technology and Held in London, U.K., 24–25 March 1993*; Springer: Dordrecht, The Netherlands, 1993; pp. 115–139.
3. Schäffer, H.A. Second-order wavemaker theory for irregular waves. *Ocean Eng.* **1996**, *23*, 47–88. [CrossRef]
4. Orszaghova, J.; Taylor, P.H.; Borthwick, A.G.L.; Raby, A.C. Importance of second-order wave generation for focused wave group run-up and overtopping. *Coast. Eng.* **2014**, *94*, 63–79. [CrossRef]
5. Sriram, V.; Schlurmann, T.; Schimmels, S. Focused wave evolution using linear and second order wavemaker theory. *Appl. Ocean Res.* **2015**, *53*, 279–296. [CrossRef]
6. Zhang, H.; Schäffer, H.A. Approximate Stream Function wavemaker theory for highly non-linear waves in wave flumes. *Ocean Eng.* **2007**, *34*, 1290–1302. [CrossRef]
7. Zhang, H.; Schäffer, H.A.; Jakobsen, K.P. Deterministic combination of numerical and physical coastal wave models. *Coast. Eng.* **2007**, *54*, 171–186. [CrossRef]
8. Fenton, J.D.; Rienecker, M.M. Accurate Numerical Solutions for Nonlinear Waves. In *Coastal Engineering 1980*; American Society of Civil Engineers: New York, NY, USA, 1980; pp. 50–69.
9. Méhauté, B. *An Introduction to Hydrodynamics and Water Waves*; Springer: Berlin/Heidelberg, Germany, 1976.
10. Lykke Andersen, T.; Clavero, M.; Frigaard, P.; Losada, M.; Puyol, J.I. A new active absorption system and its performance to linear and non-linear waves. *Coast. Eng.* **2016**, *114*, 47–60. [CrossRef]
11. Lykke Andersen, T.; Clavero, M.; Eldrup, M.R.; Frigaard, P.; Losada, M. Active Absorption of Nonlinear Irregular Wwaves. In Proceedings of the Coastal Engineering Conference, Baltimore, MD, USA, 30 July–3 August 2018.
12. Lynett, P.; Liu, P.L.-F. A two-layer approach to wave modelling. *Proc. R. Soc. Lond. Ser. A Math. Phys. Eng. Sci.* **2004**, *460*. [CrossRef]
13. Hsiao, S.-C.; Lynett, P.; Hwung, H.-H.; Liu, P.L.-F. Numerical simulations of nonlinear short waves using a multilayer model. *J. Eng. Mech.* **2005**, *131*, 231–243. [CrossRef]

14. Teixeira, P.R.F.; Pinheiro, L.; Fortes, C.M.J.; Carreiros, C.; Grande, R. Comparison of Three Nonlinear Models to Analyze Wave Propagation Over Submerged Trapezoidal Breakwaters. In Proceedings of the V European Conference on Computational Fluid Dynamics, Lisbon, Portugal, 14–17 June 2010; pp. 14–17.
15. Eldrup, M.R.; Lykke Andersen, T. Estimation of Incident and Reflected Wave Trains in Highly Nonlinear Two-Dimensional Irregular Waves. *J. Waterw. Port Coast. Ocean Eng.* **2019**, *145*.

Paper B

Estimation of Incident and Reflected Components in Highly Nonlinear Regular Waves

Thomas Lykke Andersen
Mads Røge Eldrup
Peter Frigaard

The paper has been published in
Coastal Engineering, ISSN: 0378-3839, 119, 2017, pp. 51-64.
DOI: 10.1016/j.coastaleng.2016.08.013

Coastal Engineering 119 (2017) 51–64

Contents lists available at ScienceDirect

Coastal Engineering

journal homepage: www.elsevier.com/locate/coastaleng

Estimation of incident and reflected components in highly nonlinear regular waves

Thomas Lykke Andersen *, Mads Røge Eldrup, Peter Frigaard

Department of Civil Engineering, Aalborg University, Thomas Manns Vej 23, DK-9220 Aalborg Ø, Denmark

ARTICLE INFO

Article history:
Received 14 January 2016
Received in revised form
1 July 2016
Accepted 28 August 2016
Available online 17 November 2016

Keywords:
Wave reflection analysis
Nonlinear waves
Regular waves
Bound superharmonics

ABSTRACT

Knowledge of the incident and reflected waves present in laboratory experiments is a key issue in order to correctly assess the behaviour of the tested structure. Usual applied reflection separation algorithms are based on linear wave theory. These linear methods might result in unreliable estimates of the incident and reflected waves in case the waves are nonlinear. In the present short paper a new nonlinear reflection separation algorithm optimized for regular waves is presented. The method separates the superharmonics into bound/free and incident/reflected components. The separation in bound and free components is possible because they travel with different celerity. The new method is an extension of the Lin and Huang (2004) method as they used linear dispersion so indirectly assumed the bound waves to be of 2nd order maximum. They did thus not take into account the amplitude dispersive effect of nonlinear waves (3rd and higher order). The present method uses nonlinear wave celerity in order to overcome this limitation. It is shown in the present paper that for highly nonlinear regular waves none of the existing state-of-the-art tools are reliable. The new method showed on the other hand a good match for all of the tested synthetically generated wave conditions including shallow and deep water and proved also to be robust to noise. Even though the new method is developed for horizontal sea bed it is demonstrated to provide reasonable results on numerical data for vertical asymmetric waves on mildly sloping foreshores.

1. Introduction

In model test experiments it is a key element to accurately determine the incident waves the models are exposed to. For reflective structures this involves the separation of the incident and reflected wave trains. Alternatively waves might be calibrated without the structure in place, but this requires additional testing time and there is anyway no guarantee for the incident waves to be identical with the structure in place. This requires namely a perfect active absorption system to avoid re-reflection at the paddle and it also requires no interaction of incident and reflected waves. Wave breaking is one example of a phenomena that is dependent on the combination of incident and reflected waves and might therefore be different with and without structure in-place. Therefore, accurate and robust methods to determine the incident and reflected waves with the structure in-place are important.

The first significant work on separation of incident and reflected waves was the linear two-gauge methods of [4]. This method was extended to a more robust 3 gauge linear method by [9] in order to minimize effects of noise and singularities. Mansard and Funke method was further extended to arbitrary number of wave gauges by [11].

The nonlinear LASA V model proposed by [3] is a local time domain solution. LASA is based on fitting the parameters of the incident and reflected profiles in each local time window by using simulating annealing as fitting algorithm. In LASA V the wave profile used in each local time window is a 5th order Stokes profile for both incident and reflected waves. This means basically an assumption of no free energy to be present which does not necessarily reflect physical model test conditions. The present paper demonstrates that LASA V results are not reliable for highly nonlinear waves even though tests cases have no free energy. Moreover, the computational cost of LASA V is a major downside of this method in practical applications.

All of above methods are applicable for regular and irregular waves, but might have problems with nonlinearities. For regular waves an alternative method was proposed by [6] that in addition to separate in incident and reflected primary components also consider free and bound superharmonics. However, their method is shown in the present paper to provide accurate results only for

* Corresponding author.
E-mail addresses: tla@civil.aau.dk (T. Lykke Andersen), mre@civil.aau.dk (M.R. Eldrup), pf@civil.aau.dk (P. Frigaard).

http://dx.doi.org/10.1016/j.coastaleng.2016.08.013
0378-3839/

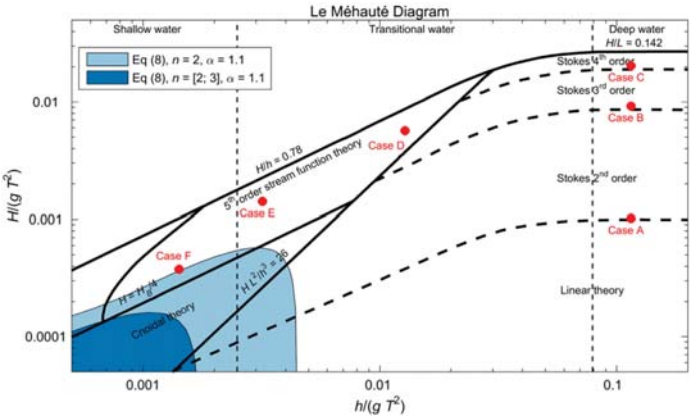

Fig. 1. Diagram by [5] describing the nonlinearity of the regular test cases (cases A–F). Hatched areas show criteria in Eq. (8) for $\alpha = 1.1$.

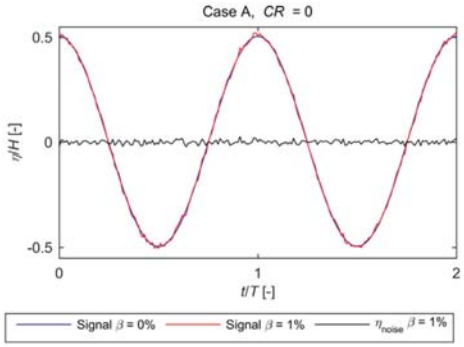

Fig. 2. Example of signals without and with noise for $\beta = 1\%$.

mildly nonlinear waves because amplitude dispersion was ignored.

An extension of the Lin and Huang method is proposed in the present paper by inclusion of amplitude dispersion in their method. Moreover, a problematic region where bound and free components have identical celerity is identified and a correction is suggested that is applicable to present method as well as Lin and Huang method.

The separation in bound and free harmonics is very relevant when analysing model tests. This is because if bound superharmonics are not properly generated by the wavemaker then unwanted free waves will exist. Unwanted free incident waves will also exist in case the active absorption system of the wavemaker is not ideal. Moreover, when the incident waves reach a structure part of the incident energy will be absorbed and part of it will be reflected. This means the reflected wave cannot bind the same amount of energy as the incident one. As a consequence reflected harmonics will always be partly free and partly bound. If the reflection is small or medium they will mainly be free, whereas if reflection is large bound reflected components might be significant. With the present method the details of the waves can be assessed including quality of the wave generation and active absorption systems, see for example [7]. This is very important in order to correctly analyse model tests with regular waves.

2. Lin-Huang method

The bound superharmonic components travel with the celerity of the regular wave, but the free components travel with their own celerity as given by the dispersion equation. This makes it possible to separate bound and free components as suggested by [6]. This separation is quite unique for this method and completely different to linear methods where all energy is assumed free. The mathematical model of the surface for N^{th} order waves as function of time (t) and coordinate of gauge number m (x_m) measured positive in the incident wave direction is taken as:

$$\begin{aligned}\eta(x_m,t) = {} & a_I^{(1)}\cos\left(kx_m - \omega t + \varphi_I^{(1)}\right) \\ & + a_R^{(1)}\cos\left(kx_m + \omega t + \varphi_R^{(1)}\right) \\ & + \sum_{n=2}^{N} a_{I,B}^{(n)}\cos\left[n\left(kx_m - \omega t\right) + \varphi_{I,B}^{(n)}\right] \\ & + \sum_{n=2}^{N} a_{R,B}^{(n)}\cos\left[n\left(kx_m + \omega t\right) + \varphi_{R,B}^{(n)}\right] \\ & + \sum_{n=2}^{N} a_{I,F}^{(n)}\cos\left[k^{(n)}x_m - n\omega t + \varphi_{I,F}^{(n)}\right] \\ & + \sum_{n=2}^{N} a_{R,F}^{(n)}\cos\left[k^{(n)}x_m + n\omega t + \varphi_{R,F}^{(n)}\right] \\ & + e_m(t)\end{aligned} \tag{1}$$

where subscript I and R represent incident and reflected components, respectively. Subscript B and F denote bound and free components. a is the amplitude, k the wave number, $\omega = 2\pi/T$ is the cyclic frequency, T the period of the wave (primary component) and φ the phase. k denotes the wave number of the primary components and $k^{(n)}$ the wave number of the n^{th} order free component. These were determined by linear dispersion:

$$(n\omega)^2 = gk^{(n)}\tanh\left(k^{(n)}h\right) \tag{2}$$

where g is the gravity acceleration and h the water depth. Lin and Huang do not explicitly mention how the wave number of the

Table 1
Errors in percent on estimated incident wave height from reflection analysis with $\beta = 0$. For methods that separate bound and free components the wave height is including bound components, but excluding free components.

	Zelt and Skjelbreia			LASA V			Lin and Huang			Present method		
Case \ CR	0	0.5	1	0	0.5	1	0	0.5	1	0	0.5	1
A	0.0	0.1	0.1	1.9	2.6	3.2	0.0	0.0	0.0	0.0	0.0	0.0
B	−0.8	−1.1	1.1	−0.4	−0.4	−1.1	−0.5	−0.6	0.1	0.0	0.0	0.0
C	−3.9	−3.3	−0.6	−3.7	−4.8	−3.9	−2.2	−2.6	−2.6	−0.2	−0.2	−0.3
D	−5.7	−5.0	−4.3	−2.2	−1.0	−4.2	2.8	2.9	3.4	−0.1	−0.1	−0.2
E	−19.1	−16.4	−5.2	0.4	3.2	−4.1	−4.1	11.7	16.1	−0.5	0.0	−0.1
F	−12.6	−11.5	−6.7	−7.5	−3.7	−19.8	−1.9	−1.4	39.5	−1.2	−0.3	0.0
F_{FREE}	–	–	–	–	–	–	0.1	0.4	37.9	−0.9	−0.1	0.1
E_{ASYM}	−11.6	–	–	−1.7	–	–	8.1	–	–	−2.4	–	–
F_{ASYM}	−6.0	–	–	−0.5	–	–	4.9	–	–	−4.1	–	–

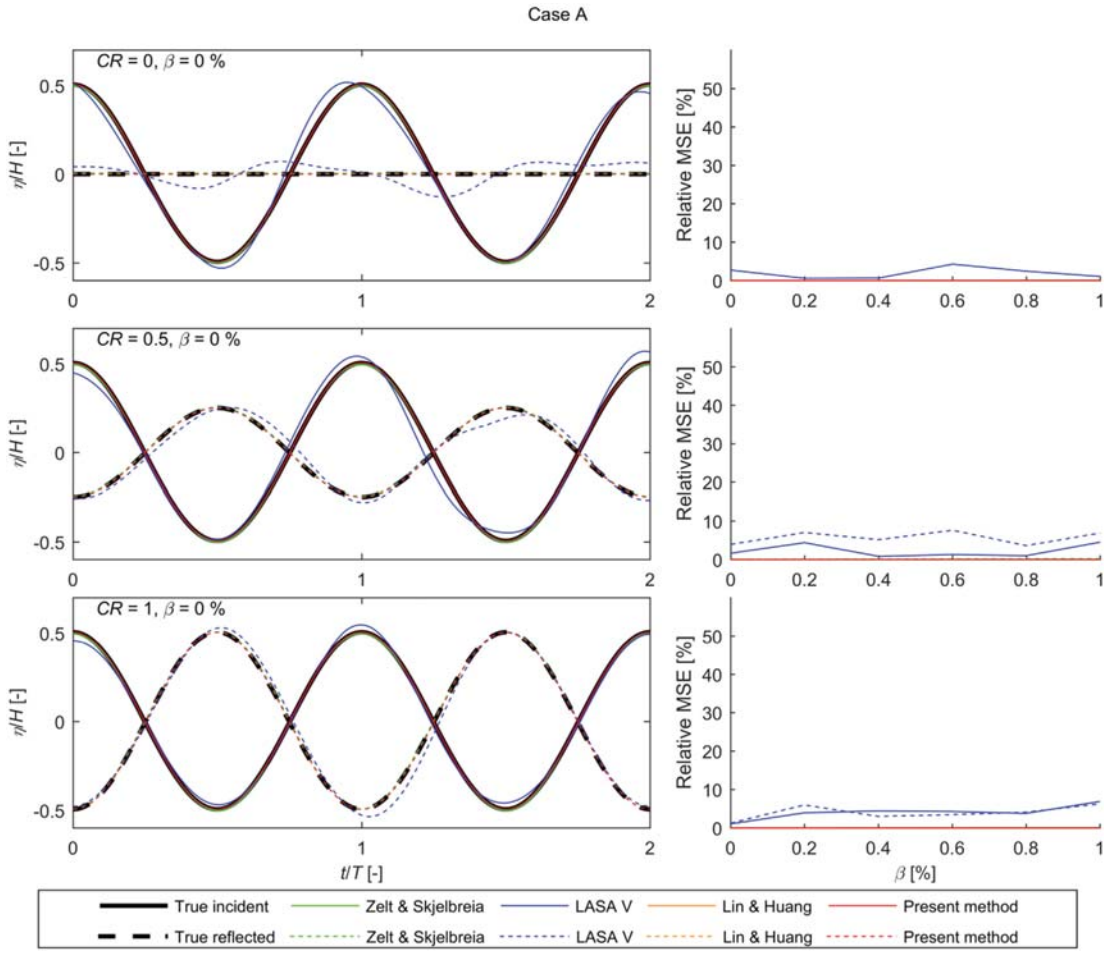

Fig. 3. Comparison of calculated and actual surface elevations for case A. The relative MSE is shown with the different levels of noise.

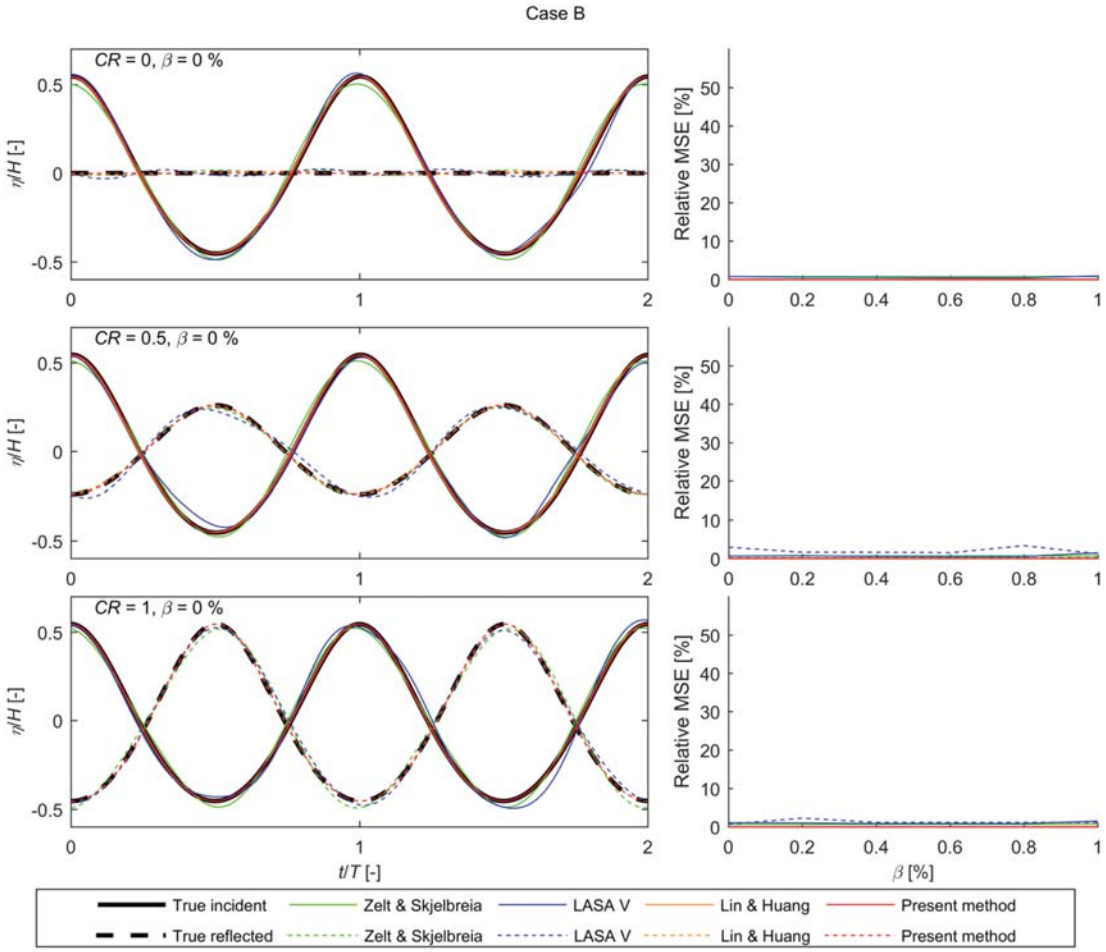

Fig. 4. Comparison of calculated and actual surface elevations for case B. The relative MSE is shown with the different levels of noise.

primary component k is determined, but indirectly it appears that it must also be based on linear dispersion (i.e. Eq. (2) with $n = 1$). Another reason for this is that the same value of k is used for incident and reflected waves. The linear dispersion is only valid to 2nd order so they indirectly have assumed mildly nonlinear waves (2nd order theory valid).

3. New method: the Lykke Andersen method

The Lin-Huang method uses the linear dispersion equation, while higher order waves are in reality amplitude dispersive. The consequence of neglecting the amplitude dispersion is that for highly nonlinear waves the estimated distribution of energy among components will be somewhat disturbed from reality. This is especially the case when using few wave gauges, but as demonstrated in this paper also when using an overdetermined system.

The present method corrects that by applying a higher order wave length estimate. The wave numbers of the primary component (and bound components) thus depends additionally on the wave height (H) and will thus be different for incident and reflected waves. The wave period to be applied in the dispersion relation is usually known beforehand as the method applies to lab data only, but can also be estimated based on the signals for example by zero down crossing analysis or from the frequency of the first Fourier coefficient with significant energy. However, the incident and reflected wave height needed for the nonlinear dispersion relation is part of the solution and is thus unknown to begin with. Therefore, the following iterative procedure is used for the wave length estimation:

1. Calculate the wave number based on linear dispersion, i.e. for infinitesimally small wave height. Use this estimate as a starting guess for the incident and reflected wave numbers (k_I, k_R).
2. Calculate 1st to N^{th} order incident and reflected components using Eqs. (3)–(10). For bound components use latest estimated incident and reflected wave numbers (k_I, k_R) calculated in either

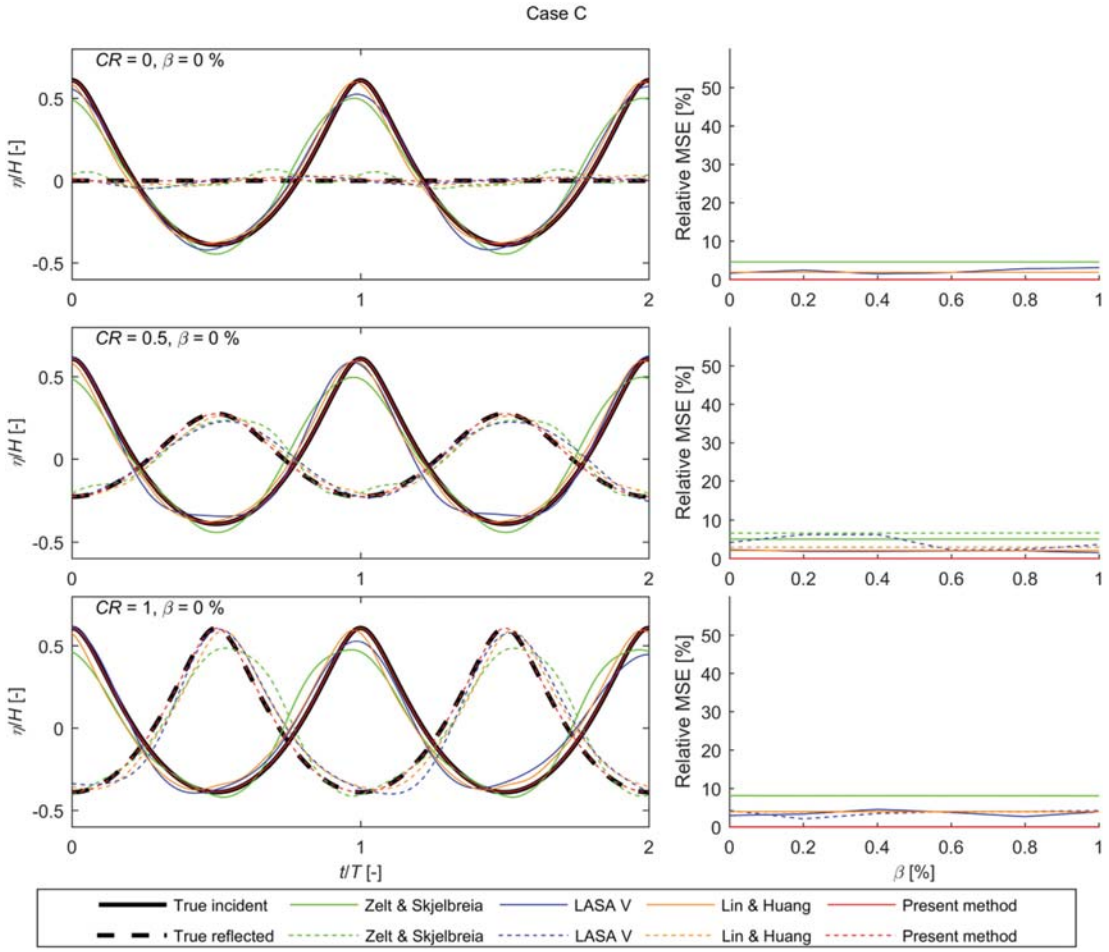

Fig. 5. Comparison of calculated and actual surface elevations for case C. The relative MSE is shown with the different levels of noise.

step 1 for first iteration or step 3 for following iterations. Free components will normally be of much smaller height and linear assumption is assumed valid for those.

3. Calculate the incident and reflected wave heights based on incident and reflected surface elevations including bound superharmonic components. Calculate updated values of incident and reflected wave numbers including amplitude dispersion (k_I, k_R). The nonlinear dispersion applied is Stokes V order theory when it is valid (deep water). If Stokes V is not valid wave number is calculated by stream function theory using [2] method. It is believed that the wave length estimate of [1] could also be applied without significant degradation of the proposed method.
4. Repeat step 2 to 3 until convergence is obtained for the incident and reflected wave numbers.

The applied mathematical model is thus:

$$\begin{aligned}\eta(x_m,t) = {} & a_I^{(1)}\cos\left(k_I x_m - \omega t + \varphi_I^{(1)}\right) \\ & + a_R^{(1)}\cos\left(k_R x_m + \omega t + \varphi_R^{(1)}\right) \\ & + \sum_{n=2}^{N} a_{I,B}^{(n)}\cos\left[n\left(k_I x_m - \omega t\right) + \varphi_{I,B}^{(n)}\right] \\ & + \sum_{n=2}^{N} a_{R,B}^{(n)}\cos\left[n\left(k_R x_m + \omega t\right) + \varphi_{R,B}^{(n)}\right] \\ & + \sum_{n=2}^{N} a_{I,F}^{(n)}\cos\left[k^{(n)} x_m - n\omega t + \varphi_{I,F}^{(n)}\right] \\ & + \sum_{n=2}^{N} a_{R,F}^{(n)}\cos\left[k^{(n)} x_m + n\omega t + \varphi_{R,F}^{(n)}\right] \\ & + e_m(t)\end{aligned} \tag{3}$$

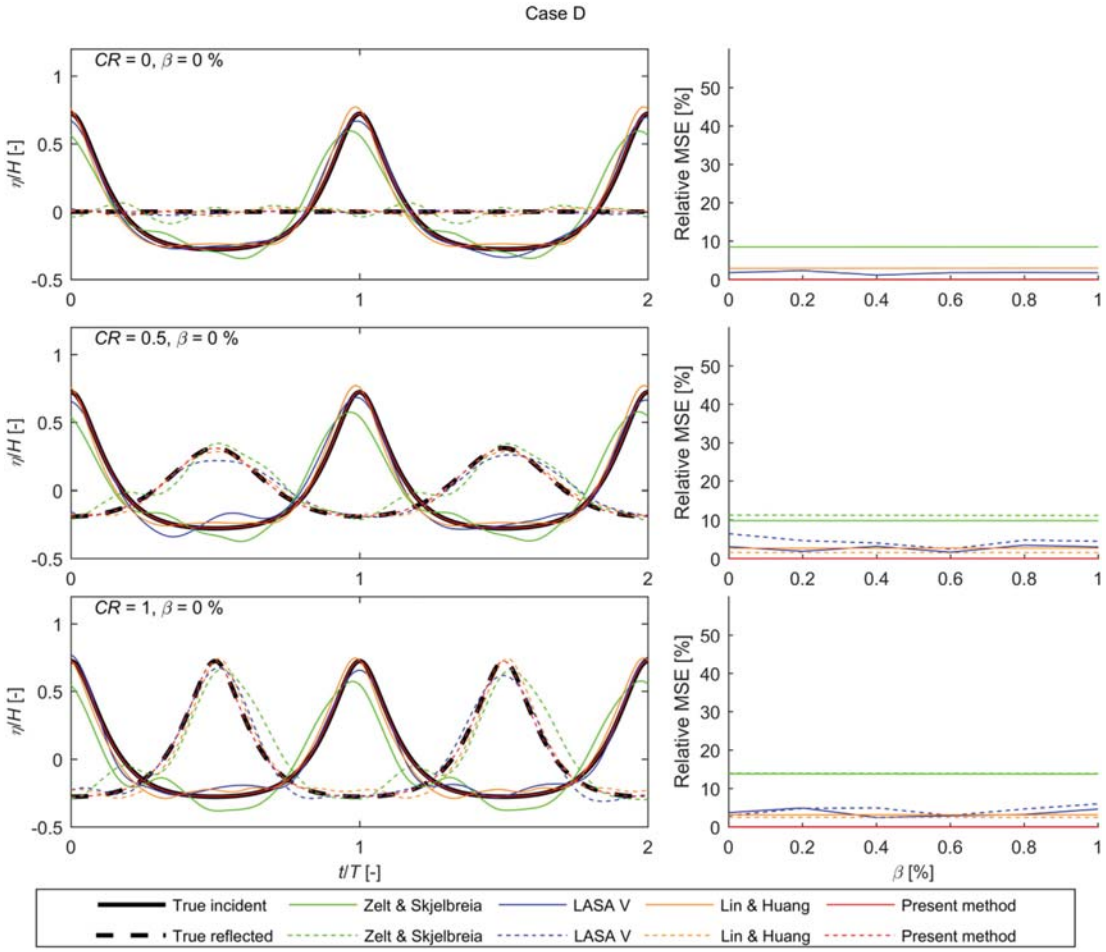

Fig. 6. Comparison of calculated and actual surface elevations for case D. The relative MSE is shown with the different levels of noise.

Note that the only difference to Eq. (1) is the wave numbers used for the incident and reflected bound waves (k_I and k_R) calculated based on above listed iterative procedure. Eq. (3) can be written up in frequency domain. For primary component ($n = 1$), i.e. at the frequency ω, the following is obtained:

$$\begin{aligned}
\hat{\eta}^{(1)}(x_m) &= C_I^{(1)} X_I^{(1)} + C_R^{(1)} X_R^{(1)} + \Omega_m^{(1)} \\
X_I^{(1)} &= a_I^{(1)} \exp\left[-i\left(k_I x_1 + \varphi_I^{(1)}\right)\right] \\
X_R^{(1)} &= a_R^{(1)} \exp\left[i\left(k_R x_1 + \varphi_R^{(1)}\right)\right] \\
C_I^{(1)} &= \exp(-ik_I \Delta x_m) \\
C_R^{(1)} &= \exp(ik_R \Delta x_m)
\end{aligned} \tag{4}$$

where $\Delta x_m = x_m - x_1$ and $\Omega_m{}^{(1)}$ is the Fourier transformation of $e_m(t)$ at frequency ω.

For the higher harmonics ($n > 1$) the Fourier transformation of Eq. (3) at frequency $n\omega$ gives:

$$\begin{aligned}
\hat{\eta}^{(n)}(x_m) &= C_{I,B}^{(n)} X_{I,B}^{(n)} + C_{R,B}^{(n)} X_{R,B}^{(n)} + C_{I,F}^{(n)} X_{I,F}^{(n)} + C_{R,F}^{(n)} X_{R,F}^{(n)} + \Omega_m^{(n)} \\
X_{I,B}^{(n)} &= a_{I,B}^{(n)} \exp\left[-i\left(nk_I x_1 + \varphi_{I,B}^{(n)}\right)\right] \\
X_{R,B}^{(n)} &= a_{R,B}^{(n)} \exp\left[i\left(nk_R x_1 + \varphi_{R,B}^{(n)}\right)\right] \\
X_{I,F}^{(n)} &= a_{I,F}^{(n)} \exp\left[-i\left(k^{(n)} x_1 + \varphi_{I,F}^{(n)}\right)\right] \\
X_{R,F}^{(n)} &= a_{R,F}^{(n)} \exp\left[i\left(k^{(n)} x_1 + \varphi_{R,F}^{(n)}\right)\right] \\
C_{I,B}^{(n)} &= \exp(-ink_I \Delta x_m) \\
C_{R,B}^{(n)} &= \exp(ink_R \Delta x_m) \\
C_{I,F}^{(n)} &= \exp\left(-ik^{(n)} \Delta x_m\right) \\
C_{R,F}^{(n)} &= \exp\left(ik^{(n)} \Delta x_m\right)
\end{aligned}$$

where $\Omega_m{}^{(n)}$ is the Fourier transformation of $e_m(t)$ at frequency $n\omega$.

The values of the complex parameters $X_I{}^{(1)}$, $X_R{}^{(1)}$, $X_{I,B}{}^{(n)}$, $X_{R,B}{}^{(n)}$,

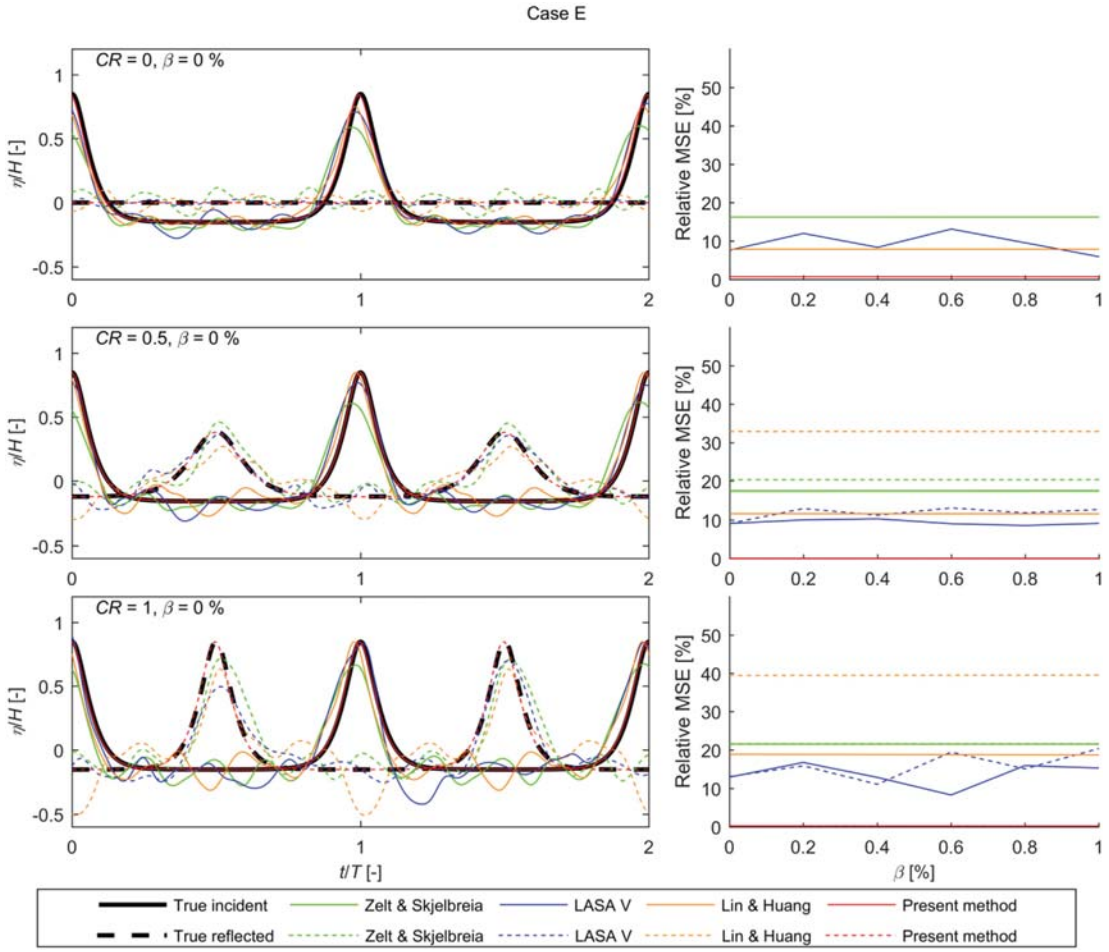

Fig. 7. Comparison of calculated and actual surface elevations for case E. The relative MSE is shown with the different levels of noise.

$X_{I,F}^{(n)}$ and $X_{R,F}^{(n)}$ are determined by fitting the equation to the measurement. The fitting is performed by minimization of the noise term $\Omega_m^{(n)}$. This gives for $n = 1$ (see [6]):

$$\begin{bmatrix} A_{11} & A_{12} \\ A_{21} & A_{22} \end{bmatrix} \begin{bmatrix} X_I^{(1)} \\ X_R^{(1)} \end{bmatrix} = \begin{bmatrix} B_1 \\ B_2 \end{bmatrix} \tag{6}$$

and for $n > 1$ (see [6]):

$$\begin{bmatrix} D_{11} & D_{12} & D_{13} & D_{14} \\ D_{21} & D_{22} & D_{23} & D_{24} \\ D_{31} & D_{32} & D_{33} & D_{34} \\ D_{41} & D_{42} & D_{43} & D_{44} \end{bmatrix} \begin{bmatrix} X_{I,B}^{(n)} \\ X_{R,B}^{(n)} \\ X_{I,F}^{(n)} \\ X_{R,F}^{(n)} \end{bmatrix} = \begin{bmatrix} E_1 \\ E_2 \\ E_3 \\ E_4 \end{bmatrix} \tag{7}$$

The detailed background for these two systems of equations as well as the expressions for A_{ij}, B_i, D_{ij} and E_i were derived by [6]. The coefficients are for completion of the present method also repeated in the appendix.

In addition to the amplitude dispersive effect the Lin and Huang method is corrected to solve a problematic range of application, namely when the bound and free superharmonics have almost identical celerity. It is usually so that the bound superharmonic component travel much faster than the free one, but in shallow water this is not the case with infinite small wave height. With finite wave height and amplitude dispersion included the problems are less, but still relevant in few cases. If this issue is not corrected it can lead to erroneous results. In such cases it is proposed to assume all incident energy is bound and all reflected energy is free at the problematic frequency (given order n). This assumption should be valid if incident waves are properly generated and perfect absorption at the wave generator (no free incident waves) and when only testing mildly reflective structures (bound reflected waves very small). Note that the problem usually only occurs for the 2nd order superharmonic component unless the wave is an extremely shallow water wave.

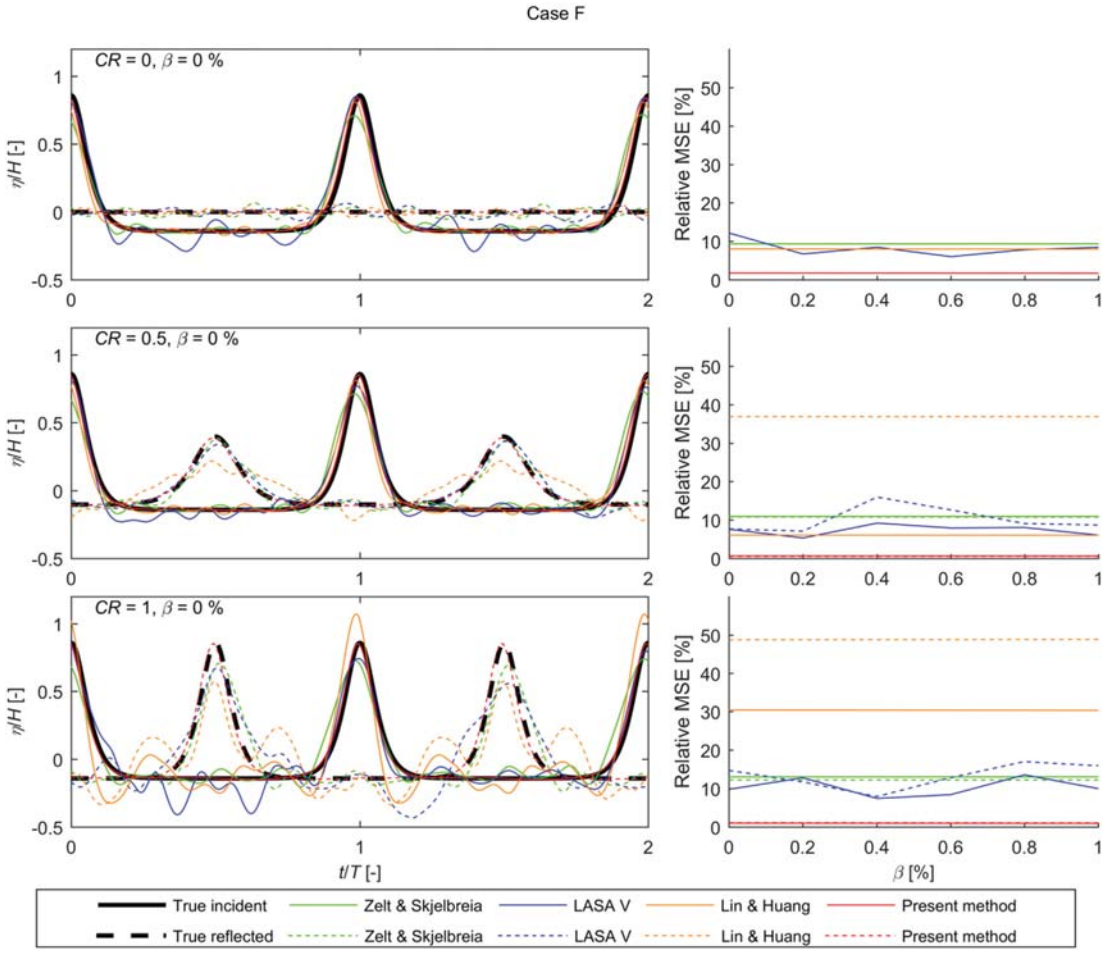

Fig. 8. Comparison of calculated and actual surface elevations for case F. The relative MSE is shown with the different levels of noise.

The correction is performed when:

$$\frac{c_{bound}}{c_{free}} = \frac{k^{(n)}}{n \cdot k_I} < \alpha \tag{8}$$

Mathematically $\alpha = 1.0$ corresponds to the matrix in Eq. (7) becomes singular because $n \cdot k_I = k^{(n)}$, but it is not sufficient that $\alpha > 1.0$ as otherwise small errors on the bound or free celerity or gauge positions will influence results significantly. A safe value for α seems to be 1.15, while for $\alpha = 1.05$ to 1.15 sometimes reliable results are obtained, but sensibility of results has to be checked. Fig. 1 shows the area fulfilling Eq. (8) for $n = 2$ and $n = 3$ based on $\alpha = 1.1$. From the figure it appears that the correction will be carried out (if done at all) most often for $n = 2$, and less often for higher n-values. This is because, the larger n, the free wave will be shorter and thus run with a sufficiently smaller celerity. It also appears that the correction is only done for shallow water waves of small amplitude.

The applied mathematical model for the superharmonics in case Eq. (8) is fulfilled (correction needed) are in Fourier domain:

$$\hat{\eta}^{(n)}(x_m) = C_{I,B}^{(n)} X_{I,B}^{(n)} + C_{R,F}^{(n)} X_{R,F}^{(n)} + \Omega_m^{(n)} \tag{9}$$

This gives the following linear system to be solved:

$$\begin{bmatrix} D_{11} & D_{14} \\ D_{41} & D_{44} \end{bmatrix} \begin{bmatrix} X_{I,B}^{(n)} \\ X_{R,F}^{(n)} \end{bmatrix} = \begin{bmatrix} E_1 \\ E_4 \end{bmatrix} \tag{10}$$

For cases where incident wave separation is reliable (Eq. (8) is not fulfilled) the reflected wave separation can still be unreliable. This has to be checked by replacing k_I with k_R in Eq. (8). If conclusion is that separation of reflected components is unreliable a correction has to be performed. Results have showed that incident waves are relatively unaffected by this so a simple correction is to add the estimated bound reflected component to the free for such cases. In fact, this seems to provide slightly better incident waves than the more obvious solution of solving the following system of equations:

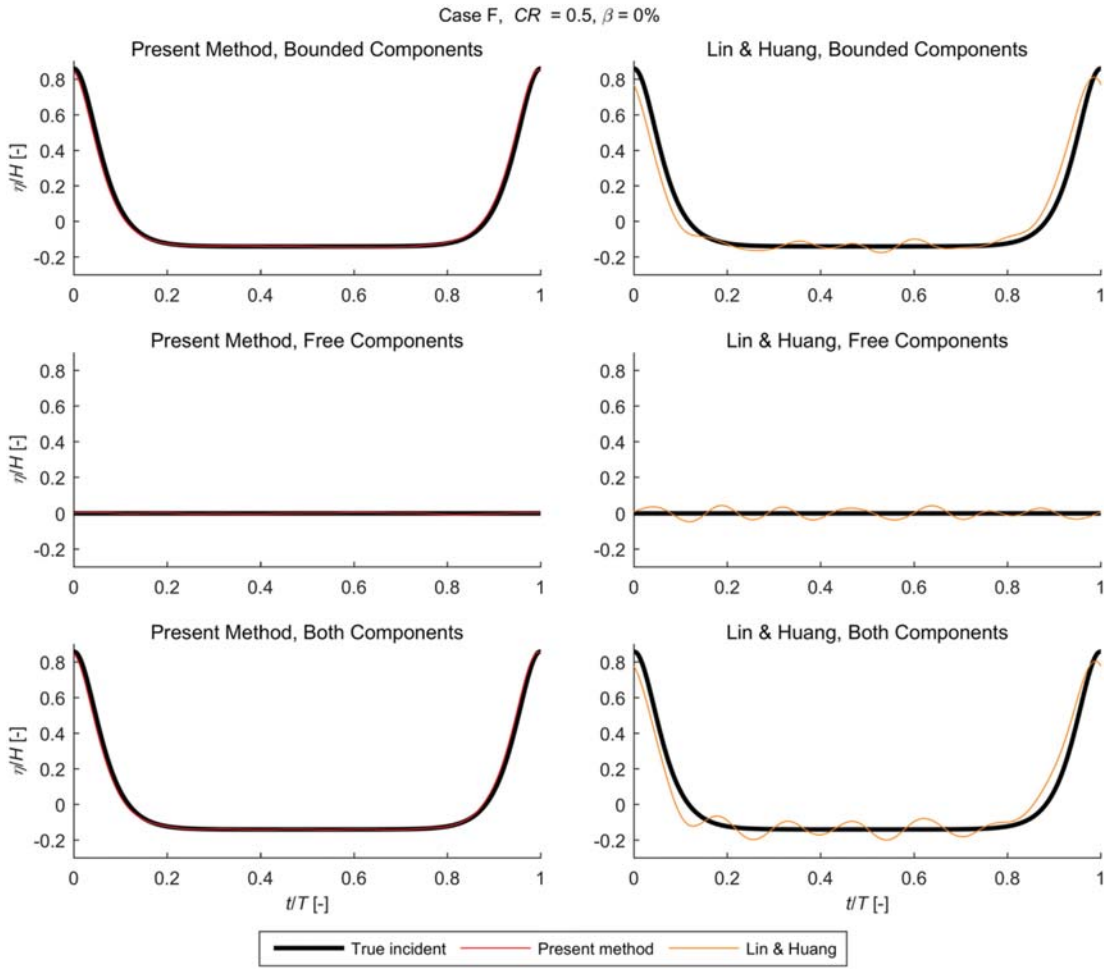

Fig. 9. Estimated free and bound surface elevations by the new method and Lin & Huang for Case F.

$$\begin{bmatrix} D_{11} & D_{13} & D_{14} \\ D_{31} & D_{33} & D_{34} \\ D_{41} & D_{43} & D_{44} \end{bmatrix} \begin{bmatrix} X_{I,B}^{(n)} \\ X_{I,F}^{(n)} \\ X_{R,F}^{(n)} \end{bmatrix} = \begin{bmatrix} E_1 \\ E_3 \\ E_4 \end{bmatrix} \tag{11}$$

The new method requires minimum four wave gauges (Eq. (7) is 4 complex equations with 4 complex unknowns). However, minimum five wave gauges are recommended in order to have an overdetermined system. For a significant part of the existing laboratory test data only three wave gauges are available. In case such test data involve highly nonlinear waves and only lightly reflective conditions, a better analysis method than existing 3-gauge methods might be to solve Eq. (11), i.e. assuming all reflected waves to be free.

The new method has been implemented in the wave analysis software [10] as the default method for reflection analysis of regular waves.

4. Test conditions and analysis methodology

Six synthetic regular wave standard cases were defined and shown in Fig. 1. The figure describes the nonlinearity of the waves according to the diagram by [5]. The six test cases cover a large range of nonlinearities as well as deep and shallow water and all test cases are outside the problematic area defined by Eq. (8). For each case synthetic test data was generated for amplitude reflection coefficients $CR = H_r/H_i = 0$, 0.5 and 1. The waves were synthetically generated based on stream function theory ([2]) in order to estimate performance of existing methods on nonlinear waves.

An additional case (F_{FREE}) was identical to case F, but additionally with synthetically generated free 2nd order energy with amplitude 0.015 m. In [7] application of the new model was demonstrated on physical model test data on horizontal sea bed for highly nonlinear waves. In the present paper additional numerical test cases (E_{ASYM} and F_{ASYM}) on a 1:100 slope was used to study applicability of the new method on vertical asymmetric waves on mildly sloping foreshores for $CR = 0$. These test cases were generated by the COULWAVE Boussinesq model ([8]). The waves were

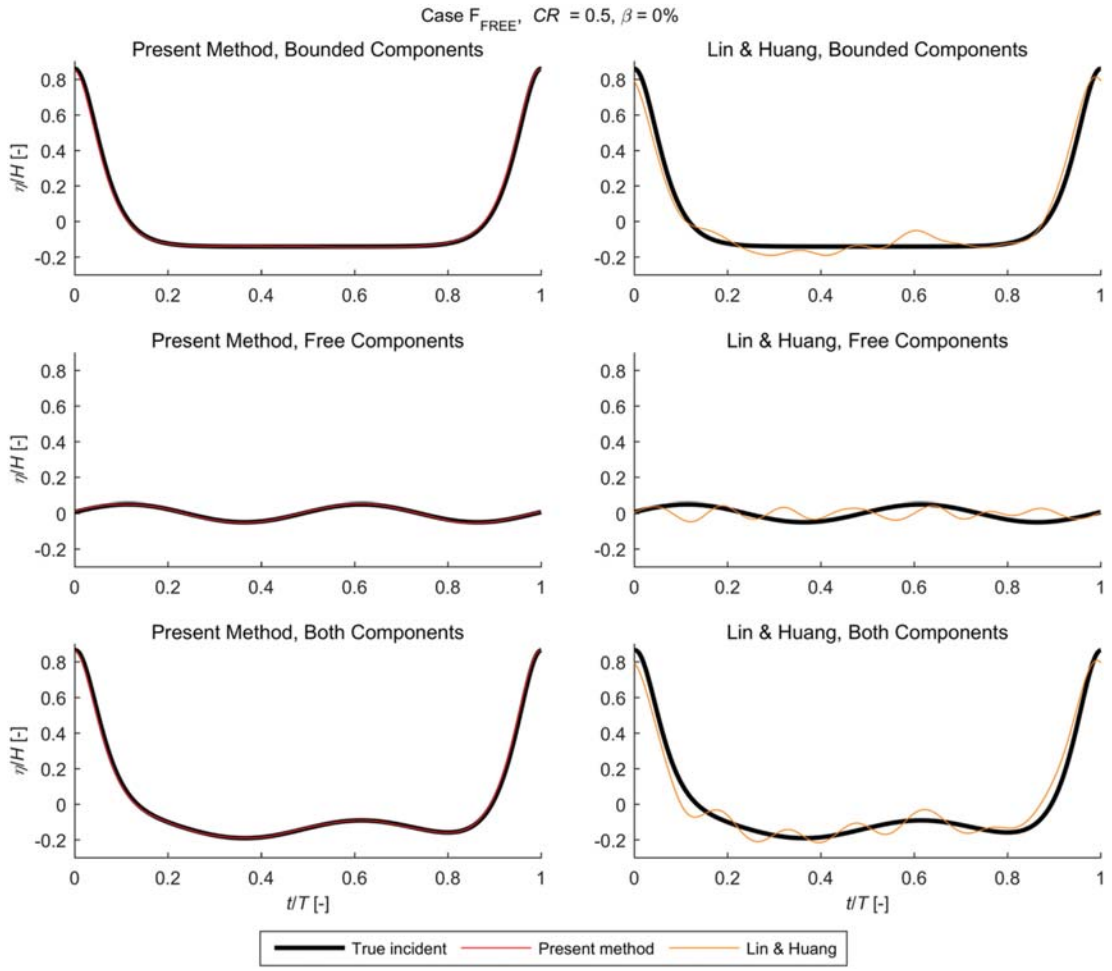

Fig. 10. Estimated free and bound surface elevations by the new method and Lin & Huang for Case F_{FREE}.

generated in COULWAVE on a depth corresponding to where linear wave theory is valid. The waves were shoaling over a long 1:100 slope to reach wave height and water depth in accordance with cases E and F. The discretization in the numerical model was $\Delta x = L_{generator}/400$ and 2 vertical layers and the time step was based on the Courant number, $C = c_0\,\Delta t/\Delta x = 0.5$.

For the standard test cases the signals were added with Gaussian White Noise with different levels to test the robustness of the reflection analysis methods to noise. The tested standard deviation of the noise was 0–1% of the wave height. Noise signals for the five wave gauges are assumed uncorrelated and were calculated by the central limit theorem according to:

$$noise = \left(-\frac{N}{2} + \sum_{i=1}^{N} x_i\right)\sqrt{\frac{12}{N}}$$
$$\eta_{noise}(t) = noise(t)H\beta \qquad (12)$$

where

H	is the wave height
x_i	is a random number between 0 and 1
β	is the amount of noise (0–1%)
N	is a sufficient large integer value

Fig. 2 shows an example of time series without and with noise for $\beta = 1\%$.

An array of 5 gauges was used and optimized to each test based on the wave length (L). The applied gauge separations in terms of $\Delta x_m/L$ were 0.05, 0.12, 0.21 and 0.31. This wave gauge configuration is following the recommendations by [4] that $\Delta x/L$ should be between 0.05 and 0.45 for all pairs. Furthermore, no pairs have identical separation. For the COULWAVE cases (E_{ASYM} and F_{ASYM}) the gauge positions not exactly matched above due to the spatial discretization.

The [6] method is used with the proposed correction for shallow water waves (Eqs. (8)–(10)). Therefore, the only difference

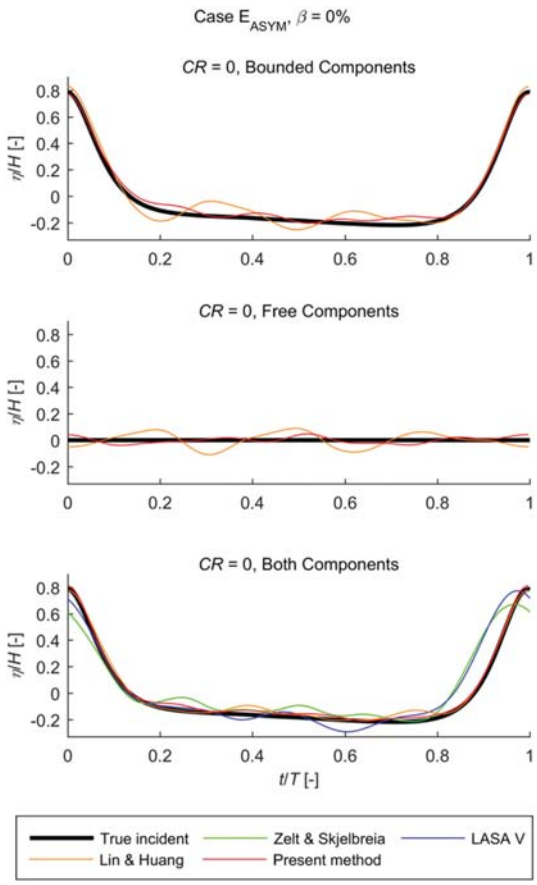

Fig. 11. Estimated free and bound surface elevations by the new method and Lin & Huang for Case E_{ASYM}.

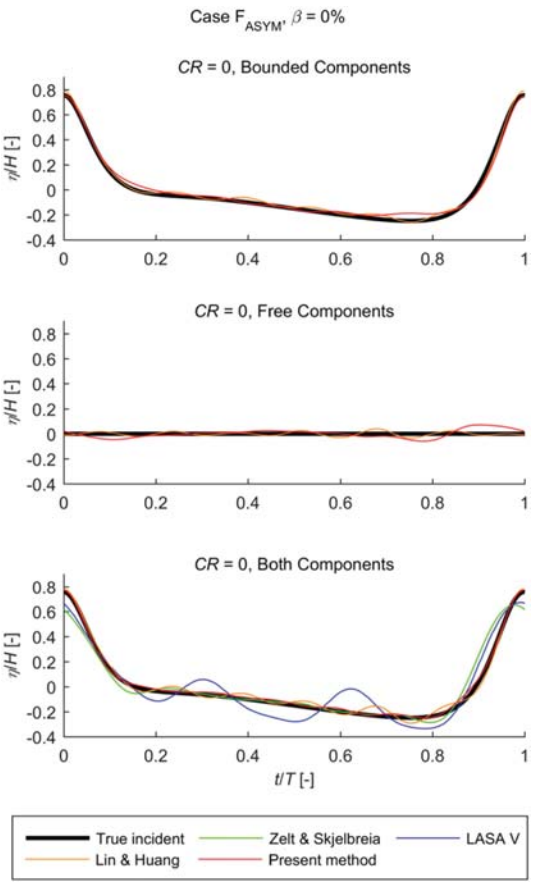

Fig. 12. Estimated free and bound surface elevations by the new method and Lin & Huang for Case F_{ASYM}.

between results of present method and Lin and Huang method is due to the inclusion of amplitude dispersion.

For the cases with sloping foreshore (E_{ASYM} and F_{ASYM}) the water depth used in the analyses is the depth in the middle of the wave gauge array.

Incident and reflected wave trains were calculated at $x = x_1$ for all test cases.

5. Results

The overall results can be seen in Table 1 with respect to the estimated incident wave height. [11] provided only correct wave heights for case A (linear waves), which was also expected since it is a linear method. For the nonlinear cases large errors were observed, especially for the most nonlinear cases (E and F) which provide 5–20% underprediction of the incident wave height. LASA V provided in most cases better results than Zelt and Skjelbreia, but was still unreliable for the highly nonlinear cases (0–20% error on incident wave height). [6] method is reliable in mildly nonlinear waves as expected (2nd order waves), but in highly nonlinear waves the problem of neglecting amplitude dispersion leads to quite erroneous results (0–40% error). The method is in shallow water thus not better than the linear method of Zelt and Skjelbria. The present method provided correct wave heights for all cases on horizontal sea bed with only minor deviations in a few cases because the estimated wave period deviated slightly from the target. The free incident 2nd order energy in case F_{FREE} does not influence the estimated height of the bound wave. For the 1:100 sea bed slope (case E_{ASYM} and case F_{ASYM}) the new method gives 2–4% errors on the estimated height of the bound wave as shoaling was neglected in the mathematical model (Eq. (3)). This result in part of the bound energy to be estimated free even though only bound energy exists in the data. Including the incident free components in the wave height calculations leads to a maximum errors of 2% similar to LASA V results. It should be noted that LASA V assumes all energy to be bound which is actually correct for these test cases, but not necessarily in physical model test conditions.

In Figs. 3–12 the calculated surface elevations by the different methods are shown for the nine test cases and compared to the actual generated. In the figures the relative mean squared error for the different levels of noise is also reported. The error is calculated by:

Table 2
Amplitudes of components (in millimetres) for all cases with $CR = 0$. * indicate all incident energy is assumed bound due to Eq. (8). † indicate all reflected energy is assumed free due to Eq. (8).

		Incident							Reflected						
		$a_I^{(1)}$	$a_{I,B}^{(2)}$	$a_{I,B}^{(3)}$	$a_{I,B}^{(4)}$	$a_{I,F}^{(2)}$	$a_{I,F}^{(3)}$	$a_{I,F}^{(4)}$	$a_R^{(1)}$	$a_{R,B}^{(2)}$	$a_{R,B}^{(3)}$	$a_{R,B}^{(4)}$	$a_{R,F}^{(2)}$	$a_{R,F}^{(3)}$	$a_{R,F}^{(4)}$
Case A	Target	5.00	0.05	0.00	0.00	0.00	0.00	0.00	0.00	0.00	0.00	0.00	0.00	0.00	0.00
	Lin-Huang	5.00	0.05	0.00	0.00	0.00	0.00	0.00	0.00	0.00	0.00	0.00	0.00	0.00	0.00
	Present	5.00	0.05	0.00	0.00	0.00	0.00	0.00	0.00	0.00	0.00	0.00	0.00	0.00	0.00
Case B	Target	44.43	4.04	0.56	0.09	0.00	0.00	0.00	0.00	0.00	0.00	0.00	0.00	0.00	0.00
	Lin-Huang	44.26	4.09	0.52	0.08	0.17	0.06	0.00	0.79	0.04	0.04	0.00	0.08	0.07	0.01
	Present	44.43	4.03	0.55	0.08	0.00	0.00	0.00	0.00	0.00	0.00	0.00	0.00	0.00	0.00
Case C	Target	92.45	18.99	6.16	2.42	0.00	0.00	0.00	0.00	0.00	0.00	0.00	0.00	0.00	0.00
	Lin-Huang	91.20	19.42	5.94	2.93	2.99	1.57	0.55	6.54	0.24	0.89	0.71	1.30	1.76	1.02
	Present	92.39	19.00	6.18	2.43	0.11	0.09	0.01	0.26	0.02	0.07	0.02	0.06	0.08	0.03
Case D	Target	202.14	89.26	37.02	16.34	0.00	0.00	0.00	0.00	0.00	0.00	0.00	0.00	0.00	0.00
	Lin-Huang	200.00	111.50	40.77	16.65	24.35	9.51	2.15	10.03	5.86	6.62	3.36	5.56	8.12	3.15
	Present	202.10	89.80	37.08	16.31	0.62	0.26	0.05	0.34	0.17	0.18	0.09	0.17	0.22	0.11
Case E	Target	136.23	101.71	67.83	42.91	0.00	0.00	0.00	0.00	0.00	0.00	0.00	0.00	0.00	0.00
	Lin-Huang	134.60	97.36*	106.40	35.70	0.00*	43.75	17.24	9.42	0.00†	7.92	26.15	6.62†	6.45	31.23
	Present	136.30	101.40	67.55	42.62	0.58	0.14	0.25	0.24	0.00†	0.13	0.24	0.24†	0.13	0.28
Case F	Target	77.75	61.26	43.20	28.42	0.00	0.00	0.00	0.00	0.00	0.00	0.00	0.00	0.00	0.00
	Lin-Huang	77.22	60.03*	41.14*	48.16	0.00*	0.00*	21.60	3.43	0.00†	0.00†	7.93	2.28†	0.23†	8.44
	Present	77.93	60.39	42.33	27.54	1.63	0.65	0.70	0.34	0.00†	0.00†	0.00†	0.32†	0.26†	0.26†
Case F_{FREE}	Target	77.75	61.26	43.20	28.42	15.00	0.00	0.00	0.00	0.00	0.00	0.00	0.00	0.00	0.00
	Lin-Huang	77.20	52.73*	41.22*	48.61	0.00*	0.00*	22.00	3.47	0.00†	0.00†	8.21	2.40†	0.24†	8.73
	Present	77.91	60.65	42.58	27.75	13.89	0.50	0.56	0.27	0.00†	0.00†	0.00†	0.27†	0.20†	0.20†
Case E_{ASYM}	Target	149.70	107.30	66.57	38.41	0.00	0.00	0.00	0.00	0.00	0.00	0.00	0.00	0.00	0.00
	Lin-Huang	145.60	105.10*	99.65	31.17	0.00*	34.48	15.72	9.01	0.00†	5.27	21.87	5.42†	4.09	26.10
	Present	147.50	97.36	65.68	39.51	12.39	5.66	6.48	1.85	0.00†	0.99	7.94	0.74†	0.86	9.86
Case F_{ASYM}	Target	84.61	61.00	40.55	24.42	0.00	0.00	0.00	0.00	0.00	0.00	0.00	0.00	0.00	0.00
	Lin-Huang	81.75	61.04*	41.65*	25.81*	0.00*	0.00*	0.00*	3.41	0.00†	0.00†	0.00†	3.41†	0.00†	0.00†
	Present	82.54	53.62	39.10	25.07	10.74	7.22	4.18	1.63	0.00†	0.00†	0.00†	0.67†	0.07†	0.36†

$$\text{Relative MSE} = \overline{(\eta_{actual} - \eta_{calculated})^2} \Big/ \overline{(\eta_{actual})^2} \tag{13}$$

From the figures it can be seen that the calculated surface elevation by LASA V is not stationary, not even in the linear wave case (see Fig. 3). The reason for this is because the method is a local approximation method. LASA V fits new wave parameters for each time window and therefore the results can be different for each wave, even though the waves are stationary. From all cases it also appears that the relative error is not increasing with increased noise. Therefore, none of the methods are sensitive to white noise.

In Figs. 3–5 results for deep water cases are shown (cases A, B and C). All methods provide small errors for linear waves (case A) as expected, and also acceptable estimates for the mildly nonlinear waves (case B). For these two cases the LASA V method provides the worst results because of the non-stationary solution for a stationary wave. In the 4th order stoke regime (case C) the method based on linear theory (Zelt and Skjelbreia) give profiles that deviate significantly from the correct ones. LASA V is in that case better than the linear method. Lin and Huang gives correct results for case A and B as expected as they are within validity of 2nd order theory. For case C their method also gives reasonable results and better then the Zelt and Skjelbreia and LASA V methods.

The test cases for nonlinear waves in intermediate and shallow water (cases D–F) are shown in Figs. 6–8. LASA V is better than Zelt and Skjelbreia for cases D and E, and for case D the results of LASA V are acceptable. However, for the cases in shallower depth the results of all existing methods deviate significantly from target. It appears also that the missing amplitude dispersion of Lin and Huang method leads to completely wrong separation in bound/free and incident/reflected components. This is further demonstrated in Fig. 9 where the free individual components are also shown.

Results of test case F_{FREE} which include free 2nd order energy are given in Fig. 10. It appears that the present method correctly estimate both the free and bound components, while the missing amplitude dispersion in Lin and Huang method lead to unreliable separation of free and bound components.

For the cases on sloping foreshore (E_{ASYM} and F_{ASYM}) the separation in free and bound components is not accurate with either Lin and Huang or present method. However, results are still much better than Zelt and Skjelbreia as well as LASA V that both gives strong undulations in the wave trough. Concerning the estimated incident total wave (bound and free incident components) the profile of the new method is very close to the target and better than Lin and Huang that have larger undulations.

In addition to the figures the amplitude of the estimated components for $n \leq 4$ are shown in Table 2 for Lin and Huang as well as present method for all test cases. The conclusion from that table is similar to what is described above based on Figs. 3–12. Moreover, the table shows which components that cannot be separated due to needed correction when Eq. (8) is fulfilled. For the present method this occurs only for reflected components while for Lin and Huang it occurs also for incident components.

The present method provides by far the best results for all test cases on horizontal sea bed and especially for highly nonlinear waves in intermediate and shallow water. As a sloping foreshore was not included in the mathematical model for any of the applied methods larger errors are expected for such cases. The results show that especially the present method and partly also Lin and Huang method provide acceptable errors for mildly sloping foreshores while the other methods are unreliable. The overall conclusion of the test cases is that for all nonlinear wave cases the present method is better than any of the existing methods.

6. Conclusion

In the present paper a new method for separating incident and reflected regular waves is proposed. The present method is an extension of [6] method by generalisation to highly nonlinear waves by inclusion of amplitude dispersion. Moreover, a problematic region with the bound/free separation is identified and a correction is suggested. The problematic region is when bound and free components travel with almost identical celerity. This occurs only in very shallow water and only for certain harmonic components.

Synthetic data was generated for regular stream function waves and these tests have been analysed by the new separation method,

the linear method of [11] and the nonlinear LASA V method (Stokes fifth order wave model) by [3] as well as the [6] method. The present method is proved to be significantly better than existing methods when waves are nonlinear and especially in shallow water. The present method provided exact estimations for the wave heights and a good match of the surface elevations in all cases. In all tests the used methods were very robust to noise.

The new method was also tested on numerical model data for waves on sloping foreshores with vertical asymmetry. The method is developed for horizontal bed only, but results showed that for mildly sloping sea bed the new method provides acceptable results and better than any of the existing methods. Extension of the method to irregular waves and steep foreshores is currently under investigation.

Acknowledgment

A special thanks to Professor Josep R. Medina from the Laboratory of Ports and Coasts of the Universidad Politécnica de Valencia for providing the LASA V software.

Appendix A

Elements of A_{ij}

$$A_{11} = \sum_{m=1}^{M} \left[C_I^{(1)}\right]^2 \tag{14}$$

$$A_{12} = A_{21} = \sum_{m=1}^{M} \left[C_I^{(1)} C_R^{(1)}\right] \tag{15}$$

$$A_{22} = \sum_{m=1}^{M} \left[C_R^{(1)}\right]^2 \tag{16}$$

where M is the number of gauges.

Elements of B_i:

$$B_1 = \sum_{m=1}^{M} \left[\hat{\eta}^{(1)}(x_m) C_I^{(1)}\right] \tag{17}$$

$$B_2 = \sum_{m=1}^{M} \left[\hat{\eta}^{(1)}(x_m) C_R^{(1)}\right] \tag{18}$$

Elements of D_{ij}:

$$D_{11} = \sum_{m=1}^{M} \left[C_{I,B}^{(n)}\right]^2 \tag{19}$$

$$D_{12} = D_{21} = \sum_{m=1}^{M} \left[C_{I,B}^{(n)} C_{R,B}^{(n)}\right] \tag{20}$$

$$D_{13} = D_{31} = \sum_{m=1}^{M} \left[C_{I,F}^{(n)} C_{I,B}^{(n)}\right] \tag{21}$$

$$D_{14} = D_{41} = \sum_{m=1}^{M} \left[C_{R,F}^{(n)} C_{I,B}^{(n)}\right] \tag{22}$$

$$D_{22} = \sum_{m=1}^{M} \left[C_{R,B}^{(n)}\right]^2 \tag{23}$$

$$D_{23} = D_{32} = \sum_{m=1}^{M} \left[C_{I,F}^{(n)} C_{R,B}^{(n)}\right] \tag{24}$$

$$D_{24} = D_{42} = \sum_{m=1}^{M} \left[C_{R,F}^{(n)} C_{R,B}^{(n)}\right] \tag{25}$$

$$D_{33} = \sum_{m=1}^{M} \left[C_{I,F}^{(n)}\right]^2 \tag{26}$$

$$D_{34} = D_{43} = \sum_{m=1}^{M} \left[C_{R,F}^{(n)} C_{I,F}^{(n)}\right] \tag{27}$$

$$D_{44} = \sum_{m=1}^{M} \left[C_{R,F}^{(n)}\right]^2 \tag{28}$$

Elements of E_i:

$$E_1 = \sum_{m=1}^{M} \left[\hat{\eta}^{(n)}(x_m) C_{I,B}^{(n)}\right] \tag{29}$$

$$E_2 = \sum_{m=1}^{M} \left[\hat{\eta}^{(n)}(x_m) C_{R,B}^{(n)}\right] \tag{30}$$

$$E_3 = \sum_{m=1}^{M} \left[\hat{\eta}^{(n)}(x_m) C_{I,F}^{(n)}\right] \tag{31}$$

$$E_4 = \sum_{m=1}^{M} \left[\hat{\eta}^{(n)}(x_m) C_{R,F}^{(n)}\right] \tag{32}$$

References

[1] H.-K. Chang, S.-C. Lin, An explicit approximation to the wavelength of

nonlinear waves, Ocean Eng. 26 (1999) 147–160.
[2] J.D. Fenton, M.M. Rienecker, Accurate numerical solution for nonlinear waves, in: Proceedings, 17th Conference of Coastal Engineering, Volume 1, Sydney, 1980, pp. 50–69.
[3] M. Figueres, J.M. Garrido, J.R. Medina, Cristalización Simulada para el Análisis de Oleaje Incidente y Reflejado con un Modelo de Onda Stokes-V, in: VII Jornadas de Puertos Y Costas, Almeria, 2003.
[4] Y. Goda, Y. Suzuki, Estimation of incident and reflected waves in random wave experiments, in: 15th International Conference on Coastal Engineering, Volume 1, Honolulu, 1976, pp. 828–845.
[5] B. Le Méhauté, An introduction to hydrodynamics and water waves, water wave theories, in: Volume 2, TR ERL 118-POL-3-2, U.S. Department of Commerce, ESSA, Washington, DC, 1969.
[6] C.-Y. Lin, C.-J. Huang, Decomposition of incident and reflected higher harmonic waves using four wave gauges, Coast. Eng. 51 (5) (2004) 395–406.
[7] T. Lykke Andersen, M. Clavero, P. Frigaard, M. Losada, J.I. Puyol, A new active absorption system and its performance to linear and non-linear waves, Coast. Eng. 114 (2016) 47–60 (August 2016).
[8] P. Lynett, P.L.-F. Liu, A two-layer approach to wave modelling, Proc. R. Soc. Lond. A 460 (2004) 2637–2669 (2004).
[9] E.P.D. Mansard, E.R. Funke, The measurement of incident and reflected spectra using a least squares method, in: 17th International Conference on Coastal Engineering, Volume 1, Sydney, 1980, pp. 154–172.
[10] WaveLab 3, Wave Data Acquisition and Analysis Software, Aalborg University, Department of Civil Engineering, 2015 (http://www.hydrosoft.civil.aau.dk/wavelab/).
[11] J.A. Zelt, J.E. Skjelbreia, Estimating incident and reflected wave fields using an arbitrary number of wave gauges, Coast. Eng. Proc. 1 (23) (1992).

Paper C

Estimation of Incident and Reflected Wave Trains in Highly Nonlinear Two-Dimensional Irregular Waves

Mads Røge Eldrup
Thomas Lykke Andersen

The paper has been published in
Journal of Waterway Port Coastal and Ocean Engineering, ISSN: 1943-5460, 145(1), 2017.

Estimation of Incident and Reflected Wave Trains in Highly Nonlinear Two-Dimensional Irregular Waves

Mads Røge Eldrup[1] and Thomas Lykke Andersen[2]

Abstract: Most existing methods for separation of two-dimensional (long-crested) waves into incident and reflected components are based on linear wave theory. Recently, a new method for separation of incident and reflected nonlinear regular waves was presented including separation of bound and free superharmonics. The present paper extends this method to irregular waves. Irregular waves are much more complicated to separate because bound components are caused by interaction of many different frequencies, thus, some simplifications are needed. The presented nonlinear separation method is based on narrowband approximation. Second-order wave theory is used to demonstrate that errors for more broad-banded spectra are acceptable. Moreover, for highly nonlinear waves, amplitude dispersion occurs and is included by a simplified amplitude dispersion correction factor. Both assumptions are evaluated based on numerical and physical model data. The overall conclusion is that existing reflection separation methods are reliable only for linear and mildly nonlinear nonbreaking irregular waves, whereas the present method seems reliable for the entire interval from linear to highly nonlinear nonbreaking irregular waves. The present method is shown to be an efficient and practical approximation for an unsolved theoretical problem in the analysis of waves in physical models. **DOI: 10.1061/(ASCE)WW.1943-5460.0000497.**

Author keywords: Wave reflection analysis; Nonlinear waves; Irregular waves; Bound waves.

Introduction

In physical or numerical tests with irregular waves, only the total waves (sum of incident and reflected waves) can be measured. Therefore, a mathematical method is needed for separation of the total waves into incident and reflected waves (reflection analysis method). Separation of the waves is important because the response of most tested structures is related to the incident waves. Moreover, for many types of structures, the response is very nonlinearly dependent on the incident wave height; thus, small errors on the estimated waves lead to much greater uncertainties on the response. Furthermore, separation of incident and reflected waves is needed to calculate the reflection coefficient. The most commonly applied reflection analysis methods are based on linear wave theory (Goda and Suzuki 1976; Mansard and Funke 1980; Zelt and Skjelbreia 1992). The performance of these linear methods is generally unknown when applied to nonlinear irregular waves. Medina (2001), Figueres et al. (2003), and Figueres and Medina (2004) have presented methods for separation of nonlinear regular and irregular waves. Moreover, Lin and Huang (2004) and Lykke Andersen et al. (2017) have presented methods for nonlinear regular waves.

The nonlinear local approximation using simulated annealing (LASA) methods proposed by Medina (2001), Figueres et al. (2003), and Figueres and Medina (2004) are based on local time domain solutions using various wave theories. Figueres et al. (2003) presented LASA V in which a fifth-order Stokes wave is fitted in each time window. It is, however, questionable to apply this method to cases in which free superhamonic energy exists. All the LASA methods are computationally demanding because they are based on time domain solutions in local windows, which make them less practical for daily use compared with frequency domain solutions. Moreover, Lykke Andersen et al. (2017) demonstrated that the LASA V method is not reliable, not even for linear and mildly nonlinear regular waves.

For regular waves, Lin and Huang (2004) developed a method to separate superharmonics into bound/free and incident/reflected components. This method assumes waves of maximum second-order due to neglecting amplitude dispersion. Lykke Andersen et al. (2017) recently developed an extension of the Lin and Huang (2004) method to include amplitude dispersion. The Lykke Andersen method was validated on linear, mildly nonlinear, and highly nonlinear regular waves, and proved to be a significant improvement compared with the previously mentioned existing methods. The improvement applies to both synthetic stream function waves and numerical model data for vertical asymmetric waves on mildly sloping seabeds.

Recently, Qi et al. (2018a) developed a high-order method for reconstruction of nonlinear wavefields (HOR), but the method is computationally demanding and not applicable to reflected waves.

The present paper extends the Lykke Andersen method to nonlinear irregular waves.

Problem Statement

Surface elevation of irregular two-dimensional (2D) waves including both incident and reflected wave components can be described by

$$\eta(x,t) = \sum_{n=1}^{N} a_{I,n}\cos\left(k_{I,n}\mathrm{x} - \omega_{I,n}t + \varphi_{I,n}\right) + a_{R,n}\cos\left(k_{R,n}x - \omega_{R,n}t + \varphi_{R,n}\right) \quad (1)$$

[1]Ph.D. Student, Dept. of Civil Engineering, Aalborg Univ., Thomas Manns Vej 23, 9220 Aalborg Ø, Denmark (corresponding author). Email: mre@civil.aau.dk

[2]Associate Professor, Dept. of Civil Engineering, Aalborg Univ., Thomas Manns Vej 23, 9220 Aalborg Ø, Denmark. Email: tla@civil.aau.dk

Note. This manuscript was submitted on November 30, 2017; approved on July 13, 2018; published online on November 13, 2018. Discussion period open until April 13, 2019; separate discussions must be submitted for individual papers. This paper is part of the ***Journal of Waterway, Port, Coastal, and Ocean Engineering***, © ASCE, ISSN 0733-950X.

where η = surface elevation; x = given location in the wavefield; t = time; N = number of wave components; a = wave amplitude; ω = cyclic frequency; φ = phase; k = wave number; and subscripts I and R = incident and reflected components, respectively. Note that at a given frequency both free and bound wave components can exist with different wave numbers.

In a recent paper by Qi et al. (2018b) a description of the predictable zone was given, which also for the present model leads to a finite space-time domain in which the surface elevation can be accurately predicted. Unless the waves should be predicted far from the measurement locations, above limitation will only affect the accuracy in the start and the end of typical long duration irregular tests. Moreover, any deviation from the mathematical model [Eq. (1)], for example, due to shoaling and breaking waves or errors on assumed wave number (celerity), will gradually decrease the accuracy of the predicted incident and reflected surface elevation time series with distance from the measurement locations. In the present paper only prediction accuracy within the measurement locations are investigated, and the predictable zone due to these deviations needs further research.

The scope of the present paper is to determine the amplitude, wave number, and phase for both incident/reflected as well as bound/free wave components for each frequency in the wavefield. The bound and free components can be separated due to the difference in celerity. The celerity of the bound components is calculated based on second-order wave theory and a narrowband assumption for the primary spectrum together with a simplified amplitude dispersion. The amplitude dispersion is calibrated against two nonlinear numerical model test data.

The present paper explains the Lykke Andersen et al. (2017) method for regular waves, followed by a presentation of the extension of the method to irregular long-crested waves. The related simplifying assumptions have been evaluated based on second-order wave theory and numerical tests. Subsequently, the numerical test conditions and results are presented. Additionally, the sensitivity to noise and array design is discussed. Finally, application of the new method to laboratory data is demonstrated, and conclusions are drawn.

Lykke Andersen Method

The method by Lykke Andersen et al. (2017) applies to regular linear and nonlinear waves. This method considers bound and free superharmonics to be present just as in the Lin and Huang (2004) method. Bound components exist if the wave is not of infinitely small amplitude. Free (unwanted) incident components exist if the bound superharmonics are not correctly generated in the numerical or physical model. When the incident waves hit a partially reflecting structure, the reflected waves will contain less bound subharmonic and superharmonic energy, which is why part of the bound wave becomes free.

Separation of bound and free components is possible because a bound superharmonic travels with higher celerity than a free component at the same frequency. This separation is not included in linear methods in which all energy is assumed free. The free superharmonics in the Lykke Andersen et al. (2017) method are assumed of such small amplitudes that linear dispersion is valid. Assuming free superharmonics are small amplitudes also means that any interaction of these with the primary component as well as the bound superharmonic components can be ignored. The celerity of the bound superharmonics equals the celerity of the primary component, which is different for the incident and reflected waves due to amplitude dispersion. Lykke Andersen et al. (2017) applied the mathematical model of the surface elevation for Nth-order regular waves

$$\begin{aligned}\eta(x,t) = {} & a_I^{(1)}\cos\left(k_I x - \omega t + \varphi_I^{(1)}\right) \\ & + a_R^{(1)}\cos\left(k_R x + \omega t + \varphi_R^{(1)}\right) \\ & + \sum_{n=2}^{N} a_{I,B}^{(n)}\cos\left[n(k_I x - \omega t) + \varphi_{I,B}^{(n)}\right] \\ & + \sum_{n=2}^{N} a_{R,B}^{(n)}\cos\left[n(k_R x + \omega t) + \varphi_{R,B}^{(n)}\right] \\ & + \sum_{n=2}^{N} a_{I,F}^{(n)}\cos\left[k^{(n)}x - n\omega t + \varphi_{I,F}^{(n)}\right] \\ & + \sum_{n=2}^{N} a_{R,F}^{(n)}\cos\left[k^{(n)}x + n\omega t + \varphi_{R,F}^{(n)}\right] + \text{noise} \end{aligned} \tag{2}$$

where subscript I and R = incident and reflected components, respectively; subscripts B and F = bound and free components; a = amplitude; $\omega = 2\pi/T$ is the cyclic frequency; T = period of the wave (primary component); φ = phase; k = wave number of the primary components; and $k^{(n)}$ = wave number of the nth-order free component. Note that this mathematical model assumes stationarity, which can be assumed if the time window is selected correctly. Furthermore, no wave breaking and shoaling are assumed.

Eq. (2) can be formulated in the frequency domain at each wave gauge position (x_m). For the primary component ($n = 1$), i.e., at frequency ω, the following is obtained:

$$\begin{aligned} \widehat{\eta}^{(1)}(x_m) &= C_I^{(1)}X_I^{(1)} + C_R^{(1)}X_R^{(1)} + \Omega_m^{(1)} \\ X_I^{(1)} &= a_I^{(1)}\exp\left[-\mathrm{i}\left(k_I x_1 + \varphi_I^{(1)}\right)\right] \\ X_R^{(1)} &= a_R^{(1)}\exp\left[\mathrm{i}\left(k_R x_1 + \varphi_R^{(1)}\right)\right] \\ C_I^{(1)} &= \exp(-\mathrm{i}k_I\Delta x_m) \\ C_R^{(1)} &= \exp(\mathrm{i}k_R\Delta x_m) \end{aligned} \tag{3}$$

where $\Delta x_m = x_m - x_1$; and $\Omega_m^{(1)}$ = Fourier transformation of the noise at gauge m at frequency ω.

For the higher harmonics ($n > 1$) the Fourier transformation of Eq. (2) at frequency $n\omega$ gives

$$\begin{aligned} \widehat{\eta}^{(n)}(x_m) &= C_{I,B}^{(n)}X_{I,B}^{(n)} + C_{R,B}^{(n)}X_{R,B}^{(n)} + C_{I,F}^{(n)}X_{I,F}^{(n)} + C_{R,F}^{(n)}X_{R,F}^{(n)} + \Omega_m^{(n)} \\ X_{I,B}^{(n)} &= a_{I,B}^{(n)}\exp\left[-\mathrm{i}\left(nk_I x_1 + \varphi_{I,B}^{(n)}\right)\right] \\ X_{R,B}^{(n)} &= a_{R,B}^{(n)}\exp\left[\mathrm{i}\left(nk_R x_1 + \varphi_{R,B}^{(n)}\right)\right] \\ X_{I,F}^{(n)} &= a_{I,F}^{(n)}\exp\left[-\mathrm{i}\left(k^{(n)}x_1 + \varphi_{I,F}^{(n)}\right)\right] \\ X_{R,F}^{(n)} &= a_{R,F}^{(n)}\exp\left[\mathrm{i}\left(k^{(n)}x_1 + \varphi_{R,F}^{(n)}\right)\right] \\ C_{I,B}^{(n)} &= \exp(-\mathrm{i}nk_I\Delta x_m) \\ C_{R,B}^{(n)} &= \exp(\mathrm{i}nk_R\Delta x_m) \\ C_{I,F}^{(n)} &= \exp\left(-\mathrm{i}k^{(n)}\Delta x_m\right) \\ C_{R,F}^{(n)} &= \exp\left(\mathrm{i}k^{(n)}\Delta x_m\right) \end{aligned} \tag{4}$$

where $\Omega_m^{(n)}$ = Fourier transformation of the noise at gauge m at frequency $n\omega$.

The values of the complex parameters $X_I^{(1)}$, $X_R^{(1)}$, $X_{I,B}^{(n)}$, $X_{R,B}^{(n)}$, $X_{I,F}^{(n)}$, and $X_{R,F}^{(n)}$ are determined by fitting Eqs. (3) and (4) into the measurement at the frequencies $n\omega$, where $n = 1,2\ldots N$. The fitting is performed by minimization of the noise term $\Omega_m^{(n)}$ using the least-squares method. This gives for $n = 1$ (Lin and Huang 2004)

$$\begin{bmatrix} A_{11} & A_{12} \\ A_{21} & A_{22} \end{bmatrix} \begin{bmatrix} X_I^{(1)} \\ X_R^{(1)} \end{bmatrix} = \begin{bmatrix} B_1 \\ B_2 \end{bmatrix} \tag{5}$$

and for $n > 1$ (Lin and Huang 2004)

$$\begin{bmatrix} D_{11} & D_{12} & D_{13} & D_{14} \\ D_{21} & D_{22} & D_{23} & D_{24} \\ D_{31} & D_{32} & D_{33} & D_{34} \\ D_{41} & D_{42} & D_{43} & D_{44} \end{bmatrix} \begin{bmatrix} X_{I,B}^{(n)} \\ X_{R,B}^{(n)} \\ X_{I,F}^{(n)} \\ X_{R,F}^{(n)} \end{bmatrix} = \begin{bmatrix} E_1 \\ E_2 \\ E_3 \\ E_4 \end{bmatrix} \tag{6}$$

The detailed background for these two systems of equations as well as the expressions for $\boldsymbol{A}$, $\boldsymbol{B}$, $\boldsymbol{D}$, and $\boldsymbol{E}$ were derived by Lin and Huang (2004). The coefficients are for completion of the present method repeated in the Appendix.

Ignoring any interaction of incident and reflected wavefields, the wave numbers of the incident and reflected primary components (k_I and k_R) depend, respectively, on the incident and reflected wave height (H_I and H_R). The incident and reflected wave height needed for the nonlinear dispersion relation is part of the solution and is unknown initially. Therefore, Lykke Andersen et al. (2017) used an iterative procedure for the wavelength estimation.

The bound superharmonic component usually travels much faster than the free one, but in shallow water this is not the case with an infinite small wave height. With finite wave height, the problems are less because of amplitude dispersion, but they are still relevant in a few cases. In case the bound and the free waves travel with almost the same celerity, Lykke Andersen et al. (2017) proposed to assume that all incident energy is bound and all reflected energy is free at the problematic frequency (given order n). This assumption should be valid if incident waves are properly generated and there is perfect absorption at the wave generator (no free incident waves) and when only testing mildly reflective structures (bound reflected waves are very small). The correction is performed when

$$\frac{c_{\text{bound}}}{c_{\text{free}}} = \frac{k^{(n)}}{n \cdot k_I} < \alpha \tag{7}$$

Mathematically $\alpha = 1.0$ corresponds to the matrix in Eq. (6) becomes singular because of $n{\cdot}k_I = k^{(n)}$, but it is not sufficient that $\alpha > 1.0$; otherwise, small errors on the bound or free celerity or gauge positions will influence results significantly. A safe value for α seems to be 1.15, whereas for $\alpha = 1.05$–1.15 sometimes reliable results are obtained, but the sensibility of the results has to be checked.

Application of the Lykke Andersen Method to Irregular Waves

In irregular waves, the bound superharmonics at a given frequency stem from the interaction of many different primary components; consequently, the celerity of each of these interactions is slightly different. This makes the extension of the Lykke Andersen method to irregular waves complicated. However, assuming a narrowbanded primary spectrum, an exact solution for mildly nonlinear waves (second-order waves) can be established. For a narrowbanded spectrum, all the superharmonic components at a given frequency have the same celerity and order. The bound superharmonic of nth order at angular frequency ω_n has the celerity of the primary component at angular frequency $\omega = \omega_n/n$ (self-interacting). In irregular waves, bound subharmonics (the so-called bound long waves) are also present and also included in the present mathematical model. The subharmonics at a given frequency stem also from the interaction of many different primary components. Each of these interactions has a different celerity, but for a narrowbanded spectrum, all bound subharmonics have celerity equal to the group velocity at the peak frequency. The errors related to the narrowband assumption are in the following section shown to be small for typical single-peaked primary spectra (e.g., JONSWAP with $\gamma = 3.3$).

For highly nonlinear waves, amplitude dispersion is important (Lykke Andersen et al. 2017). Because amplitude dispersion is very complicated in irregular waves, an engineering correction is used in which the celerity of the primary components is taken as the linear celerity divided with a constant factor (β)

$$\beta_I = \frac{L_{\text{linear}}}{L_{\text{incident, nonlinear}}} \tag{8}$$

$$\beta_R = \frac{L_{\text{linear}}}{L_{\text{reflected, nonlinear}}} \tag{9}$$

For waves up to the second-order $\beta = 1$, but for third and higher order waves $\beta < 1$. In irregular waves β varies in time, but, as discussed in the following, a constant characteristic value is used in the present paper to apply frequency domain solutions.

The wave spectrum is divided into sub, primary, and superharmonic segments:

1. For $\omega \le 0.5\omega_P$ it is assumed that bound subharmonics and free/primary energy exist. Eq. (10) is the mathematical model.
2. For $0.5\ \omega_P < \omega < 1.5\ \omega_P$ only primary energy exists. Eq. (11) is the mathematical model.
3. For $\omega \ge 1.5\ \omega_P$ bound superharmonics and free/primary energy exist. At a given frequency, only bound superharmonics of one order are assumed to occur. The nth order bound superharmonics are assumed to occur only in the angular frequency interval $(n - 0.5)\ \omega_P$ to $(n + 0.5)\ \omega_P$. Eq. (12) is the mathematical model.

These segments, which are valid for narrowbanded primary spectra, have been chosen to maximize applicability for broader spectra. This is further demonstrated in the following sections. The amplitude dispersion (β factor) is applied only for the primary energy in the interval $0.5\omega_P < \omega < 1.5\omega_P$ and for the bound components. The bound superharmonics thus propagate with a celerity $\omega/(n\beta k(\omega/n))$, and the bound subharmonics propagate with a celerity $c_g(f_P)/\beta$, where $c_g(f_P)$ = linear group velocity at the spectral peak frequency. For the subharmonics at the frequency ω, the following mathematical model is obtained:

$$\begin{aligned}
\widehat{\eta}(\omega, x_m) &= C_{I,B}^{(-1)} X_{I,B}^{(-1)} + C_{R,B}^{(-1)} X_{R,B}^{(-1)} + C_{I,F}^{(-1)} X_{I,F}^{(-1)} + C_{R,F}^{(-1)} X_{R,F}^{(-1)} \\
&\quad + \Omega_m \\
X_{I,B}^{(-1)} &= a_{I,B}(\omega) \exp\left[-\mathrm{i}\left(\omega \beta_I / c_g(f_P, h) x_1 + \varphi_{I,B}(\omega)\right)\right] \\
X_{R,B}^{(-1)} &= a_{R,B}(\omega) \exp\left[\mathrm{i}\left(\omega \beta_R / c_g(f_P, h) x_1 + \varphi_{R,B}(\omega)\right)\right] \\
X_{I,F}^{(-1)} &= a_{I,F}(\omega) \exp\left[-\mathrm{i}\left(k(\omega, h) x_1 + \varphi_{I,F}(\omega)\right)\right] \\
X_{R,F}^{(-1)} &= a_{R,F}(\omega) \exp\left[\mathrm{i}\left(k(\omega, h) x_1 + \varphi_{R,F}(\omega)\right)\right] \\
C_{I,B}^{(-1)} &= \exp\left(-\mathrm{i}\omega \beta_I / c_g(f_P, h) \Delta x_m\right) \\
C_{R,B}^{(-1)} &= \exp\left(\mathrm{i}\omega \beta_R / c_g(f_P, h) \Delta x_m\right) \\
C_{I,F}^{(-1)} &= \exp\left(-\mathrm{i} k(\omega, h) \Delta x_m\right) \\
C_{R,F}^{(-1)} &= \exp\left(\mathrm{i} k(\omega, h) \Delta x_m\right)
\end{aligned} \tag{10}$$

where k = wave number determined by linear dispersion. It appears that the solution can be found by Eq. (6) with the new formulas for $C_{I,B}$, $C_{R,B}$, $C_{I,F}$, and $C_{R,F}$.

For primary components at frequency ω, the following mathematical model is obtained:

$$\widehat{\eta}(\omega, x_m) = C_I^{(1)} X_I^{(1)} + C_R^{(1)} X_R^{(1)} + \Omega_m$$
$$X_I^{(1)} = a_I(\omega) \exp\left[-\mathrm{i}\left(\beta_I\, k(\omega, h)\, x_1 + \varphi_I(\omega)\right)\right]$$
$$X_R^{(1)} = a_R(\omega) \exp\left[\mathrm{i}\left(\beta_R\, k(\omega, h)\, x_1 + \varphi_R(\omega)\right)\right]$$
$$C_I^{(1)} = \exp(-\mathrm{i}\beta_I\, k(\omega, h)\Delta x_m)$$
$$C_R^{(1)} = \exp(\mathrm{i}\beta_R\, k(\omega, h)\Delta x_m) \tag{11}$$

It appears that the solution can be found by Eq. (5) with the new formulas for C_I and C_R.

For the superharmonics at frequency ω, the following mathematical model is obtained:

$$\widehat{\eta}(\omega, x_m) = C_{I,B}^{(n)} X_{I,B}^{(n)} + C_{R,B}^{(n)} X_{R,B}^{(n)} + C_{I,F}^{(n)} X_{I,F}^{(n)} + C_{R,F}^{(n)} X_{R,F}^{(n)} + \Omega_m$$
$$X_{I,B}^{(n)} = a_{I,B}(\omega) \exp\left[-\mathrm{i}\left(n\beta_I\, k(\omega/n, h) x_1 + \varphi_{I,B}(\omega)\right)\right]$$
$$X_{R,B}^{(n)} = a_{R,B}(\omega) \exp\left[\mathrm{i}\left(n\beta_R\, k(\omega/n, h) x_1 + \varphi_{R,B}(\omega)\right)\right]$$
$$X_{I,F}^{(n)} = a_{I,F}(\omega) \exp\left[-\mathrm{i}\left(k(\omega, h) x_1 + \varphi_{I,F}(\omega)\right)\right]$$
$$X_{R,F}^{(n)} = a_{R,F}(\omega) \exp\left[\mathrm{i}\left(k(\omega, h) x_1 + \varphi_{R,F}(\omega)\right)\right]$$
$$C_{I,B}^{(n)} = \exp(-\mathrm{i}n\beta_I\, k(\omega/n, h)\Delta x_m)$$
$$C_{R,B}^{(n)} = \exp(\mathrm{i}n\beta_R\, k(\omega/n, h)\Delta x_m)$$
$$C_{I,F}^{(n)} = \exp(-\mathrm{i}k(\omega, h)\Delta x_m)$$
$$C_{R,F}^{(n)} = \exp(\mathrm{i}k(\omega, h)\Delta x_m) \tag{12}$$

where $n = \lfloor f/f_P + 0.5 \rfloor$ with $\lfloor x \rfloor$ being the greatest integer function of x. It appears that the solution can be found by Eq. (6) with the new formulas for $C_{I,B}$, $C_{R,B}$, $C_{I,F}$, and $C_{R,F}$.

The mathematical problem can be solved in the frequency domain by the determination of β_I and β_R by iteration with an initial value of 1.0 corresponding to infinite small waves. The convergence of β_I and β_R is very fast. The computational effort is only a few times larger than that for linear methods such as the method of Zelt and Skjelbreia (1992). The frequency domain solution requires the sea state to be stationary. This is usually solved by excluding in the analysis the first part of the time series in which reflections are not yet fully developed and by applying a taper window to the time series. Also, for irregular waves a correction might be needed for shallow water waves because the bound and the free waves travel with almost the same celerity. The correction procedure applied for regular waves is applicable and used in the present paper.

Errors Related to Narrowband Assumption

The actual wave celerity of both the bound superharmonics and subharmonics for mildly nonlinear waves can be calculated by second-order wave theory. Application of this theory makes evaluation of the validity of the narrowband assumptions possible. Fig. 1 shows the celerity error for the superharmonics [Fig. 1(a)] and subharmonics [Fig. 1(b)], where k_0 = wave number for the primary frequency (f_0), and $f_0 = f_P$ is assumed for the subharmonic. The error in the present narrowband assumption (solid lines) is zero for $\Delta f = 0$, and increasing with increasing Δf, where Δf = frequency difference of two interacting primary components with frequencies $f_1 = f_0 - \Delta f/2$ and $f_2 = f_0 + \Delta f/2$. The error for $\Delta f = 0$ for superharmonics is 0–48% and for subharmonics it is 0–120% when linear theory (free wave assumption) is used for the bound component. For $\Delta f > 0$ it is seen that the celerity from second-order theory with narrowband assumption is higher than the real celerity based on full second-order theory. For example, for $\Delta f/f_0 = 0.2$ the celerity error of the superharmonics is for $0.17 \le k_0 h \le 1.87$ between 3 and 13% for narrowband assumption and 3 and 41% for the linear theory. For the same Δf, the real celerity of the subharmonics based on full second-order theory is 2–6% lower than the narrowband assumption and 2–134% lower than the linear theory. The errors for the narrowband assumption are significantly smaller than errors related to linear theory. Fig. 2(b) shows that mainly small Δf values contribute to the second-order superharmonic energy, and Fig. 2(c) shows that for the given example 84–95% of the second-order superharmonic energy stems from $\Delta f/f_0 < 0.2$ for which the celerity error is up to 5% for the narrowband assumption. The error would have been more significant if the example had been in deeper water, but then the amount of second-order energy would also be less significant compared with the amount of primary energy. Thus, the narrowband assumption is for practical applications expected to provide accurate estimates of the celerity of the bound waves.

Moreover, the interaction of the incident and reflected components has been ignored in the proposed method. The related errors have been studied by calculating the transfer functions (G_{nm}^- and G_{nm}^+) using second-order wave theory. The second-order transfer functions calculate the amount of second-order energy produced by the two free interacting components. See Eq. (67) in Schäffer and Steenberg (2003) for the calculation of the second-order transfer function. The error in disregarding the interaction between the incident and reflected components has been studied by comparing the second-order transfer functions (G_{nm}^- and G_{nm}^+) for two components having the same direction ($\Delta\theta = 0°$) with that for two components in the opposite direction ($\Delta\theta = 180°$). The results, presented in Fig. 3, show that the interaction between incident and reflected components is zero for the superharmonics when narrowbanded spectra are used. However, even for more broad-banded spectra, the interaction of incident and reflected waves is very small for both the superharmonics and the subharmonics. Therefore, it is reasonable to ignore the interaction when second-order theory is valid.

The previously mentioned findings are for mildly nonlinear waves for which amplitude dispersion is not relevant.

Numerical Calibration and Validation Data

A numerical model is used to generate the calibration and validation data because no analytical solution for highly nonlinear irregular waves exists. A horizontal seabed is assumed in the reflection separation method, but for the numerical model a sloping foreshore has to be included because the waves need to be described by a valid wave theory at the generation point to avoid free harmonics. The sloping foreshore is then used to transform the linear waves to nonlinear waves including shoaling and wave–wave interaction. The numerical data were generated by the one-dimensional COULWAVE Boussinesq model (Lynett and Liu 2004). Other researchers, such as Hsiao et al. (2005) and Teixeira et al. (2010), have validated the COULWAVE model, and it has proven to be a robust and accurate model for propagating waves from deep to shallow water including nonlinear effects. The discretization of the numerical model was two vertical layers and

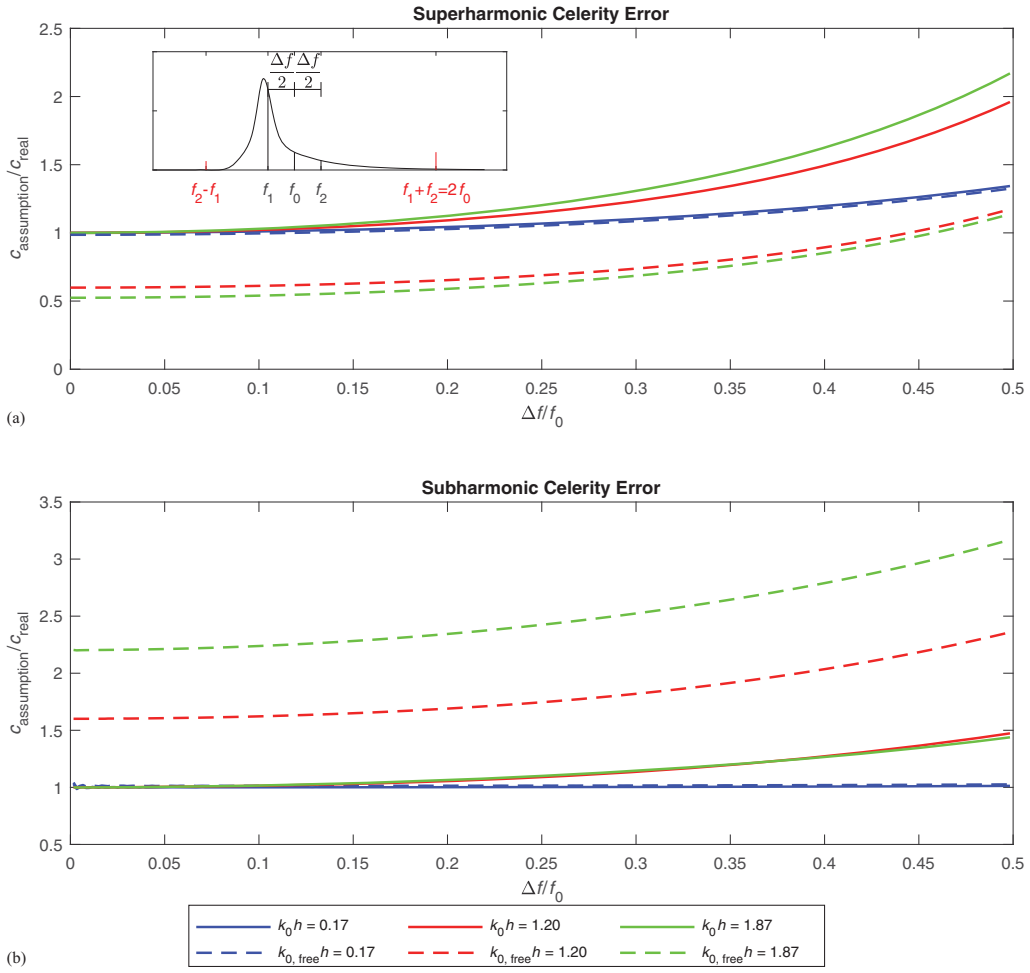

Fig. 1. Validity of linear assumption (dashed lines) and second-order narrowband assumption (solid lines), respectively, for the celerity ($c_{assumption}$) of (a) bound superharmonics; and (b) bound subharmonics as a function of $\Delta f = f_2 - f_1$, where $f_1 = f_0 - \Delta f/2$ and $f_2 = f_0 + \Delta f/2$. Calculations of c_{real} are based on full second-order theory, i.e., for mildly nonlinear waves. For the subharmonics, $f_P = f_0$ is assumed.

$\Delta x = L_P/200$, where L_P = wavelength of the peak wave period at the generation point. The time step was based on the Courant number, $C = c_0\,\Delta t/\Delta x = 0.5$, where c_0 = shallow water celerity at the generation point.

The waves were generated from a JONSWAP spectrum. A peak enhancement factor $\gamma = 10$ was used for the β calibration tests because the new method is correct to second-order for narrow-banded spectra, whereas, as demonstrated in Fig. 1, minor errors might occur for normal and wide spectra. Therefore, sea states with $\gamma = 3.3$ were generated for the validation tests to evaluate the present method for more typical spectra. Because the COULWAVE model presently only can generate linear waves, the depth at the generation point is a compromise between linear theory being valid for wave generation and not exceeding the kh limit of the two-layer model ($kh < 6$). For the sea states with $\gamma = 10$, it was chosen to generate the waves at $h/gT_P^2 = 0.068$ corresponding to $kh < 6$ for 1.5 times the peak frequency and $h/gT_P^2 = 0.017$ for $\gamma = 3.3$ corresponding to $kh < 6$ for three times the peak frequency (Fig. 4). For the nonlinear test cases, this only slightly violates the range in which no free second-order energy exists when first-order wave generation is applied.

The waves were shoaling on a 1:100 foreshore slope ensuring no significant depth induced breaking for the maximum incident wave ($H_{max}/h \le 0.62$ in all sea states). On the 1:100 slope, an array of seven wave gauges ($wg1$–$wg7$) was used with Δx_m of 0, 0.5, 0.82, 1.10, 1.39, 1.55, and 2.00 m (Fig. 5). Choosing the same array for all sea states is justified by a rather small variation in the peak wavelength and the high number of gauges. The influence of the wave gauge array design is discussed later in the paper. The waves are measured on the slope because Beji and Battjes (1993) demonstrated that a transition to a horizontal plateau would release a part of the bound wave energy, so the correct solution is unknown.

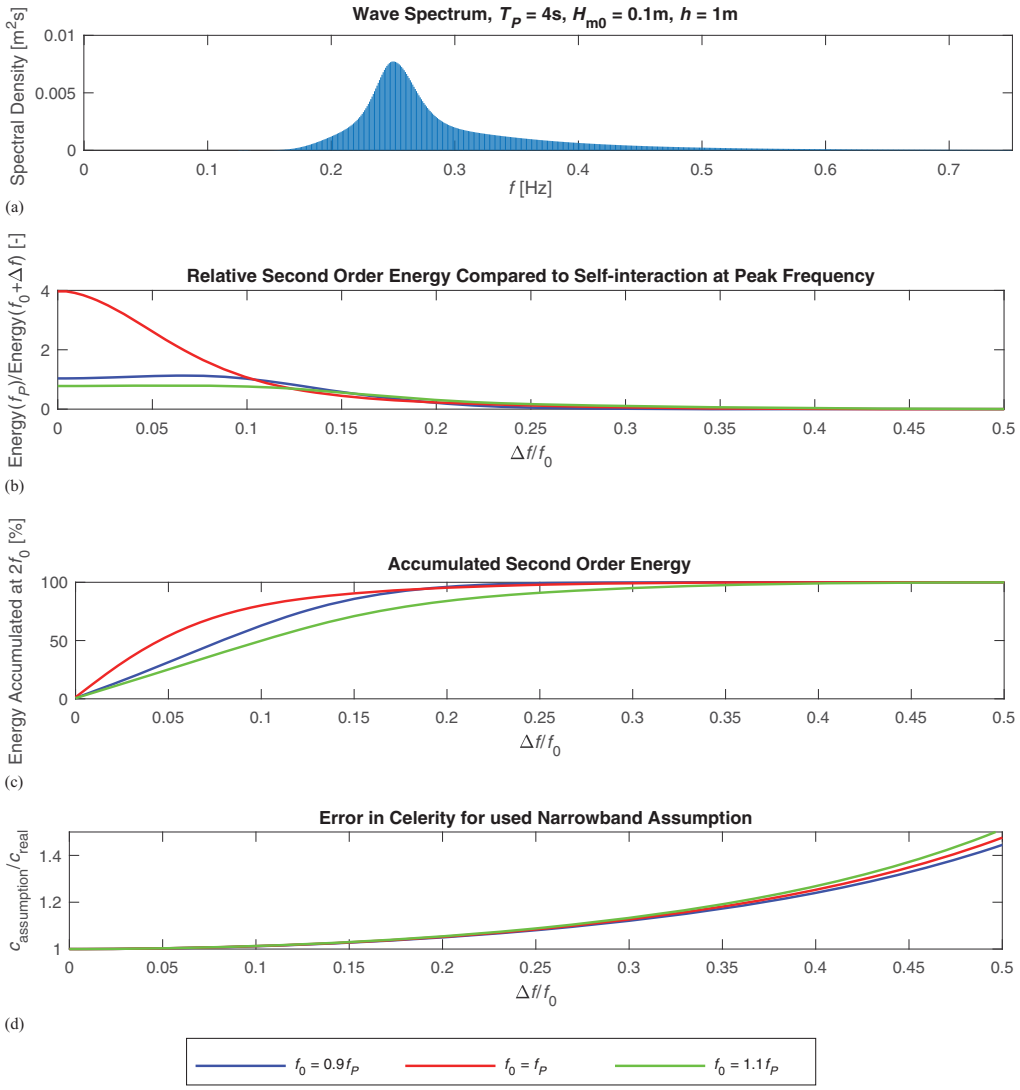

Fig. 2. (a) Example of a spectrum and related errors on superharmonic celerity; (b) relative importance of various Δf values; (c) percentage of the second-order energy having a Δf less than a given value; and (d) related errors on the celerity when using narrowband assumption.

Moreover, in typical model test setups, a sloping foreshore would also be present in front of the model. The numerical validation tests (γ = 3.3) were performed with different amounts of reflection by using a highly absorbing sponge layer corresponding to a reflection coefficient $CR = H_{m0,R}/H_{m0,I} \approx 0$ and a 1:10 slope corresponding to CR = 0.38–0.76 depending on the sea state and a fully reflective wall ($CR \approx 1$) at the end of the model. The calibration tests (γ = 10) were performed solely with the highly absorbing sponge layer because these tests were only used for calibration of β. Thus, in total 11 numerical tests were performed. Fig. 5 shows the different setups with different degrees of reflection for Sea States B and C from Table 1. The distance between the reflective structures and the closest wave gauge (Δx) in all tests fulfilled the recommendation $\Delta x > 0.4L_P$ as suggested by Klopman and van der Meer (1999).

Wave conditions were generated with parameters according to Table 1. Waves were generated using the inverse fast Fourier transform (InvFFT) principle, and each test contained approximately 1,000 waves. The diagram by Le Méhauté (1969) is used to describe the nonlinearities of the five sea states on the slope in which H_{max} and T_P are used to define each sea state (Fig. 4). The shoaling from the generation point is also shown. Sea States D and E are highly nonlinear waves used to calibrate the calculation of β based on the narrowband assumption. Sea States A, B, and C are used for validation and for comparing the present method with existing methods

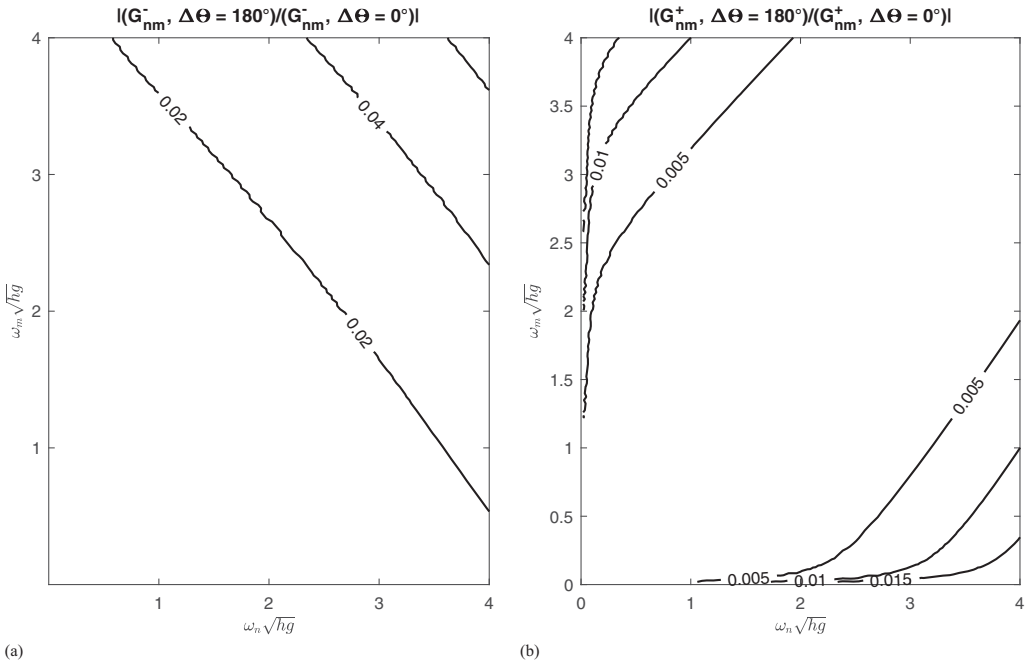

Fig. 3. Interaction between waves with opposite directions (incident and reflected) for the (a) subharmonics; and (b) superharmonics.

for a typical spectral shape. The bandwidth parameter at the wave generation point is calculated with Eq. (13) and is given in Table 1. For white noise $\nu = 1$, whereas for spectra including only one frequency, $\nu = 0$

$$\nu = \sqrt{\frac{m_0 m_2}{m_1^2} - 1} \tag{13}$$

where m_0, m_1, and m_2 are the 0th, first, and second moments of the wave spectrum.

Sea State A is linear waves for which all reflection analysis methods should be valid. Sea State B corresponds to mildly nonlinear waves for which second-order wave theory is valid for the maximum wave height. Sea State C corresponds to highly nonlinear waves in rather shallow water.

All of the present applied reflection separation methods assume a horizontal seabed. However, because the seabed slope is mild (1:100) reasonable results are expected by using the water depth in the middle of the wave gauge array.

Calibration of Nonlinear Amplitude Dispersion Factor

The calibration of β is done by comparing the measured phase shift between $wg1$ and $wg7$ in Sea States D and E with the calculated phase shift. The calculated phase shifts are given by the terms depending on Δx_m in Eqs. (10)–(12) using the assumed wave numbers in accordance with the present method. The measured phase shifts are calculated by cross-spectral analysis and computed as $\tan^{-1}$ of the ratio of the quad density estimates over the cross-density estimate. The measured phase shifts are based on subseries with $N = 4096$ ($\Delta f = 0.0104$ Hz) using 20% tapering, and overlapping of the subseries. The cross-spectral densities and quad spectral densities are then calculated as average values of the subseries (approximately 50 subseries are used).

The simplified amplitude dispersion factor, β, was calculated by stream function theory for regular waves (Fenton and Rienecker 1980) using T_P as a characteristic wave period and various characteristic wave heights H_c. The used relations for Eqs. (8) and (9) are

$$\beta_I = \frac{L(0, T_P, h)}{L(H_{c,I}, T_P, h)} \tag{14}$$

$$\beta_R = \frac{L(0, T_P, h)}{L(H_{c,R}, T_P, h)} \tag{15}$$

For the calibration of β, tests with almost 100% wave absorption were used. Therefore, only β_I can be calibrated, and it is assumed that $H_{C,I} = H_{C,R}$. The measured phase differences stem only from the incident bounded components, which makes the calibration more reliable. In Fig. 6, β_I has been calculated for Sea States D and E with $H_c = 0$, $H_c = H_{m0}$, and $H_c = 2H_{m0}$ by Eq. (14). The figure shows that in the primary part ($0.5 < f/f_P < 1.5$) both $H_c = 0$ and $H_c = H_{m0}$ provide phase differences close to the measured ones, but $H_c = H_{m0}$ was found slightly better when considering the highest waves in the time series. This is because the measured phase shift is an average value considering the entire time series, whereas the highest waves have lower β values. The bound superharmonics are mainly present in the high waves; therefore, the calculated phase

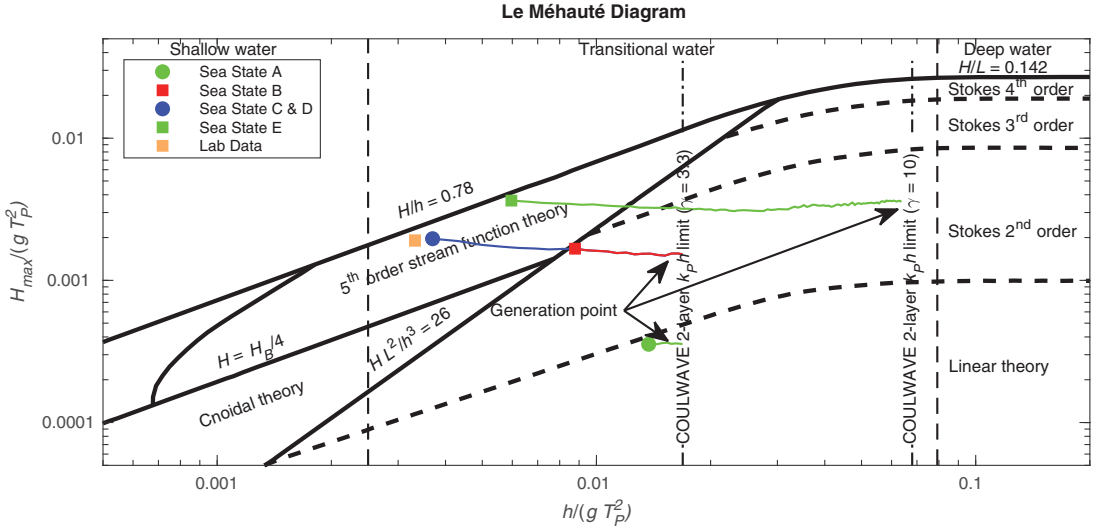

Fig. 4. Nonlinearity of the numerical irregular sea states (A–E) and the laboratory data. The lines connected to the markers illustrate the shoaling effect from the generation point to the point the results are evaluated. (Adapted from Le Méhauté 1969.)

shift in that region reflects these waves. Fig. 6 shows that β calculated with $H_c = H_{m0}$ provides the more accurate phase shift for the superharmonics when considering the frequency interval in which significant superharmonic energy is present. In this way, the assumption that the celerity of the bound higher harmonics can be calculated by assuming self-interaction with simplified amplitude dispersion has been demonstrated. Moreover, the figure shows that linear theory (primary with $H_c = 0$) leads to very wrong phase shifts for the superharmonics, especially for $n > 2$. The present method has been implemented in the wave analysis software WaveLab 3 (2017) for reflection analysis of irregular waves. In the following the present method is evaluated with β calculated with $H_c = H_{m0}$ for the test cases with wider wave spectra.

Validation on Numerical Model Data

The present method with the previously calibrated β has been applied to Sea State C with the 1:10 slope (Fig. 7). The top of the figure shows the calculated total/primary incident and reflected spectrum, and the bottom of the figure shows the surface elevation of the total spectrum, the primary segment, and the bound segments of the incident and reflected waves. The calculated primary incident spectrum corresponds to a typical shoaled JONSWAP spectrum, which gives confidence both to the method and to the division of the spectra into subharmonic, primary, and superharmonic parts. The division in the frequency bands is reasonable for the present case because no significant bound energy is present at the limits $(i + 0.5)f_P$ for $i = 0,1,2\ldots$. The figure also shows that for the specific case Eq. (7) is fulfilled for $f < 0.41$ Hz and $n = 2$ for the incident waves (shallow water exception). Thus, the incident energy cannot be separated into bound and free components in the range $1.5f_P$ to 0.41 Hz. The consequence of this is irrelevant for the overall objective of calculating the total incident time series (bound + free components), and all incident energy in this range is assumed bound. The surface displacement time series of the bound superharmonics are, as expected, when the crest occurs in the wave crest of the primary wave. The total incident waves show steep and narrow crests and wide troughs, which is typical for highly nonlinear waves.

The present separation method is further validated and compared with the other separation methods by using the numerical validation cases Sea States A, B, and C. For this the coefficient of determination R^2 for the measured waves and the predicted waves is calculated. For the method to completely agree with the actually measured waves, $R^2 = 1$. Fig. 8 shows for the three sea states with an absorber the measured and predicted incident surface elevations compared with the first, middle, and last wave gauges in the array. Because the measurements are without noise and reflections ($\eta_I = \eta_{\text{Total}}$), all points would lie on the 45° line in case of perfect agreement. For all three sea states, LASA V poorly predicts the incident surface elevations giving a coefficient of determination R^2 from 0.800 to 0.962. The linear sea state (A) gives the largest error for this method. For Sea States A and B, the Zelt and Skjelbreia (1992) method gives good results ($R^2 \geq 0.998$), but for Sea State C significant differences between predicted and measured surface elevations are observed (R^2 from 0.965 to 0.996). The predictions are best for the middle wave gauge, but the highest crests are significantly underpredicted. For the other wave gauges, the error is much larger due to the assumption of linear dispersion. The present method provides good results for all three sea states. For the middle wave gauge, $R^2 = 1.000$ is obtained for all three sea states. $R^2 = 1.000$ also is obtained for the other gauges except for Sea State C, where $R^2 = 0.998$. The reason for the slightly better predictions by the middle wave gauge might be the negligence of the shoaling on the 1:100 slope and/or small errors on the wave celerity (e.g., β factors and narrowband assumption for broader spectra).

For the test with full reflection, the estimated incident waves might be compared with cases without the structure in place. However, the numerical results indicate that the incident waves

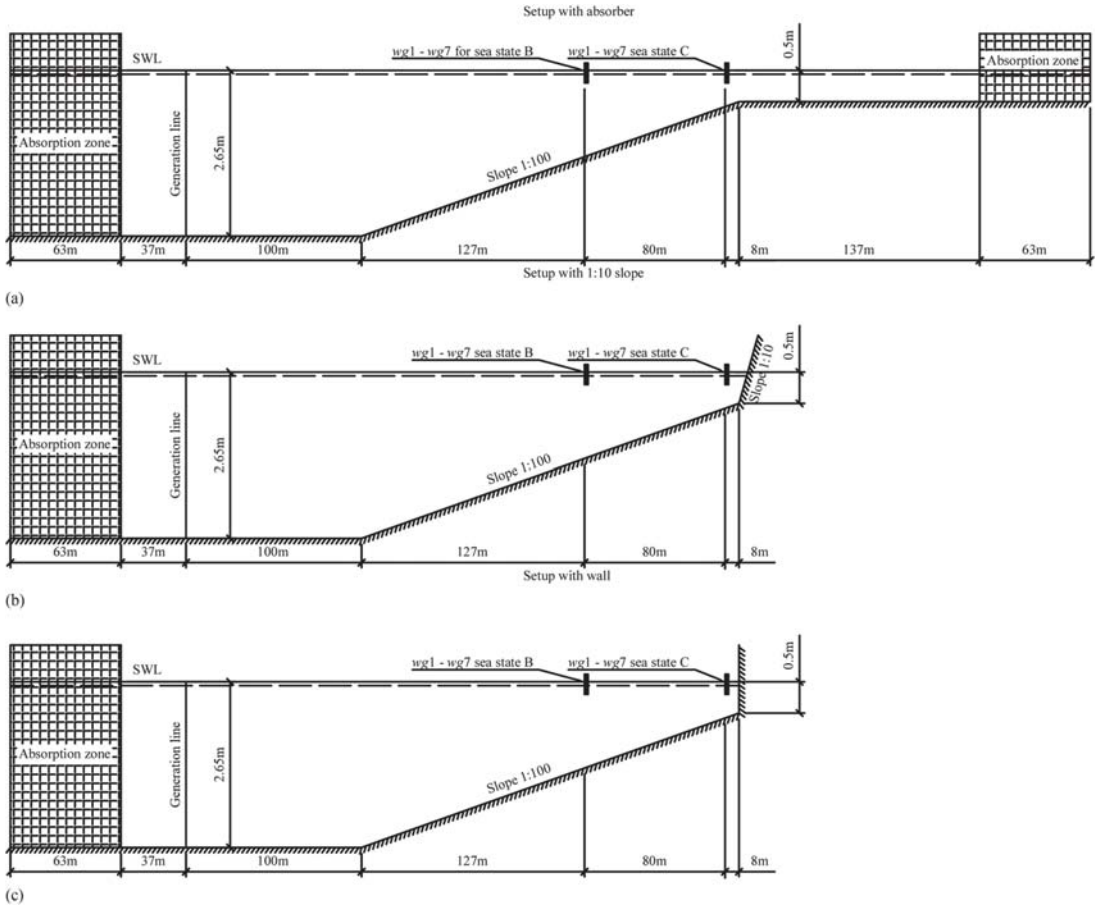

Fig. 5. Three setups (absorber, slope, and wall) in COULWAVE for Sea States B and C for (a) no reflection; (b) partly reflection; and (c) full reflection conditions. The vertical and horizontal scale is not identical. SWL = still-water level.

Table 1. Numerical test conditions (incident waves)

Sea state	h_{gen} (m)	T_P (s)	$H_{m0,\,gen}$ (m)	γ	h_{wg1} (m)	$H_{m0,\,wg1}$ (m)	$H_{max,\,wg1}$ (m)	ν
A	4.14	5	0.050	3.3	3.37	0.050	0.088	0.30
B	2.65	4	0.150	3.3	1.38	0.158	0.263	0.29
C	2.65	4	0.150	3.3	0.58	0.181	0.308	0.29
D	2.65	4	0.150	10.0	0.58	0.181	0.308	0.12
E	10.00	4	0.320	10.0	0.94	0.313	0.578	0.12

interact with the reflected waves causing the incident waves to be different without the structure in place. This effect is demonstrated in Fig. 9, in which the reflected waves appear unrealistic with deep and narrow troughs when assuming incident waves to be identical to those without the structure in place. The effect seems caused by a phase shift of the incident waves. As demonstrated previously this interaction could be neglected for mildly nonlinear waves (second-order waves). However, second-order wave theory does not consider the influence of the return currents on the celerity. Moreover, the bound long incident waves become partly long free reflected waves, which cause slow water level fluctuations influencing the celerity of the incident waves. This effect is in the present numerical data present for Sea State A because the waves shoal up to highly nonlinear waves before hitting the reflective structure. Thus, reflected waves will contain long free waves that interact with the incident waves.

Many laboratories calibrate waves without the structure in place, assuming the incident waves with and without a structure in place to

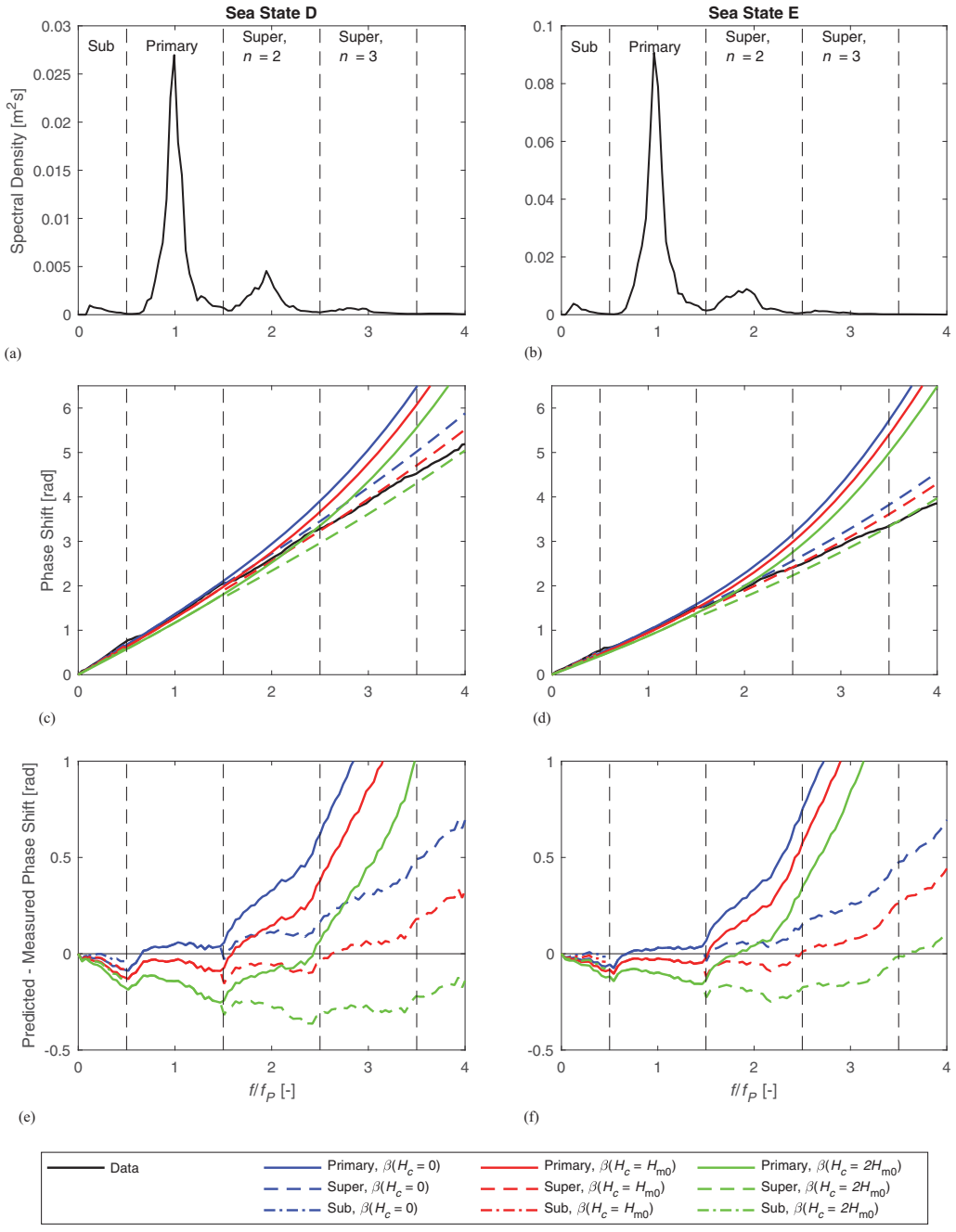

Fig. 6. (a and b) Total spectrum; (c and d) measured phase shift and predicted between *wg*1 and *wg*7; and (e and f) difference between the predicted and measured phase shift.

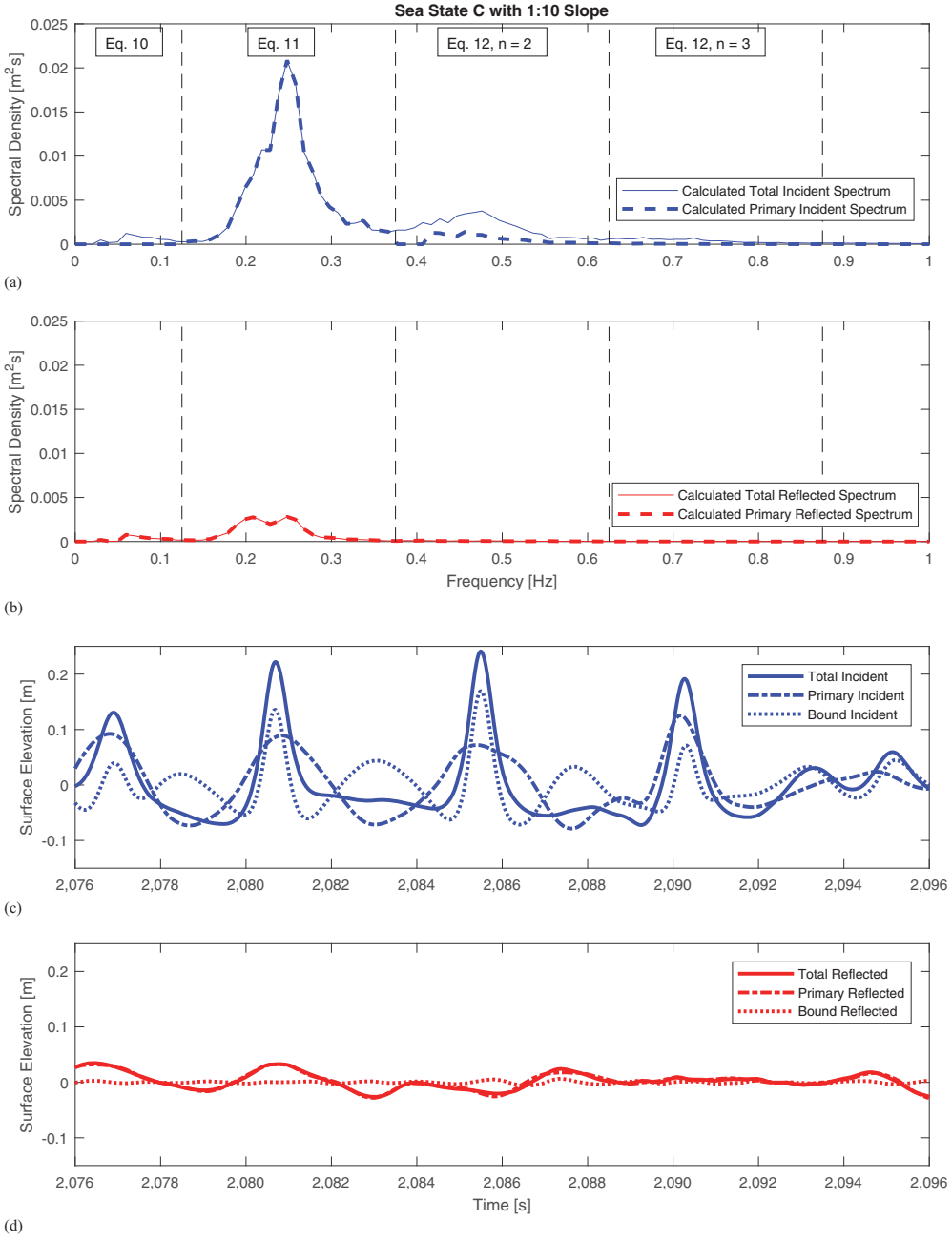

Fig. 7. (a and b) Total and primary (no superharmonic and subharmonic components) spectrum: (a) incident waves; (b) reflected waves. (c and d) Time series of the total, primary, and bound waves: (c) incident waves; (d) reflected waves. For $f < 0.41$ Hz, Eq. 7 is fulfilled for $\alpha = 1.15$ and $n = 2$; thus, separation of bound and free components is not performed. The vertical dashed lines in (a and b) separate the frequency domain into subharmonic, primary, and superharmonic parts with the related equations.

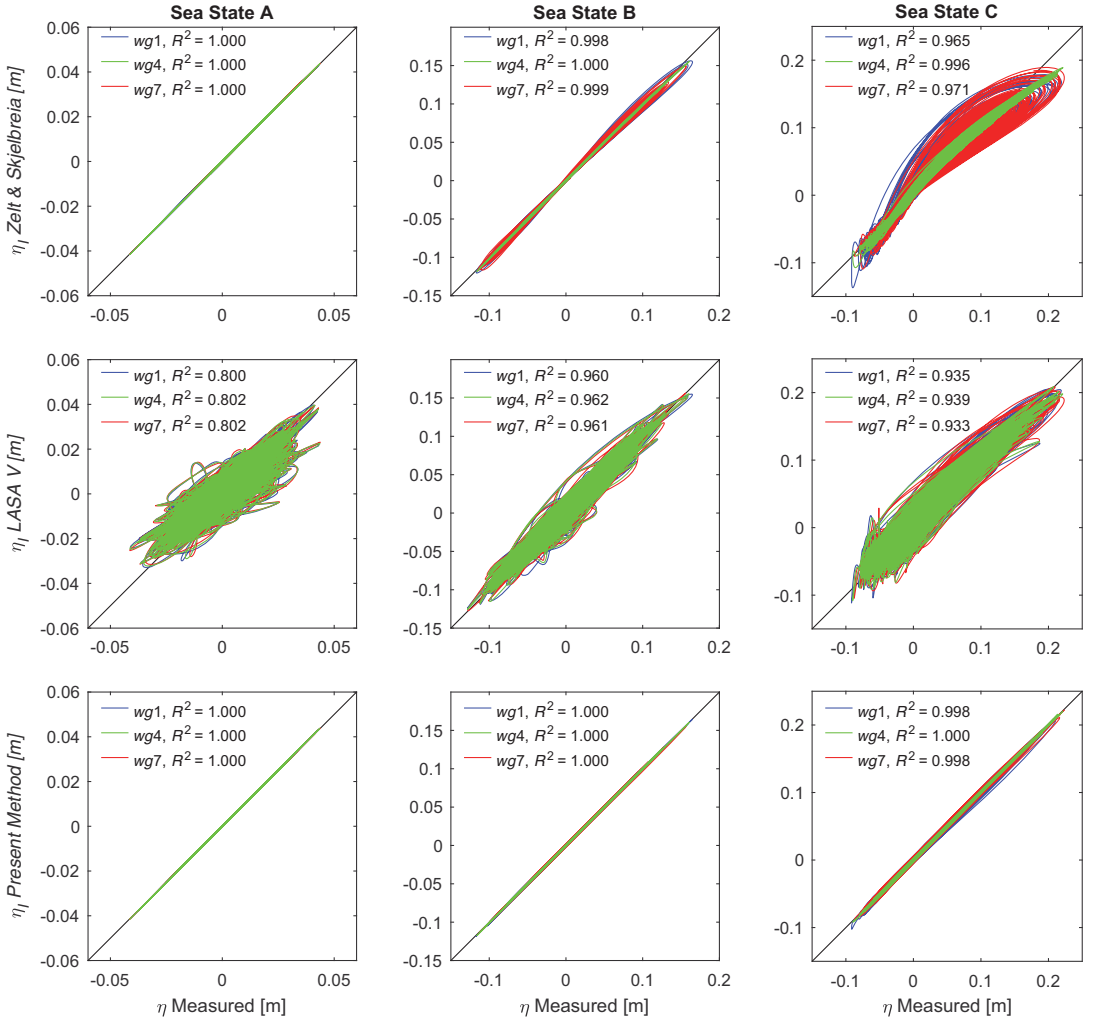

Fig. 8. Comparison of measured total and predicted incident surface elevation (η_I) for the absorber ($CR \approx 0$) and the three sea states for the wave gauges $wg1$, $wg4$, and $wg7$.

be identical. It is well known that this requires a highly absorbing beach during calibration tests and a highly effective active absorption system with the structure in place. However, it is less well known that the incident waves with the structure in place are different due to an interaction with reflected waves as Fig. 9 demonstrates. The interaction between the incident and reflected waves is important because the structural response is related to the actual incident waves with the structure in place. The previously mentioned findings also show that calibration tests might be needed if target waves are given without structure in place.

To verify how well the test data fit the mathematical model, the total predicted surface elevations ($\eta_I + \eta_R$) are compared with the total measured for each of the wave gauges. The results are shown in Table 2. The results for the three sea states with an absorber show similar results to Fig. 8, except for LASA V, which shows smaller errors on the total elevations than on the incident elevations. For the 1:10 slope, the R^2 values are similar to the case with the absorber. For the fully reflective wall, results for Sea States A and B are similar to the fully absorbing slope and the 1:10 slope. However, for the highly nonlinear waves (Sea State C), larger errors are present for the fully reflecting wall, but the present method gives acceptable results. Note that in this case reflected waves might cause breaking of the incident waves because the incident waves alone are close to depth limitation (Fig. 4).

The results for the total elevations do not necessarily indicate the real error on the incident waves when reflection is present. Therefore, time series of predicted incident waves and reflected waves are presented in Figs. 10 and 11. In those figures, the

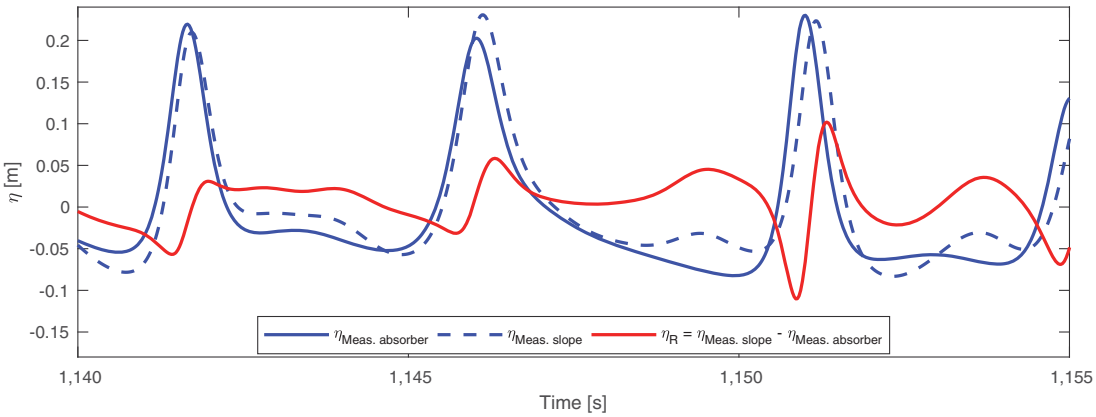

Fig. 9. Time series for Sea State C at *wg*7. The results with an absorber are used as incident waves, and the results from the slope are used to calculate the reflected wave train assuming incident waves unchanged.

measured surface elevation is compared with the predicted incident and reflected surface elevations for the different methods. The absorber case is shown in Fig. 10 for the instances in which the highest wave occurs. LASA V predictions deviate significantly from the measured waves for all sea states. For sea states A and B, the Zelt and Skjelbreia (1992) method provides acceptable results. For the highly nonlinear waves (Sea State C), results of both LASA V and Zelt and Skjelbreia (1992) are unacceptable with large underpredictions of the crests and high undulations in the trough. The present method provides good results for all sea states with only minor deviations for the highly nonlinear waves (Sea State C). Likewise, Fig. 11 presents the results of the 1:10 slope. Because of the interaction of incident and reflected waves, the incident waves cannot be directly compared with the waves without the structure in place (absorber). The wave trains with the absorber are though included in the figures for qualitative comparison. For the existing methods, the predictions have similar errors as found for the absorber case. For the present method, the estimated reflected waves are realistic and do not show the problems identified in Fig. 9. The incident waves also look realistic when taking into account the expected phase shift compared with the waves without the structure in place (interaction of incident and reflected waves). Moreover, for the linear waves (Sea State A) the present method gives identical results to the linear Zelt and Skjelbreia (1992) method. Table 3 shows the consequences of choosing the reflection separation method on characteristic wave parameters. Because of the previously mentioned interaction of the incident and reflected waves, the target wave parameters are only accurately known for the absorber case from which the following conclusions may be drawn:

1. For the linear waves (Sea State A), the Zelt and Skjelbreia (1992) and present methods give identical results and agree with the target values for all wave parameters. This is not the case for the LASA V method, which underpredicts the wave heights by 10–15%.
2. For the mildly nonlinear waves (Sea State B), all methods yield acceptable wave parameters.
3. For the highly nonlinear waves (Sea State C), the error on the H_{m0} wave height is acceptable for all three methods. However, the errors on the time domain parameters are 6–12% for the typically applied linear methods (e.g., Zelt and Skjelbreia). For LASA V and the present method, the error on the time domain parameters is acceptable, but it is smallest for the present method, in which the error on all wave height parameters is below 1%.

For the 1:10 slope and the vertical wall, the target values are not accurately known. However, it is clear from Table 3 that LASA V always gives a very significant increase in the maximum incident wave height when reflection is high. This also is the case for the linear waves (Sea State A), in which LASA V gives a 30% higher

Table 2. Coefficient of determination R^2 for the total surface elevation $(\eta_I + \eta_R)$

Sea state	Structure	Method	*wg*1	*wg*4	*wg*7
A	Absorber	Zelt and Skjelbreia	1.000	1.000	1.000
		LASA V	0.929	0.973	0.927
		Present method	1.000	1.000	1.000
	Slope	Zelt and Skjelbreia	1.000	1.000	1.000
		LASA V	0.908	0.968	0.914
		Present method	1.000	1.000	1.000
	Wall	Zelt and Skjelbreia	1.000	1.000	1.000
		LASA V	0.938	0.978	0.922
		Present method	1.000	1.000	1.000
B	Absorber	Zelt and Skjelbreia	0.999	1.000	0.999
		LASA V	0.963	0.977	0.967
		Present method	1.000	1.000	1.000
	Slope	Zelt and Skjelbreia	0.999	1.000	0.999
		LASA V	0.944	0.970	0.951
		Present method	1.000	1.000	1.000
	Wall	Zelt and Skjelbreia	0.999	1.000	0.999
		LASA V	0.930	0.964	0.936
		Present method	1.000	1.000	1.000
C	Absorber	Zelt and Skjelbreia	0.968	0.995	0.976
		LASA V	0.944	0.958	0.950
		Present method	0.999	1.000	1.000
	Slope	Zelt and Skjelbreia	0.971	0.996	0.981
		LASA V	0.933	0.957	0.947
		Present method	0.999	1.000	1.000
	Wall	Zelt and Skjelbreia	0.952	0.990	0.967
		LASA V	0.912	0.926	0.928
		Present method	0.997	0.998	0.998

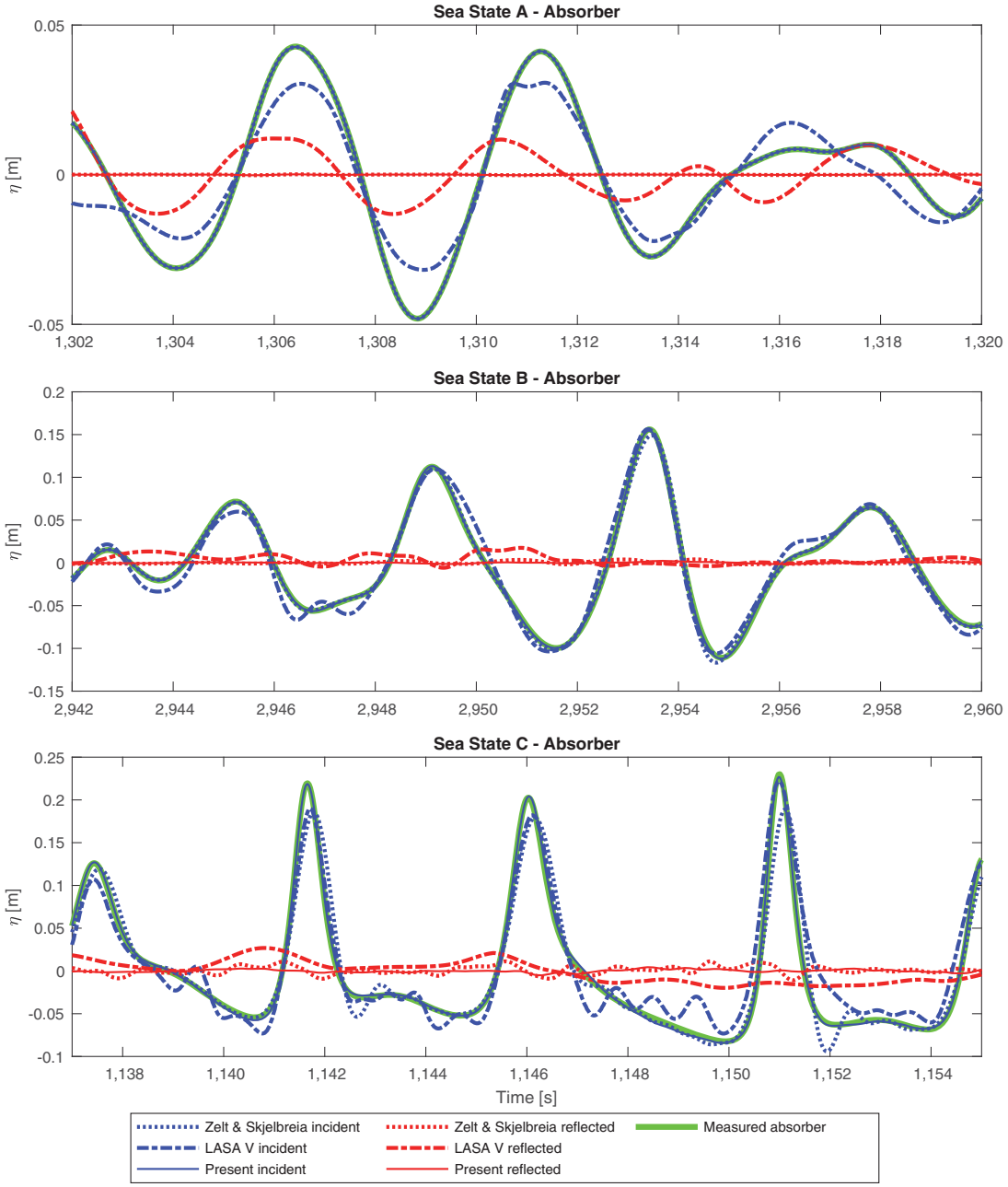

Fig. 10. Measured and predicted surface elevation time series at *wg*7 for the absorber for the instances in which the highest waves occur.

maximum wave height for the vertical wall compared with the target (absorber case). For the other two sea states, the increase in the maximum wave height predicted by LASA V is less, but it is still significantly higher than the other two methods. Fig. 11 supports the fact that this increase in maximum wave height is not correct and is due to an unrealistic wave profile predicted by LASA V. This

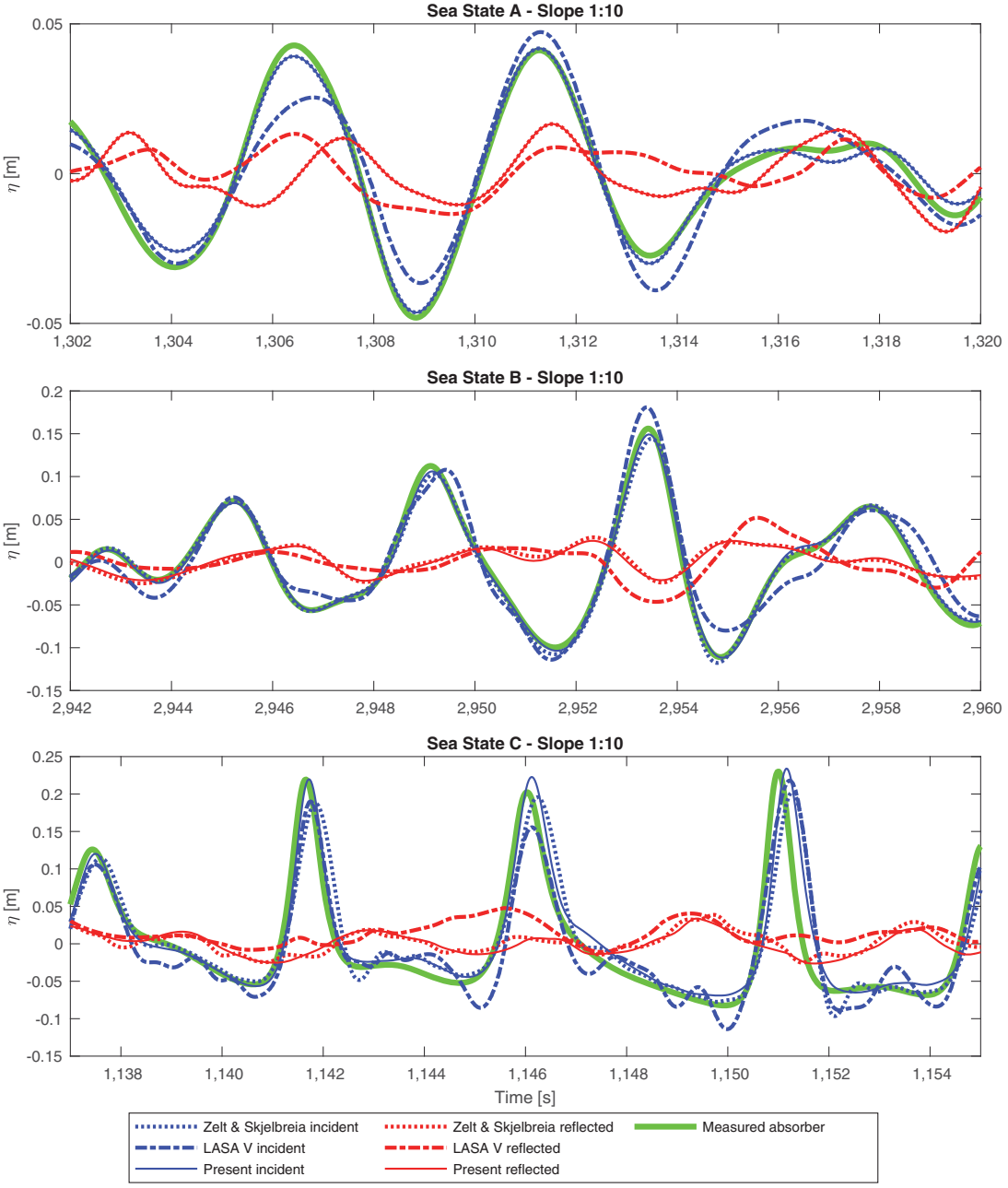

Fig. 11. Measured and predicted surface elevation time series at *wg7* for the slope 1:10 for the instances in which the highest waves occur.

is, for example, demonstrated by Sea State C, in which large undulations are predicted in the incident wave trough. These undulations are not present in the incident wave taken from the absorber case.

Overall, the numerical tests show that for linear and mildly nonlinear waves the linear separation methods provide acceptable results, but for highly nonlinear waves only the present method

Table 3. Wave heights in meters and periods in seconds for *wg*7

Sea state	Structure	Method	H_{m0}	$H_s = H_{1/3}$	$H_{2\%}$	$H_{1/50}$	$H_{\max}$	T_z
A	Absorber	Target	0.050	0.048	0.065	0.072	0.089	4.22
		Zelt and Skjelbreia	0.050	0.048	0.065	0.072	0.089	4.22
		LASA V	0.042	0.041	0.058	0.065	0.076	4.30
		Present method	0.050	0.048	0.065	0.072	0.089	4.22
	Slope	Zelt and Skjelbreia	0.048	0.046	0.062	0.069	0.089	4.13
		LASA V	0.045	0.043	0.059	0.068	0.088	4.44
		Present method	0.048	0.046	0.062	0.069	0.088	4.13
	Wall	Zelt and Skjelbreia	0.049	0.048	0.065	0.072	0.093	4.27
		LASA V	0.055	0.054	0.082	0.095	0.116	4.37
		Present method	0.049	0.048	0.065	0.071	0.093	4.27
B	Absorber	Target	0.159	0.153	0.212	0.228	0.256	3.51
		Zelt and Skjelbreia	0.159	0.153	0.211	0.226	0.250	3.52
		LASA V	0.156	0.152	0.207	0.221	0.260	3.50
		Present method	0.159	0.154	0.213	0.228	0.254	3.51
	Slope	Zelt and Skjelbreia	0.159	0.153	0.209	0.226	0.252	3.52
		LASA V	0.159	0.156	0.208	0.231	0.283	3.52
		Present method	0.159	0.154	0.212	0.229	0.253	3.51
	Wall	Zelt and Skjelbreia	0.158	0.153	0.212	0.227	0.264	3.54
		LASA V	0.159	0.156	0.208	0.231	0.283	3.52
		Present method	0.159	0.154	0.212	0.231	0.276	3.54
C	Absorber	Target	0.182	0.191	0.255	0.273	0.312	3.55
		Zelt and Skjelbreia	0.180	0.179	0.234	0.243	0.275	3.54
		LASA V	0.181	0.187	0.251	0.267	0.306	3.50
		Present method	0.184	0.191	0.254	0.272	0.311	3.54
	Slope	Zelt and Skjelbreia	0.180	0.181	0.240	0.250	0.280	3.58
		LASA V	0.184	0.190	0.260	0.279	0.332	3.48
		Present method	0.185	0.193	0.258	0.276	0.303	3.58
	Wall	Zelt and Skjelbreia	0.177	0.177	0.229	0.244	0.292	3.54
		LASA V	0.182	0.188	0.262	0.287	0.341	3.46
		Present method	0.184	0.193	0.262	0.285	0.317	3.54

Note: Time domain parameters are based on zero-down crossing analysis.

provides acceptable results. The LASA V method was not found to be an improvement over linear reflection separation methods for any of the tested sea states. Concerning the computational costs compared with Zelt and Skjelbreia (1992), the present method is approximately two times slower (computational time less than 1 min for one test), whereas the LASA V method is 1,500 times slower (17 h for the same test).

Sensitivity to Noise

The three separation methods have been tested for sensitivity to wave gauge noise. Highly nonlinear waves and the absorber are used in the analysis. The noise on the seven wave gauges is assumed uncorrelated Gaussian white generated in accordance with the central limit theorem as

$$\text{noise} = \left(-\frac{N}{2} + \sum_{i=1}^{N} x_i\right)\sqrt{\frac{12}{N}} \tag{16}$$

$$\eta_{\text{noise}}(t) = \text{noise}(t)\sigma$$

where x_i = random number between 0 and 1 (uniformly distributed); N = sufficiently large integer value; and σ = amount of noise (2.5% of the spectral wave height H_{m0} used).

Fig. 12 shows the results of the predicted incident wave trains with and without noise and shows the measured signal with noise. The present method proves to be very robust to noise because the predictions with and without noise are almost identical, except for small high-frequency undulations that may easily be removed by an analogue band-pass filter. The Zelt and Skjelbreia (1992) and LASA V methods are quite sensitive to noise because the predicted incident waves with and without noise deviate significantly from each other. The present method is much less sensitive to noise, which is expected to be caused by the more complete mathematical model; thus, the added noise is more likely detected as belonging to the noise term Ω. Note that this conclusion only holds if the system is overdetermined (more than four gauges are needed for the area in which both bound and free components exist); otherwise, the noise term will always be predicted to zero. Therefore, in the following section, sensitivity to noise is also studied as a function of the number of wave gauges. Note also that Lykke Andersen et al. (2017) studied the sensitivity to noise for a regular wave. For the regular waves, only specific frequencies (primary and superharmonics) are analyzed, whereas for the irregular waves many frequencies are analyzed. Therefore, sensitivity to noise is much less for regular waves compared with irregular waves.

Wave Gauge Array Design

Concerning array design, both the number of gauges and the individual gauge positions are important. For the gauge positions, it is

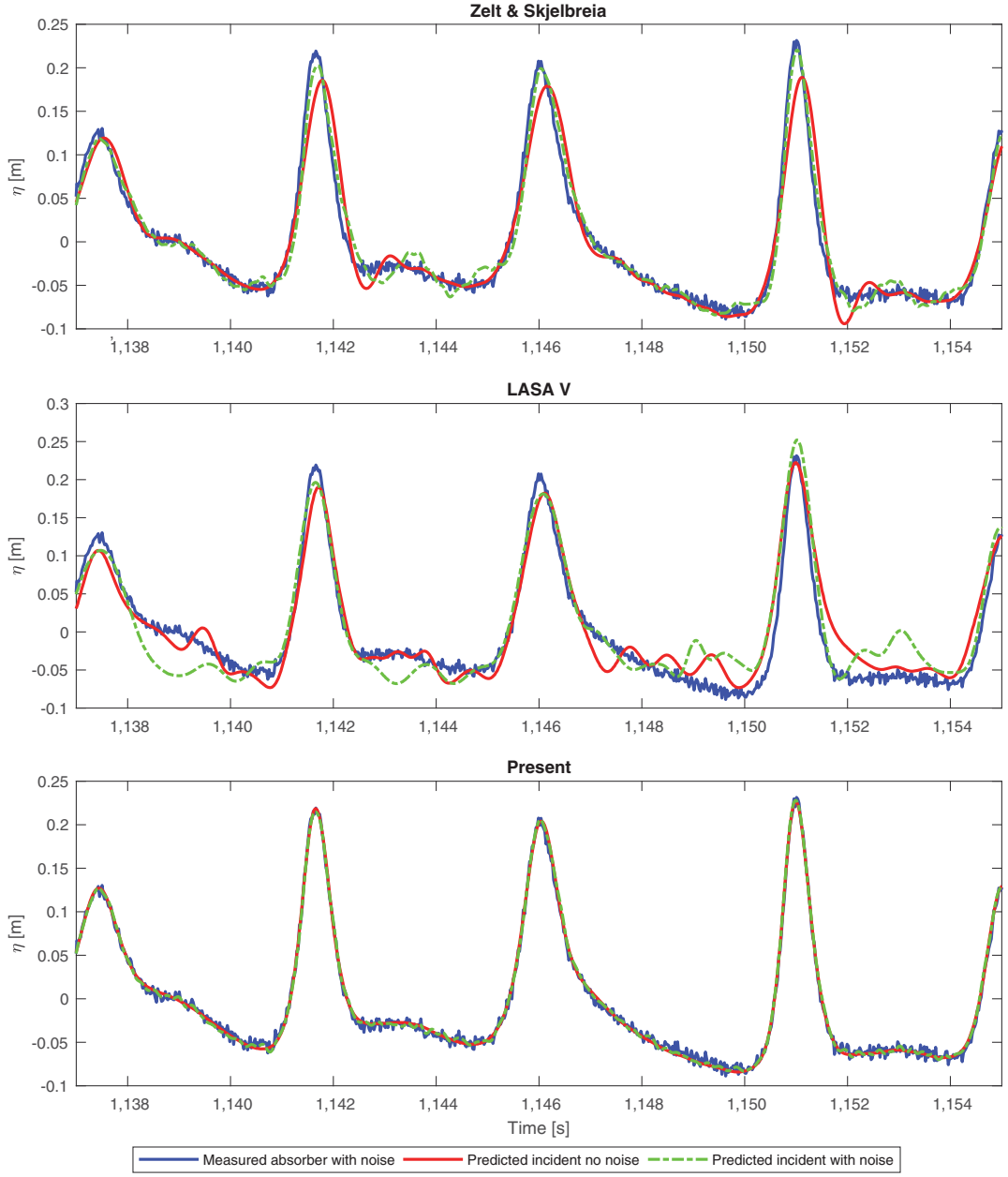

Fig. 12. Measured and predicted surface elevation time series at *wg*7 for Sea State C and absorber with and without noise.

important to note that the wavelength of a bound subharmonic or superharmonic is always between the wavelength of the primary components to which it is bound and a free component at the same frequency. Consequently, if the array is designed to separate free waves in the range in which energy is present in the spectrum, then it can also separate the bound components. For this reason, the recommendations on gauge distances presented for the linear methods are also applicable to the present method. However, it should be taken into account that when waves are nonlinear they include both lower and higher frequencies than a linear spectrum.

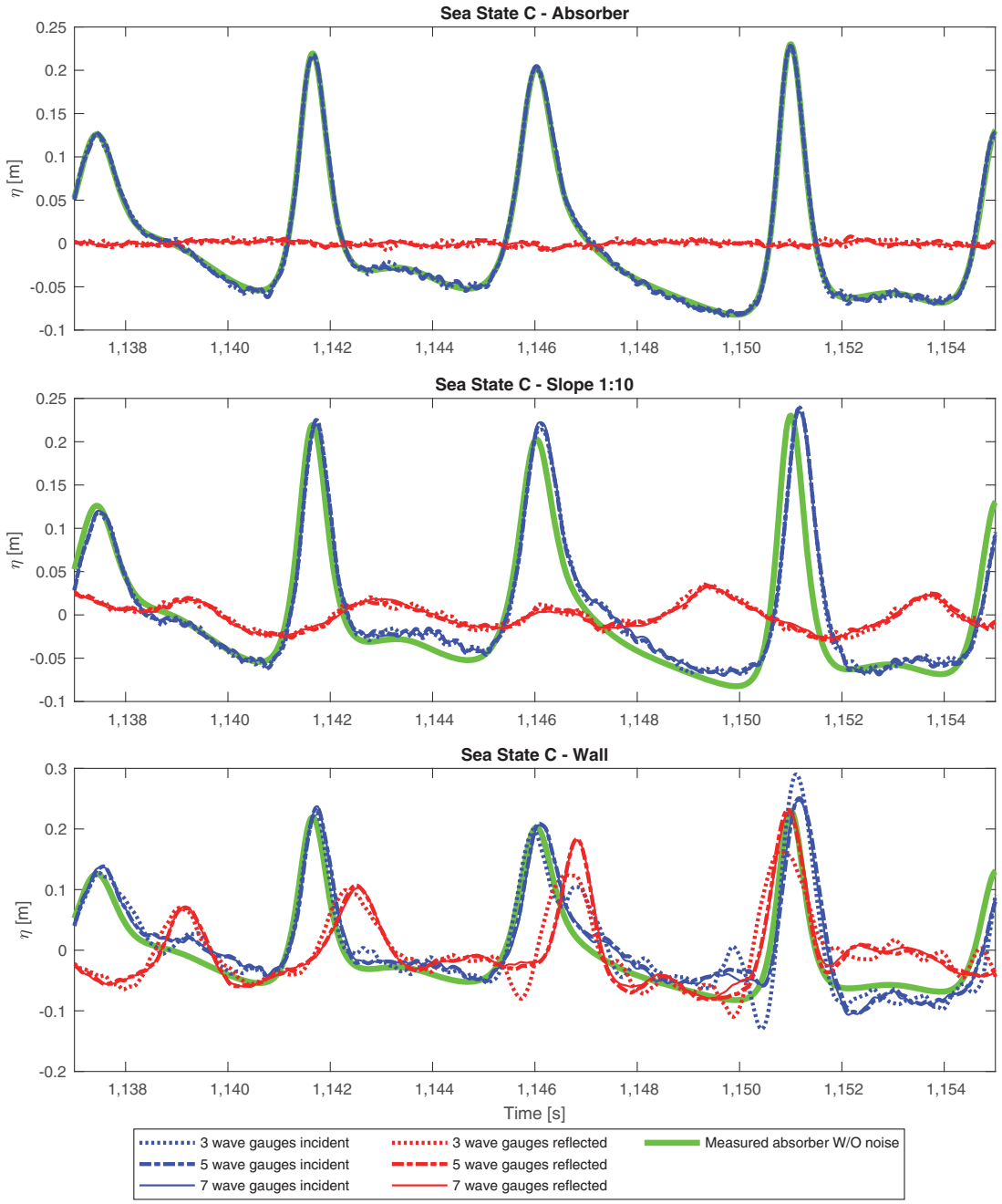

Fig. 13. Measured and predicted surface elevation time series at *wg*7 for Sea State C with use of different number of wave gauges. Signals contains noise ($\mu = 2.5\%$).

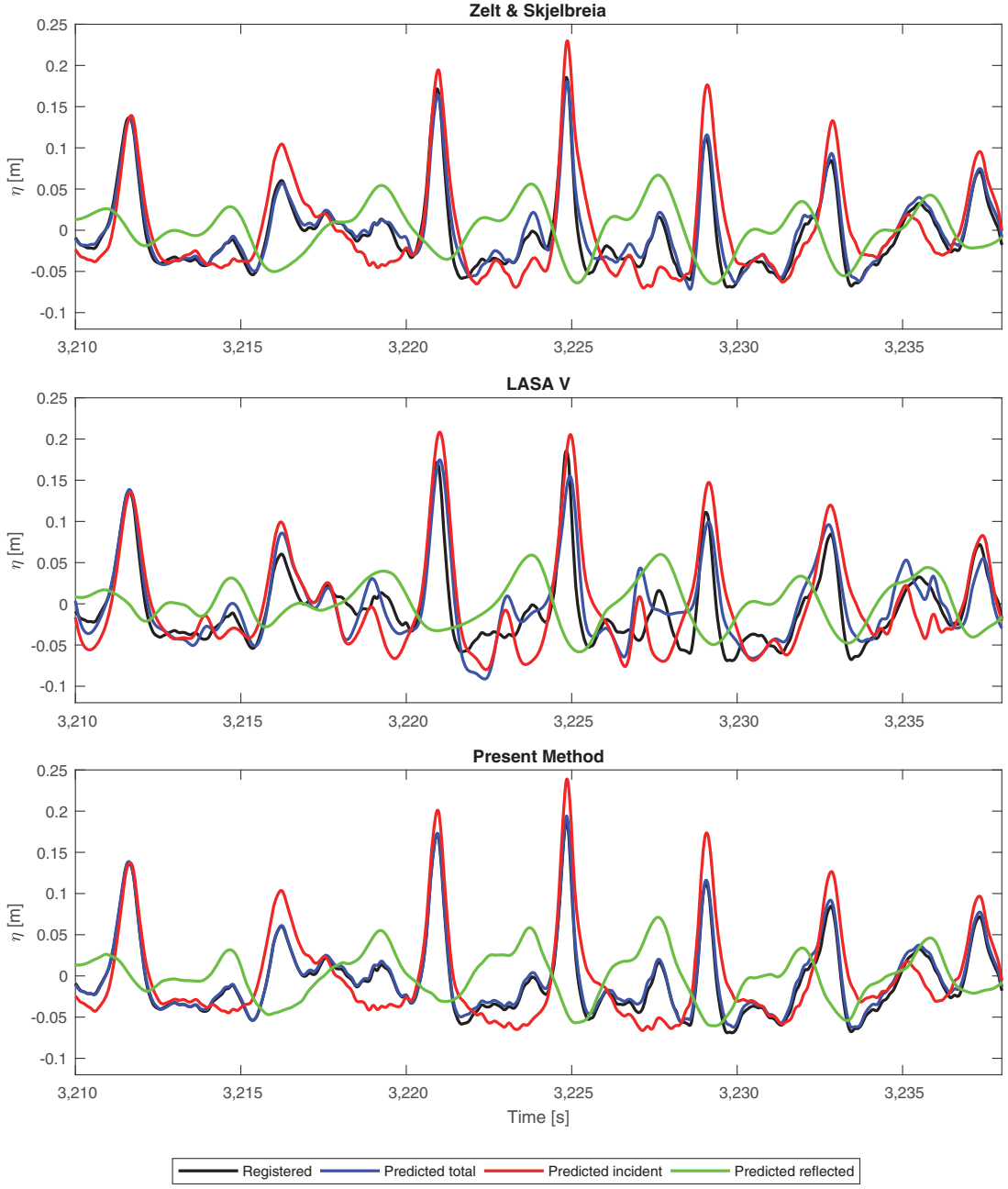

Fig. 14. Registered and predicted surface elevation time series at *wg*7 for the laboratory data for the instances in which the highest waves occur.

This is important when deciding the length of the array, which should be a minimum of 5% of the length of the longest wave component (subharmonic). Moreover, colocated singularities should be avoided, which means that distances between two gauges should not be an integer multiplied by the distance between any other pair.

The new method requires a minimum of four gauges to separate into incident/reflected and bound/free components, but a larger number of gauges is recommended to have an overdetermined system, which is less sensitive to errors (for example, noise). The sensitivity to the number of wave gauges has been tested by using three wave gauges (*wg*1, *wg*2, and *wg*7), five wave gauges (*wg*1, *wg*2, *wg*3, *wg*6, and *wg*7), and seven wave gauges for the highly nonlinear waves (Sea State C) for all three tested structures. For the array with three wave gauges, all reflected energy is assumed free. Because the influence of noise might be dependent on the number of wave gauges, the analyzed signals are those with noise added as presented in the previous section. The results are presented in Fig. 13 and show that, up to mildly reflective structures, three wave gauges give acceptable results, which is in agreement with the assumption that no bound reflected energy exists. However, the sensitivity to noise is a little higher with three gauges, whereas an array with five gauges is almost as robust to noise as seven gauges. Overall, the method is very robust to noise independent of the number of wave gauges, especially when compared with the other two methods. For highly reflective structures and highly nonlinear waves, a minimum of five wave gauges are needed for acceptable results because bound reflected components cannot be ignored.

Application to Laboratory Data

The separation methods are also tested on a laboratory test performed in a 25-m long wave flume at Aalborg University, Denmark. A piston wavemaker generated the waves by using the generation method by Zhang et al. (2007). Using the Zhang method makes it possible to accurately generate the highly nonlinear waves in shallow water. The surface elevation time series used as input for the Zhang method is obtained from a numerical Boussinesq model including a long 1:100 foreshore and using a JONSWAP spectrum with $\gamma = 3.3$ in deep water. Therefore, the long foreshore is not required in the laboratory test to reduce the generation of free waves. Consequently, the waves were measured on a short 1:100 foreshore with an array with seven gauges placed at 15.00, 15.50, 15.82, 16.10, 16.39, 16.55, and 17.00 m from the paddle. At the end of the flume a 1:2 impermeable rubble mound breakwater was present. During the test, active absorption was used [Lykke Andersen et al. (2016) method] to minimize rereflection from the wave paddle. The water depth in the middle of the wave gauge array was 0.53 m. The sea state tested is close to Sea State C used for the numerical study, but it is slightly more nonlinear (Fig. 4).

Fig. 14 shows the results of the three separation methods. The present method shows almost perfect agreement between the registered signal and the predicted total. The Zelt and Skjelbreia (1992) method also shows almost full agreement of the measured signal and the predicted total, but compared with the present method there are more significant undulations in the predicted incident wave trough because bound waves are assumed free. This supports the findings from the numerical tests in which the wave shape for nonlinear waves was only correctly predicted by the present method.

LASA V shows significant deviations when comparing the measured signal and the predicted total. Furthermore, LASA V leads to the largest undulations in the predicted incident wave trough, indicating that this method is not an improvement compared with the linear Zelt and Skjelbreia (1992) method in this case.

The overall conclusion from the laboratory data is that the findings from the numerical and physical tests are similar. This proves the high relevance of the separation of the subharmonics and superharmonics into bound and free components used in the present method.

Discussion

The present nonlinear wave separation method for long-crested irregular waves has proven to be a reliable method for the tested sea states. The mathematical model for the present separation method does not include shoaling, but the inclusion of the Baldock and Simmonds (1999) method is straightforward to account for linear shoaling. However, analysis of shoaling of nonlinear waves is very complicated because it involves the transformation of energy to the bound components. Thus, the application of the present method to nonlinear waves on steep foreshores is questionable, especially when waves are predicted far from the center of the wave gauge array. Moreover, the method assumes stationarity and does not include breaking waves, for example. Therefore, further tests are needed to quantify prediction errors for such waves. Broken waves on a very shallow foreshore are characterized by a wide spectrum without a distinct peak. For such waves the present method cannot identify the subharmonic and superharmonic segments correctly. For the same reason, the separation method is not able to separate incident and reflected waves for double-peaked primary spectra (swell + wind).

Conclusion

Lykke Andersen et al. (2017) presented a method for the separation of nonlinear regular waves into incident and reflected waves. The present paper extends this method to irregular waves. The extension is based on dividing the wave spectrum into a subharmonic part, a primary part, and a superharmonic part. To include amplitude dispersion for irregular waves, a simplified β factor is introduced and calibrated.

Nine numerical irregular wave tests with three different structures and three different wave nonlinearities were used to evaluate the present method as well as existing methods (Zelt and Skjelbreia 1992 and LASA V by Figueres et al. 2003). Zelt and Skjelbreia (1992) gave accurate results for the linear waves and reasonable results for the mildly nonlinear waves. On the other hand, for the highly nonlinear waves, that method gave an underprediction of the extreme waves by approximately 12%. The LASA V method does not provide reliable surface profiles for any of the present tests and also gives large errors on the wave heights for the linear waves. However, for nonlinear waves without reflection, the LASA V method provides accurate overall wave parameters.

The present separation method proved to be accurate for all tests. Even for the highly nonlinear waves, the error on the height of extreme waves is typically less than 1%. This is a large improvement compared with existing methods, and it shows the high relevance of the new method when analyzing nonlinear waves. The present method might not give reliable results for steep seabeds because shoaling is not included, and linear shoaling would not be accurate. The existing methods in the present paper are not expected to give reliable results in case of nonlinear waves on a steep foreshore. Furthermore, the present method is not expected to give accurate results for double-peaked spectra (combined wind and swell) or broken waves without a distinct peak.

Moreover, the present method was found less sensitive to uncorrelated white noise compared with the other two methods. This is expected to be caused by a more correct mathematical model. Finally, the methods have been applied to laboratory data, which show similar results based on the numerical data.

Appendix. Elements of *A*, *B*, *D*, and *E*

Elements of $\boldsymbol{A}$

$$A_{11} = \sum_{m=1}^{M} \left[C_I^{(1)} \right]^2 \tag{17}$$

$$A_{12} = A_{21} = \sum_{m=1}^{M} \left[C_I^{(1)} C_R^{(1)} \right] \tag{18}$$

$$A_{22} = \sum_{m=1}^{M} \left[C_R^{(1)} \right]^2 \tag{19}$$

where M is the number of gauges.

Elements of $\boldsymbol{B}$

$$B_1 = \sum_{m=1}^{M} \left[\widehat{\eta}^{(1)}(x_m) C_I^{(1)} \right] \tag{20}$$

$$B_2 = \sum_{m=1}^{M} \left[\widehat{\eta}^{(1)}(x_m) C_R^{(1)} \right] \tag{21}$$

Elements of $\boldsymbol{D}$

$$D_{11} = \sum_{m=1}^{M} \left[C_{I,B}^{(n)} \right]^2 \tag{22}$$

$$D_{12} = D_{21} = \sum_{m=1}^{M} \left[C_{I,B}^{(n)} C_{R,B}^{(n)} \right] \tag{23}$$

$$D_{13} = D_{31} = \sum_{m=1}^{M} \left[C_{I,F}^{(n)} C_{I,B}^{(n)} \right] \tag{24}$$

$$D_{14} = D_{41} = \sum_{m=1}^{M} \left[C_{R,F}^{(n)} C_{I,B}^{(n)} \right] \tag{25}$$

$$D_{22} = \sum_{m=1}^{M} \left[C_{R,B}^{(n)} \right]^2 \tag{26}$$

$$D_{23} = D_{32} = \sum_{m=1}^{M} \left[C_{I,F}^{(n)} C_{R,B}^{(n)} \right] \tag{27}$$

$$D_{24} = D_{42} = \sum_{m=1}^{M} \left[C_{R,F}^{(n)} C_{R,B}^{(n)} \right] \tag{28}$$

$$D_{33} = \sum_{m=1}^{M} \left[C_{I,F}^{(n)} \right]^2 \tag{29}$$

$$D_{34} = D_{43} = \sum_{m=1}^{M} \left[C_{R,F}^{(n)} C_{I,F}^{(n)} \right] \tag{30}$$

$$D_{44} = \sum_{m=1}^{M} \left[C_{R,F}^{(n)} \right]^2 \tag{31}$$

Elements of $\boldsymbol{E}$

$$E_1 = \sum_{m=1}^{M} \left[\widehat{\eta}^{(n)}(x_m) C_{I,B}^{(n)} \right] \tag{32}$$

$$E_2 = \sum_{m=1}^{M} \left[\widehat{\eta}^{(n)}(x_m) C_{R,B}^{(n)} \right] \tag{33}$$

$$E_3 = \sum_{m=1}^{M} \left[\widehat{\eta}^{(n)}(x_m) C_{I,F}^{(n)} \right] \tag{34}$$

$$E_4 = \sum_{m=1}^{M} \left[\widehat{\eta}^{(n)}(x_m) C_{R,F}^{(n)} \right] \tag{35}$$

Acknowledgments

Special thanks to Professor Josep R. Medina from the Laboratory of Ports and Coasts of the Universidad Politécnica de Valencia for providing the LASA V software.

References

Baldock, T. E., and D. J. Simmonds. 1999. "Separation of incident and reflected waves over sloping bathymetry." *Coastal Eng.* 38 (3): 167–176. https://doi.org/10.1016/S0378-3839(99)00046-0.

Beji, S., and J. A. Battjes. 1993. "Experimental investigation of wave propagation over a bar." *Coastal Eng.* 19 (1–2): 151–162. https://doi.org/10.1016/0378-3839(93)90022-Z.

Fenton, J., and M. Rienecker. 1980. "Accurate numerical solutions for nonlinear waves." In Chap. 2 of *Coastal Engineering, 1980*, edited by B. L. Edge, 50–69. Reston, VA: ASCE. https://doi.org/10.1061/9780872622647.002.

Figueres, M., J. M. Garrido, and J. R. Medina. 2003. "Cristalización simulada para el análisis de oleaje incidente y reflejado con un modelo de onda Stokes-V." [In Spanish.] *VII Jornadas españolas de Costas y Puertos*. CD-ROM.

Figueres, M., and J. R. Medina. 2004. "Estimating incident and reflected waves using a fully nonlinear wave model." In Vol. 4 of *Coastal Engineering 2004*, edited by J. M. Smith, 594–603. Singapore: World Scientific.

Goda, Y., and Y. Suzuki. 1976. "Estimation of incident and reflected waves in random wave experiments." Chap. 48 in *Coastal engineering, 1796*, 828–845. Reston, VA: ASCE. https://doi.org/10.1061/9780872620834.048.

Hsiao, S., P. Lynett, H. Hwung, and P. Liu. 2005. "Numerical simulations of nonlinear short waves using a multilayer model." *J. Eng. Mech.* 131 (3): 231–243. https://doi.org/10.1061/(ASCE)0733-9399(2005)131:3(231).

Klopman, G., and J. van der Meer. 1999. "Random wave measurements in front of reflective structures." *J. Waterway, Port, Coastal, Ocean Eng.* 125 (1): 39–45. https://doi.org/10.1061/(ASCE)0733-950X(1999)125:1(39).

Le Méhauté, B. 1969. In Vol. 2 of *An introduction to hydrodynamics and water waves*. Boulder, CO: Environmental Science Service Administration.

Lin, C.-Y., and C.-J. Huang. 2004. "Decomposition of incident and reflected higher harmonic waves using four wave gauges." *Coastal Eng.* 51 (5–6): 395–406. https://doi.org/10.1016/j.coastaleng.2004.04.004.

Lykke Andersen, T., M. Clavero, P. Frigaard, M. Losada, and J. I. Puyol. 2016. "A new active absorption system and its performance to linear and non-linear waves." *Coastal Eng.* 114 (Aug): 47–60. https://doi.org/10.1016/j.coastaleng.2016.04.010.

Lykke Andersen, T., M. R. Eldrup, and P. Frigaard. 2017. "Estimation of incident and reflected components in highly nonlinear regular waves." *Coastal Eng.* 119 (Jan): 51–64. https://doi.org/10.1016/j.coastaleng.2016.08.013.

Lynett, P., and P. L.-F. Liu. 2004. "A two-layer approach to wave modelling." *Proc. R. Soc. Lond., Ser. A* 460 (2049): 2637–2669. https://doi.org/10.1098/rspa.2004.1305.

Mansard, E., and E. Funke. 1980. "The measurement of incident and reflected spectra using a least squares method." Chap. 8 of *Coastal engineering, 1980*, edited by B. L. Edge, 154–172. Reston, VA: ASCE. https://doi.org/10.1061/9780872622647.008.

Medina, J. 2001. "Estimation of incident and reflected waves using simulated annealing." *J. Waterway, Port, Coastal, Ocean Eng.* 127 (4): 213–221. https://doi.org/10.1061/(ASCE)0733-950X(2001)127:4(213).

Qi, Y., G. Wu, Y. Liu, M. Kim, and D. K. P. Yue. 2018a. "Nonlinear phase-resolved reconstruction of irregular water waves." *J. Fluid Mech.* 838: 544–572. https://doi.org/10.1017/jfm.2017.904.

Qi, Y., G. Wu, Y. Liu, and D. K. P. Yue. 2018b. "Predictable zone for phase-resolved reconstruction and forecast of irregular waves." *Wave Motion* 77 (Mar): 195–213. https://doi.org/10.1016/j.wavemoti.2017.12.001.

Schäffer, H. A., and C. M. Steenberg. 2003. "Second-order wavemaker theory for multidirectional waves." *Ocean Eng.* 30 (10): 1203–1231. https://doi.org/10.1016/S0029-8018(02)00100-2.

Teixeira, P. R. F., L. Pinheiro, and C. M. J. Fortes. 2010. "Comparison of three nonlinear models to analyze wave propagation over submerged trapezoidal breakwaters." In *Proc., 5th European Conf. on Computational Fluid Dynamics*. Lisbon, Portugal: ECCOMAS CFD 2010.

WaveLab 3. 2017. "WaveLab." Dept. of Civil Engineering, Aalborg Univ. Accessed September 4, 2017. http://www.hydrosoft.civil.aau.dk/wavelab/.

Zelt, J. A., and J. E. Skjelbreia. 1992. "Estimating incident and reflected wave fields using an arbitrary number of wave gauges." Chap. 58 in *Coastal Engineering*, edited by B. L. Edge, 777–789. Reston, VA: ASCE. https://doi.org/10.1061/9780872629332.058.

Zhang, H., H. A. Schäffer, and K. P. Jakobsen. 2007. "Deterministic combination of numerical and physical coastal wave models." *Coastal Eng.* 54 (2): 171–186. https://doi.org/10.1016/j.coastaleng.2006.08.009.

Paper D

Stability of Rubble Mound Breakwaters – A Study of the Notional Permeability Factor

Mads Røge Eldrup
Thomas Lykke Andersen
Hans Falk Burcharth

The paper has been submitted to
Water, ISSN: 2073-4441.

water

MDPI

Type of the Paper (Article, Review, Communication, etc.)

Stability of Rubble Mound Breakwaters – A Study of the Notional Permeability Factor

Mads Røge Eldrup *, Thomas Lykke Andersen and Hans Falk Burcharth

Department of Civil Engineering, Aalborg University, 9220 Aalborg, Denmark; tla@civil.aau.dk (TLA); hansburcharth@gmail.com (HFB)

* Correspondence: mre@civil.aau.dk

Received: date; Accepted: date; Published: date

Abstract: The Van der Meer [1] formulae for quarry rock armour stability is commonly used in breakwater design. The formulae describes the stability as a function of the wave characteristics, number of waves, front slope angle and rock material properties. The latter includes a so called notional permeability characterising the permeability of the structure. Based on armour stability model tests with three armour layer compositions, Van der Meer determined by fitting to his formula three values of the notional permeability. Based on numerical model results he added for a typical layer composition one more value. The present paper provides notional permeability factors for seven layer compositions of which two correspond to the compositions tested by Van der Meer. The results of these two layer compositions are within the scatter of the results by Van der Meer. To help determination of the notional permeability for non-tested layer compositions, a simple empirical formula is presented.

Keywords: rock armour stability; breakwater; damage; notional permeability factor

1. Introduction

The rock armour stability of rubble mound breakwaters has been estimated with the formulae by Van der Meer [1] in the last decades. The formulae are still used worldwide even though the study was performed approximately 30 years ago. An alternative to the stability formulae by Van der Meer [1] could be a numerical model. However, computational fluid models like Volume Of Fluid (VOF) and Smoothed-Particle Hydrodynamics (SPH) are still computationally demanding and need to be coupled to a solid state model like a Discrete Element Method (DEM). Furthermore, the numerical models rely on parameters found in physical model tests, as for example, the porosity parameters used to describe the water flow inside the rubble mound breakwater. Thus numerical models cannot be used as standalone but need input parameters based on physical model tests. Sarfaraz and Pak [2], used a coupled SPH-DEM model to test the stability of cube armoured rubble mound breakwaters. They compared the numerical results to empirical formulae and the numerical results were not far from the empirical estimations. However, as the numerical results were only compared to empirical formulae the study do not show which method that is most reliable. Numerical models can though be a supplement to empirical formulae used to solve complex problems but, in most situations, empirical formulae are still highly relevant as the one by Van der Meer [1].

Van der Meer [1] performed a large number of model tests with rubble mound breakwaters exposed to irregular mainly non-breaking Rayleigh distributed waves corresponding to $H_{1/3}/h \leq 0.2$ in which $H_{1/3}$ is the significant incident wave height and h the water depth. His tests included cross-sections with five different front slopes in the range of $\cot(\alpha) = 1.5 - 6$, and three different layer compositions. The three compositions were: an armour layer on a thin filter layer on an impermeable core, an armour layer on a coarse permeable core, and a homogeneous structure, see layer compositions *A*, *H* and *M* in Figure 1. Van der Meer used the work by Thompson and Shuttler [3] as

a starting point and included their test results in his research and tested the layer composition with impermeable core also tested by Thompson and Shuttler.

By fitting to his 1988 rock armour stability formula, Van der Meer found the notational permeability values P = 0.1, 0.5 and 0.6 for the tested three layer compositions. The notional permeability parameter has no physical meaning but was introduced to ensure that the effect of permeability was taken into account. For the very typical layer composition consisting of a permeable core, underlayer and armour layer, Van der Meer [1] estimated the value P = 0.4 on the basis of above given P-values and the numerical HADEER model by Hölscher and Barends [4] which models the wave introduced flow in the porous structure of rubble mounds.

Kik [5] tested a layer composition with an impermeable geo-textile placed underneath a relatively thick second underlayer, cf. composition *F* in Figure 1, and found P = 0.37, but recommend a design value of P = 0.35 due to limited tests. Kluwen [6] tested the same structure under similar wave conditions but extended the number of data. Based on all the tests, Kluwen fitted a notional permeability of P = 0.38. Kluwen [6] also tested layer composition *L* in Figure 1 and determined P = 0.46. This layer composition is similar to the layer composition for which Van der Meer [1] estimated P = 0.4, but the composition by Kluwen [6] had a thicker armour layer, a thinner underlayer and coarser material in both underlayer and core.

Recently, Van der Meer et al. [7] studied the influence of grading and thickness of the underlayer/filter layer for a structure with an impermeable core. They observed that an underlayer with a thickness of $0.5D_{n50A}$ of the armour stone size gave complete failure, while a thickness of $1.75D_{n50A}$ reduced the damage to the armour layer by 50 % for a specific test. For the layer composition with a thick underlayer, they estimated P = 0.15-0.2, see layer composition *C* in Figure 1. Furthermore, they observed that very wide-graded underlayer material (including fine material) gave as expected more damage than narrow graded underlayer material with the same D_{n50}. Only two wave steepnesses were tested for each composition, for which reason no final recommendations on P were given.

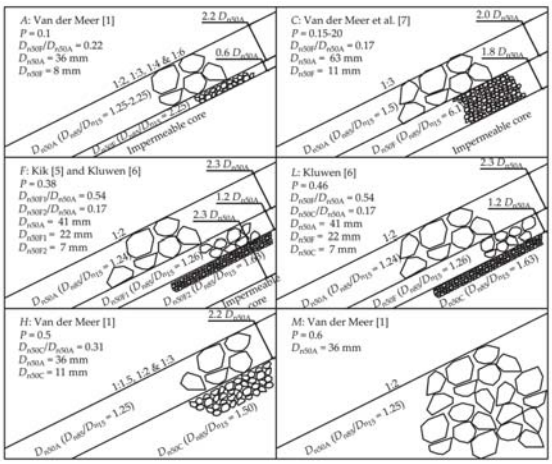

Figure 1. Fitted notional permeability factor of different layer compositions, for which *A*, *H* and *M* are given by Van der Meer [1], *F* is given by Kik [5] and Kluwen [6], *L* is given by Kluwen [6] and *C* is given by Van der Meer et al. [7]. D_{n50A} is the nominal stone size of the armour, D_{n50F} is the nominal stone size of the filter/underlayer material, and D_{n50C} is the nominal stone size of the core material.

The influence of the notional permeability value on armour stability is demonstrated in Table 1. Based on the notional permeability factors given in Figure 1, the related required rock armour masses are given as calculated from the Van der Meer [1] formula for the conditions: significant wave height $H_{1/3}$ = 4 m, front slope cot(α) = 2, damage S_d = 2, rock mass density of 2,650 kg/m^3, water mass density of 1,025 kg/m^3 and number of waves N = 1,000 waves. Three different wave steepnesses are used for

80 the comparison. As an example, Table 1 shows that changing the notional permeability from $P = 0.46$
81 to $P = 0.38$ demands an increase in armour unit mass of approximately 10 – 35%, depending on ξ_{0m}.
82 Changing the notional permeability from $P = 0.38$ to $P = 0.17$ demands an increase in armour unit
83 mass of approximately 50 – 100%. This large sensitivity of the armour mass to the notional
84 permeability motivates the determination of more notional permeability values.
85
86 **Table 1.** Estimated rock armour weight in tonnes with the use of the Van der Meer [1] formulae.

P	s_{0m} [-]	T_m [s]	ξ_{0m} [-]	s_{0m} [-]	T_m [s]	ξ_{0m} [-]	s_{0m} [-]	T_m [s]	ξ_{0m} [-]
	0.05	7.2	2.2	0.02	11.3	3.5	0.01	16.0	5.0
0.10	10.9			21.6			19.8		
0.17	8.1			16.2			17.4		
0.38	5.3			10.5			8.6		
0.46	4.8			9.5			6.3		
0.50	4.6			9.0			5.4		

87
88 A method to estimate the notional permeability was proposed by Jumelet [8]. He developed a
89 numerical volume exchange model which couples the external processes with the internal processes.
90 The external process is described by the wave run-up, and the internal process by the Forchheimer
91 equation for flow through porous media. The model was calibrated with the tests by Van der Meer
92 [1]. The model determines the notional permeability factor based on the breaker parameter ξ, the
93 ratio between the armour and core material size, and the relation between the wave run-up for a
94 rubble mound with an impermeable core and a rubble mound with a permeable core. The wave run-
95 up at the armour surface is for a permeable core dependent on the water infiltration into the core.
96 The model assumes that the surface roughness reduces the wave run-up on the armour layer with a
97 roughness factor of $\gamma_f = 0.75$ compared to a smooth slope while the run-up at the core was considered
98 to be $\gamma_{Ru} = 0.5$ of the run-up at the surface.
99 Van Broekhoven [9] conducted a range of experimental model test data to further investigate
100 these assumptions by Jumelet. He tested layer compositions with permeable and impermeable cores
101 and placed the armour material directly on the core material surface. He found that the wave run-up
102 at the armour surface was not influenced by the permeability of the core, but a clear influence from
103 the permeability was observed for the wave run-up at the core surface. Van Broekhoven [9]
104 concluded that the wave run-up below the armour layer is better correlated to the notional
105 permeability factor than the wave run-up at the armour surface. Based on that observation he
106 determined the notional permeability factor from the breaker parameter and the relation between the
107 wave run-up under the armour layer for a permeable core and an impermeable core. Van Broekhoven
108 [9] did not test layer compositions with filter layers.
109 Van der Neut [10] used the volume of fluid method, IH2VOF to estimate the notional
110 permeability on the layer compositions tested by Van der Meer [1]. He calibrated the numerical
111 model against small scale stability tests and found relations between the notional permeability and
112 four different dimensionless parameters determined from the numerical model. Thus the model is
113 not a simulation of the stability, but is a coupling between rock armour stability tests and some
114 dimensionless parameters describing the notional permeability factor.
115
116 The aim of the present paper is to get estimates of P for a wider range of layer compositions. For
117 this purpose, new rock armour stability model tests were carried out with seven different layer
118 compositions having different permeabilities.
119 Following a short presentation of the stability formulae by Van der Meer [1] the model setup
120 and the test procedure are presented. Wave generation, wave analysis, damage measuring
121 techniques, model setup and model materials are explained. The results of each tested layer
122 composition and the related fitted notional permeabilities are presented and discussed. Finally, a

discussion of possible methods to estimate the notional permeability is given and a simple empirical method for the estimation of the notional permeability is presented.

2. Stability Formulae by Van der Meer

The Van der Meer [1] formula for stability of rock armoured non-overtopped breakwaters is as follows, Equation (1);

Plunging waves ($\xi_{0m} < \xi_{0m,cr}$ or $\cot(\alpha) \geq 4$):

$$\frac{H_{1/3}}{\Delta D_{n50A}} = 6.2 P^{0.18} \left(\frac{S_d}{\sqrt{N}}\right)^{0.2} \xi_{0m}^{-0.5}$$

Surging waves ($\xi_{0m} \geq \xi_{0m,cr}$ and $\cot(\alpha) < 4$):

$$\frac{H_{1/3}}{\Delta D_{n50A}} = P^{-0.13} \left(\frac{S_d}{\sqrt{N}}\right)^{0.2} \sqrt{\cot(\alpha)}\ \xi_{0m}^{P} \quad (1)$$

Transition between plunging and surging formula:

$$\xi_{0m,cr} = \left(6.2\ P^{0.31} \sqrt{\tan(\alpha)}\right)^{\frac{1}{P+0.5}}$$

Here $\Delta = \varrho_{armour}/\varrho_{water} - 1$ is the reduced relative density of the armour stones. $D_{n50A} = \sqrt[3]{W_{50A}/\varrho_{armour}}$ is the nominal size of the armour stones based on the median armour stone mass W_{50A} as described in the Rock Manual [11]. P is the notional permeability. α is the angle of the seaward slope of the structure. $\xi_{0m} = \tan(\alpha)/s_{0m}^{0.5}$ is the surf similarity parameter where the wave steepness ($s_{0m} = H_{1/3}/L_{0m}$) is calculated based on the significant wave height ($H_{1/3}$) and the mean wave period (T_m) at the toe, using deep water wavelength formulae ($L_{0m} = T_m^2 g/2\pi$). The tested range of ξ_{0m} was 0.7 – 7. N is the number of waves (no more than 8,500 waves should be used). The waves in the present tests deviated to some extend from Rayleigh distributed waves in that $H_{2\%}/H_{1/3}$ = 1.19-1.47. For such cases, Van der Meer recommends $H_{1/3}$ in Equation (1) replaced by $H_{2\%}/1.4$.

3. Model Test Setup and Model Materials

The new tests were carried out in a wave flume at Aalborg University with dimensions of 25.0 x 1.5 x 1.0 m (l x w x h). For the present tests a 1:100 foreshore was used in order to make it possible to generate depth-limited waves without wave breaking at the wavemaker. Figure 2 illustrates the wave flume.

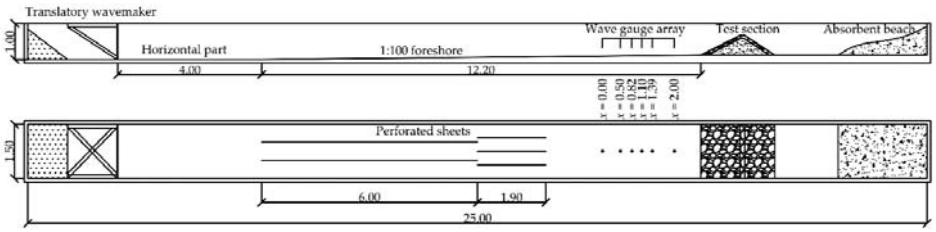

Figure 2. Experimental setup of the flume. Measurements are in meters.

In the present tests, five different rock materials were used for the tested layer compositions. Table 2 lists the properties of the materials and Figure 3 shows the tested armour rocks. Figure 4 shows the grading curves of the materials listed in Table 2.

151 **Table 2.** Test materials used for all layer compositions.

Rock class	Median weight, W_{50} [g]	Mass density, ϱ [kg/m³]	Nominal diameter, D_{n50} [m]	Gradation, $f_g = D_{n85}/D_{n15}$
I	221.0	2,620	0.044	1.30
II	32.2	2,618	0.023	1.40
III	9.0	2,768	0.015	1.36
IV	4.0	2,485	0.012	1.33
V	0.7	2,936	0.006	1.36

152

153 **Figure 3.** Class I rocks used in the armour layer for the present tests.

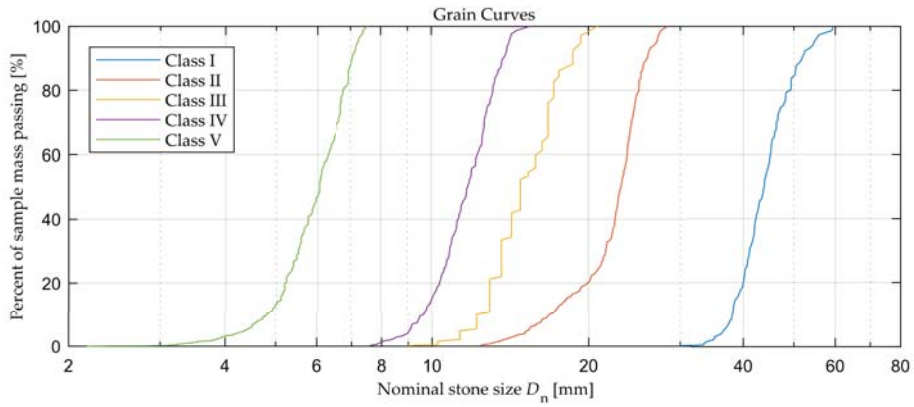

154 **Figure 4.** Grain curves of the rock material used in the present tests.

155 The layer composition with an impermeable core proved to be difficult to model. In the first
156 tests, the impermeable membrane was made of a plywood plate on which the underlayer were
157 directly placed. Unfortunately, sliding of the underlayer was observed when exposed to low
158 steepness waves. An attempt to increase the roughness between the underlayer and the impermeable
159 membrane was made by replacing the plywood plate by concrete slabs with an impermeable

membrane below. However, sliding still occurred. Finally, a solution with Class V rocks glued to the plywood plate was found acceptable, see Figure 5. This shows that the interface between the rock material and the core is important. If not modelled correctly this could lead to incorrect stability results. To ensure that the plate was stable and no displacement of the plate could occur, the plywood plate was placed on top of Class V rocks, see Figure 6.

Figure 5. Plywood plate with glued Class V rocks. Used to increase the roughness of the impermeable interface.

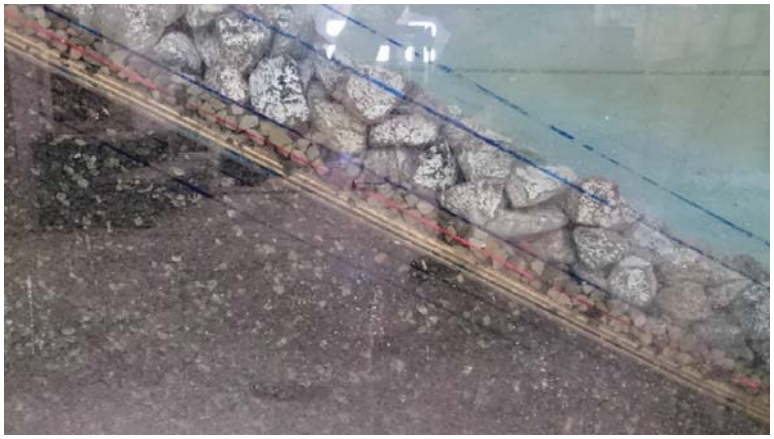

Figure 6. One of the layer compositions with the impermeable core. The figure shows the plywood plate placed on the Class V rocks.

Seven layer compositions as given in Figure 7 were tested. Two of them are similar (compositions *B* and *I*) to what Van der Meer [1] tested (compositions *A* and *H* in Figure 1). The first composition (*B*) consists of an armour layer, underlayer and an impermeable core. The composition has an armour thickness of $1.9D_{n50A}$ and an underlayer thickness of $0.5D_{n50A}$ with a rock size of $0.27D_{n50A}$. The second composition (*I*) consists of an armour layer and a permeable core. The composition has an armour thickness of $1.9D_{n50A}$ with a core rock size of $0.34D_{n50A}$. These are made in order to verify that the Van der Meer [1] formula is valid for the present model setup. The third composition, *G*, consists of an armour layer, an underlayer and a permeable core, see Figure 7. The armour layer has a thickness of $1.9D_{n50A}$, and the underlayer has a thickness of $1.4D_{n50A}$ with a rock size of $0.52D_{n50A}$. The core has a rock size of $0.14D_{n50A}$. This layer composition is similar to the non-tested ($P = 0.4$) layer composition by Van der Meer [1]. Furthermore, it is also similar to what Kluwen

[6] tested, but she had thicker armour layer and underlayer with a slightly coarser material in the core. The fourth layer composition, *D*, has an armour layer with two underlayers and an impermeable core, see Figure 7. The armour layer has a thickness of $1.9D_{n50A}$ and the first underlayer a thickness of $1D_{n50A}$ and a rock size of $0.52D_{n50A}$. The second underlayer has a thickness of $0.5D_{n50A}$ and has a rock size of $0.27D_{n50A}$. This composition will show how sensitive the notional permeability is to the underlayer thickness when an impermeable core is present and thus provide additional insight to the study by Van der Meer et al. [7], Kik [5] and Kluwen [6]. Finally, three additional compositions were tested, see layer compositions *E*, *J* and *K* in Figure 7. These layer compositions have an armour layer thickness of $2.9D_{n50A}$ compared to $1.9D_{n50A}$ which is used for layer compositions *B*, *I* and *G*. This will give additional information of the notional permeability and the influence of the layer thickness for the armour material.

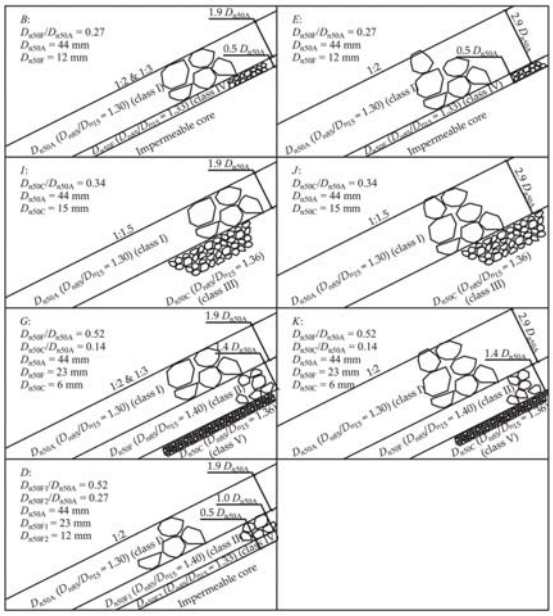

Figure 7. Layer compositions tested in the present study.

4. Wave Generation and Wave Analysis

The waves were generated by the software AwaSys 7 [12]. Second-order wave generation was used when it was valid according to the guidelines given by Eldrup and Lykke Andersen [13]. For cases where second-order theory according to Eldrup and Lykke Andersen [13] was not valid (shallow water cases), the wave generation method by Zhang et al. [14] was used. The method by Zhang et al. [14] uses a depth-averaged velocity as input, which for the present study was generated by MIKE 21 BW by propagating waves from deep to shallow water by a 1:100 foreshore. During all tests, active absorption of reflected waves was used based on wave gauges at the paddle face using the Lykke Andersen et al. [15] method which has been proven effective also for nonlinear irregular waves, cf. Lykke Andersen et al. [16]. JONSWAP spectra with peak enhancement factor $\gamma = 3.3$ were used in all tests.

To measure and separate incident and reflected waves, six resistant type wave gauges placed in front of the structure with a distance of 0.50, 0.82, 1.10, 1.39 and 2.00 m were used, cf. Fig 2. The distance from the breakwater to the structure was approximately $0.4L_P$ (peak wavelength) based on the recommendation given by Klopman and Van der Meer [17]. The water depth in the middle of the array was approximately 1.7 cm larger than at the toe, and due to that, depth-limited waves would be slightly smaller at the toe than at the wave gauge array. The difference in $H_{2\%}$ in the middle of the

array compared to the toe is estimated by linear shoaling and Battjes and Groendjik [18] to be maximum 1% which is judged acceptable compared to the scatter in the stability results. In case a steeper foreshore was used the difference would have been significantly larger. If the seabed was steeper it would thus be recommended to also measure the waves at the toe without the structure in place. The nonlinear method by Eldrup and Lykke Andersen [19] was used to separate the incident and reflected waves. This separation method includes both bound and free components which is essential for accurate determination of low exceedance wave parameters in nonlinear sea states. The method is included in the software package WaveLab 3 [20].

5. Damage Measurement

After each test, the reshaped profile was measured by a computer controlled non-contact laser profiler run by the software EPro [21], cf. Figure 8. The measurement grid had a spacing of 10 mm in length and 5 mm in width. The eroded area A_e and the damage $S_d = A_e/D_{n50A}^2$ given in the present paper are based on average values where 20 cm on each side of the flume was disregarded to minimise effects from the walls. Furthermore, only the part of the eroded area where a clear erosion is observed was evaluated, which means that small settlements on the upper part of the slope are not included in the eroded area. This is in agreement with the procedure used by Van der Meer [1].

Figure 8. Profiler used to measure the eroded area.

To get more exact measurements, the flume was emptied for water before laser profiling. Figure 9 shows an example of the averaged measured profile after two consecutive tests.

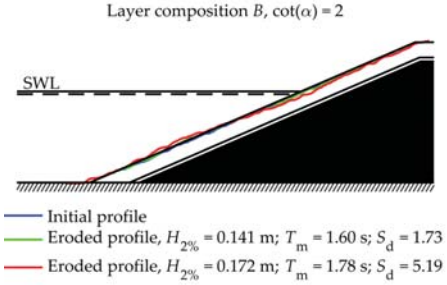

Figure 9. Example of averaged measured profiles showing the damage development in two consecutive tests.

6. Test Programme and Test Procedure

In total 149 model tests have been performed to non-breaking and slightly breaking wave attack on the seven different permeabilities. Table 3 shows the parameter ranges covered by the tests. To ensure that viscous scale effects are small the Reynolds number, given in Equation (2), should be larger than a critical value typically taken as $Re_{crit} = 3 \cdot 10^4$ (Dai and Kamel [22]).

$$Re = \frac{\sqrt{g\,H_{1/3}}D_{n50A}}{\nu} > Re_{crit} \tag{2}$$

where ν is the kinematic viscosity, D_{n50A} the nominal armour stone size and $\sqrt{g\,H_{1/3}}$ is the characteristic velocity. This is fulfilled for all layer compositions, cf. Table 3.

In each test series, the wave height was increased in steps, while the wave steepness remained constant. Accumulated damage was measured after each test in the series. For some of the test series, the initial sea state corresponded to a small wave height, giving only minor damage. For other test series the initial wave height gave significant damage. Test series were terminated when the underlayer was visible and as such exposed and, after that, the structure was rebuilt for a new test series. The water depth at the toe was 0.5 m in all tests. In each test, 1,000 waves were used. Van der Meer [1] assumed all structures to be non-overtopped when the dimensionless freeboard ($A_c/H_{1/3}$) > 1-2, which is valid for all the present tests.

The present test procedure was not identical to that of Van der Meer [1]. He did not measure accumulated damage, but instead the damage after 1,000 waves and 3,000 waves was measured. Afterwards, the breakwater was rebuilt, and a new sea state was tested. His wave series had a constant wave period with different wave heights. Based on these wave series, he fitted a damage curve for a constant wave period from which he extracted the relation between the wave heights and the damage values in the interval of S_d = 2-17. Thus his stability formulae were established on fitting to the damage curves. The present tests were made with 1-5 wave heights for each wave steepness. Damage curves for each of the present wave series were fitted in the present work. However, because most of the data correspond to accumulated damage, a conversion to non-accumulated damage by use of Equation (3) was made in order to comply with the basis of the Van der Meer formulae. The conversion is based on the relations found by Van der Meer [1] between damage, wave height and number of waves. The remaining parameters in the Van der Meer formulae are kept constant in the test series and are thus included in A. A is the slope of the continuous line seen in Figure 10 which describes the relation between the damage, the number of waves and the wave height. For the accumulated test series ($i > 1$) an extra number of waves $N_{extra,i}$ are added to the number of waves N_i used in the test. Because the extra number of waves is a function of A, an iterative procedure is applied to Equation (3) until convergence of A is found.

$$\begin{aligned} \frac{H_{2\%,i}}{\Delta D_{n50A}} &= A\left(\frac{S_{d,i}}{\sqrt{N_i}}\right)^{0.2} \\ N_{extra,i} &= \frac{A^{10}S_{d,i\text{-}1}^2}{\left(\frac{H_{2\%,i}}{\Delta D_{n50A}}\right)^{10}} \\ N_{total,i} &= N_i + N_{extra,i} \end{aligned} \tag{3}$$

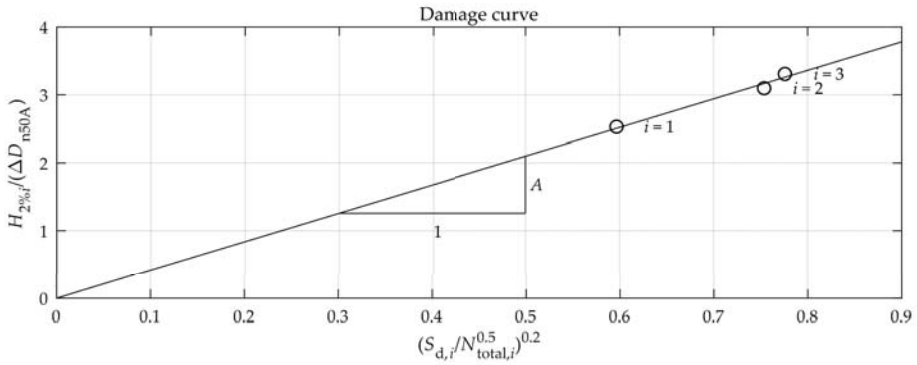

Figure 10. Damage curve for accumulated tests. The tests are shown with markers and the test number in the wave series is given by i. A and $N_{total,i}$ are found by iterating Equation (3) until convergence of A is obtained.

Because Van der Meer [1] and Thompson and Shuttler [3] tests do not have test series with a constant breaker parameter, their tests series do not have a constant A. As their tests are not with accumulated damage the raw data is instead plotted. Therefore, larger scatter is expected compared to points based on the fitted damage curves must be expected. This will however also give an indication of the spreading that can be observed in rubble mound stability tests.

Table 3. Test materials used for all layer compositions.

Layer composition, cf. Figure 7	*B*	*E*	*I*	*J*	*G*	*K*	*D*
Number of tests	28	14	20	17	34	23	13
Breaker parameter, ζ_{0m}	1.57 - 6.86	2.29 - 6.90	2.82 - 9.34	3.50 - 6.91	1.56 - 7.04	2.26 - 5.27	2.29 - 6.91
Wave steepness, s_{0m}	0.005 - 0.048	0.005 - 0.048	0.005 - 0.056	0.009 - 0.036	0.005 - 0.049	0.009 - 0.049	0.005 - 0.048
Relative wave height, $H_{1/3}/h$	0.20 - 0.34	0.21 - 0.33	0.23 - 0.40	0.23 - 0.40	0.24 - 0.51	0.23 - 0.41	0.22 - 0.34
Relative wave breaking, $H_{2\%}/H_{1/3}$	1.30 - 1.46	1.32 - 1.44	1.29 - 1.44	1.29 - 1.43	1.19 - 1.44	1.29 - 1.47	1.30 - 1.41
Relative wave length, L_{0m}/h	6.00 - 59.26	6.11 - 59.15	5.05 - 59.47	7.35 - 38.03	6.46 - 56.38	6.42 - 37.20	6.40 - 59.50
Relative freeboard, $A_c/H_{1/3}$	1.57 - 2.66	1.65 - 2.59	1.37 - 2.33	1.57 - 2.66	1.07 - 2.30	1.33 - 2.36	1.60 - 2.49
Stability number, $H_0 = H_{1/3}/\Delta D_{n50}$	1.43 - 2.42	1.47 - 2.30	1.63 - 2.78	1.65 - 2.80	1.65 - 3.56	1.61 - 2.85	1.52 - 2.38
Reynolds number for armour layer stones, *Re*	$3.4\ 10^4$ - $4.4\ 10^4$	$3.4\ 10^4$ - $4.3\ 10^4$	$3.6\ 10^4$ - $4.7\ 10^4$	$3.6\ 10^4$ - $4.7\ 10^4$	$3.6\ 10^4$ - $5.3\ 10^4$	$3.6\ 10^4$ - $4.7\ 10^4$	$3.5\ 10^4$ - $4.3\ 10^4$

7. Comparison with Physical Tests of Van der Meer [1]

The layer compositions (*B* and *I*) similar to the composition tested by Van der Meer [1] are shown in Figure 11. Also shown are the results of Thompson and Shuttler [3]. The waves in the tests by Van der Meer [1] and Thompson and Shuttler [3] are all in deeper water for which wave heights can be assumed Rayleigh distributed, i.e. $H_{2\%} = 1.4H_{1/3}$. The results are shown for measured damage levels in the range $2 \le S_d \le 8$ for cot(α) = 1.5 and 2, and damage levels in the range $2 \le S_d \le 12$ for cot(α) = 3. Minimisation of the Root Mean Square Error (RMSE) on $H_{2\%}/(\Delta D_{n50A}(S_d/N^{0.5})^{0.2})$ is used for the estimation of the notional permeability of the present compositions in the context of the formulae by Van der Meer [1].

Figure 11 a) and b) show the results of the composition with an impermeable core for slopes cot(α) = 2 and 3, i.e. compositions *A* and *B*. While the results for cot(α) = 3 seems in fair agreement with a fitted $P = 0.10$, the results for the steeper cot(α) = 2 disagree in the surging wave domain. Quite higher stability in the surging domain and $P = 0.21$ are found for cot(α) = 2 in the present tests compared to the stability and $P = 0.1$ found in the Van der Meer tests.

In the present layer composition *B*, the gradation of the filter layer is $D_{n85}/D_{n15} = 1.33$ compared to $D_{n85}/D_{n15} = 2.25$ used in the tests by Van der Meer [1]. This difference makes the present filter layer more permeable due to a larger porosity which increases the stability. Furthermore, Van der Meer [1] tested two gradation of the armour layer for the impermeable layer composition. $D_{n85}/D_{n15} = 2.25$ was tested with cot(α) = 2, 3, 4 and 6 while $D_{n85}/D_{n15} = 1.25$ was tested with cot(α) = 3 and 4. Thus he did not test the impermeable layer composition with $D_{n85}/D_{n15} = 1.25$ for $\xi_{0m} >> 4$, see Figure 11 b). Comparing the armour layer for compositions *A* and *B* for cot(α) = 2 shows that the present compositions has a more narrow gradation and thus a more permeable armour layer. The combination of a more permeable armour layer and filter layer might be the reason for the increase in armour stability of the present tests for $\xi_{0m} > 4$ for cot(α) = 2. The results are too few to prove a significant change to the notional permeability factor and it is kept to $P = 0.1$ to be on the safe side.

Figure 11 c) shows the results of layer compositions *H* and *I*. The present data are for most of the tests within the scatter of the data by Van der Meer [1]. Two of the tests ($\xi_{0m} \approx 9$) are significantly more unstable than predicted by the formula with $P = 0.5$. These two tests with very low steepness waves are outside the applicability range ($0.7 < \xi_{0m} < 7$) of the Van der Meer [1] formula and therefore not used in the fitting of *P*. However, the reason for the two tests deviating might be related to the lower water depth used in the present tests as the wavelength of the large wave period is significantly more affected by the water depth compared to smaller wave periods. It should also be noted that Van der Meer has two significant outliers at $\xi_{0m} \approx 6$. The present tests has a fitted $P = 0.44$ which is lower than the value $P = 0.5$ given by Van der Meer [1]. However, it should be noted that the Van der Meer formulae with $P = 0.5$ overpredicts the stability for all of his own data for cot(α) = 1.5. If fitting his formulae to all of his tests with layer composition *H*, the value $P = 0.44$ is obtained.

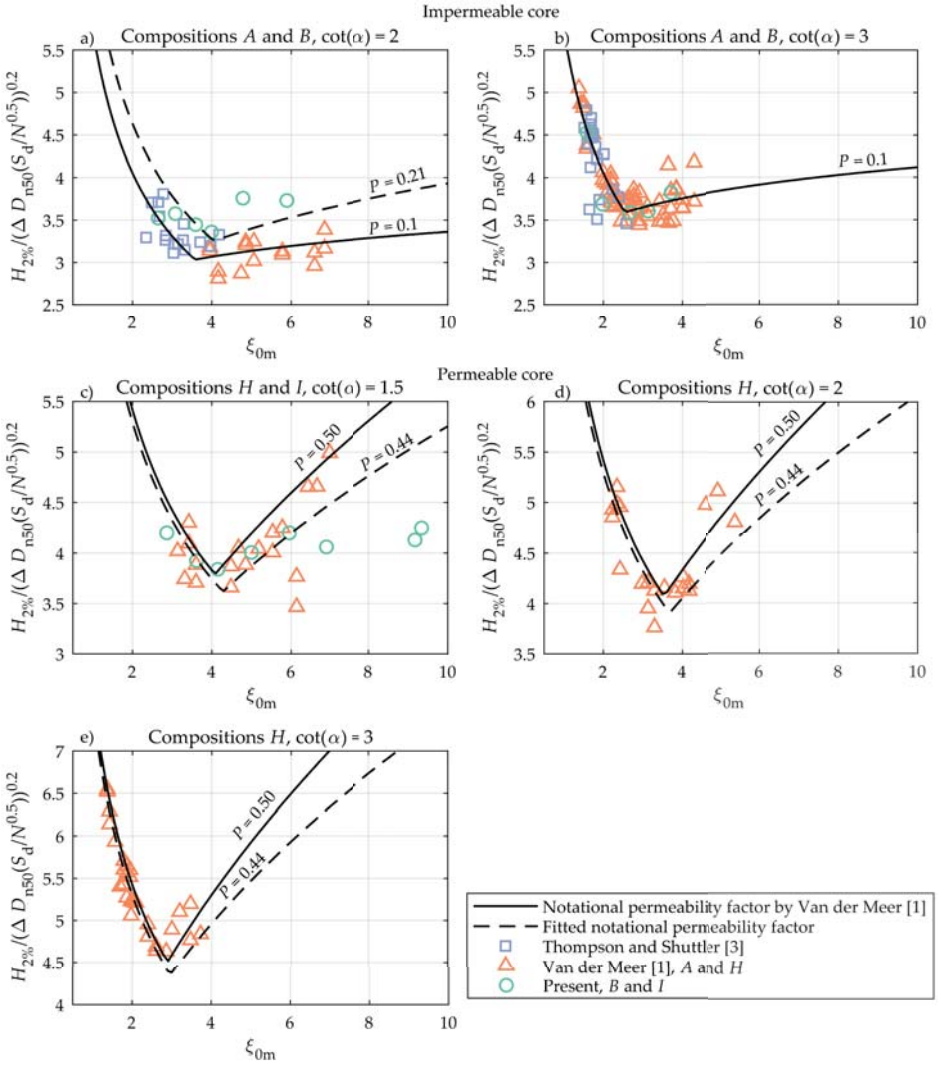

Figure 11. Tests with layer compositions *A*, *B*, *H* and *I* and front slope of cot(α) = 1.5, 2 and 3. Continuous lines indicate the given *P* by Van der Meer [1] and his formulae. Dashed lines indicate fitted values of *P* with use of the Van der Meer [1] formulae. Markers indicate the results.

Considering the differences in layer compositions, there seems to be a fair agreement between the present results and the results of Van der Meer. Therefore, new layer compositions can be tested and a notional permeability factor can be fitted with use of the formulae by Van der Meer [1].

8. Notional Permeability for New Layer Compositions

Notional permeability factors are fitted to the new layer compositions by minimisation of the Root Mean Square Error (RMSE) on $H_{2\%}/(\Delta D_{n50A}(S_d/N^{0.5})^{0.2})$. The compositions with an armour layer thickness of three rocks can suffer more damage before failure than an armour layer thickness of two rocks. Therefore, Figures 12 - 14 are shown with damage levels in the range $2 \le S_d \le 12$ for cot(α) = 1.5 and 2. The results of the new layer compositions having an armour layer thickness of approximately

two rocks are shown in Figures 14 - 15 for measured damage levels in the range $2 \leq S_d \leq 8$ for $\cot(\alpha) = 2$, and damage levels in the range $2 \leq S_d \leq 12$ for $\cot(\alpha) = 3$.

Figure 12 show the results of layer composition *E* with an impermeable core, thin filter layer and an armour layer thickness of three rocks. Layer composition *E* has a best fitted $P = 0.30$ and the results are only having small deviations with the Van der Meer formulae at the transition between the plunging and surging formulae. Comparing the results to layer composition *B* in Figure 11 a) shows that an increase in the armour layer thickness increases the notional permeability factor significantly. Thus the notional permeability for structures with an impermeable core seems very sensitive to the layer thickness and material size of the permeable layers. This was also observed by Van der Meer et al. [7].

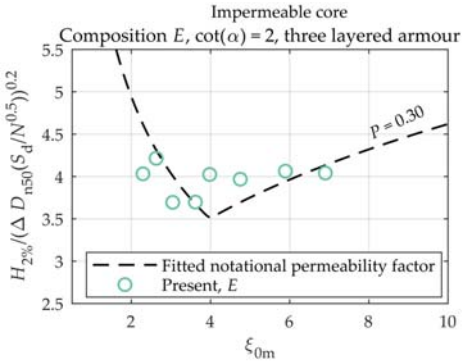

Figure 12. Tests with layer compositions *E* and front slope of $\cot(\alpha) = 2$. Dashed lines indicate fitted values of *P* with use of the Van der Meer [1] formulae. Markers indicate the results.

Figure 13 shows the results of layer compositions *J* with a permeable core and an armour layer thickness of three rocks. The best fitted notional permeability factor is found for $P = 0.45$. The results are a close match to the formulae by Van der Meer [1]. Comparing the results to layer composition *I* in Figure 11 c) shows that an increase in the armour layer thickness has no significant change to the notional permeability factor. This shows the effect of armour layer thickness for a coarse permeable core is far from being as significant as found for an impermeable core.

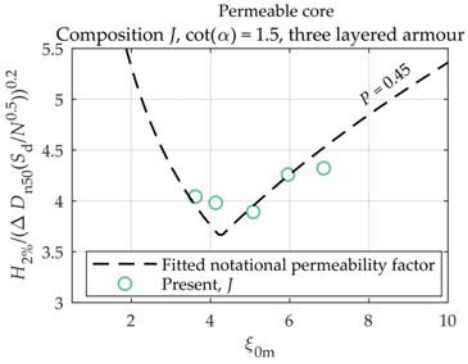

Figure 13. Tests with layer compositions *J* and front slope of $\cot(\alpha) = 1.5$. Dashed lines indicate fitted values of *P* with use of the Van der Meer [1] formulae. Markers indicate the results.

Figure 14 shows the results of the layer compositions *G* and *K* with a permeable core and one underlayer for different armour thickness. By fitting the present results of layer composition *G* to the formulae by Van der Meer, a notional permeability of $P = 0.37$ is found for the lowest RMSE for both front slopes. This notional permeability is significantly lower than $P = 0.46$ found by Kluwen [6] for

a similar composition though with larger layer thicknesses, see layer composition *L*. It could be expected that the composition by Kluwen had a larger *P* factor as the composition had a 20% thicker armour layer and a 20% coarser core material. The composition with three layers of armour rocks (composition *K*) has higher stability, and a fitted notional permeability factor of 0.45. For the finer core material the influence of the armour layer thickness is higher, but not as significant as for the impermeable core. The results with the fitted *P* are in good agreement with the Van der Meer formulae for layer composition *G*, but a slight underprediction is observed for the data in the plunging regime in Figure 14 a) and c). The scatter is significantly larger for layer composition *K* in Figure 14 b) but it is clear that the stability is increased when comparing Figure 14 a) and b). Therefore, an increase of the notional permeability factor is also expected when using the formulae by Van der Meer.

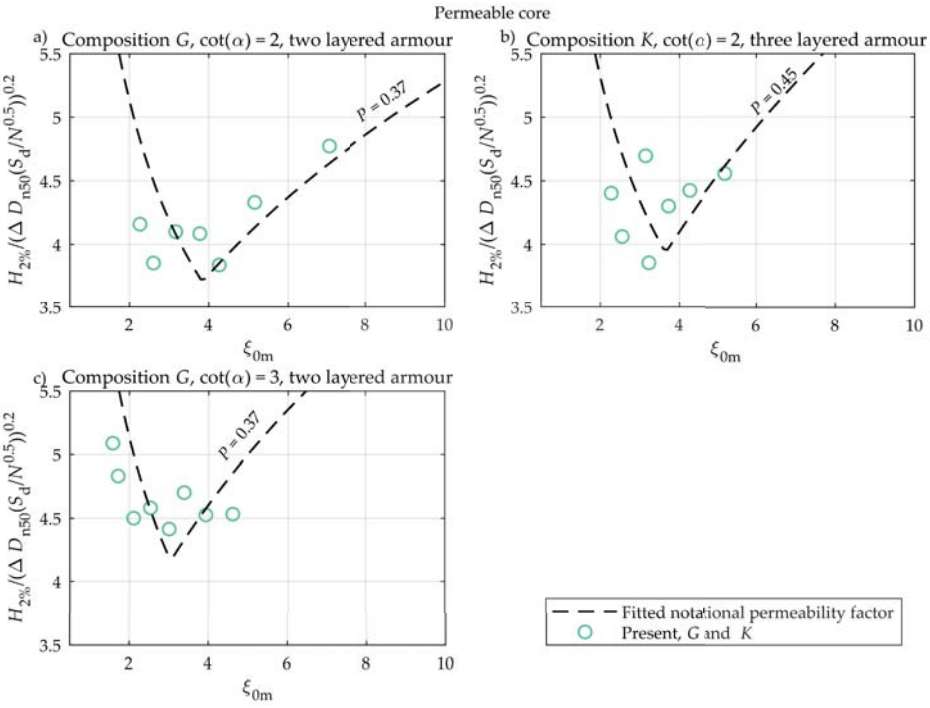

Figure 14. Tests with layer compositions *G* and *K* and front slope of cot(α) = 2 and 3. Dashed lines indicate fitted values of *P* with use of the Van der Meer [1] formulae. Markers indicate the results.

Figure 15 shows the results of layer composition *D* having two underlayers and an impermeable core. The lowest RMSE was found for a notional permeability of 0.29. This notional permeability is significantly larger than *P* = 0.1 given for layer composition *A* and *B* which also has an impermeable core, cf. Figure 11 a). Even though the fitted notional permeability factor for layer composition *B* is *P* = 0.21 the increase of the notional permeability factor for layer composition *D* is significant. The notional permeability factor is significantly influenced by the layer thickness of the permeable layers for compositions with an impermeable core. The results with the fitted *P* are in good agreement with the Van der Meer formulae, but a slight underprediction is observed for the data in the plunging regime and overprediction in the surging regime.

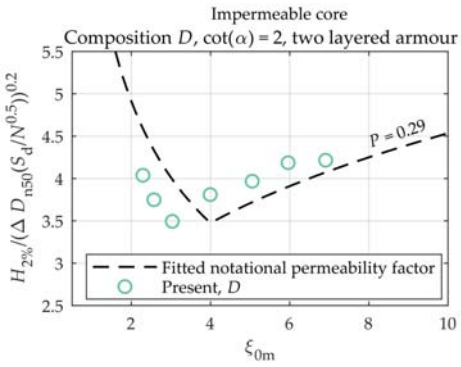

370 **Figure 15.** Tests with layer composition *D* and front slope of cot(α) = 2. Dashed lines indicate fitted
371 values of *P* with use of the Van der Meer [1] formulae. Markers indicate the results.

372 The results show that the influence of the thickness of the armour layer on the notional
373 permeability factor is largest for impermeable layer compositions and smallest for permeable layer
374 compositions, see Table 4.

375 **Table 4.** Influence of armour layer thickness.

Rock class	Layer composition	Notional permeability factor		Influence
		Two layers	Three layers	
Impermeable core	*B* & *E* for cot(α) = 2	0.10	0.30	Significant
Permeable core no filter	*I* & *J* for cot(α) = 1.5	0.44	0.45	Insignificant
Conventional layer composition	*G* & *K* for cot(α) = 2	0.37	0.45	Moderate

376 **9. New Method for the Estimation of the Notional Permeability Factor**

377 The approach of using model tests for the determination of *P* for new layer compositions is time-
378 consuming and costly and has no meaning in relation to specific projects as the model tests show
379 directly the stability of the armour. Therefore, a desk method for the estimation of the notional
380 permeability factor is needed. In the introduction was explained that numerical models can help
381 estimating the notional permeability. However, direct determination from basic physical principles
382 is not possible because it is a parameter fitted to a complex formula fitted to physical model tests of
383 armour stability. The notional permeability has no physical meaning as also explained by Van der
384 Meer [1]. It could be indirectly related to phenomena as run-up and porous flow
385 resistance/dissipation. However, while the value of the notional permeability is fixed for a specific
386 layer composition, the other phenomena vary with the wave conditions. A pragmatic approach to
387 obtain a tool for the prediction of the notional permeability would be to fit a formula to all the
388 parameter values obtained in model tests for all tested layer configurations. Such a formula is
389 presented in the following. Figure 16 shows the applied collection of fitted notional permeability
390 factors for the different layer compositions.

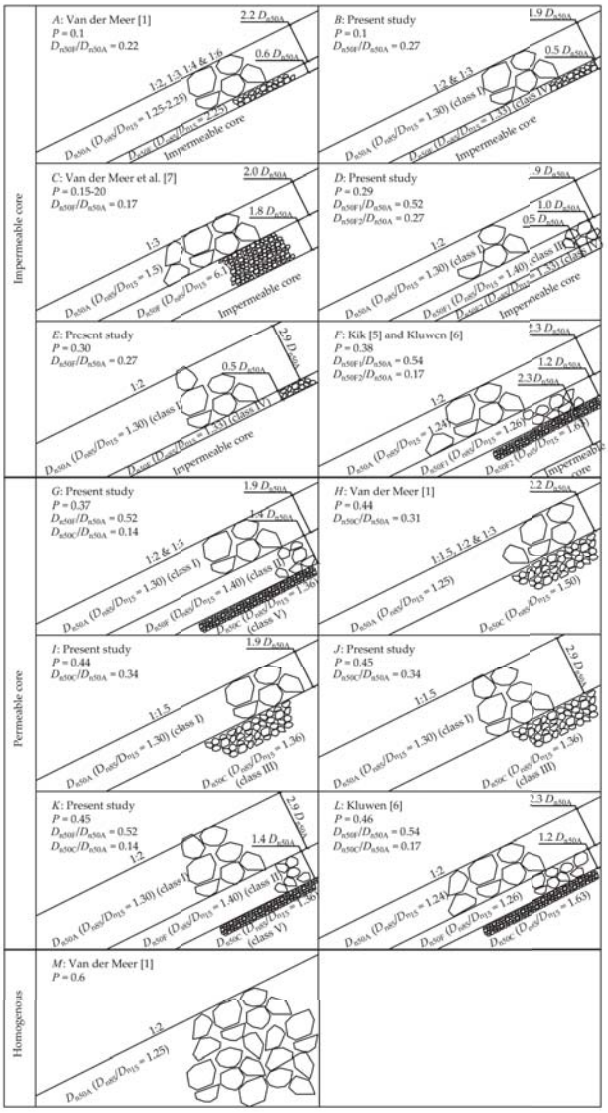

391 **Figure 16.** Collection of notional permeability factors for different layer compositions from previous
392 and present studies.

393 The new formula will include the known physical processes in an empirical way. It is well
394 known that a homogenous structure has the largest *P* factor, and when introducing a core with
395 smaller size material the wave run-up and the loads on the armour units will increase corresponding
396 to a reduction in the *P* factor. This is partly due to higher porous flow resistance and a decrease in the
397 buffer capacity of the permeable layers. This effect on the *P* factor is clearly seen when comparing
398 composition *M* with *I* and *G* in Figure 16. Furthermore, the present tested layer compositions show
399 that the layer thickness of each layer has an influence. Comparing the tests with an armour layer
400 thickness of two rocks with the compositions with a thickness of three rocks, it can be seen that the
401 increase in *P* is largest for compositions where the impermeable layer is closest to the armour layer.
402 This shows that the effect on the *P* factor from the material size is decreasing with increasing distance
403 into the breakwater. To describe the relative distance from each layer to the surface of the armour

layer, a relative distance $z^* = z/D_{n50A}$ is used. The distance z is perpendicular to the front slope, see Figure 17.

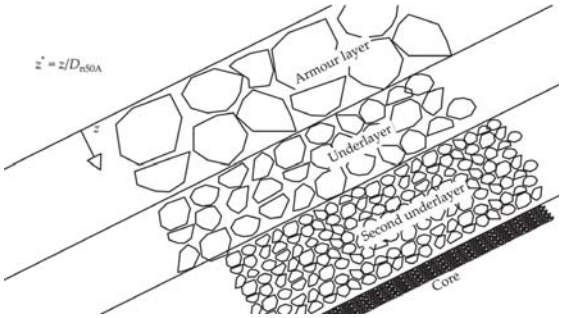

Figure 17. Definition of the relative depth z^* as a function of z and the nominal size of the armour stones D_{n50A}.

The grading of the materials plays a role as a very wide grading has a small porosity. However, this effect cannot be studied based on the present tests as all gradings were narrow with $D_{n85}/D_{n15} < 2.25$. Therefore, the developed empirical formula is limited to narrow graded materials. Based on above considerations, the empirical formula for the P factor must be a function of rock size and the relative depth z^*. The functions f and g defined in Equation (4) and plotted in Figure 18 are empirically fitted to model the influence of the rock size and the relative depths, respectively.

$$f = 0.79\left(1 - \exp\left(-4.1\frac{D_{n50,z^*}}{D_{n50,A}}\right)\right) \text{ for } \frac{D_{n85}}{D_{n15}} < 2.5$$
$$g = \exp(-0.62\, z^*) \tag{4}$$

here D_{n50A} is the nominal size of the armour units, and D_{n50,z^*} is the nominal size of the units in the given layer at relative depth z^*.

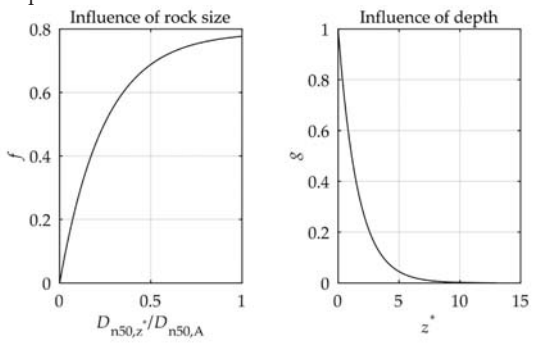

Figure 18. Influence of relative rock size on (f) and influence of relative layer depth on (g). The subplots are plotted with the use of Equation (4).

The g function implies that the layers with the largest influence on the permeability are those close to the slope surface, whereas the f function implies that large material is more permeable than the fine material. Analysis has shown that an integration function, k of the influence from the relative rock size and the relative depth can be used estimate the notional permeability factor, $P(k)$. The integration function k is given by Equation (5).

$$k = \int_0^{z^*_{max}} f(z^*)g(z^*)dz^* \tag{5}$$

z^*_{max} is the value of z^* for the impermeable layer, but has a maximum value of 13. For a layer composition consisting of N permeable layers the integration function Equation (5) can be rewritten into a closed form as

$$k = \sum_{i=1}^{N} 0.79\text{-}0.79 \exp\left(-4.1 \frac{D_{n50,i}}{D_{n50,A}}\right)\left(\frac{\exp\left(-0.62 z_1^*\right) - \exp\left(-0.62 z_2^*\right)}{0.62}\right) \quad (6)$$

where $D_{n50,i}$ is the nominal size of the units in the given layer. Figure 19 shows the definition of z_1^* and z_2^* for $i = 2$ in Equation (6). z_2^* should stop at the impermeable layer or at a maximum value of 13.

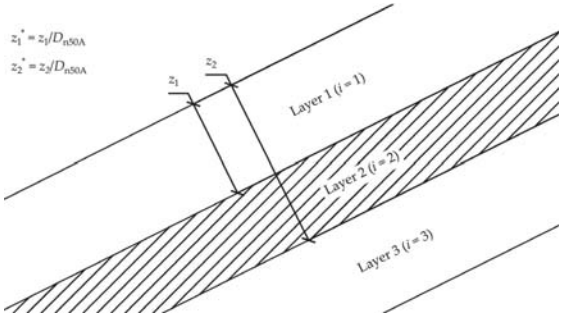

Figure 19. Example of the definition of the relative depth z_1^* and z_2^* for $i = 2$ in Equation (6) with D_{n50A} as the nominal size of the armour stones.

Based on the integration function k the new empirical formula for estimating P can be given as

$$P = \max\begin{cases} 0.1 \\ 1.72k - 1.58 \end{cases} \quad (7)$$

Equation (7) is limited to compositions in which the material size decreases from the armour layer to the core. For example, if a layer composition with identical core and armour layer is used, but a thin and almost impermeable layer is separating these layers, the integration function k should stop at the impermeable layer, and the material size should never increase with z.

Figure 20 shows the estimated P factors from Equation (7) compared with the fitted P factors given in Figure 16. Good correlation is found for all layer compositions having a typical deviation of ± 0.03 between the estimated and the fitted notional permeability factor.

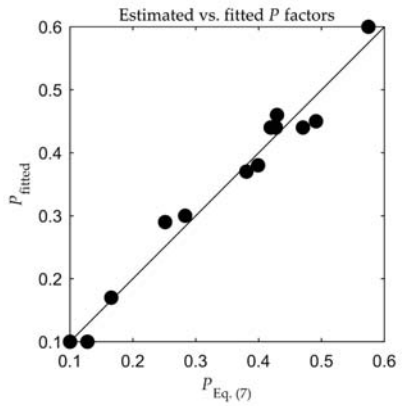

Figure 20. Comparison between the fitted P factors shown in Figure 16 and the estimated P factors calculated by Equation (7).

10. Conclusion

The present paper presents notional permeabilities for various rock armoured layer compositions based on hydraulic model tests. The model test programme included two layer compositions similar to those previously tested by Van der Meer [1].

Notional permeability factors were determined for two new layer compositions, one with an impermeable core and one with a permeable core. Furthermore, three additional compositions similar to previously tested compositions but having a 50% thicker armour layer were tested. In total seven layer compositions were added to the database with known notional permeability factors.

Based on notional permeability factors for all 13 layer compositions, an empirical formula for the estimation of the notional permeability was established. Given typical deviations of 0.03, the formula showed good agreement with the known *P* factors determined from model tests.

Increasing the armour layer thickness from two to three layers of rocks, the notional permeability factor and the related armour stability are increased. For compositions with impermeable core, the increase is significant. For conventional layer compositions with filter layer(s) and quarry rock core, the increase is moderate. For compositions with armour layer placed directly on a very permeable core, the increase is insignificant.

Author Contributions: MRE and TLA planned the test campaign for the paper in cooperation. The experimental tests and the analysis of the results were performed by the MRE. A common discussion on the outline of the analysis was done in a shared effort between the authors. The outline of the paper was written by MRE. TLA and HFB performed a detailed review on the draft paper and contributed with valuable suggestions.

Funding: This research received no external funding.

Conflicts of Interest: The authors declare no conflict of interest.

References

1. Van der Meer, J.W. *Rock slopes and gravel beaches under wave attack*; Delft Hydraulics, 1988;
2. Sarfaraz, M.; Pak, A. An integrated SPH-polyhedral DEM algorithm to investigate hydraulic stability of rock and concrete blocks: Application to cubic armours in breakwaters. *Eng. Anal. Bound. Elem.* **2017**, doi:10.1016/j.enganabound.2017.08.002.
3. Thompson, D.M.; Shuttler, R.M. *Riprap design for wind-wave attack, a laboratory study in random waves*; 1975;
4. Hölscher, P.; Barends, F.B.J. *Transport in porous media*; 1986;
5. Kik, R. The notional permeability of breakwaters: experimental research on the permeability factor P, Delft University of Technology, 2011.
6. Kluwen, J.G.M. Physical model tests of the notional permeability on breakwaters, Delft University of Technology, 2012.
7. Van der Meer, J.W.; Van Gent, M.R.A.; Wolters, G.; Heineke, D. *New Design Guidance for Underlayers and Filter Layers for Rock Armour under Wave Attack*; 2018;
8. Jumelet, H.D. The influence of core permeability on armour layer stability, Delft University of Technology, 2010.
9. Van Broekhoven, P.J.M. The influence of armour layer and core permeability on the wave run-up, Delft University of Technology, 2010.
10. Van der Neut, E.M. Analysis of the notional permeability of rubble mound breakwaters by means of a VOF model, Delft University of Technology, 2015.
11. CIRIA/CUR/CETMEF *The Rock Manual. Teh use of rock in hydraulic engineering*; 2007;
12. Aalborg University AwaSys 7 Available online: www.hydrosoft.civil.aau.dk/awasys.
13. Eldrup, M.R.; Andersen, T.L. Applicability of Nonlinear Wavemaker Theory. *J. Mar. Sci. Eng.* **2019**, *7*, 14,

487 doi:10.3390/jmse7010014.
488 14. Zhang, H.; Schäffer, H.A.; Jakobsen, K.P. Deterministic combination of numerical and physical coastal
489 wave models. *Coast. Eng.* **2007**, *54*, 171–186, doi:10.1016/j.coastaleng.2006.08.009.
490 15. Lykke Andersen, T.; Clavero, M.; Frigaard, P.; Losada, M.; Puyol, J.I. A new active absorption system
491 and its performance to linear and non-linear waves. *Coast. Eng.* **2016**, *114*, 47–60,
492 doi:10.1016/j.coastaleng.2016.04.010.
493 16. Lykke Andersen, T.; Clavero, M.; Eldrup, M.R.; Frigaard, P.; Losada, M. Active Absorption of Nonlinear
494 Irregular Wwaves. In *Proceedings of the Coastal Engineering Conference*; Baltimore, USA, 2018.
495 17. Klopman, G.; Meer, J.W. van der Random Wave Measurements in Front of Reflective Structures. *J.*
496 *Waterw. Port, Coastal, Ocean Eng.* **1999**, doi:10.1061/(ASCE)0733-950X(1999)125:1(39).
497 18. Battjes, J.A.; Groenendijk, H.W. Wave height distributions on shallow foreshores. *Coast. Eng.* **2000**, *40*,
498 161–182.
499 19. Eldrup, M.R.; Lykke Andersen, T. Estimation of Incident and Reflected Wave Trains in Highly Nonlinear
500 Two-Dimensional Irregular Waves. *J. Waterw. Port, Coastal, Ocean Eng.* **2019**, *145*,
501 doi:10.1061/(ASCE)WW.1943-5460.0000497.
502 20. Aalborg University WaveLab Available online: www.hydrosoft.civil.aau.dk/wavelab.
503 21. Aalborg University EPro Available online: www.hydrosoft.civil.aau.dk/epro/.
504 22. Dai, Y.B.; Kamel, A.M. *SCALE EFFECT TESTS FOR RUBBLE-MOUND BREAKWATERS: Hydraulic Model*
505 *Investigation*; Mississippi, 1969;
506 23. Van der Meer, J.W. Stability of rubble mound revetments and breakwaters. In *Proc. ICE, Developments in*
507 *Breakwaters*; 1985; p. Discussion pp 191-202.
508

509

Paper E

New Formulae for Rock Armour Stability in Shallow Water

Mads Røge Eldrup
Thomas Lykke Andersen

The paper has been submitted to
Coastal Engineering, ISSN: 0378-3839.

New Formulae for Rock Armour Stability in Shallow Water

Mads Røge Eldrup [a*], Thomas Lykke Andersen[b]

[a] Ph.D. student, Department of Civil Engineering, Aalborg University, Thomas Manns Vej 23, 9220 Aalborg Ø, Denmark, mre@civil.aau.dk

[b] Associate professor, Department of Civil Engineering, Aalborg University, Thomas Manns Vej 23, 9220 Aalborg Ø, Denmark, tla@civil.aau.dk

[*] Corresponding author: Mads Røge Eldrup, mre@civil.aau.dk

The present paper presents a new formula for hydraulic stability of the main armour layer on rock armoured conventional rubble mound structures. Eldrup et al. (2019) performed hydraulic model tests with shallow foreshore conditions and few tests with deep water conditions. They observed some deviations from the stability formula by Van der Meer (1988) for shallow foreshore conditions and large surf similarity parameters ($\xi_{0m} > 7$). Furthermore, Herrera et al. (2017) tested rubble mound stability with a 1:50 foreshore and observed that the spectral wave height H_{m0} described better the stability compared to $H_{1/3}$ or $H_{2\%}$. In the present study, new stability tests were performed covering both mild (1:100) and steep (1:30) foreshores. The tests covered nonbreaking and breaking waves on the foreshore with low steepness waves. Van Gent et al. (2004) tested shallow to very shallow foreshore conditions for intermediate to large wave steepness causing breaking and broken waves. The present tests with the 1:30 foreshore showed to be significantly more stable in the surging domain than predicted with the modified Van der Meer formula by Van Gent et al. (2004). This was attributed to nonlinear waves with significantly larger $H_{1/3}$ than H_{m0}. New stability formulae are presented and fitted to the data by Van Gent et al. (2004), Eldrup et al. (2019) and the present tests. The new formulae provide a significantly increase in the reliability for nonlinear waves compared to the modified Van der Meer formulae by Van Gent et al. (2004).

Keywords; rock armour stability; breakwater; damage; shallow water waves; long waves; foreshore; nonlinear waves

1. INTRODUCTION

Stability of conventional rubble mound breakwaters has been investigated by several authors. Some of the first researchers who investigated the stability of rubble mound breakwaters were Irribarren (1938), Hudson (1959) and Thompson and Shuttler (1975). Their research covered deep water conditions and thus not depth-induced wave breaking at the toe of the structure which occur when $H_{m0,deep}/h > 0.25$, cf. Hofland et al. (2017). Here $H_{m0,deep}$ is the offshore spectral wave height, and h is the water depth at the toe of the structure. Based on model tests with regular waves Irribarren (1938) and Hudson (1959) described the stability as a function of wave height, front slope angle and characteristics of the armour stone material. Thompson and Shuttler (1975) introduced a stability formula based on model tests with irregular waves.

Van der Meer (1988) used the data by Thompson and Shuttler (1975) and performed new tests to extend their research. Van der Meer performed tests on different layer compositions with different permeabilities compared to Thompson and Shuttler (1975). His model tests were also mainly with deep water wave conditions. Few tests were though performed with depth-induced wave breaking

$H_{1/3}/h \leq 0.72$, here is $H_{1/3}$ the significant wave height from time domain analysis at the toe. Van der Meer (1988) developed a set of widely used stability formulae as a function of wave height, front slope angle, characteristics of the armour stone material, wave period, number of waves and the breakwater permeability.

Rubble mound breakwaters are often located with shallow foreshore conditions with breaking waves. Van Gent et al. (2004) conducted new experiments with both depth-limited and non-breaking waves on the foreshore. Both single peaked and double peaked offshore spectra were tested. Furthermore, he also tested broken waves which are characterised by a single peaked offshore wave spectrum and a flat wave spectrum with no significant peak at the breakwater. The breaking affect the energy wave period $T_{-1,0} = m_{-1}/m_0$ which increases as the waves breaks on the shallow foreshore, here m_n is the n^{th} order spectral moment. Based on new experiments with foreshore slopes of 1:100 and 1:30, he modified the formulae by Van der Meer (1988) by replacing the mean wave period from time domain T_m with the energy wave period $T_{-1,0}$. Besides this Van Gent et al. (2004) proposed a new formula not containing the wave steepness as the influence was considered insignificant compared to the scatter of the data.

The slope of the foreshore influences the wave characteristics at the toe of the structure and is thus important for the stability of rubble mound breakwaters. Muttray and Reedijk (2009) reanalysed earlier stability results of rubble mound breakwaters with a 1:30 and a 1:8 foreshore. They found that the damage to the rubble mound breakwater was larger for the steep foreshore. They also observed that similar offshore wave heights resulted in larger wave heights at the toe of the structure for the steep foreshore. However, when using the spectral wave height H_{m0} at the toe of the structure the effect of the foreshore slope on the stability was insignificant. Herrera et al. (2017) performed stability tests on a rubble mound breakwater with a 1:50 foreshore. They observed that the H_{m0} wave height better described the stability than $H_{1/3}$ and $H_{2\%}$. Herrera et al. (2017) also observed that the formulae by Van der Meer (1988) and the modified Van der Meer formulae by Van Gent et al. (2004) overestimated the damage for tests with a 1:50 foreshore and a front slope of $\cot(\alpha) = 1.5$. Therefore, they made a new formula as a function of wave height, and characteristics of the armour stone material.

Melby and Hughes (2004) were the first to derive a stability formula based on the maximum wave momentum flux. They assumed that the maximum wave momentum flux is proportional to the maximum forces on the armour units. They used the approximated maximum momentum flux equation by Hughes (2004) which depends on the water depth, wave period and wave height. Melby and Hughes (2004) concluded that with the inclusion of water depth in the stability formulae, a better description for breaking waves was found. The formula was calibrated with use of the data by Van der Meer (1988). They established a formula for plunging waves and one for surging waves, but these formulae do not intersect at the defined transition point. This makes the formulae unreliable as a small change in wave steepness might lead to completely different stability being predicted.

New tests by Eldrup et al. (2019) were performed with a broad range of wave steepness and slope angles. They tested different layer compositions to extend the database on known notional permeability factors (P) used in the Van der Meer (1988) formulae. They tested two compositions that were similar to those tested by Van der Meer (1988) in order to validate the notational permeability for these layer compositions. However, they observed some deviations to the Van der Meer (1988) formulae especially for large surf similarity parameters ($\xi_{0m} > 7$) which was outisde the range covered by Van der Meer (1988). Furthermore, they tested five compositions not tested by Van der Meer and fitted a notional permeability factor to each composition. Based on a total of 13 layer compositions, they introduced a simple empirical formulation to estimate the notional permeability factor.

Eldrup et al. (2019) observed some deviations for large surf similarity parameters, but these tests were with shallow foreshore conditions which was not covered in depth by Van der Meer (1988). Therefore, tests with low steepness waves with shallow foreshore conditions are tested more extensively in the present paper to verify the observations by Eldrup et al. (2019). New model data with nonlinear waves on steep foreshores are included to investigate if H_{m0} is a better shallow water wave height than $H_{2\%}$ as observed by Herrera et al. (2017). The present tests and the tests by Eldrup et al. (2019) are compared to the modified Van der Meer formulae by Van Gent et al. (2004) valid for shallow foreshore conditions. The data by Thompson and Shuttler (1975) and Van der Meer (1988) are not included in the present analysis as H_{m0} and $T_{-1,0}$ are not available for their data. Finally, new rock armour stability formulae valid for shallow foreshore conditions are given, and conclusions are drawn.

2. NEW MODEL TESTS

The present test programme includes stability tests of rubble mound breakwaters with foreshore slopes of 1:30 and 1:100. The tests are performed in two different flumes at Aalborg University, cf. Figs 1 - 2, but using the same methodology. Both flumes are equipped with a piston-type wavemaker which is controlled with the software AwaSys 7, cf. Aalborg University (2018a). For the present study state-of-the-art methods for nonlinear wave generation was used and new methods for nonlinear wave analysis was developed.

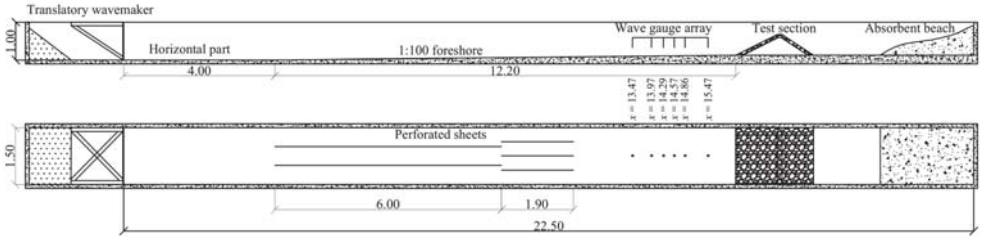

Figure 1: Flume layout with the 1:100 foreshore. Measurements are in meters.

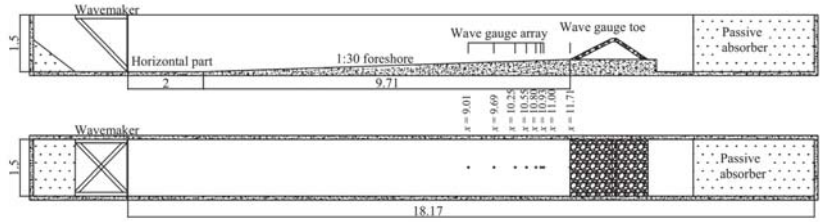

Figure 2: Flume layout with the 1:30 foreshore. Measurements are in meters.

Second-order wave generation (Schäffer, 1996) was used with modification by Eldrup and Lykke Andersen (2019). If the guidelines by Eldrup and Lykke Andersen (2019) suggest that second-order wavemaker method is not valid, the wave generation method by Zhang et al. (2007) was used. That method uses a depth-averaged velocity in the wave direction and the nonlinear surface elevation time series as input for the paddle movement and active absorption correction. For the present tests, these timeseries were obtained from the CELERIS software developed by Tavakkol and Lynett (2017). CELERIS is a Boussinesq type wave model that is based on the extended Boussinesq equations derived by Madsen and Sørensen (1992). However, the CELERIS model runs on the Graphics Processing Unit (GPU) which significantly reduces the time for preparing the input signal for the wavemaker. During all tests, active wave absorption was used based on wave gauges at the paddle face using the Lykke Andersen et al. (2016) method. The active absorption system has shown also to be highly effective for nonlinear irregular waves, cf. Lykke Andersen et al. (2018).

Wave separation into incident and reflected waves was performed with use of the nonlinear method by Eldrup and Lykke Andersen (2019). This method was specifically developed with the present tests in mind. Similar methods were developed for regular and bichromatic waves, cf. Lykke Andersen et al. (2019, 2017). These methods separate the incident and reflected waves into free and bound components, which is important to properly reconstruct nonlinear waves. The methods are included in the software package WaveLab 3, cf. Aalborg University (2018b). The wave gauge array was placed with a distance of approximately $0.4L_P$ (peak wavelength) to the waterline of the structure according to the recommendation given by Klopman and Van der Meer (1999). For the tests with a 1:100 foreshore the water depth at the wave gauge array was approximately 1.7 cm larger than at the toe of the breakwater. Because of that, the waves might deviate from those at the toe due to depth induced wave breaking and shoaling. However, for the 1:100 foreshore the difference in $H_{2\%}$ from the array to the toe is found to be maximum 1% based on nonlinear shoaling by Kweon and Goda (1996) and the wave height distribution by Battjes and Groendjik (2000). This small difference in wave height is found acceptable compared to the amount of scatter in the stability results. Therefore, for the 1:100 foreshore the wave parameters at the toe are based on the incident waves from the wave separation analysis. However, the tests

with a 1:30 foreshore were carried out both with and without the structure in-place, with identical control signals prior to active absorption correction. The reason for this was due to an estimated nonlinear shoaling coefficient from the array and to the toe of the structure of up to 1.2. Comparing the total waves without the structure in place at wave gauge $x = 10.25$ and $x = 11.71$ (cf. Fig. 2) a maximum increase of 19% for $H_{1/3}$ was observed and thus confirming the nonlinear shoaling results. Therefore, the incident wave parameters with a 1:30 foreshore are taken as the total measured waves at the toe of the structure without the structure in place.

To describe the degree of shallow foreshore conditions, the work by Hofland et al. (2017) is used. They described the degree of shallow foreshore by the water depth at the toe of the structure h and the offshore spectral wave height $H_{m0,deep}$. Fig. 3 shows the degree of shallow water for the test by Eldrup et al. (2019), Van Gent et al. (2004) and the present tests. The present tests and the tests by Eldrup et al. (2019) covers mainly shallow foreshore conditions and few with deep water conditions. The data by Van Gent et al. (2004) covers shallow and very shallow foreshore conditions. Thereby, considering tests with a foreshore slope of 1:100 the present tests and the tests by Eldrup et al. (2019) cover less shallow foreshore conditions compared to the data by Van Gent et al. (2004). Furthermore, it can be seen that present tests and the tests by Eldrup et al. (2019) includes tests with lower wave steepness compared to Van Gent et al. (2004).

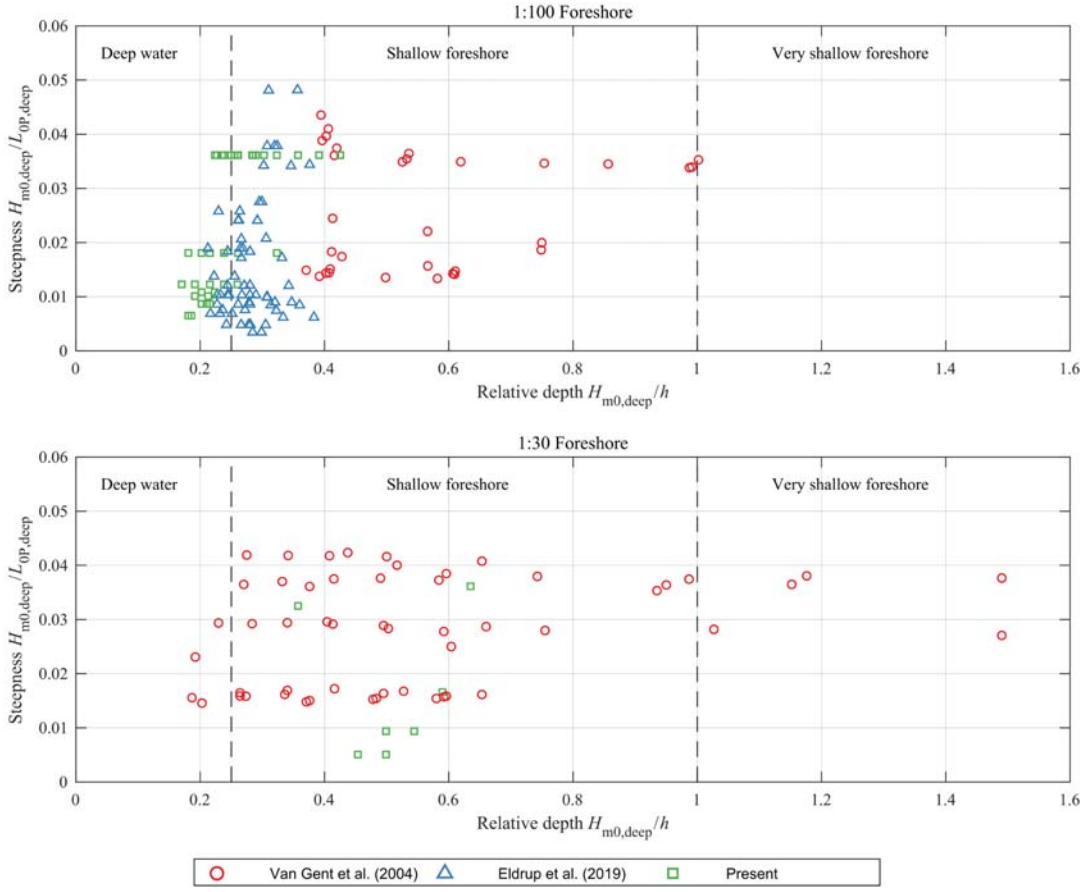

Figure 3: Description of shallow foreshore conditions of the used data by Hofland et al. (2017).

For highly nonlinear nonbreaking waves, $H_{1/3}$ can be much larger than the spectral wave height H_{m0}. Goda (2010) described the ratio $H_{1/3}/H_{m0}$ by the nonlinearity parameter Π_0, see Eq. 1.

$$\Pi_0 = \frac{H_{m0,deep}}{L} \coth^3 \frac{2\pi h}{L} \quad (1)$$

Here $H_{m0,deep}$ is the offshore spectral wave height, L the small amplitude wave length calculated with the peak wave period T_P and h is the water depth at the toe of the structure.

Fig. 4 shows $H_{1/3}/H_{m0}$ compared to Π_0 for the Van Gent et al. (2004), Eldrup et al. (2019) and the present tests. All data sets have $H_{1/3}/H_{m0} \approx 1$ for $\Pi_0 < 0.2$, but a clear difference between the data sets are observed for $\Pi_0 > 0.2$. The data by Eldrup et al.

126 (2019) shows an increase in $H_{1/3}/H_{m0}$ with Π_0 and especially when $\Pi_0 > 0.2$. This is as expected according to the diagram by Goda
127 (2010) and due to their tests include low steepness waves which first starts to break for larger Π_0 compared to waves with a higher
128 wave steepness. The data by Van Gent et al. (2004) does not include low steepness waves, and this might explain the reduction of
129 $H_{1/3}/H_{m0}$ for $\Pi_0 > 0.2$. However, their tests shows smaller values than expected by the diagram, but considering the amount of scatter
130 in the data used by Goda (2010) the deviation in the Van Gent et al. (2004) data is judged acceptable. $\Pi_0 > 0.2$ occur only for the
131 present test with the 1:30 foreshore. These tests have $H_{1/3}/H_{m0} >> 1$ and are even larger than expected, but the deviations are not
132 larger than the scatter found in the Goda (2010) data.
133 So far it has not been verified if $H_{1/3}$ or H_{m0} describes best the stability for nonlinear waves. The deep water tests by Thompson
134 and Shuttler (1975) and Van der Meer (1988) would most likely have $H_{1/3}/H_{m0} \approx 1$ and the data by Van Gent et al. (2004) and
135 Eldrup et al. (2019) have $H_{1/3}/H_{m0} \approx 0.9$-1.1. Therefore, the present tests with highly nonlinear waves with $H_{1/3}/H_{m0} >> 1$ will reveal
136 if time domain wave height as suggested by Van Gent et al. (2004) or frequency domain height as suggested by Herrera et al. (2017)
137 should be used.
138
139

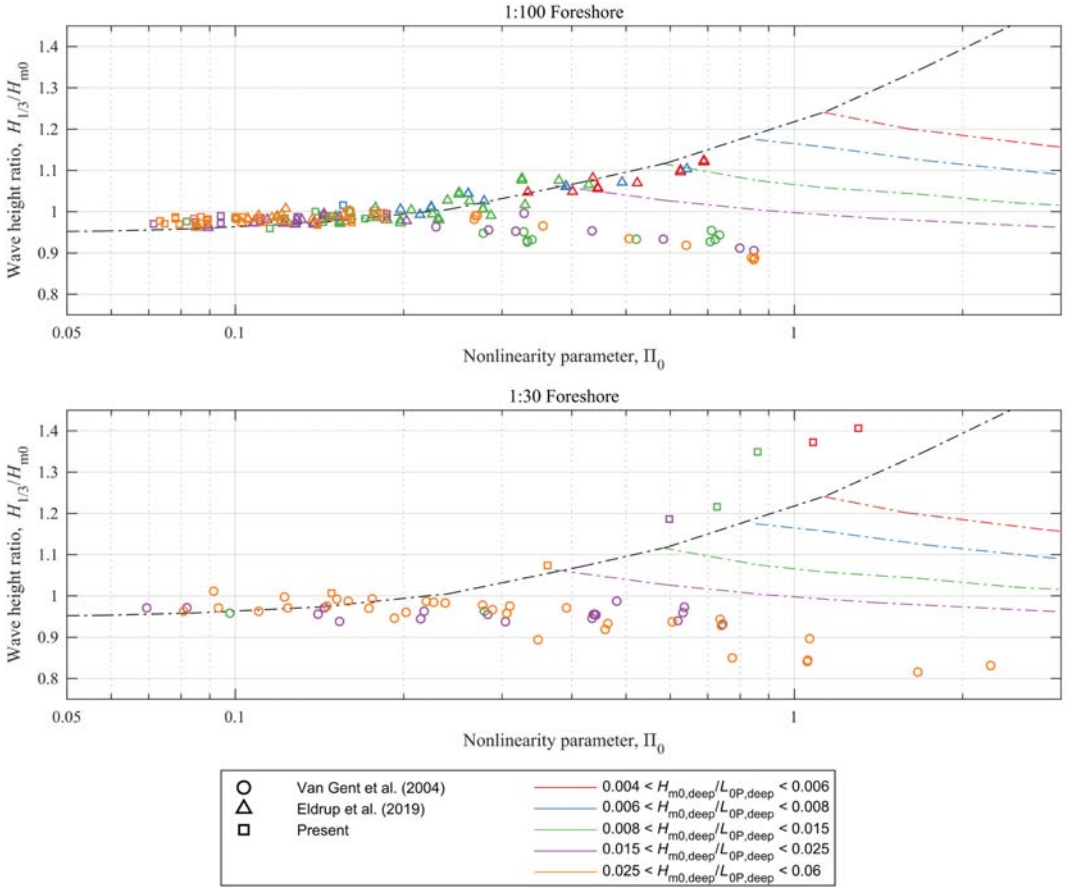

Figure 4: Description of wave height ratio $H_{1/3}/H_{m0}$ of the used data related to the nonlinearity parameter Π_0 by Goda (2010).

Damage on the front slope in the present tests was measured with a non-contact laser profiler which was controlled by the software EPro, cf. Aalborg University (2016). After each test, the reshaped profile was measured with a grid of 10 mm in length and 5 mm in width. The eroded area A_e and the damage $S_d = A_e/D_{n50}^2$ given in the present paper are based on average values disregarding 20 cm on each side of the flume to minimise wall effects. Furthermore, only the part of the slope where a clear erosion was visible was used in the calculation of the eroded area as also done by Van der Meer (1988). By only including the part of the slope where a clear erosion is observed, the small settlements that can be observed in the upper part is not considered. This has largest effect for small damage values with surging waves where a large wave run-up is observed. To get the most reliable measurements, the flume was emptied for water before profiling.

149 Five different cross-sections were tested with identical layer compositions. Eldrup et al. (2019) found for the same layer
150 composition a notional permeability factor of $P = 0.44$ and this is used in the present paper. In Figs. 5 - 6 the different tested cross-
151 sections are shown. Two different heights of the breakwater were tested with a 1:100 foreshore. Tests with larger water depths were
152 performed in order to reduce the wave breaking and as a consequence of that, a breakwater height of 0.9m was needed to keep the
153 wave overtopping to a minimum.

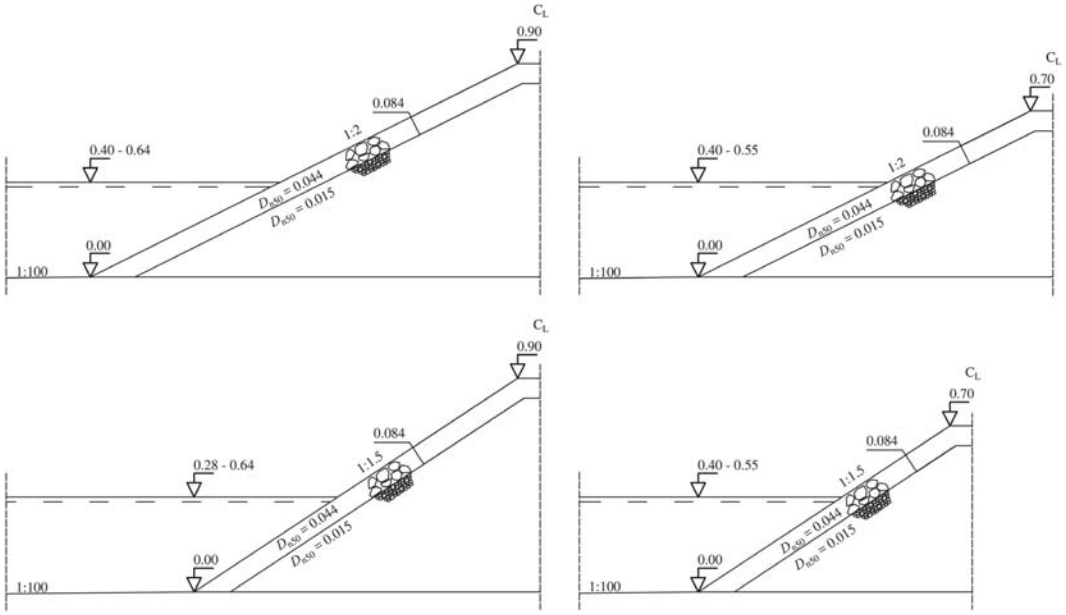

Figure 5: Cross-sections tested with a 1:100 foreshore. Measurements are in meters.

154

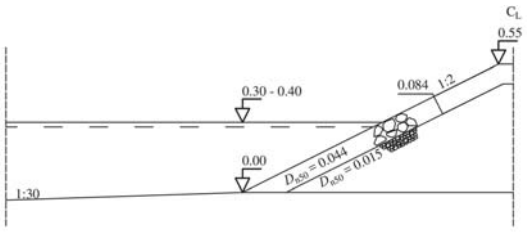

Figure 6: Cross-section tested with a 1:30 foreshore. Measurements are in meters.

155

156 The tested rubble mound breakwaters consist of two rock classes, one for the core and another for the armour. Table 1 lists the
157 properties of the materials used in the present tests. The grain curves for the materials listed in Table 1 are shown in Fig. 7.

Table 1: Test materials used for all tests.

Type	Armour	Core
Median weight, W_{50} [g]	221.0	9.0
Mass density, ρ_s [kg/m^3]	2,620	2,768
Nominal diameter, D_{n50} [m]	0.044	0.015
Gradation, $f_g = D_{n85} / D_{n15}$	1.30	1.36

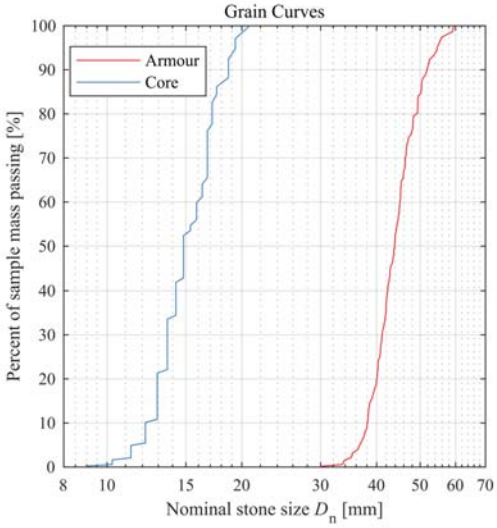

Figure 7: Grain curves of the rock material used in the present tests.

In total 68 model tests were performed to study breaking and non-breaking wave attack and the effect of the foreshore slope. To ensure that viscous scale effects are small the Reynolds number, given in Eq. 2, should be larger than a critical value typically taken as $Re_{crit}= 3{\cdot}10^4$ (Dai and Kamel, 1969).

$$Re = \frac{\sqrt{g\,H_{1/3}}\;D_{n50}}{\nu} > Re_{crit} \tag{2}$$

where ν is the kinematic viscosity, D_{n50} the nominal armour stone size and $\sqrt{g\,H_{1/3}}$ is the characteristic velocity. This is fulfilled for all present tests, cf. Table 2.

Table 2 shows the parameter ranges covered by the tests. The tests were carried out in a number of test series with constant wave steepness. In each test series, the wave height was increased in steps. Accumulated damage was measured after each test in the series. Test series were terminated when the core was visible and exposed, after that, the structure was rebuilt for a new test series. In each test, 1,000 waves were used. In order to compare the accumulated tests with the non-accumulated tests a correction is needed for the accumulated tests. The procedure by Van der Meer (1985) is used to estimate the non-accumulated damage from the accumulated damage. In this procedure, the number of waves corresponding to the previously estimated damage is added to the number of waves in the actual test based on the used stability formulae assuming $S_d \propto N^{0.5}H^5$. The wave height was increased significantly in each step and thus any errors related to this method is rather small.

Table 2: Model tests parameter ranges.

Foreshore slope	1:100	1:100	1:100	1:100	1:30
Breakwater height [m]	0.70	0.70	0.90	0.90	0.55
Front slope cot(α)	1.5	2	1.5	2	2
Number of tests	17	7	15	17	12
Breaker parameter, ζ_{0m}	3.24-6.77	2.41-4.20	3.35-6.04	2.41-5.04	2.36-5.2
Wave steepness, s_{0m}	0.010-0.042	0.014-0.043	0.012-0.040	0.010-0.043	0.009-0.045
Relative significant wave height, $H_{1/3}/h$	0.15-0.33	0.20-0.39	0.15-0.30	0.17-0.31	0.27-0.76
Relative 2% wave height, $H_{2\%}/h$	0.17-0.43	0.33-0.58	0.20-0.60	0.24-0.45	0.37-0.98
Relative spectral wave height, $H_{1/3}/H_{m0}$	0.96-1.08	0.97-1.10	0.97-1.06	0.97-1.07	1.00-1.41
Relative wave length, L_{0m}/h	3.90-19.31	4.92-14.72	6.47-16.27	4.37-18.39	6.39-72.37
Relative freeboard, $A_c/H_{1/3}$	1.12-3.39	1.11-4.40	2.00-4.16	1.96-4.06	1.09-2.16
Stability number, $H_0 = H_{1/3}/\Delta D_{n,50}$	1.20-1.89	1.38-2.19	1.34-1.86	1.49-2.10	1.51-3.22
Reynolds number for armour layer stones, *Re*	$3.1\cdot10^4$-$3.9\cdot10^4$	$3.3\cdot10^4$-$4.2\cdot10^4$	$3.3\cdot10^4$-$3.8\cdot10^4$	$3.4\cdot10^4$-$4.1\cdot10^4$	$3.4\cdot10^4$-$5.0\cdot10^4$

3. EVALUATION OF THE MODIFIED VAN DER MEER STABILITY FORMULAE BY VAN GENT ET AL. (2004)

Van Gent et al. (2004) presented a new set of tests covering breaking and broken wave conditions. The tests were performed with front slopes cot(α) = 2 and 4, and surf similarity parameter in the range $\xi_{s,-1}$ = 1.3 - 15. His modified Van der Meer formula reads:

Surf similarity:

$$\xi_{s,-1} = \frac{\tan(\alpha)}{\sqrt{\frac{2\pi H_{1/3}}{g T_{-1,0}^2}}}$$

Plunging waves ($\xi_{s,-1} < \xi_c$) or cot (α) ≥ 4:

$$\frac{H_{2\%}}{\Delta D_{n50}} = c_{\text{plunging}} P^{0.18} \left(\frac{S_d}{\sqrt{N}}\right)^{0.2} \xi_{s,-1}^{-0.5} \quad (3)$$

Surging waves ($\xi_{s,-1} \geq \xi_c$):

$$\frac{H_{2\%}}{\Delta D_{n50}} = c_{\text{surging}} P^{-0.13} \left(\frac{S_d}{\sqrt{N}}\right)^{0.2} \sqrt{\cot(\alpha)}\ \xi_{s,-1}^{P}$$

Transition between plunging and surging formula:

$$\xi_c = \left(c_{\text{plunging}} / c_{\text{surging}}\ P^{0.31} \sqrt{\tan(\alpha)}\right)^{\frac{1}{P+0.5}}$$

Here $\Delta = \rho_{\text{armour}}/\rho_{\text{water}} - 1$ is the reduced relative density of the armour stones. $D_{n50} = \sqrt[3]{W_{50}/\delta_{armour}}$ is the nominal size of the armour stones. P is the notional permeability factor. α is the angle of the seaward slope of the structure. $\xi_{s,-1}$ is the surf similarity parameter and N is the number of waves (not more than 8,500 waves should be used). For the mean value estimations, the following coefficients were given by Van Gent et al. (2004) $c_{\text{plunging}} = 8.4$, $c_{\text{surging}} = 1.3$.

Fig. 8 presents the Van Gent et al. (2004) stability formulae (Eq. 3) together with the present data. The present tests with a 1:100 foreshore are shown with open markers while the test on a 1:30 foreshore are shown with filled markers. The modified Van der Meer formulae by Van Gent et al. (2004) are shown with continuous lines. Only tests with a measured damage level of $1 \leq S_d \leq 8$ are shown in the figure. The present data with a 1:100 foreshore shows some scatter, but not more than what can be expected considering the typical scatter found in rock armour stability tests. However, the present data with a 1:30 foreshore deviates significantly. Van Gent et al. (2004) also performed tests with a 1:30 foreshore, but most of the tests by Van Gent et al. (2004) were with breaking and broken waves. The present tests with 1:30 foreshore was with highly nonlinear waves with only a few of the waves in the train breaking. The figure clearly shows that the predicted stability is underestimated with use of $H_{2\%}$ for the tests with highly nonlinear waves.

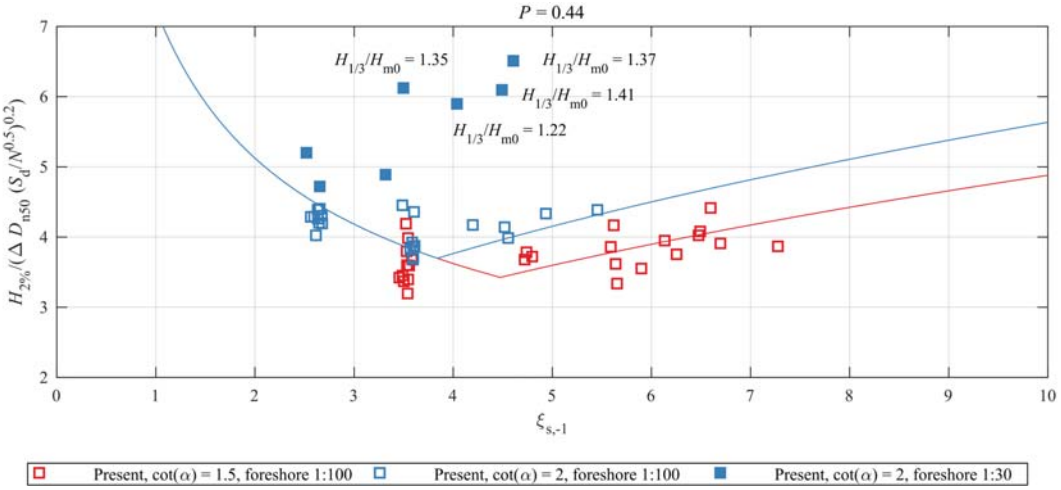

Figure 8: Present data for *P* = 0.44 and a front slope cot(α) = 1.5 and 2 compared to the modified Van der Meer formulae by Van Gent et al. (2004).

Stability numbers with different characteristic wave heights are compared in Fig. 9 with the use of the present data. It is seen from the figure that the scatter is significantly reduced by using H_{m0} in the stability number, which also was observed by Herrera et al. (2017) on a 1:50 foreshore. Using H_{m0}, the 1:30 and 1:100 data come together.

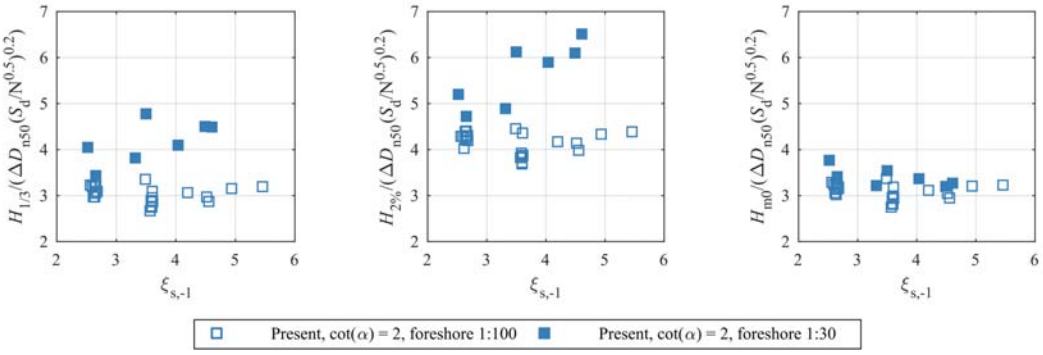

Figure 9: Present data with front slope cot(α) = 2 compared to stability numbers with different characteristic wave heights.

4. EXISTING STABILITY DATA BY VAN GENT ET AL. (2004)

A reliable notional permeability factor is important when estimating the stability of rubble mound breakwaters. Van Gent et al. (2004) did not fit any notional permeability factors for their tests, but simply assumed different notional permeability factors based

on experience. The notional permeability factors can be fitted for each structure based on the stability results and the modified Van der Meer formulae by Van Gent et al. (2004). However, the variation of $\xi_{s,-1}$ is small for each structure tested by Van Gent et al. (2004) and thus the fitting of the notional permeability factor would be unreliable. Therefore, in the present study the notional permeability factors for their structures are estimated with the Eldrup et al. (2019) formula. Van Gent et al. (2004) only gave information on the armour and core material size D_{n50}. Therefore, it is assumed that the armour layer had a thickness of $2D_{n50}$ and that no filter layers were used in the tests with a permeable core. The tests with an impermeable core are assumed to have a thin filter layer, see Table 3. Based on these assumptions, notional permeability factors given in Table 3 were estimated.

Table 3: Estimated notional permeability factors based on the formula by Eldrup et al. (2019).

Structure, cf. Van Gent et al. (2004)	1	2	3	4	5	6	7
Core $D_{n50,core}$	0.01	0.01	0.01	0.009	0.009	-	-
Assumed filter, $D_{n50,filter}$	-	-	-	-	-	0.006	0.006
Assumed filter thickness	-	-	-	-	-	$0.5D_{n50,armour}$	$0.5D_{n50,armour}$
Armour $D_{n50,armour}$	0.035	0.022	0.022	0.026	0.026	0.026	0.026
Assumed armour thickness	$2.0D_{n50,armour}$	$2.0D_{n50,armour}$	$2.0D_{n50,armour}$	$2.0D_{n50,armou}$	$2.0D_{n50,armour}$*	$2.0D_{n50,armour}$	$2.0D_{n50,armour}$
Notional permeability factor, P	0.39	0.49	0.49	0.43	0.43	0.1	0.1

5. NEW STABILITY FORMULA AND COMPARISON WITH EXISTING FORMULAE

It has been shown that the existing stability formulae are highly conservative for the present data with highly nonlinear waves and thus improved stability formulae are needed. For the present tests with highly nonlinear waves on a 1:30 foreshore it was observed that H_{m0} described the stability better (see Fig. 9). Furthermore, Van Gent et al. (2004) observed that the wave period $T_{-1,0}$ reduced the scatter of the stability results when comparing broken and non-breaking waves. For design purpose, H_{m0} and $T_{-1,0}$ are also very robust wave parameters compared to a low exceedance wave height like $H_{2\%}$. Furthermore, H_{m0} and $T_{-1,0}$ are typical the output parameters from numerical spectral wave models and thus they are typically available for the design without use of empirical relations. This is not the case with time domain parameters, where a wave height distribution is needed. The new formula is fitted to the data by Van Gent et al. (2004), Eldrup et al. (2019) and the present tests.

In the surging domain the stability is almost independent of the surf similarity parameter when using H_{m0} and $T_{-1,0}$ as wave parameters, cf. Fig. 10. However, Van der Meer (1988) observed that for permeable and homogenous structures the stability increased in the surging domain. This deviation might be a difference when comparing deep water conditions with shallow foreshore conditions. In the surging domain very few data with $\cot(\alpha) > 2$ are available, cf. Fig. 10. The scares amount of data seems though

225 to indicate that stability does not increase with the slope angle for cot(α) > 2. Finally, in the plunging domain the stability decreases
226 with increasing surf similarity parameter. The relation between damage and number of waves have not been verified in the present
227 study, but the relation found by Van der Meer (1988) is assumed valid also for shallow water conditions. The new stability formula
228 reflecting the fitted lines in Fig. 10 reads:
229

Surf similarity:

$$\xi_{-1,0} = \frac{\tan(\alpha)}{\sqrt{\frac{2\pi H_{m0}}{g T_{-1,0}^2}}}$$

Plunging waves ($\xi_{-1,0} < \xi_{-1,0,cr}$):

$$\frac{H_{m0}}{\Delta D_{n50}} = c_{plunging} \left(\frac{S_d}{\sqrt{N}}\right)^{0.2} 1.6^P \xi_{-1,0}^{(0.4P-0.67)} \quad (4)$$

Surging waves ($\xi_{-1,0} \geq \xi_{-1,0,cr}$):

$$\frac{H_{m0}}{\Delta D_{n50}} = c_{surging} \left(\frac{S_d}{\sqrt{N}}\right)^{0.2} P^{0.17} \min\{\cot(\alpha), 2\}^{0.23}$$

Transition between plunging and surging formula:

$$\xi_{-1,0,cr} = \left(\frac{c_{surging} P^{0.17} \min\{\cot(\alpha),2\}^{0.23}}{c_{plunging} 1.6^P}\right)^{\frac{1}{0.4P-0.67}}$$

230

231 Here $\Delta = \rho_{armour}/\rho_{water} - 1$ is the reduced relative density of the armour stones. $D_{n50} = \sqrt[3]{W_{50}/\delta_{armour}}$ is the nominal size of the
232 armour stones. P is the notional permeability factor. α is the angle of the seaward slope of the structure. $\xi_{-1,0}$ is the surf similarity
233 parameter calculated with the deep water linear wave formula based on incident $T_{-1,0}$ and H_{m0} at the toe of the structure. N is the
234 number of waves (not more than 8,500 waves should be used). For the mean value estimations are $c_{plunging} = 4.5$, $c_{surging} = 3.1$.
235

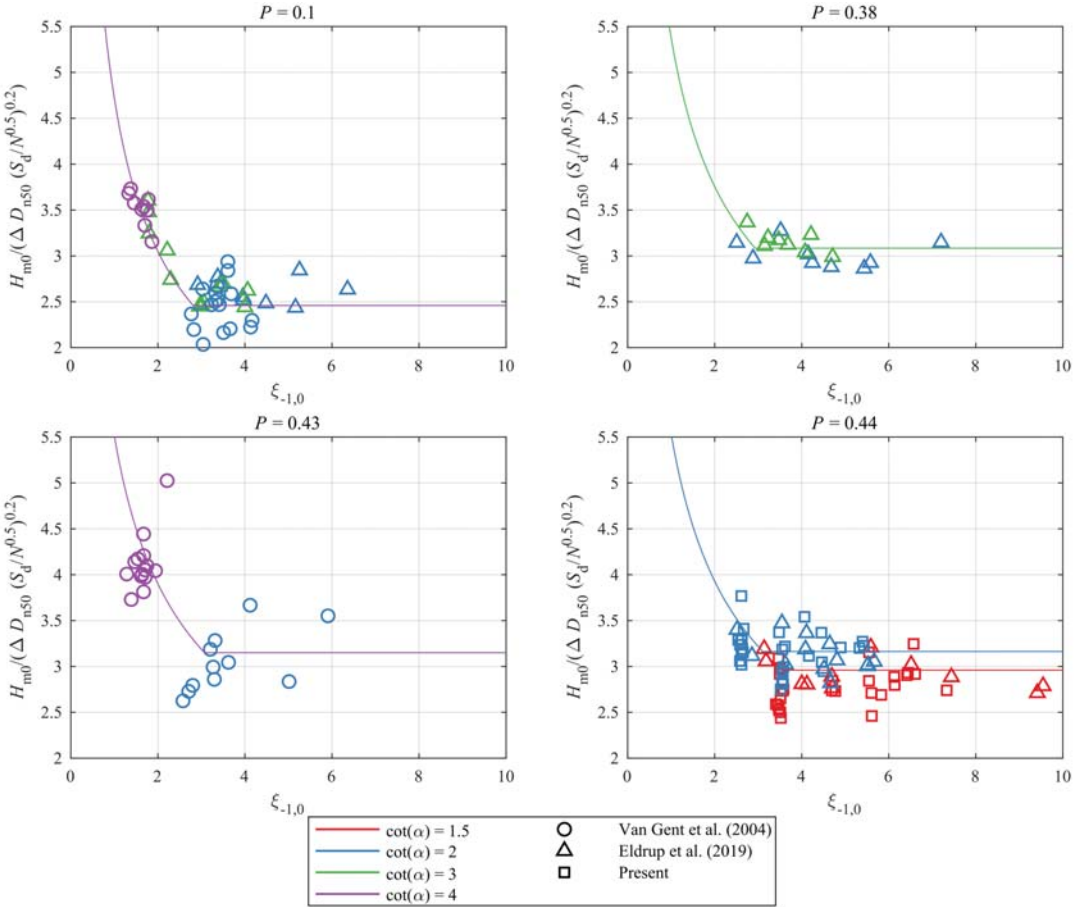

Figure 10: Present stability formulae compared to four different *P* factors.

Fig. 11 shows the same data as Fig. 10 but with the modified Van der Meer formulae by Van Gent et al. (2004). Comparing Figs. 10 and 11 a clear difference is seen in the surging domain for $P = 0.38$ and $\cot(\alpha) = 2$. In Fig. 11 it is clear that the stability increases in the surging domain, which is not seen in Fig. 10. The difference is caused by the ratio of $H_{2\%}/H_{m0}$ which is highly dependent on the nonlinearity and breaking of the waves. For the nonlinear nonbreaking waves, the ratio $H_{2\%}/H_{m0}$ increases which is why the stability also seems to increase. By using H_{m0} instead of $H_{2\%}$, better predictions are also obtained for the present tests with a 1:30 foreshore. This is seen when comparing Fig. 10 and Fig. 11 for $P = 0.44$ and $\cot(\alpha) = 2$, where some of the present tests are significantly more stable than predicted in Fig. 11. This overprediction is not present in Fig. 10.

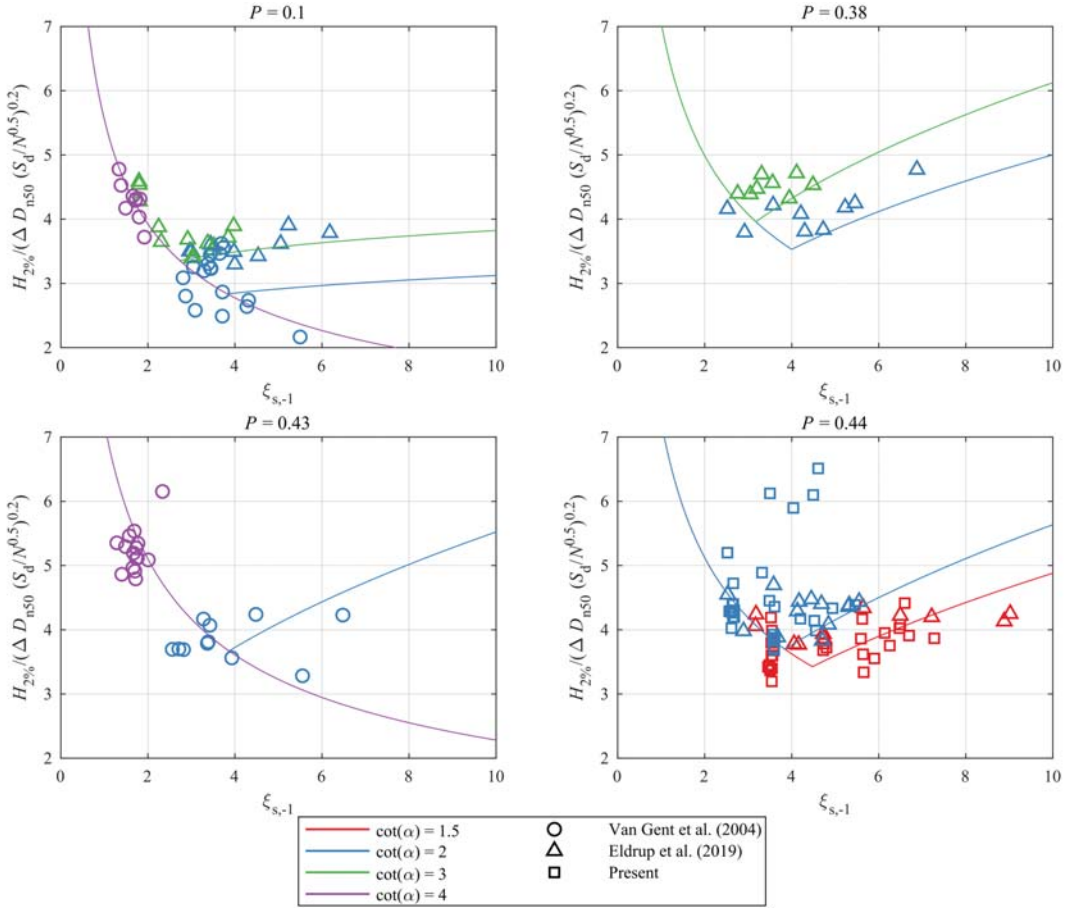

Figure 11: Modifed Van der Meer formulae by Van Gent et al. (2004) compared to four different *P* factors.

6. RELIABILITY ANALYSIS OF STABILITY FORMULAE

The coefficient of variation *CV* on the difference between the measured and predicted S_d for damage levels between $0 < S_d < 1.5S_{d,failure}$ are shown for each formula and layer composition in Table 4. $S_{d,failure}$ is the damage level where failure occur for each front slope angle as described by Van der Meer (1988). For the data by Van Gent et al. (2004) the present formulae show the lowest CV values for two of the compositions while the Van Gent et al. (2004) formulae shows lower CV values for the two other layer compositions. For the Eldrup et al. (2019) as well as the present data, the present formulae show lowest *CV* values for all the layer compositions tested. Significantly difference between the present formulae and the modified Van der Meer formulae by Van Gent

et al. (2004) are observed for the present data with a 1:30 foreshore where highly nonlinear waves with shallow foreshore conditions were tested. Considering all the used data, the present formulae shows a significant lower uncertainty than the modified Van der Meer formulae by Van Gent et al. (2004). Moreover, all data groups have rather similar uncertainty with the present formulae.

Table 4: Coefficient of variation on the difference between measured and predicted S_d.

Dataset	*P*	New formulae	Modifed Van der Meer formulae
Van Gent et al. (2004)	0.10	0.36	0.44
	0.39	0.26	0.39
	0.43	0.37	0.32
	0.49	0.39	0.27
Eldrup et al. (2019)	0.10	0.30	0.82
	0.28	0.19	0.68
	0.32	0.28	0.79
	0.38	0.21	0.74
	0.44	0.27	0.54
	0.45	0.25	0.38
Present	0.44 (1:100)	0.39	0.56
	0.44 (1:30)	0.40	6.85
All data	-	0.39	0.86

Fig. 12 shows the measured and predicted damage for each formula with the 90% confidence band. In order to include small damage levels inside the confidence band a constant damage value δ is added to S_d in the stability formulae. Furthermore, the coefficients $c_{plunging}$ and $c_{surging}$ are changed with a factor β. δ = 1 leads to an acceptable band for small damage levels and β is adjusted until 90% of the data are inside the confidence band. The 90% confidence band is established based on the 5% and 95% damage values which for the new formulae can be predicted with the values of δ, $c_{plunging}$ and $c_{surging}$ given in Table 5. Using the same δ values the β values have been calculated also for the modified Van der Meer formulae by Van Gent et al. (2004), cf. Fig. 12.

Table 5: Confidence levels for Eq. 4.

Exceedance level	$c_{plunging}$	$c_{surging}$	δ
5%	5.04	3.41	-1
Mean	4.50	3.10	0
95%	4.02	2.82	1

Fig. 12 shows that the present formulae has the lowest β coefficient. The largest β coefficient is observed for the Van Gent et al. (2004) surging formula with large deviations of the present tests with highly nonlinear waves on a 1:30 foreshore. The Van Gent et al. (2004) plunging formula shows a single significant outlier.

The measured vs predicted damage S_d is separated into the different notional permeability factors, front slopes and data sets in the appendix and shown in Figs. 13 - 14.

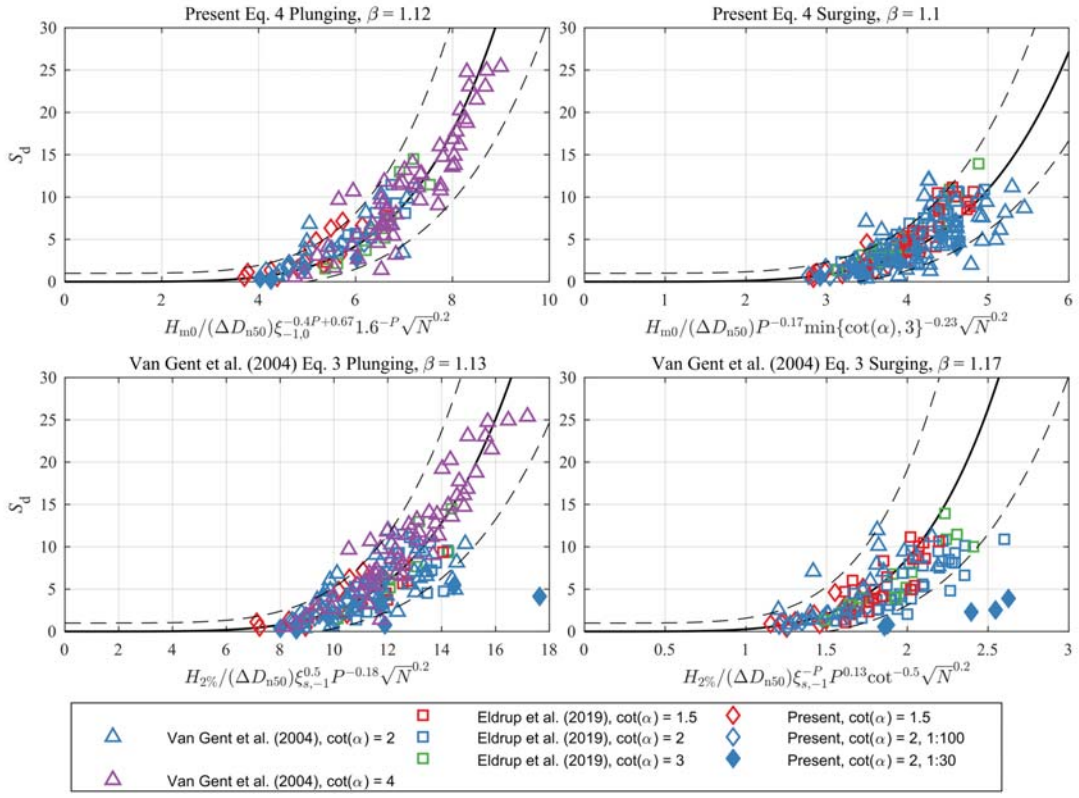

Figure 12: Comparison of the present formulae and the modified Van der Meer formulae by Van Gent et al. (2004).

7. CONCLUSION

The present paper presents new stability formulae valid for shallow foreshore wave conditions based on existing and new stability tests on rubble mound breakwaters. In the present tests the breakwaters consisted of a core and an armour layer. Both a 1:100 and a 1:30 foreshore were tested. The Modified Van der Meer formula by Van Gent et al. (2004) showed to be reliable for the 1:100 foreshore tests. However, the formulae underestimated the stability significantly for a part of the present tests with the 1:30 foreshore. These tests included highly nonlinear waves, but not broken waves as tested by Van Gent et al. (2004). The reason for the discrepancies with the modifed Van der Meer formulae for these tests seems to be a significant difference between the spectral wave height and the significant wave height ($1.22 < H_{1/3}/H_{m0} < 1.41$) which can be observed for highly nonlinear waves in shallow water. The scatter in the stability results for the two different foreshore slopes was insignificant when the spectral wave height H_{m0} was used instead of $H_{1/3}$ or $H_{2\%}$ in the stability number.

New stability formulae were derived based on H_{m0} and $T_{-1,0}$. The present formulae showed similar reliability as the Modified Van der Meer formulae on the data by Van Gent et al. (2004). For the data by Eldrup et al. (2019) and the present tests, the present formulae lead to a significantly smaller uncertainties than the modified Van der Meer formulae. Based on all the data sets, the present formulae showed to be a significant improvement. Additionally, H_{m0} and $T_{-1,0}$ are robust wave parameters typical output parameters from numerical spectral models which further increases the reliability of the new formulae for design purpose.

The present formulae are based on 1:30 and 1:100 foreshores, and more research is needed for gentler and steeper foreshore slopes to prove the validity covering the entire interval from deep water conditions to extremely shallow foreshores on various slopes. Tests with permeable or homogenous layer compositions with wave conditions in the surging domain are necessary to clarify when the increasing stability observed by Van der Meer (1988) are present in shallow water. Furthermore, tests with extremely shallow foreshore conditions are needed in order to investigate if the constant stability in the surging domain is also valid for $\xi_{-1,0} >> 10$.

291 **REFERENCES**

292 Aalborg University, 2018a. AwaSys 7 [WWW Document]. URL www.hydrosoft.civil.aau.dk/awasys

293 Aalborg University, 2018b. WaveLab [WWW Document]. URL www.hydrosoft.civil.aau.dk/wavelab

294 Aalborg University, 2016. EPro [WWW Document]. URL www.hydrosoft.civil.aau.dk/epro/

295 Dai, Y.B., Kamel, A.M., 1969. SCALE EFFECT TESTS FOR RUBBLE-MOUND BREAKWATERS: Hydraulic Model Investigation.
296 Mississippi.

297 Eldrup, M.R., Andersen, T.L., 2019. Applicability of Nonlinear Wavemaker Theory. J. Mar. Sci. Eng. 7, 14.
298 https://doi.org/10.3390/jmse7010014

299 Eldrup, M.R., Lykke Andersen, T., 2019. Estimation of Incident and Reflected Wave Trains in Highly Nonlinear Two-Dimensional
300 Irregular Waves. J. Waterw. Port, Coastal, Ocean Eng. 145. https://doi.org/10.1061/(ASCE)WW.1943-5460.0000497

301 Eldrup, M.R., Lykke Andersen, T., Burcharth, H.F., 2019. Notional Permeability for Rubble Mound Breakwaters. Submitt. to Coast.
302 Eng.

303 Goda, Y., 2010. Reanalysis of Regular and Random Breaking Wave Statistics. Coast. Eng. J. 52, 71–106.
304 https://doi.org/10.1142/S0578563410002129

305 Herrera, M.P., Gómez-Martín, M.E., Medina, J.R., 2017. Hydraulic stability of rock armors in breaking wave conditions. Coast. Eng.
306 127, 55–67. https://doi.org/10.1016/j.coastaleng.2017.06.010

307 Hofland, B., Chen, X., Altomare, C., Oosterlo, P., 2017. Prediction formula for the spectral wave period T m-1,0 on mildly sloping
308 shallow foreshores. Coast. Eng. 123, 21–28. https://doi.org/10.1016/j.coastaleng.2017.02.005

309 Hudson, R.Y., 1959. Laboratory Investigation of Rubble-Mound Breakwaters. J. Waterw. Harb. Div. 85, 93–122.

310 Hughes, S.A., 2004. Wave momentum flux parameter: a descriptor for nearshore waves. Coast. Eng. 51, 1067–1084.
311 https://doi.org/10.1016/j.coastaleng.2004.07.025

312 Irribarren, R.., 1938. Una formula para el calcula de los diques de escollera (A formula for the calculation of rock-fill dikes).
313 Pasajes, Guipúzcoa.

314 Klopman, G., Meer, J.W. van der, 1999. Random Wave Measurements in Front of Reflective Structures. J. Waterw. Port, Coastal,
315 Ocean Eng. https://doi.org/10.1061/(ASCE)0733-950X(1999)125:1(39)

316 Kweon, H.-M., Goda, Y., 1996. A Parametric Model for Random Wave Deformation by Breaking on Arbitrary Beach Profiles, in:
317 Coastal Engineering 1996. American Society of Civil Engineers, New York, NY, pp. 261–274.
318 https://doi.org/10.1061/9780784402429.021

319 Lykke Andersen, T., Clavero, M., Eldrup, M.R., Frigaard, P., Losada, M., 2018. Active Absorption of Nonlinear Irregular Wwaves,
320 in: Proceedings of the Coastal Engineering Conference. Baltimore, USA.

321 Lykke Andersen, T., Clavero, M., Frigaard, P., Losada, M., Puyol, J.I., 2016. A new active absorption system and its performance
322 to linear and non-linear waves. Coast. Eng. 114, 47–60. https://doi.org/10.1016/j.coastaleng.2016.04.010

323 Lykke Andersen, T., Eldrup, M.R., Clavero, M., 2019. Separation of Long-Crested Nonlinear Bichromatic Waves into Incident and
324 Reflected Components. J. Mar. Sci. Eng. 7.
325 Lykke Andersen, T., Eldrup, M.R., Frigaard, P., 2017. Estimation of incident and reflected components in highly nonlinear regular
326 waves. Coast. Eng. 119. https://doi.org/10.1016/j.coastaleng.2016.08.013
327 Madsen, P.A., Sørensen, O.R., 1992. A new form of the Boussinesq equations with improved linear dispersion characteristics. Part
328 2. A slowly-varying bathymetry. Coast. Eng. 18, 183–204. https://doi.org/10.1016/0378-3839(92)90019-Q
329 Melby, J.A., Hughes, S.A., 2004. Armor Stability Based on Wave Momentum Flux, in: Coastal Structures 2003. American Society
330 of Civil Engineers, Reston, VA, pp. 53–65. https://doi.org/10.1061/40733(147)5
331 Muttray, M., Reedijk, B., 2009. REANALYSIS OF BREAKWATER STABILITY WITH STEEP FORESHORE, in: Coastal
332 Engineering 2008. World Scientific Publishing Company, pp. 3346–3357. https://doi.org/10.1142/9789814277426_0277
333 Schäffer, H.A., 1996. Second-order wavemaker theory for irregular waves. Ocean Eng. 23, 47–88. https://doi.org/10.1016/0029-
334 8018(95)00013-B
335 Tavakkol, S., Lynett, P., 2017. Celeris: A GPU-accelerated open source software with a Boussinesq-type wave solver for real-time
336 interactive simulation and visualization. Comput. Phys. Commun. 217, 117–127. https://doi.org/10.1016/j.cpc.2017.03.002
337 Thompson, D.M., Shuttler, R.M., 1975. Riprap design for wind-wave attack, a laboratory study in random waves.
338 Van der Meer, J.W., 1988. Rock slopes and gravel beaches under wave attack. Delft Hydraulics.
339 Van der Meer, J.W., 1985. Stability of rubble mound revetments and breakwaters, in: Proc. ICE, Developments in Breakwaters. p.
340 Discussion pp 191-202.
341 Van Gent, M.R.A., Smale, A.J., Kuiper, C., 2004. Stability of Rock Slopes with Shallow Foreshores, in: Coastal Structures 2003.
342 American Society of Civil Engineers, Reston, VA, pp. 100–112. https://doi.org/10.1061/40733(147)9
343 Zhang, H., Schäffer, H.A., Jakobsen, K.P., 2007. Deterministic combination of numerical and physical coastal wave models. Coast.
344 Eng. 54, 171–186. https://doi.org/10.1016/j.coastaleng.2006.08.009
345
346

347 **APPENDIX**

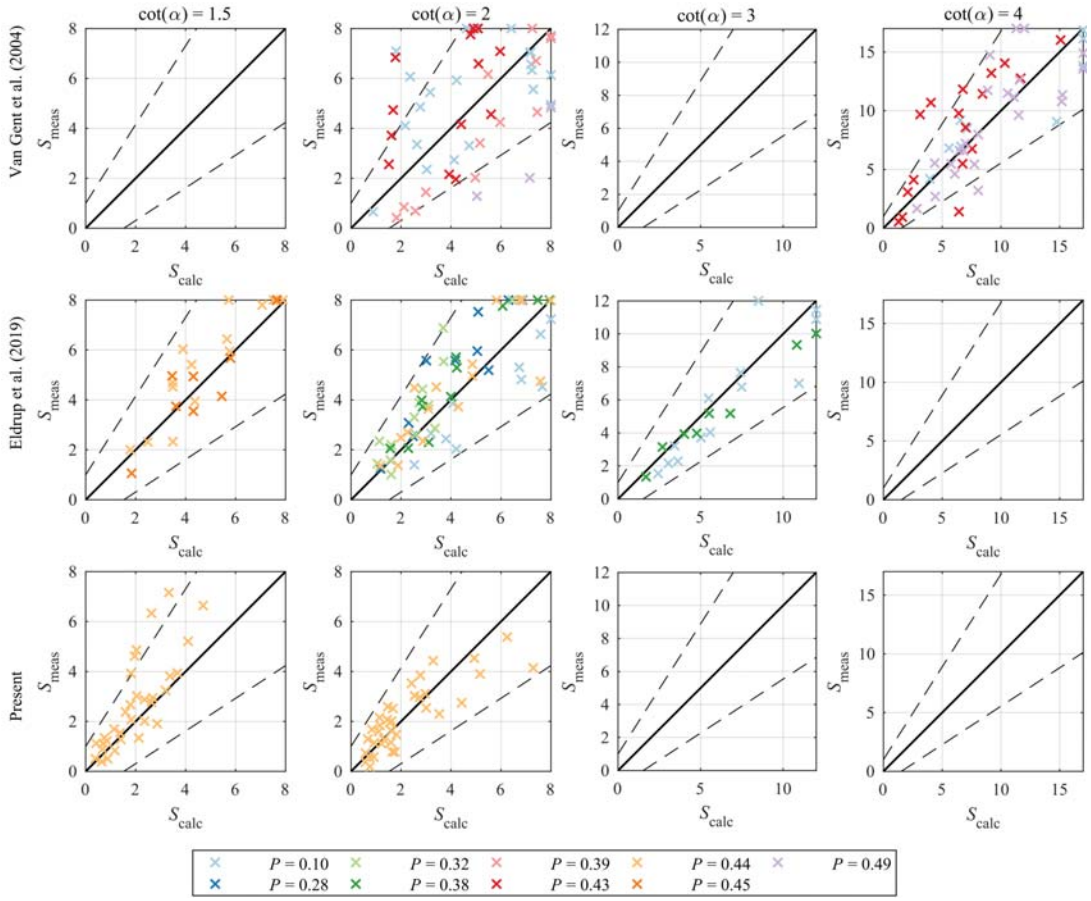

Figure 13: Measured damage compared to the predicted damage by the present formulae. Confidence bands are those valid for the present surging formula. Data outside the figure is plotted on the edge.

348

349

350

351

352

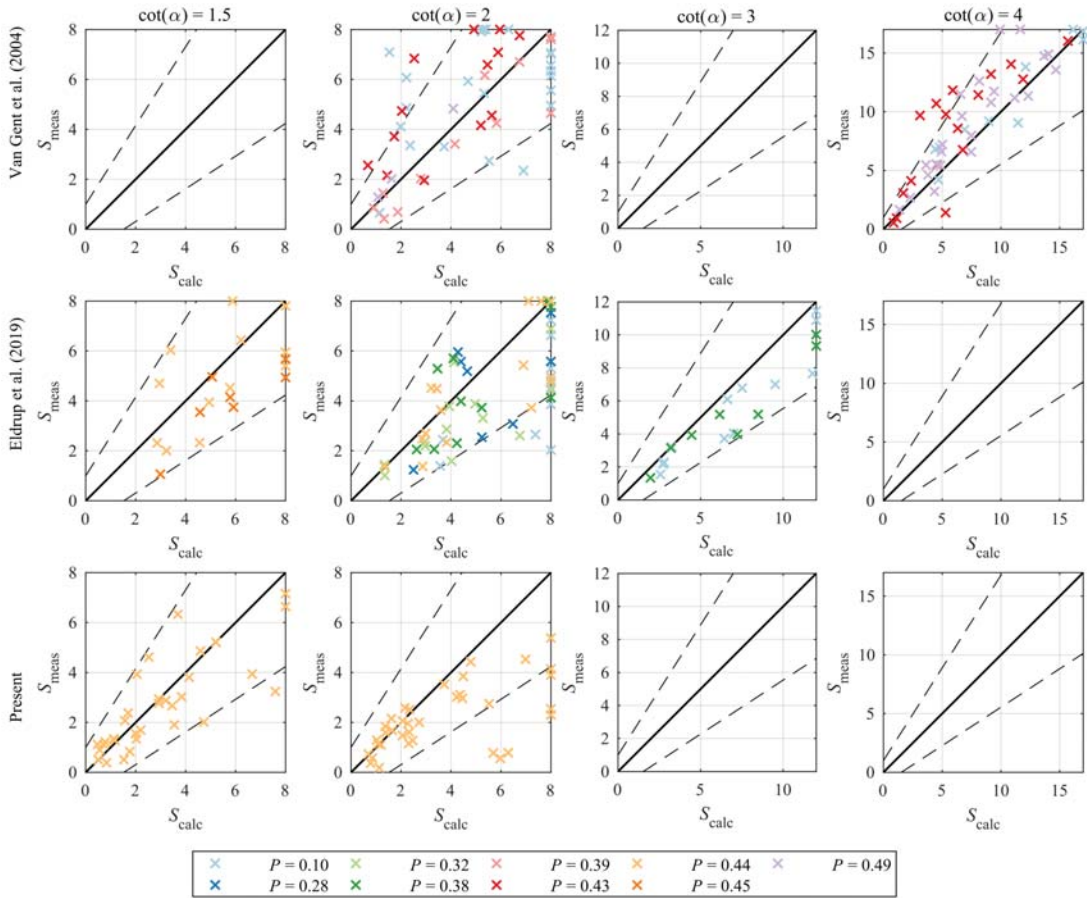

Figure 14: Measured damage compared to the predicted damage of the modified Van der Meer formulae by Van Gent et al. (2004). Confidence bands are those valid for the present surging formula. Data outside the figure is plotted on the edge.

353

Paper F

Overtopping on Rubble Mound Breakwaters for Low Steepness Waves in Deep and Depth Limited Conditions

Nicole Færch Christensen
Mads Røge Eldrup
Jonas Bjerg Thomsen
Thomas Lykke Andersen
Hans Falk Burcharth
Jørgen Quvang Harck Nørgaard

The paper has been published in
Coastal Engineering Proceedings, ISSN 2156-1028, 1(34), 2014
DOI: https://doi.org/10.9753/icce.v34.structures.6

OVERTOPPING ON RUBBLE MOUND BREAKWATERS FOR LOW STEEPNESS WAVES IN DEEP AND DEPTH LIMITED CONDITIONS

Nicole Færch Christensen[1], Mads Sønderstrup Røge[1], Jonas Bjerg Thomsen[1], Thomas Lykke Andersen[1], Hans F. Burcharth[1], Jørgen Quvang Harck Nørgaard[1]

In this paper, the investigation of overtopping on rubble mound breakwaters for low steepness waves in both deep and shallow-water conditions are presented. The existing formulae provide quite different results for long waves for both conventional and berm breakwaters. Therefore, new model tests with focus on long waves have been performed for both types of breakwaters. The new model tests showed some deviation from the formulae. Therefore, limitations in the use of the present methods and an update for one of the methods are presented.

Keywords: overtopping; conventional rubble mound breakwater; berm breakwater; long waves

INTRODUCTION

Wave overtopping is an important quantity to investigate when constructing a breakwater as it sets restrictions to the crest level for proper functioning of the breakwater and areas behind.

Wave overtopping on rubble mound breakwaters has been analysed by several authors, and has led to different methods for prediction of the mean overtopping discharge. The EurOtop Manual (2007) provides two formulae depending on the surf similarity; one for breaking waves and one for non-breaking waves. For the non-breaking waves the overtopping reaches an upper limit, and the overtopping becomes independent on the wave steepness. The EurOtop Manual (2007) does not state a validity range for the formulae, which may lead to unreliable results for conditions outside of the validated area. Furthermore, the procedure for calculation of the overtopping discharge described for rubble mound breakwaters is not always clear, since needed information is not given in the same chapter.

For berm breakwaters, Lykke Andersen (2006) proposed an overtopping formula based on several model tests. The formula depends on the sea state, geometric parameters, and a stability parameter, which describe the reshaping of the breakwater. The formula predicts an increase in overtopping with decreasing wave steepness. The formula is based on model tests with wave steepness $s_{0p} > 0.01$.

The CLASH Neural Network (Van Gent et al. (2007)) is a prediction tool based on a database with more than 10,000 model tests from several laboratories. Even though the method includes a variety of geometries and sea state conditions for both conventional and berm breakwaters, there is a lack of data in certain fields of application. The CLASH Neural Network predicts an increase in overtopping with decreasing wave steepness. The method is applicable for wave steepness $s_{0p} > 0.003$.

The existing overtopping formulae provide a significant difference in the predicted overtopping discharges, especially for low steepness waves, which are often referred to as long waves.

The purpose of the present study is to investigate the overtopping for both conventional and berm breakwaters, especially for long waves in both deep and depth-limited conditions. The presented model test results are not corrected for possible scale effects as they are compared solely to formulae that are also based on model tests. The existing formulae and their validity ranges are discussed based on the new model tests.

MODEL TESTS AND OVERTOPPING MEASUREMENT

The overtopping data used in this paper was measured in the tests presented in Røge et al. (2014) for conventional breakwaters, and in Thomsen et al. (2014) for the berm breakwaters. For details about the model set-up, tests programme and wave generation see these papers.

The tested conditions are given in Table 1 for both conventional and berm breakwaters. All the tests were performed on a statically stable structure with only little damage.

[1] Department of Civil Engineering, Aalborg University, Sofiendalsvej 9-11, DK-9200 SV, Denmark, nicolefaerch@hotmail.com, msr@civil.aau.dk, jbt@civil.aau.dk, tla@civil.aau.dk, hansburcharth@gmail.com, jhn@civil.aau.dk

Table 1: Tested parameters.		
	Conventional breakwater	Berm breakwater
Deep water peak wave steepness, s_{0p}	0.004 - 0.042	0.004-0.040
Relative depth, H_{m0}/h	0.13 - 0.46	0.15-0.50
Relative freeboard, A_c/H_{m0}	0.95 - 7.11	1.17-3.63
Front slope, cot α	1.5, 2.0, 3.0	1.25, 1.5
Reynold number, Re	$3.03 \cdot 10^4$ - $4.47 \cdot 10^4$	$2.14 \cdot 10^4$ - $3.05 \cdot 10^4$

The overtopping discharge was measured by a 0.30 m wide overtopping tank with a depth gauge. When the water level reached a certain level a pump automatically emptied the tank. The set-up with the overtopping tank is shown in Fig. 1.

Figure 1: Set-up of overtopping tank.

Example of measured overtopping time series is shown in Fig. 2.

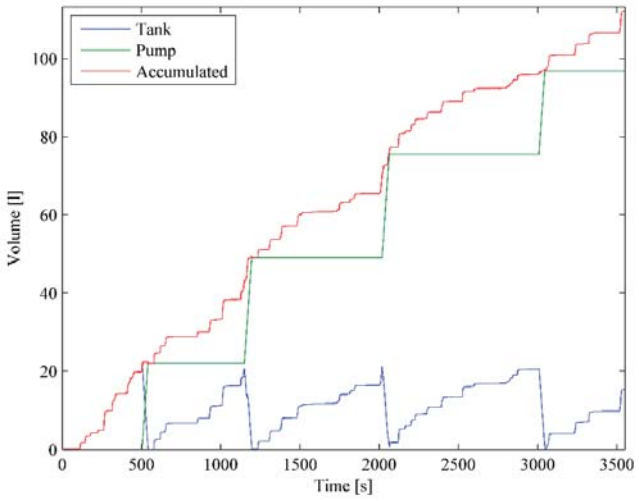

Figure 2: Example of overtopping time series.

SCALE EFFECTS

It has been shown both experimentally and by full scale measurements that significant scale effects occur related to small wave overtopping discharges on rubble mounds, cf. Burcharth (2004), Helgason and Burcharth (2006), Burcharth and Lykke Andersen (2007), EurOtop Manual (2007) and Lykke Andersen et al. (2011).

Model tests are considered unreliable due to scale effects when the dimensionless overtopping volumes are smaller than 10^{-6}. The CLASH Neural Network gives an adjusted estimation if scale effects are present. EurOtop (2007) and Lykke Andersen et al. (2011) provide procedures to scale the overtopping from model scale to prototype. These methods are not used in the present paper since the new model tests are compared with formulae based on model tests.

It is not known if scale effects exist in the present tests with waves with low wave steepness. EurOtop (2007) states that no scale effects are present for a roughness factor > 0.9. For waves with a low wave steepness, it is shown in the present study that the roughness factor increases and thereby no or only small scale effects are expected. Until prototype or large scale tests have been compared with the present model tests it is recommended to use the existing procedure to compensate for scale effects to obtain safe results.

EVALUATION OF EXISTING FORMULAE FOR CONVENTIONAL BREAKWATERS

EurOtop Manual (2007) has presented formulae based on several tests, but no ranges of validity by means of wave conditions and structural conditions are given for the formulae. Eq. (1) and (2) provide the dimensionless average wave overtopping discharge for head on waves and no superstructure.

$$\frac{q}{\sqrt{g\,H_{m0}^3}} = \frac{0.067}{\sqrt{\tan\alpha}}\,\gamma_b\,\xi_{m\text{-}1,0}\,exp\left(-4.75\,\frac{A_c}{H_{m0}}\,\frac{1}{\xi_{m\text{-}1,0}\,\gamma_b\,\gamma_f}\right) \tag{1}$$

with a maximum discharge given by:

$$\frac{q}{\sqrt{g\,H_{m0}^3}} = 0.2\,exp\left(-2.6\,\frac{A_c}{H_{m0}}\,\frac{1}{\gamma_f}\right) \tag{2}$$

where q is the average wave overtopping per unit length, H_{m0} the significant wave height in the frequency domain at the toe of the structure, A_c the crest height above still water level, α the front slope angle and $\xi_{m\text{-}1,0}$ the surf similarity parameter given by the spectral wave period $T_{m\text{-}1,0}$ and defined in Eq. (3).

$$\xi_{m\text{-}1,0} = \frac{\tan\alpha}{\sqrt{s_{m\text{-}1,0}}},\quad s_{m\text{-}1,0} = \frac{H_{m0}}{L_{m\text{-}1,0}} \tag{3}$$

The effect of roughness and permeability of the structure is included through the influence factor γ_f. For two-layer armour rocks on a permeable core, the roughness factor is $\gamma_f = 0.4$.

Another method for prediction of the overtopping discharge is the CLASH Neural Network (Van Gent et al. 2007), which is based on a database with a large amount of overtopping tests. To use this model, different geometrical and wave parameters have to be specified including the roughness factor which is $\gamma_f = 0.5$ for two layer armour rocks on a permeable core.

The measured overtopping in the new model tests is plotted in Fig. 3 against the overtopping determined by the EurOtop (2007) formula and the CLASH Neural Network method. The data is separated for different wave steepnesses in deep-water conditions $H_{m0}/h \leq 0.2$ and shallow-water conditions $H_{m0}/h > 0.2$.

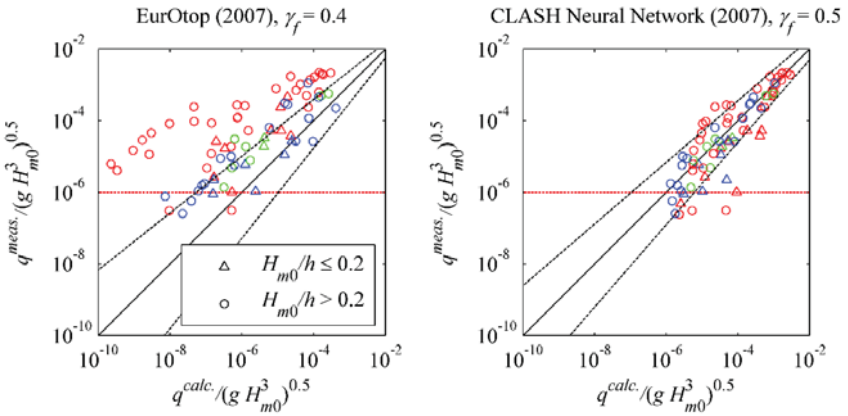

Figure 3: Comparison between calculated and measured dimensionless overtopping for conventional breakwater. Red: $s_{0m} \le 0.015$, green: $0.015 < s_{0m} \le 0.030$, blue: $s_{0m} > 0.030$. The dashed lines are the 90% confidence band. The red dashed line illustrates low overtopping, where large scale effects may exist.

Fig. 3 shows that the formulae by EurOtop (2007) provide a significant underestimation for long waves (red markers) for conventional breakwaters. The figure also indicates that the overtopping increases for long waves, which is not included in the upper limit (Eq. (2)) in the formulae by EurOtop (2007). In general, the CLASH Neural Network method provides a reliable estimate for the present tests, although some scatter for the small overtopping discharges is present. As illustrated in the figure, the CLASH Neural Network does not give any prediction for dimensionless overtopping smaller than 10^{-6}, and it provides less reliable results for measured values below 10^{-5}. In such cases only a few waves overtop and the scatter will be much higher.

For the long waves a large volume of water hits the breakwater which fills the pores with water and causes most of the flow to be in the outer layer of the breakwater. To include this effect in the overtopping formulae by EurOtop (2007), the roughness factor γ_f in Eq. (2) should depend on the wave steepness. When estimating run-up by EurOtop (2007) the upper limit is using a roughness factor, $\gamma_{fsurging}$, that depends on the wave steepness (see Eq. (4)). Therefore it is proposed to introduce in Eq. (2) the roughness factor defined by Eq. (4).

$$\gamma_{fsurging} = \gamma_f + \frac{\left(\xi_{m-1,0}\text{-}1.8\right)\left(1\text{-}\gamma_f\right)}{8.2} \tag{4}$$

When using $\gamma_{fsurging}$ in Eq. (2) much less scatter is obtained as illustrated in Fig. 4. The measured values below $q/\left(g\,H_{m0}^3\right)^{0.5} < 10^{-6}$ provide some scatter which is because a few waves are overtopping.

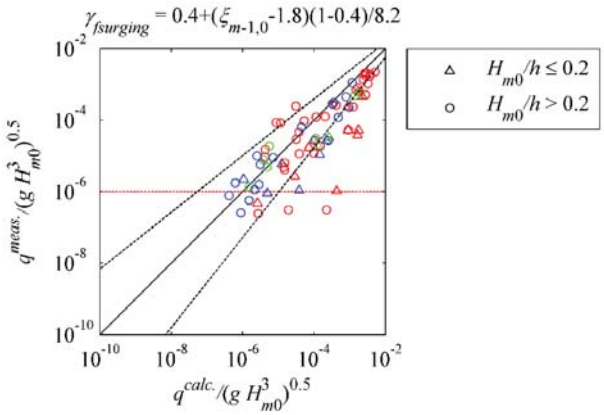

Figure 4: **Comparison between calculated and measured dimensionless overtopping for conventional breakwater by the formulae by EurOtop (2007) with adjusted roughness γ_f. Red: $s_{0m} \le 0.015$, green: $0.015 < s_{0m} \le 0.030$, blue: $s_{0m} > 0.030$. The dashed lines are the 90% confidence band. The red dashed line illustrates low overtopping, where large scale effects may exist.**

EVALUATION OF EXISTING FORMULAE FOR BERM BREAKWATERS

To use the formulae by EurOtop (2007) for berm breakwaters additional factors have to be included. When the upper and lower front slope of the breakwater are different, an average slope has to be calculated by Eq. (5), where L_{slope} is the horizontal length of the breakwater from 1.5 H_{m0} below SWL to $z_{2\%}$ (cf. Eq. (7) and (8)) above SWL.

$$\tan\alpha = \frac{1.5H_{m0} + z_{2\%}}{L_{slope} - B} \tag{5}$$

The influence of a berm is included by γ_b defined in Eq. (6) consisting of two parts; one that takes the berm width B into account and one that takes the elevation of the middle of the berm in relation to the SWL h_b into account. The influence of a berm is largest when the berm is at SWL and decreases for larger or smaller berm elevations.

$$\gamma_b = 1 - \frac{B}{L_{berm}}\left(0.5 + 0.5\cos\left(\pi\frac{h_b}{x}\right)\right) \text{ with } 0.6 \le \gamma_b \le 1.0$$
$$x = \begin{cases} z_{2\%} & \text{for } z_{2\%} > -h_b > 0 \\ 2H_{m0} & \text{for } 2H_{m0} > h_b \ge 0 \end{cases} \tag{6}$$

Here h_b is the water depth above the berm, L_{berm} is the horizontal length of the breakwater from H_{m0} below the berm to H_{m0} above the berm and $z_{2\%}$ is the run-up height exceeded by 2% of the incident waves predicted by iteration of Eq. (7) and (8).

$$\frac{z_{2\%}}{H_{m0}} = 1.65\,\gamma_b\,\gamma_f\,\xi_{m-1,0} \tag{7}$$

with a maximum of:

$$\frac{z_{2\%}}{H_{m0}} = \gamma_{fsurging}\left(4.0 - \frac{1.5}{\sqrt{\xi_{m-1,0}}}\right) \tag{8}$$

For hardly and partly reshaping berm breakwaters Sigurdarson and Van der Meer (2013) proposed another roughness factor $\gamma_f = \gamma_{BB}$ given by Eq. (9) to be used in the upper limit of the overtopping defined in Eq. (2). This makes the overtopping for berm breakwaters (steep slopes) dependent on the wave steepness opposed to formulae for conventional rubble mound breakwaters.

$$\gamma_{BB} = 0.68 - 4.5 s_{0p} - 0.05 B/H_s \tag{9}$$

Another formula to determine overtopping on berm breakwaters is given by Lykke Andersen (2006):

$$\frac{q}{\sqrt{g\,H_{m0}^3}} = 1.79\cdot 10^{-5}\left(f_{H0}^{1.34} + 9.22\right) s_{0p}^{-2.52} \exp\left(-5.63 R_*^{0.92} - 0.61 G_*^{1.39} - 0.55 h_{b*}^{1.48} B_*^{1.39}\right)$$

$$R_* = \frac{A_c}{H_{m0}};\quad h_{b*} = \begin{cases} \dfrac{3H_{m0} - h_b}{3H_{m0} + A_c} & \text{for} \quad h_b < 3H_{m0} \\ 0 & \text{for} \quad h_b \geq 3H_{m0} \end{cases} \tag{10}$$

The amount of overtopping is effected by the stability number of the breakwater which the parameter f_{H_0} accounts for. For the present tests only hardly and partly reshaping berm breakwaters are considered and for such cases $f_{H_0} = 0$. For other cases, see Lykke Andersen (2006).

The tests by Lykke Andersen (2006) were performed on a front slope $\cot\alpha = 1.25$. For other front slopes the berm width B and crest width G_c have to be corrected by Eq. (11), so the volume of the breakwater is unchanged. B is also corrected so that the distance from where the berm meets the upper slope to the back of the crest corresponds to a front slope $\cot\alpha = 1.25$ by Eq. (11).

$$G_* = \frac{G_c + 0.5(A_c + h_b)(\cot\alpha_u - 1.25)}{H_{m0}}$$

$$B_* = \frac{B + 0.5(A_c + h_b)(\cot\alpha_u - 1.25) + 0.5(h - h_b)(\cot\alpha_u - 1.25)}{H_{m0}} \tag{11}$$

When using the CLASH Neural Network method for berm breakwaters the roughness factor for hardly reshaping berm breakwaters (Icelandic berm breakwaters, Van Gent et al. (2007)) $\gamma_f = 0.4$ is applied.

The measured overtopping for the berm breakwaters is in Fig. 5 shown with the formula by Lykke Andersen (2006) and the CLASH Neural Network method together with the formulae by EurOtop (2007) with the roughness coefficient for berms γ_{BB} by Sigurdarson and Van der Meer (2013) in the upper limit.

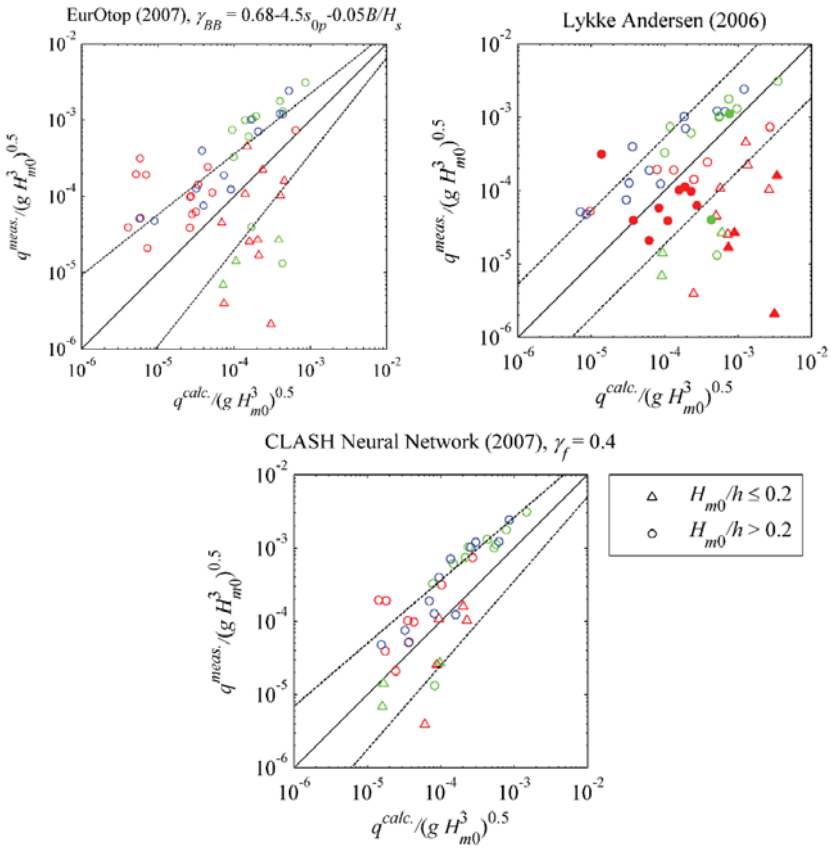

Figure 5: **Comparison between calculated and measured dimensionless overtopping for berm breakwaters. Red: $s_{0m} \le 0.015$, green: $0.015 < s_{0m} \le 0.030$, blue: $s_{0m} > 0.030$. The dashed lines are the 90% confidence band. The filled markers are tests with a high berm elevation $H_{m0}/h_b \ge 0.73$ outside the validated area by Lykke Andersen (2006).**

Fig. 5 shows that the formulae by EurOtop (2007) with γ_{BB} provide some scatter and in general also an overestimation for deep-water conditions. The formula by Lykke Andersen (2006) provides the same tendency with an overestimation for all deep-water conditions. Lykke Andersen (2006) did not test high berms (filled markers) and waves with low wave steepness (red markers) as in the present tests.

The CLASH Neural Network provides the most reliable results for the present test conditions, but as seen in Fig. 5, the amount of data is reduced, due to no prediction for certain conditions. For berm elevations higher than H_{m0}, which existed in some of the present tests, no predictions are given. These were also the tests which deviated most from the Lykke Andersen formula (2006).

DISCUSSION OF PRESENT PREDICTION METHODS

For the conventional breakwaters the CLASH Neural Network provides small scatter compared to the other methods. Moreover it provides the best estimations of all the methods based on the standard deviations of the difference between the logarithmic of the measured and calculated dimensionless overtopping, which could be because of no predictions for configurations of the breakwater and wave conditions outside the validation area.

For the conventional breakwater the formula by EurOtop (2007) provides a significant underestimation of the overtopping discharge for the long waves when not including the wave steepness in the upper limit as a strong dependency of the wave steepness was found in the present tests. If the roughness coefficient in the upper limit is changed to include the wave period as in the upper limit in the run-up formula by EurOtop (2007), the formulae provides much less scatter. When using the formula by EurOtop (2007) for long waves on a conventional breakwater, it is recommended to use the varying roughness factor to avoid underestimations. When using the varying roughness factor the standard deviation of the difference between the logarithmic of the measured and calculated dimensionless overtopping decreases from $\sigma = 1.41$ for constant roughness factor to $\sigma = 0.55$.

CLASH Neural Network and EurOtop (2007) with the roughness factor γ_{BB} provide both in general a safe bias for deep-water conditions and an unsafe bias for shallow water conditions for the present overtopping measurements on berm breakwaters.

Lykke Andersen's (2006) formula provides a safe bias for the tests in deep-water conditions, which were outside the validated range of the formula due to low steepness waves and different berm configurations.

Using the formula by EurOtop (2007) significant scatter is obtained and with no validity ranges of the formula it is difficult to determine if the reason is other berm configurations or wave steepnesses.

The methods for conventional rubble mound breakwaters and berm breakwater showed some scatter for dimensionless overtopping $< 10^{-5}$ and significant scatter for $< 10^{-6}$, which could be caused by scale effects or simply because of statistical uncertainty due to few overtopping waves.

The standard deviations for the different methods are given in Table 2 and Table 3 based on the difference between the logarithmic of the dimensionless measured and calculated overtopping discharge.

Table 2: Standard deviations σ of the difference between the logarithmic of the measured and calculated dimensionless overtopping for conventional breakwater. Data with $q/(g H_{m0}^3)^{0.5} > 10^{-6}$ and breakwaters with no failure.

	$H_{m0}/h \le 0.2$			$H_{m0}/h > 0.2$		
	$s_{0m} \le 0.015$	$0.015 < s_{0m} < 0.030$	$s_{0m} \ge 0.030$	$s_{0m} \le 0.015$	$0.015 < s_{0m} < 0.030$	$s_{0m} \ge 0.030$
EurOtop Manual (2007)	1.34	0.34	0.55	2.08	0.45	0.83
EurOtop Manual (2007) with $\gamma_{fsurging}$	0.85	0.37	0.81	0.61	0.19	0.32
CLASH Neural Network (2007)	0.59	0.14	0.69	0.50	0.18	0.31

Table 3: Standard deviations σ of the difference between the logarithmic of the measured and calculated dimensionless overtopping for berm breakwaters. Data with $q/(g H_{m0}^3)^{0.5} > 10^{-6}$ and breakwaters with no failure.

	$H_{m0}/h \le 0.2$			$H_{m0}/h > 0.2$		
	$s_{0m} \le 0.015$	$0.015 < s_{0m} < 0.030$	$s_{0m} \ge 0.030$	$s_{0m} \le 0.015$	$0.015 < s_{0m} < 0.030$	$s_{0m} \ge 0.030$
EurOtop Manual (2007) with γ_{BB}	0.94	1.02	-	0.88	0.80	0.64
Lykke Andersen (2006)	1.55	1.12	-	0.52	0.68	0.60
CLASH Neural Network (2007)	0.60	0.38	-	0.60	0.52	0.46

CONCLUSION

The EurOtop (2007), CLASH Neural Network and Lykke Andersen (2006) prediction methods have been analysed against new model tests, also covering low steepness waves in deep and shallow water, with both conventional and berm breakwaters. The analysis showed that overtopping increases with decreasing wave steepness. Using a varying roughness factor $\gamma_{fsurging}$ in the formulae by EurOtop (2007), the effect of the long waves feeling a less rough surface of the breakwater is included, and the formulae provide much more reliable results for long waves.

The formula by Lykke Andersen (2006) and EurOtop (2007) for berm breakwaters provide a lot of scatter for deep-water wave conditions but a safe bias. The reason for the conservative results by Lykke Andersen's (2006) formula is that the present tests are outside the validated ranges. For EurOtop (2007) it is not known whether the new tests are outside the validated ranges since these are not given in the manual.

The analysis showed that the CLASH Neural Network method provides the best estimates for berm breakwaters and for conventional breakwaters for the tested conditions. Furthermore, it is a simple method to use. However, more data covering larger berm elevations should be added.

REFERENCES

Burcharth, H.F. (2004). On Scale Effect Related to Runup and Overtopping for Rubble Mound Structures. Report of EU-research project CLASH.

Burcharth, H.F. and Lykke Andersen, T. (2007). Scale effects related to Small Physical Modelling of Overtopping of Rubble Mound Breakwaters. Proc. Coastal Structures, Venice, 2007.

EurOtop Manual. (2007). Overtopping Manual; Wave Overtopping of Sea Defences and Related Structures - Assessment Manual. UK: Allsop, N.W.H, Pullen, T., Bruce, T. NL: van der Meer, J.W., DE: Schüttrumpf, H., Kortenhaus, A. www.overtopping-manual.com.

Helgason, E. and Burcharth, H.F. (2006). Comparison between Overtopping Discharge in Small and Large Scale Models. Proc. Int. Conference on Coastal Engineering 2006. San Diego, California, U.S.A.

Lykke Andersen, T. 2006. Hydraulic Response of Rubble Mound Breakwaters: scale effects - berm breakwaters. Ph.D.-thesis, Hydraulics & Coastal Engineering Laboratory, Department of Civil Engineering, Aalborg University, Aalborg. Series Paper, nr. 27.

Lykke Andersen, T., Burcharth, H.F., Gironella, X. 2011 Comparison of new large and small scale overtopping tests for rubble mound breakwaters Coastal Engineering, 58, pp. 351-373.

Røge, M. S., Thomsen, J. B., Christensen, N. F., Andersen, T. L., Burcharth, H. F. 2014. Rock Armour Stability in Shallow Water Waves of Low Steepness. A New Stability Formula, Submitted to Coastal Engineering for review

Sigurdarson, S. and J. W. van der Meer. 2013. Design of berm breakwaters, recession, overtopping and reflection. Proc. ICE, Coasts, Marine Structures and Breakwaters 2013, Edinburgh, UK.

Thomsen, J.B., Røge, M.S., Christensen, N.F., Andersen, T.L. and van der Meer, J.W. 2014. Stability of Hardly Reshaping Berm Breakwaters Exposed to Long Waves. Proceedings of the 34th International Conference on Coastal Engineering, 2014, Seoul, Korea.

Van Gent, M.R.A., van den Boogaard, H.F.P., Pozueta, B, Medina, J.R. 2007. Neural network modelling of wave overtopping at coastal structures.

Paper G

Recalibration of Overtopping Roughness Factors of Different Armour Types

Mads Røge Eldrup
Thomas Lykke Andersen

The paper has been published in
Coasts, Marine Structures and Breakwaters 2017, ISBN 978-0-7277-6317-4, 2018.
DOI: www.icevirtuallibrary.com/doi/abs/10.1680/cmsb.63174.1011

Recalibration of Overtopping Roughness Factors of Different Armour Types

Mads Røge Eldrup, Department of Civil Engineering, Aalborg University, Denmark
Thomas Lykke Andersen, Department of Civil Engineering, Aalborg University, Denmark

Abstract
The present paper presents new overtopping results for permeable and impermeable rock armoured rubble mound breakwaters. The new tests show that EurOtop II and similar type of formulae underpredicts the overtopping for long waves and especially for structures with a permeable core. A new method is proposed to include the effect from long waves which corrects this bias and reduces the scatter significantly. This involves also a readjustment of the roughness factors as previous values were biased due to being fitted partly to long waves. The new method was also tested on other types of armour units for which new roughness factors were calibrated. Although, the tests with other armour units did not contain long waves a reduction in the scatter was achieved. Roughness factors for the new method were calibrated for different armour units.

Introduction

Background
Overtopping is the key parameter when a designer determines the needed crest level of a breakwater. Overtopping could lead to failure of the rear slope, damage of nearby structures or equipment, and increased wave transmission. Many researchers have proposed prediction methods for the mean overtopping discharge (q) for different types of breakwaters that is exposed to different sea states. The most used methods today are found in the EurOtop (2007) manual which uses two formulae to determine the mean overtopping discharge; one for breaking waves (flat slopes and short waves) and one for non-breaking waves (steep slopes and long waves). However, new tests by Christensen et al. (2014) showed a significant underprediction of overtopping discharge for high breaker parameters ($\xi_{m-1,0} > 5$). In prototype, it would for example for a swell with a wave period of 20 s correspond to significant heights less than 6.25 m with a front slope of 1:2 so it covers all swell conditions. This underestimation was solved by using a roughness factor ($\gamma_{f,\ surging}$) that is dependent on the breaker parameter instead of a constant (γ_f). The γ_f values given in EurOtop (2007) were calibrated to tests with different armour units in the paper by Bruce et al. (2009). In that paper, it is also mentioned that γ_f is dependent on the front slope angle, in such a way that γ_f is increasing with increasing front slope angle. This supports the statement by Christensen et al. (2014) of having a roughness factor, that increase for high breaker parameters.
A new version of the EurOtop manual has just been released (EurOtop II 2016) where the two overtopping formulae have been modified to give better predictions for zero freeboard. Furthermore, EurOtop II included a varying roughness factor ($\gamma_{f,\ mod}$), but it is only giving corrections when $\xi_{m-1,0} > 5$ whereas the $\gamma_{f,\ surging}$ as proposed by Christensen et al. (2014) gives corrections for $\xi_{m-1,0} > 1.8$. An upper limit for $\gamma_{f,\ mod}$ is further introduced for permeable cores. Small corrections to the γ_f values has also been made in EurOtop II (2016) compared to EurOtop (2007).

Outline of This Paper
In the present paper, the proposed method by Christensen et al. (2014) is tested for permeable and impermeable rock slopes and compared with the new procedure in EurOtop II (2016). Furthermore, the given values of the γ_f found in EurOtop II (2016) is recalibrated for the use with $\gamma_{f,\ surging}$ and the reduction factor for crest width C_r. Finally, the reliability of EurOtop II, the present method and Clash Neural Network (Van Gent et al. 2007) are compared when applied to standard cross sections.

EurOtop II

The two overtopping formulae by EurOtop II (2016) can be seen by Eqs. 1 and 2.

$$\frac{q}{\sqrt{g\,H_{\mathrm{m0}}^3}} = \frac{0.023}{\sqrt{\tan\alpha}}\ \xi_{\mathrm{m\text{-}1,0}}\ exp\left(-\left(4.75\,\frac{A_{\mathrm{c}}}{H_{\mathrm{m0}}}\ \frac{1}{\xi_{\mathrm{m\text{-}1,0}}\ \gamma_{\mathrm{f}}}\right)^{1.3}\right) \quad \text{(breaking waves)} \tag{1}$$

with a maximum discharge given by:

$$\frac{q}{\sqrt{g\,H_{\mathrm{m0}}^3}} = 0.09\ exp\left(-\left(1.5\,\frac{A_{\mathrm{c}}}{H_{\mathrm{m0}}}\ \frac{1}{\gamma_{\mathrm{f}}}\right)^{1.3}\right) \quad \text{(non-breaking waves)} \tag{2}$$

where q is the time averaged wave overtopping per unit length, g the gravity acceleration, H_{m0} the spectral significant wave height at the toe of the structure, α the front slope angle, γ_{f} the constant reduction factor dependent on the roughness of the breakwater, A_{c} the crest height above still water level and $\xi_{\mathrm{m\text{-}1,0}}$ the surf similarity parameter given by the spectral wave period $T_{\mathrm{m\text{-}1,0}}$ defined in Eq. 3.

$$\xi_{\mathrm{m\text{-}1,0}} = \frac{\tan\alpha}{\sqrt{s_{\mathrm{m\text{-}1,0}}}},\quad s_{\mathrm{m\text{-}1,0}} = \frac{H_{\mathrm{m0}}}{\frac{g}{2\pi}T_{\mathrm{m\text{-}1,0}}^2} \tag{3}$$

EurOtop II suggests to use the method by Besley (1999) to account for a permeable crest.

$$C_{\mathrm{r}} = 3.06\ exp\left(-1.5\,\frac{G_{\mathrm{c}}}{H_{\mathrm{m0}}}\right), \text{with a maximum of } C_{\mathrm{r}} = 1 \tag{4}$$

where G_{c} is the crest width and C_{r} is the reduction factor on the overtopping discharge for a permeable crest. EurOtop II suggest to only use the reduction factor for crest width (C_{r}) for $G_{\mathrm{c}} > 3D_{\mathrm{n}}$. EurOtop II recommends using $\gamma_{\mathrm{f,\,mod}}$ instead of γ_{f} when using Eq. 1 and Eq. 2 for $\xi_{\mathrm{m\text{-}1,0}} > 5$. The calculation of $\gamma_{\mathrm{f,\,mod}}$ is given by:

$$\gamma_{\mathrm{f,mod}} = \gamma_{\mathrm{f}} + (\xi_{\mathrm{m-1,0}} - 5)(1 - \gamma_{\mathrm{f}})/5, \text{with a maximum of } \gamma_{\mathrm{f,mod}} = \begin{cases} 1.0 \text{ for impermeable core} \\ 0.6 \text{ for permeable core} \end{cases} \tag{5}$$

Present Method

The present paper proposes to use EurOtop II with $\gamma_{\mathrm{f,\,surging}}$ as originally proposed by Christensen et al. (2014). The $\gamma_{\mathrm{f,\,surging}}$ is already being used in EurOtop II for wave run-up, but it is not used for wave overtopping even though these phenomena are highly related. Research by Shankar and Jayaratne (2003) shows that the relation between overtopping and run-up can be described by an exponential function, which support the present method. The varying roughness factor $\gamma_{\mathrm{f,\,surging}}$ that is proposed to use instead of $\gamma_{\mathrm{f,\,mod}}$ is calculated by:

$$\gamma_{\mathrm{f,surging}} = \gamma_{\mathrm{f}} + (\xi_{\mathrm{m-1,0}} - 1.8)(1 - \gamma_{\mathrm{f}})/8.2, \text{with a maximum of } \gamma_{\mathrm{f,surging}} = 1 \tag{6}$$

Moreover, is proposed to use C_{r} also for narrow crests. These two corrections have though required a recalibration of the roughness factors proposed in EurOtop II.

Present Tests

Model tests were performed on permeable and impermeable rock armoured rubble mound breakwaters to test the usability of the varying roughness factor for these structures. Table 1 shows the tested conditions for the two different permeabilities. As the tests were part of a parametric study a specific scale was not used, but the scale would approximately be 1:25 if the largest wave periods for the tests would correspond to approximately $T_P \approx 20$ s in prototype. The tested structures are seen in Fig. 1.

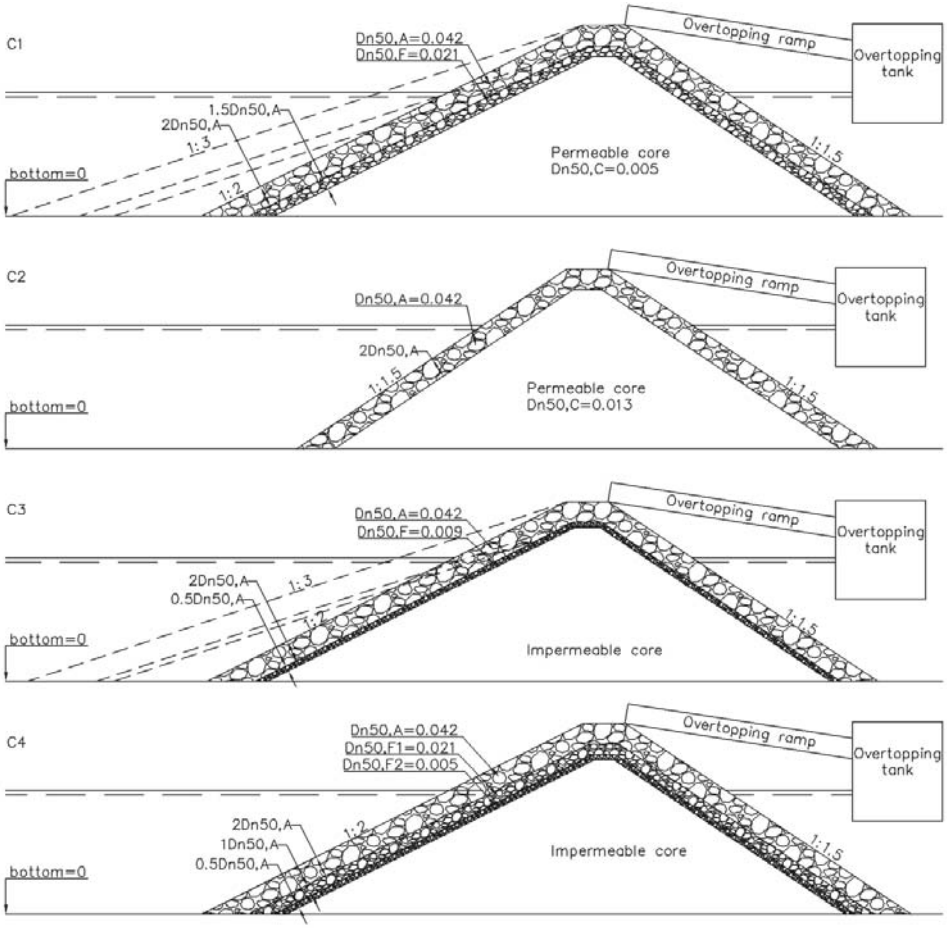

Figure 1: Tested structures for the present study with results shown in Fig. 2. Measures are in meters.

The tests were performed in a wave flume at Aalborg University in Denmark with the dimension 25 x 1.5 x 1 m (L x W x H). The slope of the bottom in front of the breakwater was 1:100. The waves were generated based on a JONSWAP spectrum γ = 3.3 with the software package AwaSys 7 (2016). The long waves are difficult to generate correctly but using the method by Zhang et al. (2007) good results were achieved. Active absorption also effective for long waves was applied, cf. Lykke Andersen et al. (2016). The waves were separated into incident and reflected wave trains with the WaveLab 3 (2016) software using the nonlinear method by Eldrup and Lykke Andersen (2017). The overtopping discharge was measured by a 0.30 m wide overtopping ramp placed at the rear side of the crest, cf. Fig 1.

Table 1: Tested conditions for the permeable and impermeable breakwater.

Parameter	**Permeable**	**Impermeable**
No. tests	61	41
Deep water peak wave steepness, s_{0p}	0.004 - 0.058	0.005 - 0.059
Relative depth, H_{m0}/h	0.24-0.56	0.21-0.35
Relative freeboard, A_c/H_{m0}	0.96-3.79	1.56-2.55
Front slope, cotα	1.5, 2.0, 3.0	2.0, 3.0

Fig. 2 shows the relative measured overtopping for the present tests. The results show that for the same relative freeboard the overtopping rate is increased with increasing breaker parameter.

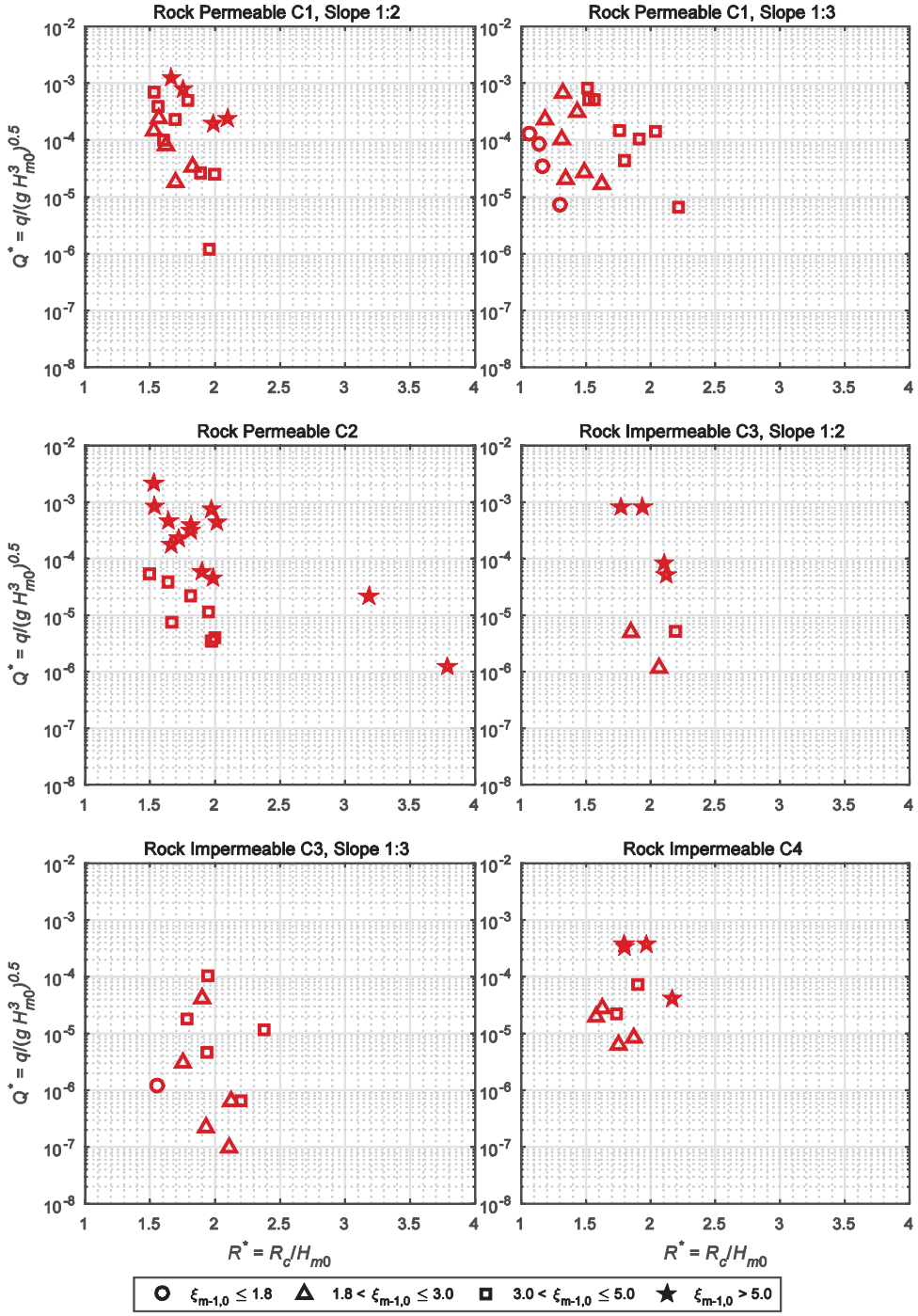

Figure 2: Measured dimensionless overtopping compared to relative freeboard and breaker parameter. See Fig. 1 for the tested structures.

The goodness of fit for the different predictions methods are determined by the Root Mean Squared Error of the logarithm of the dimensionless discharge.

$$RMSE = \sqrt{\left(log10\left(\frac{q_{meas.}}{\sqrt{g H_{m0}^3}}\right) - log10\left(\frac{q_{calc.}}{\sqrt{g H_{m0}^3}}\right)\right)^2} \quad (7)$$

For the present tests, the measured overtopping is compared to the predicted overtopping with γ_f, $\gamma_{f,\,mod}$ and $\gamma_{f,\,surging}$, with and without C_r correction factor. Fig. 3 shows the calculated and measured overtopping for the present tests with an impermeable core.

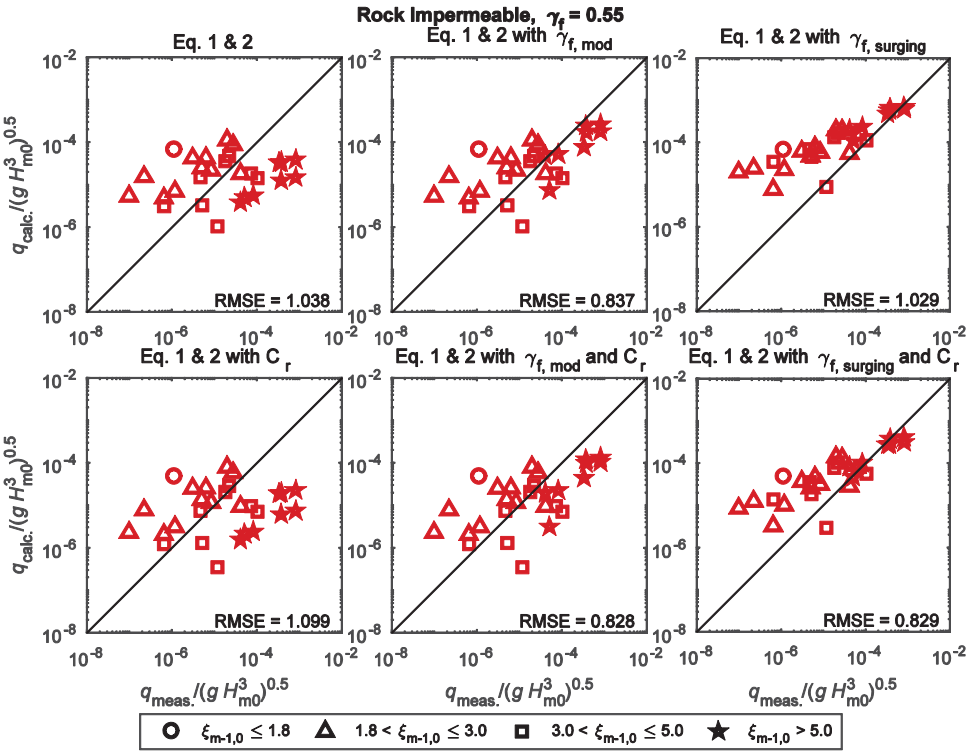

Figure 3: Calculated and measured dimensionless overtopping with EurOtop II (2016) with γ_f, $\gamma_{f,\,mod}$, $\gamma_{f,\,surging}$ with C_r and without C_r. Data is from the present tests.

Fig. 3 shows the scatter is reduced when using $\gamma_{f,\,mod}$ for $\xi_{m-1,0} > 5$ (star markers) compared to γ_f. However, when using $\gamma_{f,\,surging}$ the scatter is further decreased especially for $1.8 < \xi_{m-1,0} \leq 5$ but a bias is observed. This bias indicate that a new roughness factor should be used for impermeable rubble mound breakwaters compared to the EurOtop roughness factor when $\gamma_{f,\,surging}$ is used. These conclusions apply both with and without C_r correction.

Fig. 4 shows the results for the tests with the permeable core including also data from Bruce et al. (2009), Lykke Andersen and Burcharth (2009) and Christensen et al. (2014).

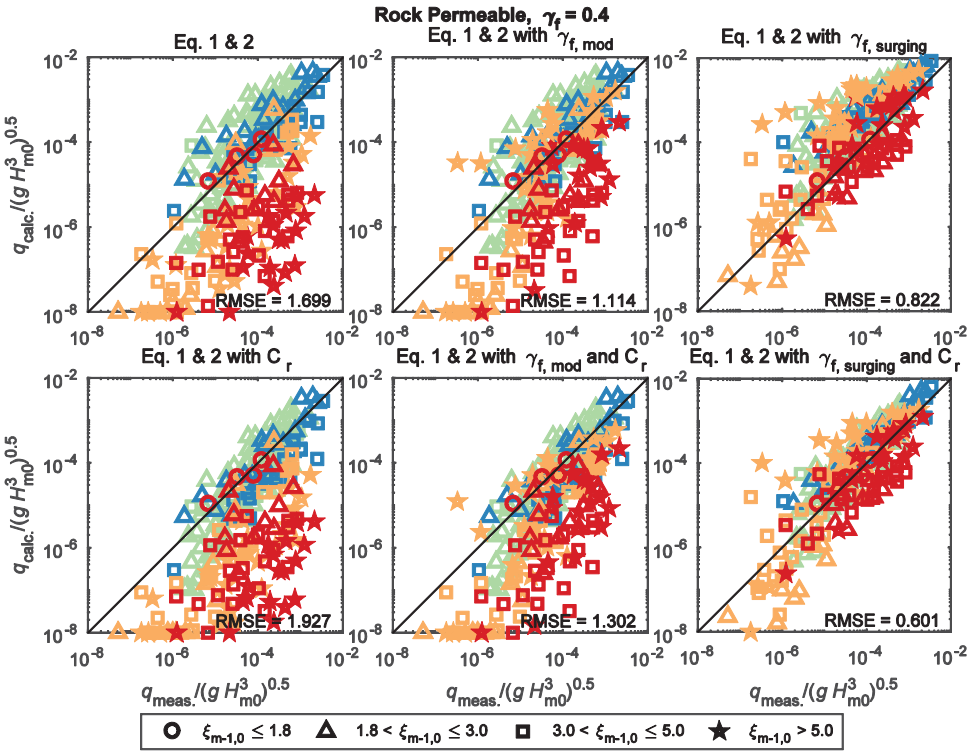

Figure 4: Calculated and measured dimensionless overtopping with EurOtop II (2016) with γ_f, $\gamma_{f, mod}$, $\gamma_{f, surging}$ with C_r and without C_r. The different data sets are symbolised by: Bruce et al. (2009) (green), Lykke Andersen and Burcharth (2009) (blue), Christensen et al. (2014) (orange) and present (red).

Fig. 4 shows that using $\gamma_{f, mod}$ improves the predictions for $\xi_{m-1,0} > 5$ compared to γ_f, but significant scatter is still seen for all $\xi_{m-1,0}$ values. Using $\gamma_{f, surging}$ the scatter is reduced and the predictions for $\xi_{m-1,0} \leq 5$ are improved compared to $\gamma_{f, mod}$. Using $\gamma_{f, surging}$ an overprediction for some of the tests with $\xi_{m-1,0} > 5$ are observed which might be because $\gamma_{f, surging}$ should have an upper limit lower than 1 for the permeable core, but this influence needs further investigation. The use of C_r reduces the scatter when using $\gamma_{f, surging}$.

From the results with rock armour the use of $\gamma_{f, surging}$ and C_r clearly improves the predictions. The underprediction for large and medium $\xi_{m-1,0}$ values are reduced significantly for rock armour. The use of $\gamma_{f, surging}$ is in the following tested for other armour types as well. Lykke Andersen and Burcharth (2009) and Bruce et al. (2009) data include different armour units, but the data does not include large $\xi_{m-1,0}$. However, it is tested if using $\gamma_{f, surging}$ is reducing scatter for medium values of $\xi_{m-1,0}$.

Fig. 5 shows the results for HARO and Cube placed in two layers using $\gamma_f = 0.47$ as given by the EurOtop II.

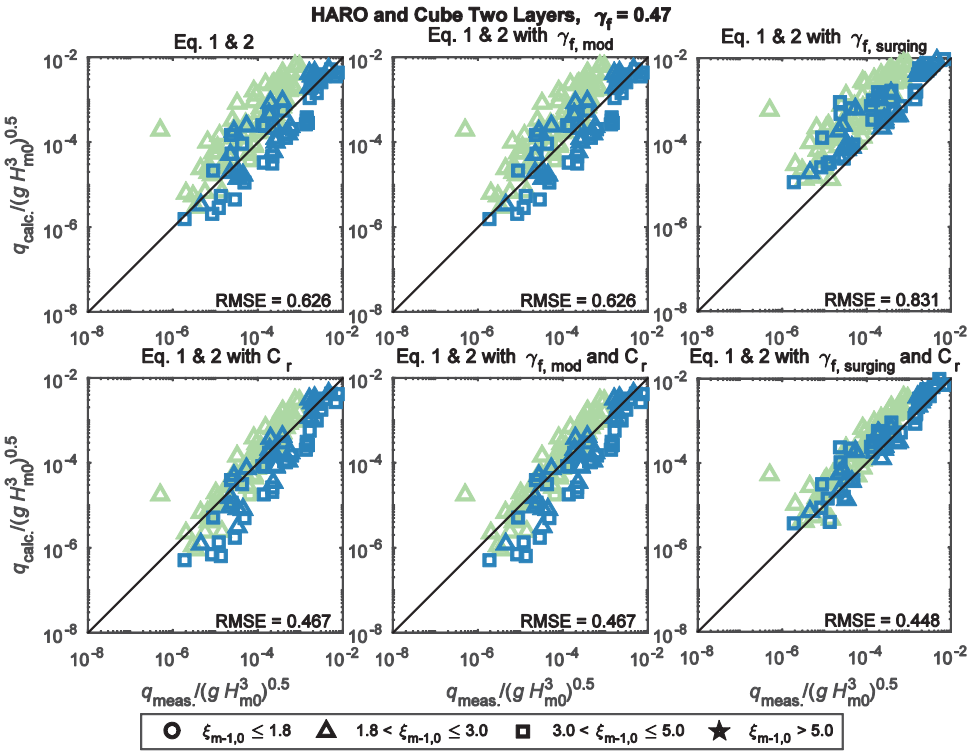

Figure 5: Calculated and measured dimensionless overtopping with EurOtop II (2016) with γ_f, $\gamma_{f, mod}$, $\gamma_{f, surging}$ with C_r and without C_r. The different data sets are symbolised by: Bruce et al. (2009) (green) and Lykke Andersen and Burcharth (2009) (blue).

Fig. 5 shows that using $\gamma_{f, mod}$ does not change the prediction compared to γ_f as no data has $\xi_{m-1,0} > 5$. Using $\gamma_{f, surging}$ the scatter is reduced as the data with $3 < \xi_{m-1,0} \leq 5$ is now on top of the data with $1.8 < \xi_{m-1,0} \leq 3$. The use of C_r seems to reduce the scatter for all three methods.

By using $\gamma_{f, surging}$ and C_r the scatter is reduced for both rock armour as well as for HARO and Cubes in two layers. Therefore, the roughness factor γ_f for all the different armour units available from the data sets are recalibrated. The calibrations are based on tests $\xi_{m-1,0} \leq 3$ so the $\gamma_{f, surging}$ has minor influence on the calibration. Furthermore, tests with $\frac{q_{meas.}}{\sqrt{g H_{m0}^3}} < 10^{-5}$ were neglected in the calibration as large scale or model effects might be present for these. The result of the recalibration including also data excluded during fitting of γ_f is shown in Fig. 6. In the figure the optimal roughness factors are also given.

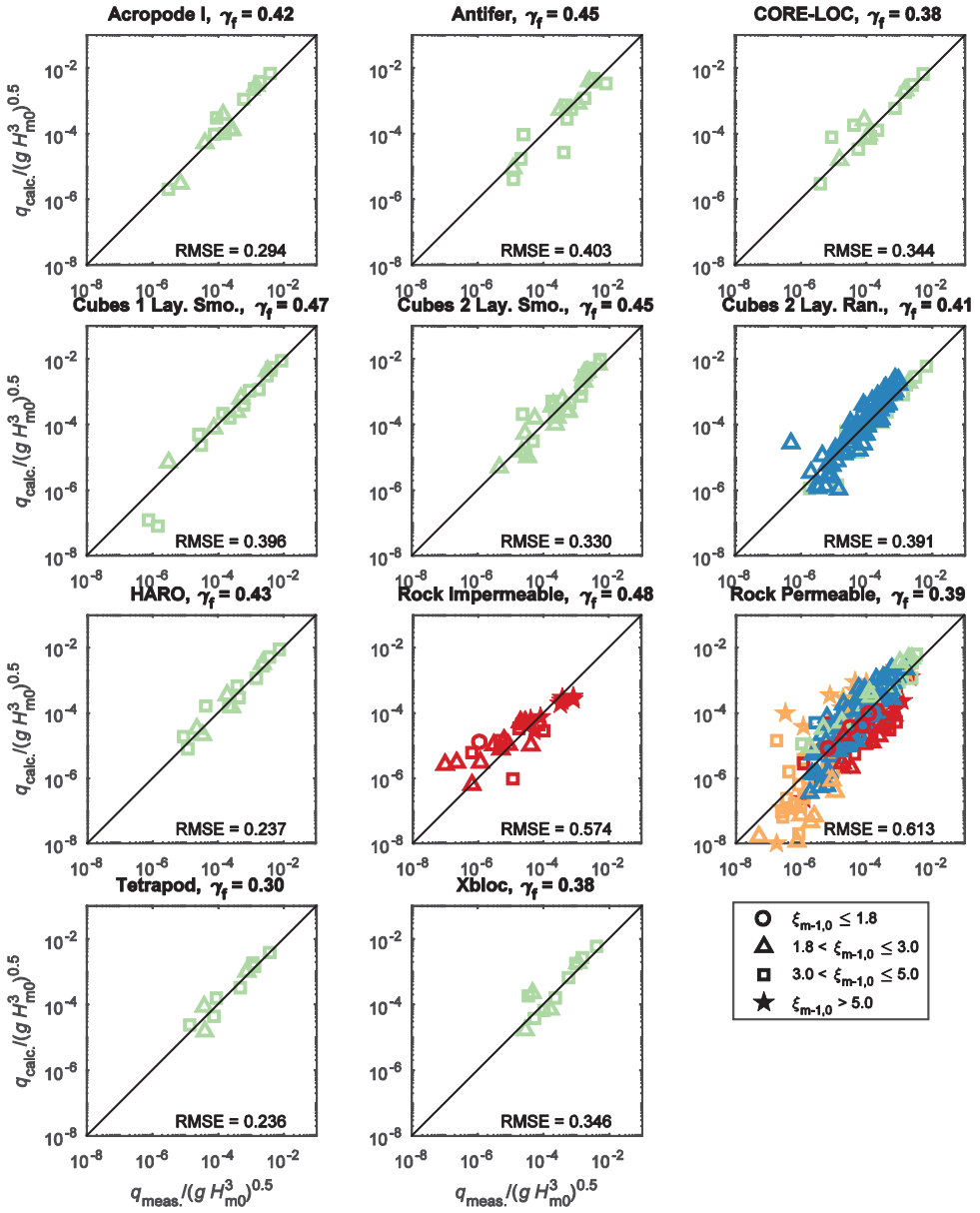

Figure 6: Refitted values of the γ_f. The different data sets are symbolised by: Bruce et al. (2009) (green), Lykke Andersen and Burcharth (2009) (blue), Christensen et al. (2014) (orange) and present (red).

A comparison of the refitted γ_f to those given in EurOtop II is shown in Table. 1.

Table 1: Roughness factors for different types of armour types and calculation methods

Type of armour	No Layers	EurOtop II (2016)	Present
Acropode™ I	1	0.46	0.42
Antifer	2	0.50	0.45
CORE-LOC™	1	0.44	0.38
Cubes smooth	1	0.49	0.47
Cubes smooth	2	0.47	0.45
Cubes random	2	0.47	0.41
HARO	2	0.47	0.43
Rock impermeable	2	0.55	0.48
Rock permeable	2	0.40	0.39
Tetrapod	2	0.38	0.30
Xbloc®	1	0.44	0.38

Table 1 shows that all the γ_f values have decreased for the present method compared to those by EurOtop II. The roughness for rock with permeable core has not decreased significantly while for rock with impermeable core a significant decrease is obtained. It can also be seen that rock with impermeable core and cubes smooth in one layer almost have the same roughness factor while other armour units have lower roughness factors. Tetrapod still has the lowest roughness factor of the armour units in Table 1.

The results by using EurOtop II with C_r and the present method with $\gamma_{f,\,surging}$ and C_r is shown together with the results by CLASH NN in Fig. 7.

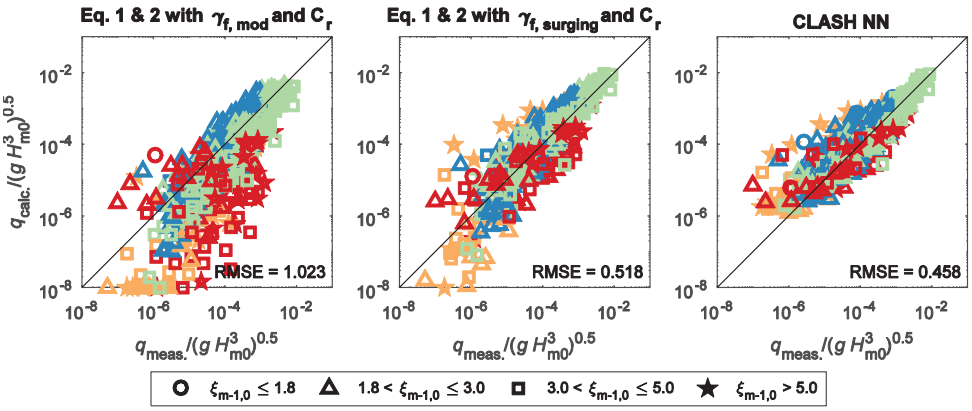

Figure 7: Comparison with EurOtop II (2016), Present method and CLASH NN. The different data sets are symbolised by: Bruce et al. (2009) (green), Lykke Andersen and Burcharth (2009) (blue), Christensen et al. (2014) (orange) and present (red).

In Fig. 7 the present method shows a significant reduction in the scatter compared to EurOtop II. The CLASH NN shows a further slight reduction in the scatter especially for smaller overtopping discharges. If removing data with $\frac{q_{meas.}}{\sqrt{g\,H_{m0}^3}}<10^{-6}$ the RMSE for EurOtop II, present and CLASH NN are respectively 0.893, 0.465 and 0.403. The tested method with the lowest error is CLASH NN, but a neural network model is not giving insight into the physics. Therefore, the simple empirical formulae are relevant and with the present update the error is similar to CLASH NN.

Conclusion

In the present paper, an improvement to the EurOtop II overtopping formula to cover the entire range from steep to long waves has been suggested. The original method showed significant under prediction for large breaker parameters ($\xi_{m-1,0} > 5$) and significant scatter for smaller breaker parameters ($\xi_{m-1,0} \leq 5$) for rubble mound breakwaters armoured with rocks. The scatter was also observed for other kinds of armour units, ex. cubes and HARO.

The method proposed in the present paper use a varying roughness factor based on Christensen et al. (2014) work and was validated on new experimental data. The present method showed a significant reduction in the scatter compared to the method by EurOtop II. Furthermore, new roughness factors were recalibrated based on the present method.
To further improve the prediction, more research in an upper limit for $\gamma_{f,\ surging}$ for impermeable and permeable structures are needed. A study on the crest width reduction factor tested for long waves could also improve the results. Finally, has only rock armoured rubble mounds been tested for long waves in this study, so validation on other armour units could be recommended.

Acknowledgement

The staff of the Hydraulics & Coastal Engineering Laboratory at Aalborg University is acknowledged for the contribution to the physical model tests.

References

Besley P. (1999) *Overtopping of seawalls – design and assessment manual*, R & D Technical Report W 178, Environment Agency, Bristol, ISBN 1 85705 069 X.
Bruce T., Van der Meer J.W., Franco, L. & Pearson, J.M. (2009) *Overtopping performance of different armour units for rubble mound breakwaters*, Coastal Engineering, vol. 56, pp. 166–179.
Christensen N.F., Røge M.S., Thomsen J.B., Lykke Andersen T., Burcharth H.F. & Nørgaard J.Q.H. (2014) *Overtopping on rubble mound breakwaters for low steepness waves in deep and depth limited conditions*, Proceedings of the Coastal Engineering Conference.
Eldrup M.R. & Lykke Andersen T. (2017) *Estimation of Incident and Reflected Wave Trains in Highly Nonlinear Irregular Waves*, Under Review at Coastal Engineering Journal.
EurOtop (2007) *European Manual for the Assessment of Wave Overtopping*. Pullen T., Allsop N.W.H., Bruce T., Kortenhaus A., Schüttrumpf H., and Van der Meer J.W., At: www.overtoppingmanual.com
EurOtop II (2016) *European Manual for the Assessment of Wave Overtopping*. Pullen T., Allsop N.W.H., Bruce T., Kortenhaus A., Schüttrumpf H., and Van der Meer J.W., At: www.overtoppingmanual.com
Lykke Andersen T. & Burcharth H.F. (2009) *Three-dimensional investigations of wave overtopping on rubble mound structures*, Coastal Engineering, vol. 56, pp. 180–189.
Lykke Andersen, T., Clavero, M., Frigaard, P., Losada, M., Puyol, J.I. 2016. *A new active absorption system and its performance to linear and non-linear waves*. Coastal Engineering, Volume 114, August 2016, Pages 47-60.
Shankar, N. J. & Jayaratne M. P. R. (2003) *Wave run-up and overtopping on smooth and rough slopes of coastal structures*, Ocean Engineering, vol. 30, Issue 2, pp. 221-238.
Van Gent M.R.A., van den Boogaard H.F.P., Pozueta B., Medina J.R. (2007) *Neural network modelling of wave overtopping at coastal structures*.
Zhang H., Schäffer H.A., and Jakobsen K. P. (2007) *Deterministic combination of numerical and physical coastal wave models*, Coastal Engineering, Volume 54, p. 171-186,

Paper H

Overtopping of Breakwaters with a Permeable Crest

Mads Røge Eldrup
Thomas Lykke Andersen
Jonas Bjerg Thomsen
Hans Falk Burcharth

The paper has been published in
Coastal Engineering Proceedings, ISSN 2156-1028, 1(36), 2018
DOI: https://doi.org/10.9753/icce.v36.papers.17

OVERTOPPING OF BREAKWATERS WITH A PERMEABLE CREST

Mads Røge Eldrup[1], Thomas Lykke Andersen[1], Jonas Bjerg Thomsen[1] and Hans Falk Burcharth[1]

In model tests, the wave overtopping discharge is typically measured at the rear corner of the armour crest. So far, all overtopping formulae have been calibrated to predict this specific overtopping discharge. The EurOtop Manual however proposed a formula to include also the discharge trough the permeable armour crests. The total overtopping including the discharge trough the crest armour is relevant in relation to rear armour stability. The discharge trough the armour depends also on the permeability of the core material. In order to study this effect, new model tests were performed with a permeable and an impermeable core. A method for the prediction of the total overtopping discharge is given.

Keywords: wave overtopping discharge; relative freeboard; permeable crest

INTRODUCTION

Wave overtopping on rubble mound breakwaters influences the rear slope stability as well as the safety of operations and installation on and behind the breakwater. The wave overtopping discharge is thus the governing parameter when designing the height of a rubble mound breakwater. The armour freeboard, A_c, the crest freeboard, R_c, and the crest width, G_c, are main structural parameters used in the prediction of the overtopping discharge q. The crest freeboard is in the EurOtop Manual by Van der Meer et al. (2016) defined as the height on the structure from where the water can no longer flow back to the seaside, see Fig. 1. This could, for example, be the crown wall freeboard ($R_{c,wall}$) or the freeboard of an impermeable or only slightly permeable core ($R_{c,core}$).

The wave overtopping discharge is dependent on where it is measured. Fig. 1 shows three different locations. The discharge caused by wave overtopping is given by q_{crest}, while the extra discharge through the permeable crest is q_{armour}. Typically, the discharge has been measured only at the armour crest or at the crown wall. In the existing database of overtopping tests, $q_{crest}+q_{armour}$ never seems to have been measured for structures without a crown wall. For such cases, reliable estimations of $q_{crest}+q_{armour}$ are essential for predictions of the total overtopping volume behind a revetment in order to estimate the needed drainage capacity. Molines et al. (2018) use q_{crest} to predict the wave loads on crown walls, but this means that if $q_{crest} = 0$ then the forces are also zero. This is clearly not correct as water can still flow in the permeable crest and cause loads on the crown wall. Therefore, it might be better to estimate the wave forces on a crown wall on the basis of $q_{crest}+q_{armour}$. This discharge is also relevant for rear slope stability. The wave overtopping discharge at the armour crest q_{armour} is the relevant parameter for estimating loads on installations on top of the armour crest and for assessing of operations behind the breakwater.

The EurOtop Manual (Pullen et al., 2007) has recently been updated (Van der Meer et al. 2016). The 2007 version used the crest freeboard, $R_{c,core}$ or $R_{c,wall}$ to predict the overtopping $q_{crest}+q_{armour}$, see Fig. 1. The second version has for cases without a crown wall changed the procedure to use an average between the armour freeboard, A_c and the core freeboard, $R_{c,core}$. They argue that using A_c would provide an underestimation, and using $R_{c,core}$ would provide an overestimation of the wave overtopping. This is contradictory to all other formulae that have used q_{crest}. For cases with a crown wall, the second version recommends the use of the maximum of A_c and $R_{c,wall}$. This recommendation is not in line with structures without a crown wall and can lead to underestimations of the overtopping discharge if A_c is larger than $R_{c,wall}$ as shown in Fig. 1b. Also, it might lead to strange designs where crown walls are added without any real purpose.

From above is seen that different freeboard recommendations are given in EurOtop for estimating the wave overtopping behind the breakwater ($q_{crest}+q_{armour}$), but it has not been validated for cases without crown wall. The manual does not provide any guidelines on estimating q_{crest} which is the important parameter for some overtopping hazards. For example, using the recommendation given by the second version of the EurOtop Manual to design the height of the cross-section shown in Fig. 1a the result would end in a too high structure as the estimation would be for $q_{crest}+q_{armour}$ if the design criteria is given as q_{crest}.

The scope of the present paper is to investigate the validity of the given recommendations in EurOtop for predicting the discharges q_{crest} and $q_{crest}+q_{armour}$ for cross-sections without a crown wall. The paper first presents the recent wave overtopping discharge formulae by Van der Meer et al. (2016) and the

[1] Civil Engineering, Aalborg University, Thomas Manns Vej 23, Aalborg Ø, 9220, Denmark

modifications made by Eldrup and Lykke Andersen (2018b). After this, a description of the model test setup and the test conditions are given. Finally, the wave overtopping discharge results and related conclusions are presented.

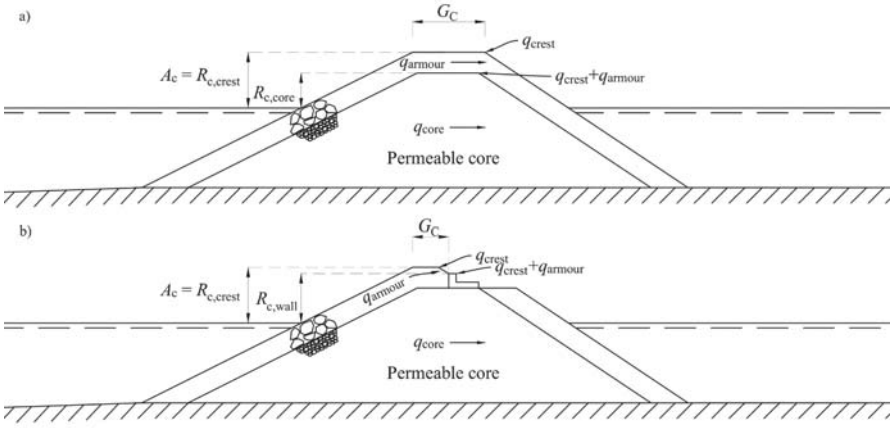

Figure 1. Illustration of armour crest freeboard A_c, core freeboard $R_{c,core}$, wall freeboard $R_{c,wall}$ and crest width G_c. Overtopping discharge passing the crest q_{crest}, trough the permeable crest, q_{armour} and trough the core, q_{core}.

EUROTOP (2016) AND ELDRUP AND LYKKE ANDERSEN (2018b) MODIFICATION

In the recent years, a significant increase in the reliability of formulae for predicting wave overtopping discharges for surging waves is seen. The first version of the EurOtop Manual (Pullen et al., 2007) used a constant roughness factor, γ_f. Christensen et al. (2014) showed that the roughness factor was dependent on the breaker parameter, $\xi_{m-1,0}$. They used a varying roughness factor, $\gamma_{fsurging}$, that was already defined in the EurOtop Manual, but only used in relation to wave run-up. This varying roughness factor increases the roughness factor for $\xi_{m-1,0} > 1.8$, thus indicating that the dissipation on the slope is reduced in surging waves compared to plunging waves. This change significantly improved the reliability of the predictions, especially for low steepness waves. The second edition of the EurOtop Manual (Van der Meer et al., 2016) included a different varying roughness factor, γ_{fmod}, but this factor only influenced predictions for $\xi_{m-1,0} > 5$ although only based on data by Bruce et al. (2009) consisting of $\xi_{m-1,0}$ in the range 2.8 - 4.5. The data by Bruce et al. (2009) was initially used to estimate γ_f for different armour units. Eldrup and Lykke Andersen (2018b) refitted γ_f, but with use of $\gamma_{fsurging}$ based on the tests by Bruce et al. (2009), Christensen et al. (2014) and their own data.

The Eurotop Manual includes the crest width reduction factor, C_r, by Besley (1999). The manual states that the crest width reduction factor should only be used if the crest width is larger than three armour units. Eldrup and Lykke Andersen (2018b) found that the reliability of the predictions was further increased if the crest reduction factor was used for all cases. However, their conclusion was based on data with a limited variation in the crest width, the main part having a crest width of approximately three armour units. Thus, it still remains to be examined if the reduction factor by Besley (1999) is valid for wider crests and low steepness waves. The formulation for wave overtopping discharge by Van der Meer et al. (2016) is shown in Eq. 1.

$$\frac{q}{\sqrt{gH_{m0}^3}}=\frac{0.023}{\sqrt{\tan\alpha}}\gamma_{b\xi_m\text{-}1,0}\exp\left(-\left(2.7\frac{R_c}{\xi_{m\text{-}1,0}H_{m0}\gamma_b\gamma_{fmod}\gamma_\beta\gamma_v}\right)^{1.3}\right)C_r$$

With a maximum of

$$\frac{q}{\sqrt{gH_{m0}^3}}=0.09\exp\left(-\left(1.5\frac{R_c}{H_{m0}\gamma_{fmod}\gamma_\beta\gamma^*}\right)^{1.3}\right)C_r$$

Crest width reduction factor

$$C_r=\begin{cases}1 & G_c/D_{n50}\leq 3 \text{ or } G_c/H_{m0}<0.75\\ 3.06\exp\left(-\frac{1.5G_c}{H_{m0}}\right) & \text{otherwise}\end{cases} \quad (1)$$

Varying roughness factor

$$\gamma_{fmod}=\begin{cases}\gamma_f & \xi_{m\text{-}1,0}\leq 5\\ \gamma_f+\frac{\left(\xi_{m\text{-}1,0}\text{-}5\right)\left(1\text{-}\gamma_f\right)}{5} & \xi_{m\text{-}1,0}>5\\ 1 & \xi_{m\text{-}1,0}>10\end{cases}$$

where γ_b is the reduction factor for a berm, γ_β is the reduction factor for wave obliquity. γ_v is the reduction factor for a wall at the end of the slope and γ^* is the reduction factor for a storm wall on a slope or promenade for non-breaking waves.

The formulation by Eldrup and Lykke Andersen is shown in Eq. 2.

$$\frac{q}{\sqrt{gH_{m0}^3}}=\frac{0.023}{\sqrt{\tan\alpha}}\gamma_{b\xi_m\text{-}1,0}\exp\left(-\left(2.7\frac{R_c}{\xi_{m\text{-}1,0}H_{m0}\gamma_b\gamma_{fsurging}\gamma_\beta\gamma_v}\right)^{1.3}\right)C_r$$

With a maximum of

$$\frac{q}{\sqrt{gH_{m0}^3}}=0.09\exp\left(-\left(1.5\frac{R_c}{H_{m0}\gamma_{fsurging}\gamma_\beta\gamma^*}\right)^{1.3}\right)C_r$$

Crest width reduction factor

$$C_r=\begin{cases}1 & G_c/H_{m0}<0.75\\ 3.06\exp\left(-\frac{1.5G_c}{H_{m0}}\right) & \text{otherwise}\end{cases} \quad (2)$$

Varying roughness factor

$$\gamma_{fsurging}=\begin{cases}\gamma_f & \xi_{m\text{-}1,0}\leq 1.8\\ \gamma_f+\frac{\left(\xi_{m\text{-}1,0}\text{-}1.8\right)\left(1\text{-}\gamma_f\right)}{8.2} & \xi_{m\text{-}1,0}>1.8\\ 1 & \xi_{m\text{-}1,0}>10\end{cases}$$

Eldrup and Lykke Andersen (2018b) used only data with q_{crest} and defined the freeboard to be used in the formula as the maximum of A_c and R_c. Most of the data had however $R_{c,wall} = A_c$. Fig. 2 shows the data by Bruce et al. (2009). The middle part of the figure shows that the scatter is slightly reduced when using $\gamma_{fsurging}$ as proposed by Christensen et al. (2014) compared to the use of γ_{fmod} as shown in the top part of the figure. This shows that even for $\xi_{m\text{-}1,0}$ in the range 2.8 - 4.5 there is an improvement when using $\gamma_{fsurging}$ instead of γ_{fmod}. Christensen et al. (2014) is though overestimating the wave overtopping

discharge and therefore a refit of the γ_f was performed by Eldrup and Lykke Andersen (2018b) seen in the lower part of the figure. Note that Eldrup and Lykke Andersen (2018b) used the crest width reduction factor C_r in all cases.

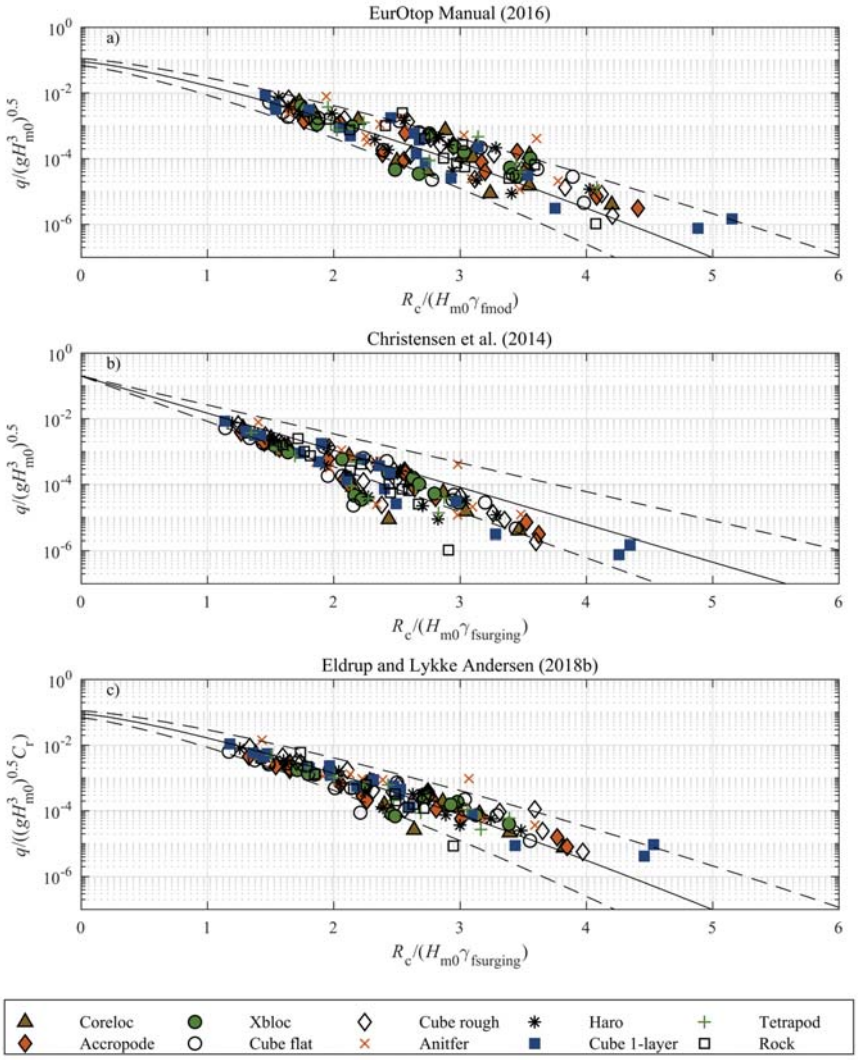

Figure 2. Comparison between different varying roughness factors with the data by Bruce et al. (2009). (a) shows the approach by EurOtop (2016), (b) Christensen et al. (2014) and (c) Eldrup and Lykke Andersen (2018b). The continuous line shows the mean value approach and the dashed lines shows the 90% confidence band.

The present test programme included steep and low steepness waves. Therefore, the formulation given by Eldrup and Lykke Andersen (2018b) is used for comparison with the present results. It is investigated which freeboard height should be used for predicting wave overtopping at the armour crest (q_{crest}) and at the core freeboard (q_{crest}+q_{armour}).

MODEL TEST SETUP AND TEST CONDITIONS

The present study includes new model tests performed in the wave flume at Aalborg University with dimensions of 18.2 m x 1.5 m x 1.5 m (l x w x h). The floor was horizontal for the first two meters in front of the wavemaker followed by a 1:30 foreshore to the toe of the breakwater, see Fig. 3.

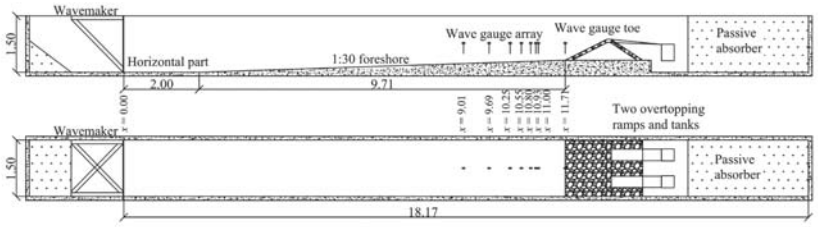

Figure 3. Flume setup.

Wave gauges were placed in front of the breakwater in order to separate waves into incident and reflected waves. The wave separation method by Eldrup and Lykke Andersen (2019) was used, which is a nonlinear method that separates the wave components not only into incident and reflected components but also into free and bound components. The method has on mild foreshore slopes shown to be reliable for the entire interval from linear to highly nonlinear waves. The waves were also measured without the structure in place, and an additional wave gauge was placed at the toe of the structure. The incident waves with the structure in place and the total waves without the structure were almost identical in the wave gauge array. However, due to the relatively steep foreshore, the waves might change significantly from the array to the toe of the structure either due to shoaling or to wave breaking. Comparing the total waves without the structure for wave gauge, $x = 11.00$ with the wave gauge at $x = 11.71$ (cf. Fig. 3), an increase in wave height is seen for all tests with a maximum increase of 7%. Therefore, the wave data measured by the wave gauge at $x = 11.71$ without the structure in place, is used for the following analysis in this paper.

The waves were generated with a piston-type wavemaker which was controlled by the AwaSys (2018) software. The waves were generated with a JONSWAP spectrum with a peak enhancement factor of $\gamma = 3.3$. Due to the generation of nonlinear waves in the present tests, the guidelines on the applicability of wavemaker theories given by Eldrup and Lykke Andersen (2018a) was followed. For the mildly nonlinear cases, second-order theory was used ($S < 2$), but for the highly nonlinear case ($S > 2$), the Zhang et al. (2007) method was used. The method by Zhang uses the surface elevation and the depth-averaged velocity as input, which was calculated with the Celeris Boussinesq wave model by Tavakkol and Lynett (2017). Both wavemaker methods are implemented in AwaSys (2018). The active wave absorption by Lykke Andersen et al. (2016) was used in the present tests, which has shown to have good performance for linear and nonlinear waves, cf. Lykke Andersen et al. (2018).

One cross-section with a permeable core, and one with an impermeable core were tested, cf. Fig. 4. Two overtopping ramps of 0.3 m width were installed, one at the armour rear crest shoulder and one at the core rear crest shoulder. The ramp located at the core crest had a protective net to prevent rocks from sliding into the overtopping tank. The water depth, h, at the toe of the structure was 37 cm, and A_c was 18 cm in all tests. For the cross-section with a permeable core, the core freeboard was $R_{c,core} = 9.6$ cm and for the impermeable core it was $R_{c,core} = 7.5$ cm. The core material had $D_{n50} = 1.5$ cm and gradation $D_{n85}/D_{n15} = 1.36$. The spectral significant wave height (H_{m0}) varied between 9 cm and 11 cm. The choice of model core material size might be motivated as follows: if for example the length scale of the applied model is 1:30, the prototype $H_{m0} \approx 3$ m and the core material can be characterised by $D_{n50} = 26$ cm and $n = 0.38$, a characteristic pore velocity will be approximately 7 cm/s, see Burcharth et al. (1999). If compensating for viscous scale effects the core material should, if well narrow graded, have a $D_{n50} = 0.14$ cm. The actually used core material in the model had $D_{n50} = 0.15$ cm, i.e. very close to the estimated $D_{n50} = 0.14$ cm. Thus, the scaling of the core material seems realistic.

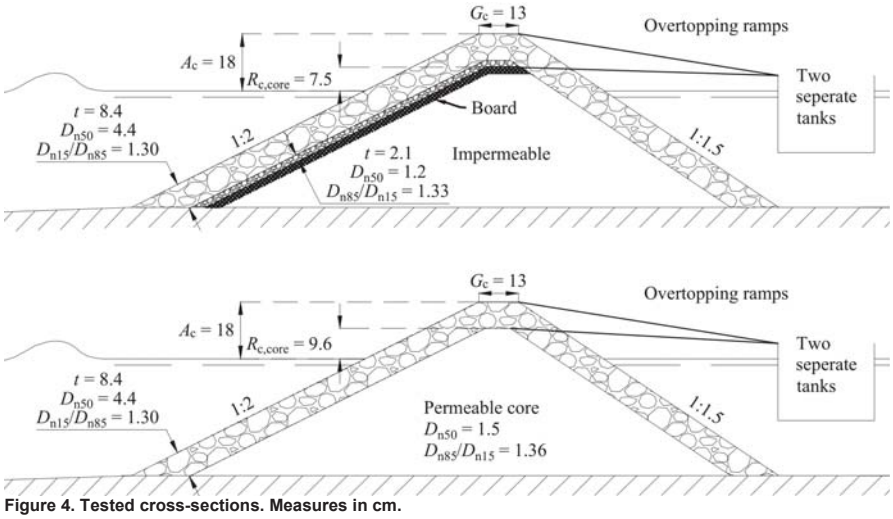

Figure 4. Tested cross-sections. Measures in cm.

Six sea states with identical wave steering signals were used in the present study for both cross-sections. Thus, 12 tests were performed in total. The tested ranges are shown in Table 1.

Table 1. Test ranges.	
R_c/H_{m0}	0.90-1.11
A_c/H_{m0}	1.68-2.09
G_c/H_{m0}	1.18-1.46
H_{m0}/h	0.23-0.29
$\xi_{m-1,0}$	2.58-6.71

OVERTOPPING RESULTS

Fig. 5 shows a comparison between the measured wave overtopping discharge q_{crest} and $q_{crest}+q_{armour}$ for the permeable and impermeable breakwater. The figure shows which proportion of the overtopping discharge (ex. discharge through the core) goes through the armour layer in the two models with permeable and impermeable cores. The proportion is much higher in the case of the impermeable core. However, the two cases permeable and impermeable are not directly comparable because the core freeboard $R_{c,core}$ is 9.6 cm and 7.5 cm, respectively. Also, the discharge through the core in the model with permeable core is unknown. Even so, a relatively much higher discharge seems to go through the armour layer in the case of the impermeable core, actually a factor of up to 15 as compared to a factor of four. The results show that there is a clear difference in measured overtopping discharge at the armour crest (q_{crest}) and at the core ($q_{crest}+q_{armour}$). This is especially the case when the core is impermeable and therefore hinder infiltration from the permeable crest into the core. Thus, more water will reach the overtopping tank connected to the core shoulder.

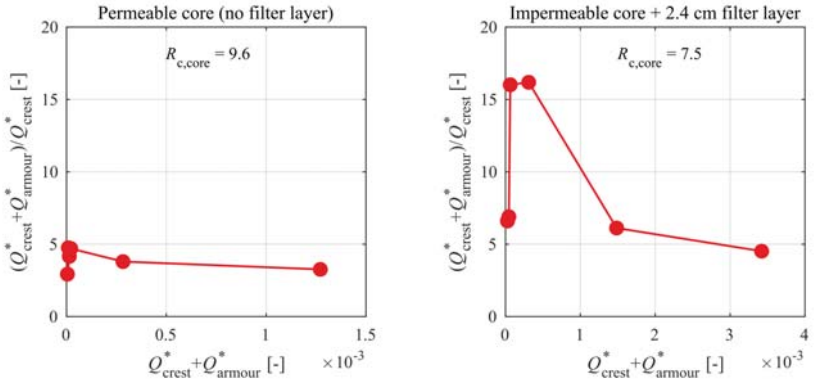

Figure 5. Comparison of measured dimensionless overtopping discharge at the armour crest and the core crest, $Q^* = q/(gH_{m0}^3)^{0.5}$.

COMPARISON OF EUROTOP RECOMMENDATIONS FOR DISCHARGE TROUGH ARMOUR

The previously discussed recommendations given in the EurOtop manual for the predictions of the wave overtopping discharge through the permeable armour layer is tested. The recommendations are tested against the wave overtopping discharge measured on the armour crest level (q_{crest}) for the permeable and impermeable cross-sections, see Fig. 6. The continuous line illustrates the predicted wave overtopping discharge with use of the formulae (2) by Eldrup and Lykke Andersen (2018b) and the dashed lines shows the 90% confidence band. Using a relative freeboard $R^* = A_c/(H_{m0}\gamma_{fsurging})$ in the formulae (2), the predictions fit well with the measured overtopping discharge with all the data inside the 90% confidence band. Like all other overtopping formulae, formulae (2) predicts an increase in discharge with a decrease in the freeboard. Therefore, if using the lower relative freeboard by Pullen et al. (2007) ($R^* = R_c/(H_{m0}\gamma_{fsurging})$) the overtopping discharge is overestimated when using the tested formulae (2). Similarly, when using the relative freeboard recommended by Van der Meer et al. (2016) ($R^* = (A_c+R_c)/(2H_{m0}\gamma_{fsurging})$) in (2) the overtopping discharge is also overestimated, however to a lesser degree. Based on the test results, it can be concluded that A_c should be used as the freeboard for estimating the wave overtopping discharge q_{crest} for cases without a crown wall.

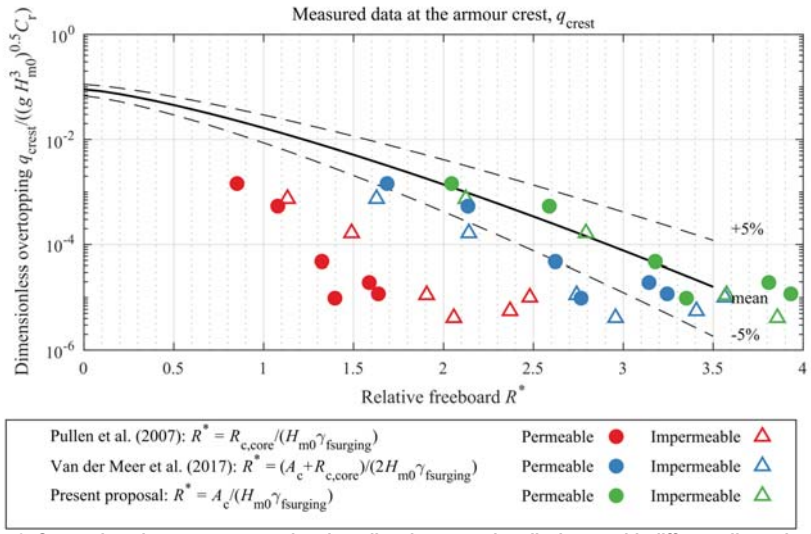

Figure 6. Comparison between measured and predicted overtopping discharge with different dimensionless freeboard definitions. Data is for the measurements on top of the armour crest. The continuous line shows the predicted wave overtopping discharge by Eldrup and Lykke Andersen (2018b), and the dashed lines show the 90% confidence band.

Fig. 7 shows the wave overtopping measured at the core (q_{crest}+q_{armour}). Using A_c as the freeboard in the formulae, slightly smaller values of the wave overtopping discharge are estimated compared to the measured discharge. Using the definition by Van der Meer et al. (2016), the data is well predicted by (2) with all data inside the 90% confidence band. It should be noted that the formulae provide slightly larger overtopping values for the tests with an impermeable core and slightly smaller values with a permeable core. Using the freeboard definition by Pullen et al. (2007) in the formulae (2), significantly larger wave overtopping discharges are estimated at the core rear shoulder (q_{crest}+q_{armour}). From the present tests, the freeboard recommendation given by Van der Meer et al. (2016) seems to be valid when predicting wave overtopping discharge q_{crest}+q_{armour} by formulae (2) even though they did not have tests to validate it.

There is a clear separation of the results for the impermeable and the permeable core when estimating the wave overtopping discharge at the core. More tests with permeable and impermeable cores are needed in order to investigate the influence from the core permeability on the discharge q_{crest}+q_{armour}. Furthermore, an even larger difference between q_{crest}+q_{armour} and q_{armour} is expected for wider crests than tested which is not included in the crest width reduction factor by Besley (1999).

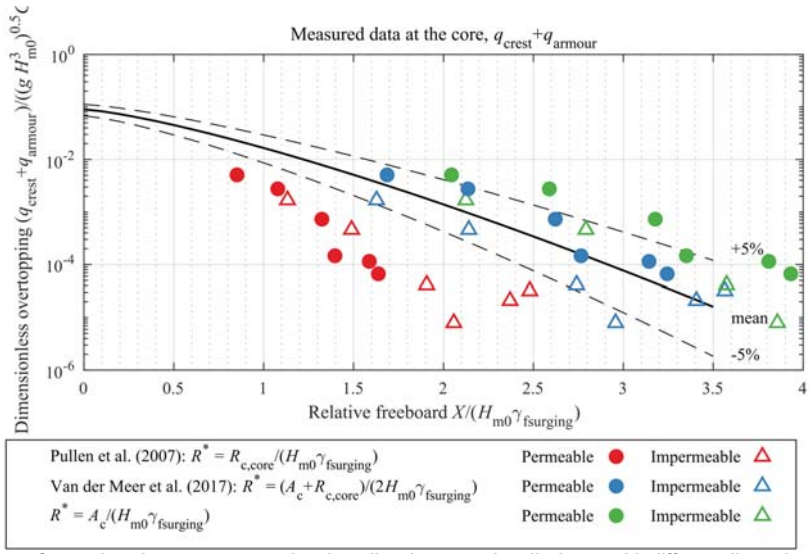

Figure 7. Comparison between measured and predicted overtopping discharge with different dimensionless freeboard definitions. Data is for the measurements on top of the core. The continuous line shows the predicted wave overtopping discharge by Eldrup and Lykke Andersen (2018b), and the dashed lines show the 90% confidence band.

DISCUSSION

New model tests with measurements of wave overtopping discharge at the rear shoulder of the armour crest and the core crests were made. Models with permeable and impermeable core were used. The results showed that in the model with impermeable core, relatively much larger discharges through the armour layer took place than in the model with permeable core. The results also showed that reliable predictions of the discharge over the armour crest plus the discharge through the armour layer can be obtained when using $(A_c+R_{c,core})/2$ as the relative freeboard in the formula by Eldrup and Lykke Andersen (2018b). Furthermore, the results showed that the discharge overtopping the armour crest could be estimated by using A_c as freeboard in the formula by Eldrup and Lykke Andersen (2018b).

Recommendations given in the first and the second editions of the EurOtop Manual with respect to the relative freeboard in wave overtopping predictions are discussed. The manual recommends only one value for estimation of the wave overtopping, while the present paper recommends more freeboards to be used dependent on the failure mode under investigation. For example, installations on top of the armour crest are only exposed to discharges over the armour crest, while the rear slope is also exposed to the discharge through the armour layer.

As the present research included a limited number of tests more tests should be performed in order to verify the recommendation for relative freeboard in prediction of overtopping discharges through the armour layer. Furthermore, it is recommended to study the influence of the discharge on the rear slope stability.

REFERENCES

Besley, P. 1999. Overtopping of seawalls – design and assessment manual, *R & D Technical Report W 178*, Environment Agency, Bristol, ISBN 1-85705-069-X.

Bruce, T., Van der Meer, J.W., Franco, L., and Pearson, J.M. 2009. Overtopping performance of different armour units for rubble mound breakwaters, *Coastal Engineering*, 56, pp. 166–179.

Burcharth, H.F., Liu, Z., and Troch, P. 1999. Scaling of Core Material in Rubble Mound Breakwater Model Tests, *Fifth International Conference on Coastal and Port Engineering in Developing Countries,* COPEDEC, Cape Town, pp. 1518-1528.

Christensen, N.F., Røge, M.S., Thomsen, J.B., Lykke Andersen, T., Burcharth, H.F., and Nørgaard, J.Q.H. 2014. Overtopping on rubble mound breakwaters for low steepness waves in deep and depth limited conditions, *Coastal Engineering Proceedings*, 34.

Eldrup, M.R., and Lykke Andersen T. 2018a. Applicability of Nonlinear Wavemaker Theory. *Proceedings of the 7th International Conference on the Application of Physical Modelling in Coastal and Port Engineering and Science*, Santander, Spain.

Eldrup, M.R., and Lykke Andersen T. 2018b. Recalibration of Overtopping Roughness Factors of Different Armour Types. *The 11th Coasts, Marine Structures and Breakwaters Conference*, ISBN 978-0-7277-6317-4, pp. 1011-1020.

Eldrup, M.R., and Lykke Andersen T. 2019. Estimation of Incident and Reflected Wave Trains in Highly Nonlinear Two-Dimensional Irregular Waves, *Journal of Waterway, Port, Coastal, and Ocean Engineering*, Volume 145, Issue 1.

EurOtop, 2007. European Manual for the Assessment of Wave Overtopping. Pullen, T., Allsop, N.W.H., Bruce, T., Kortenhaus, A., Schüttrumpf, H., and Van der Meer, J.W., At: www.overtoppingmanual.com

EurOtop, 2016. Manual on wave overtopping of sea defences and related structures. An overtopping manual largely based on European research, but for worldwide application. Van der Meer, J.W., Allsop, N.W.H., Bruce, T., De Rouck, J., Korenhaus, A., Pullen, T., Schüttrumpf, H., Troch, P., and Zanuttigh, B., www.overtoppingmanual.com

Lykke Andersen, T., Clavero, M., Frigaard, P., Losada, M., Puyol, J.I. 2016. A New Active Absorption System and its Performance to Linear and Non-linear Waves. *Coastal Engineering*, 114, pp. 47-60.

Lykke Andersen, T., Clavero, M., Eldrup, M.R., Frigaard, P., Losada, M., 2018. Active Absorption of Nonlinear Irregular Waves. *Coastal Engineering Proceedings*, 36.

Molines, J., Herrera, M.P., and Medina, J.R., 2018. Estimations of Wave Forces on Crown Walls Based on Wave Overtopping Rates. *Coastal Engineering*, 132, pp. 50-62.

Tavakkol, Sasan, and Patrick Lynett, 2017. Celeris: A GPU-accelerated open source software with a Boussinesq-type wave solver for real-time interactive simulation and visualization, *Computer Physics Communications*, 217, pp. 117-127.

Zhang, H., Schäffer, H.A., and Jakobsen, K. P. 2007. Deterministic combination of numerical and physical coastal wave models, *Coastal Engineering*, 54, pp. 171-186.

Wave Overtopping and Stability Performance of Rubble Mound Breakwaters Exposed to Shallow Water Waves

by Mads Røge Eldrup

SUMMARY

Today, rubble mound breakwaters are used mainly for coastal protection or construction of harbour basins. For these structures, the typical wave conditions are breaking waves on shallow water. However, the typical design tools are mainly based on physical model tests with deep water wave conditions. Until the last decade, linear and mildly nonlinear wave generation methods existed which required a long foreshore to perform shallow water wave tests. Furthermore, no nonlinear wave separation methods existed. To measure the incident waves the tests would therefore have to be repeated without the model but with a effective passive absorption system.

This thesis investigates the applicability of existing wave generation methods. Guidelines are given for reproducing waves in the laboratory as close as possible to those found in nature. New highly nonlinear wave separation methods for regular and irregular waves are established. The work in this thesis makes it possible to perform tests on rubble mound breakwaters with shallow water waves without a long foreshore. Furthermore, the thesis investigates the stability and wave overtopping on the rubble mound breakwaters exposed to shallow water waves. The work has established prediction formulae for both topics, and these increase the reliability for shallow water waves. Furthermore, a formula for the notional permeability factor is established.

ISSN (online): 2446-1636
ISBN (online): 978-87-7210-425-6

AALBORG UNIVERSITY PRESS